

A Thesis Submitted for the Degree of PhD at the University of Warwick

Permanent WRAP URL:

<http://wrap.warwick.ac.uk/82169>

Copyright and reuse:

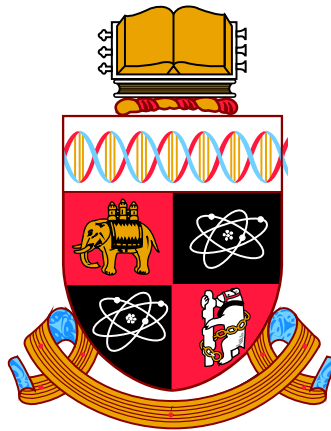
This thesis is made available online and is protected by original copyright.

Please scroll down to view the document itself.

Please refer to the repository record for this item for information to help you to cite it.

Our policy information is available from the repository home page.

For more information, please contact the WRAP Team at: wrap@warwick.ac.uk



Advanced Techniques for Extracting Structural Information from Neutron Diffraction of Glasses

by

Faizani Mohd Noor

Thesis

Submitted to the University of Warwick

for the degree of

Doctor of Philosophy

Department of Physics

July 2016

THE UNIVERSITY OF
WARWICK

Ko Ma, Raihan Idris
Ko Ayoh, Mohd Noor,
Ko Kluago.

– In memory of my loving late grandfather and nephew –

Contents

Title page	i
Contents	iii
List of tables	vii
List of figures	ix
Acknowledgements	xix
Declaration	xx
Abstract	xxi
Abbreviations	xxii

Chapter 1 – Introduction

1.1	Thesis introduction	1
1.1.1	Introduction	1
1.1.2	Objectives	1
1.1.3	Thesis structure	2
1.2	Glass definition: Structure and kinetics	4
1.3	Oxide glass structures	6
1.3.1	Tellurite glasses	6
1.3.2	Borogermanate glasses	7
1.4	References	7

Chapter 2 – Diffraction

2.1	Introduction	9
2.2	Diffraction theory: Neutron and X-ray	9
2.3	Diffraction techniques	12
2.3.1	Introduction	12
2.3.2	Null neutron diffraction technique	12
2.3.2.1	Neutron scattering length, b	12
2.3.2.2	Null neutron diffraction	13
2.3.2.3	Neutron absorption and resonances	14
2.3.3	Isostoichiometric technique	17
2.3.4	Neutron and X-ray complementary technique	17
2.4	Structural information from diffraction	19
2.4.1	Peak position and shape	19
2.4.2	Peak integrated intensity	20
2.5	References	20

Chapter 3 – Experimental and analytical techniques

3.1	Introduction	21
3.2	Glass-crystal structure comparison	21
3.3	Density measurement	21
3.4	Thermal analysis	22
3.5	Raman spectroscopy	23
3.6	X-ray powder diffraction	26
3.7	Energy dispersive x-ray spectroscopy	26
3.8	Secondary ion mass spectroscopy	27
3.9	Synchrotron X-ray diffraction	27
3.10	Nuclear magnetic resonance (NMR)	28
3.11	References	30

Chapter 4 – Tellurites

4.1	Introduction	32
4.2	TeO ₂ crystal structure	32
4.2.1	α , β , γ , and δ polymorphs of TeO ₂	32
4.2.2	Tellurium (IV) environment	33
4.3	Lithium tellurite crystals	34
4.3.1	General structure	34
4.3.2	Tellurium (IV) environment	36
4.3.3	Non-bridging oxygen environments	37
4.3.4	Lithium environment	38
4.4	Lead tellurite crystals	42
4.4.1	General structure	42
4.4.2	Tellurium (IV) environment	43
4.4.3	Non-bridging oxygen environments	47
4.4.4	Lead (II) environment	48
4.5	Glass structures and models	51
4.5.1	Pure TeO ₂ glass	51
4.5.2	Tellurite glasses	52
4.5.3	Te-O bond breaking processes	53
4.6	TeO ₂ structural models	54
4.6.1	Pure TeO ₂ glass	54
4.6.2	Alkali tellurite glasses	55
4.6.3	Non-alkali tellurite glasses	58
4.7	References	59

Chapter 5 – Lithium tellurite (IV) glasses

5.1	Introduction	61
5.2	Sample preparation and characterisation	61
5.2.1	Sample preparation	61
5.2.2	Density measurement	63
5.2.3	Thermal analysis	65
5.2.4	Secondary ion mass spectroscopy	68
5.3	Raman spectroscopy	69
5.4	Neutron diffraction	73
5.4.1	Null and natural samples	73
5.4.2	Comparison with α -TeO ₂ and relevant crystal phases	75
5.4.3	Parameterising complex Te-O distances	78
5.4.4	Extension of the TeO ₂ Model	81
5.4.4.1	Plateau region: $x < 15$ mol%	82
5.4.4.2	Post-plateau region: $x > 15$ mol%	84
5.4.5	Lithium environment	86
5.5	Conclusions	91
5.6	References	93

Chapter 6 – Lead (II) tellurite (IV) glasses

6.1	Introduction	95
6.2	Sample preparation and experimental details	95
6.3	Results – General characterisations	97
6.3.1	Sample quality	97
6.3.2	Density	98
6.3.3	X-ray diffraction	99

6.4	Raman spectroscopy	102
6.5	Total diffraction	104
6.5.1	Neutron and X-ray diffraction	104
6.5.2	Comparison with α -TeO ₂ and related tellurite crystals	106
6.5.3	Parameterising complex Te-O distances	109
6.5.3.1	TeO peak fitting	109
6.5.4	Extension of the TeO ₂ model	110
6.5.4.1	Plateau region	110
6.5.4.2	Post plateau region	111
6.5.5	Lead (II) environment	114
6.5.5.1	PbO distances and coordination number	114
6.5.5.2	Parameterising Pb-O distances	119
6.5.6	PbTe ₅ O ₁₁ and TeO ₂ glass similarity	120
6.6	Conclusion	121
6.7	References	122

Chapter 7 – Alkali borogermanate glasses

7.1	Introduction	124
7.2	Introduction to borate germanate and borogermanate glasses	125
7.2.1	Borogermanate glasses	125
7.2.2	Binary alkali borate glasses	125
7.2.2.1	Boron environment	125
7.2.3	Binary alkali germanate glasses	128
7.2.3.1	Germanium environment	128
7.2.4	Binary borogermanate glasses	130
7.2.4.1	Borate and germanate species	130
7.2.5	Alkali borogermanate glasses	131
7.3	Sample preparation and general methodology	131
7.4	Density	134
7.4.1	Results	134
7.4.2	Binary borogermanate glasses	135
7.4.3	Ternary alkali borogermanate glasses	136
7.5	Raman scattering	140
7.5.1	Introduction	140
7.5.2	Binary borogermanate glasses	141
7.5.3	Lithium borogermanate glasses	142
7.5.4	Potassium borogermanate glasses	144
7.6	¹¹ B MAS NMR	146
7.6.1	Introduction	146
7.6.2	¹¹ B NMR results	150
7.6.2.1	Binary borogermanate glasses	150
7.6.2.2	Lithium and potassium borogermanate glasses	150
7.6.3	Discussion	152
7.6.3.1	Lithium borogermanate glasses and lithium borosilicate model	152
7.6.3.2	Potassium borogermanate glasses and sodium borosilicate model	153
7.6.3.3	Boron in lithium and potassium borogermanate glasses	155
7.7	Neutron diffraction	156
7.7.1	Results	156

7.7.2	n_{BO} (^{11}B NMR and ND) and n_{GeO}	158
7.7.3	Lithium environment	165
7.8	Conclusion	168
7.9	References	168
Chapter 8 – Conclusions and future work		
8.1	Introduction	171
8.2	Tellurite glasses	171
8.3	Borogermanate glasses	174
8.4	References	176
Appendix A		
A.1	Unit nomenclature	177

List of tables

Table	Title	Page
4.1:	<i>The short range order parameters as observed in α-TeO₂, β-TeO₂, γ-TeO₂, and δ-TeO₂ phases. All oxygen atoms shown are bridging oxygen (O_{n/2}) atoms. Long (> 2 Å) axial bonds are represented by the striped cylinder and shorter equatorial bonds are represented by the solid cylinder. The TeO₂ connectivity in γ-TeO₂ is similar to α-TeO₂ but with a different torsion angle. r_{\max} is defined by the upper limit of the first coordination sphere from the T(r) as in Fig. 4.2</i>	33
4.2:	<i>Local order structural parameters in the lithium tellurite crystals.</i>	35
4.3:	<i>Te–NBO environments in alkali tellurite crystals. (O - red; Te – gold; Li – blue)</i>	37
4.4:	<i>Bond parameters of Te–O and Li–O pairs in lithium tellurite crystals.</i>	38
4.5:	<i>Average number of Li atoms bonded to O1a, O1b, and O1c for the cases of n_{LiO} = 4, 4.5, and 5, and the calculated values from the crystal phases.</i>	39
4.6:	<i>Running bond valence sum for Li–O bonds in the lithium tellurite crystals.</i>	40
4.7:	<i>Local order structural parameters in lead tellurite crystals.</i>	42
4.8:	<i>Bond valence calculation of the Te–O bonds in lead tellurite crystals.</i>	46
4.9:	<i>Bond parameters of Te–O and Pb–O pairs in lead tellurite crystals.</i>	47
4.10:	<i>Bond parameters of Te–O1b, Te–O1c, and Te–O2 in lead tellurite crystals.</i>	48
4.11:	<i>Bond parameter for Pb–O pair in lead tellurite crystals</i>	50
5.1:	<i>Glasses appearance by visual observation. The $x = 35$ mol% glass sample was made to confirm no amorphous material is obtained at this composition using this method. ^aMade using a Pt/Rh crucible, ^bMade using a Pt/Au crucible. *Made in a small batch of approximately 1 g for the purpose of Raman analysis.</i>	62
5.2:	<i>Molecular weight MW, density ρ, and molar volume MV values for natural and null $x\text{Li}_2\text{O}-(100-x)\text{TeO}_2$ glasses</i>	65
5.3:	<i>Temperatures, T_g, T_x, and T_c extracted from the differential thermal analysis curve as well as calculated glass stability (towards devitrification) parameter for each glass</i>	67
5.4:	<i>Melting environments of the same glass system taken from the SciGlass database</i>	68

5.5:	<i>Isotopic ratios of ^6Li and ^7Li isotopes in the natural, enriched, and null lithium glasses and natural lithium aluminosilicate mineral crystal. The glass samples (2, 3, 4, and 5) of $x = 20$ mol% were selected for the SIMS analysis. Sample 4 represents clear glass whereas sample 5 represents the cloudy glass with small crystalline regions of the same composition.</i>	68
5.6:	<i>Peak assignment for Raman vibration of Te-O species in TeO_2 glasses</i>	70
5.7:	<i>Peak parameters obtained from fitting of the Raman spectra</i>	72
5.8:	<i>Approximated bond parameters of Te-O1 in the lithium tellurite glasses as in related phases of liquid TeO_2 and lithium tellurite crystals.</i>	81
5.9:	<i>Peak parameters for Li-O pair correlation functions</i>	88
6.1:	<i>Neutron beam exposure time for PbO–TeO_2 glass samples</i>	97
6.2:	<i>Glass compositions and density values for PbO–TeO_2 glasses.</i>	98
6.3:	<i>Physical appearance and diffraction information. *Crystal diffraction spots were revealed in the synchrotron X-ray diffraction experiment.</i>	102
6.4:	<i>Peak parameters for Te-O and Pb-O peaks obtained from NXFit</i>	110
6.5:	<i>Peak parameters for Pb-O and O-O peaks obtained from NXFit</i>	119
7.1:	<i>Raman shift values for borate units [24-26, 28-29], b=broad, s=sharp.</i>	127
7.2:	<i>Raman shift values for germanate units [19, 37-40]</i>	129
7.3:	<i>Alkali borogermanate glasses in this study (with EDX K/Ge value, density, and neutron exposure). Typical K/Ge error is shown in parentheses</i>	132
7.4:	<i>n_{BO} for for the lithium and potassium borogermanate glasses</i>	151
7.5:	<i>Li-O peak parameters from peak fitting and integration</i>	167

List of figures

Figure	Title	Page
1.1:	<i>3-dimensional ~ 5 Å thick slices of crystalline (LEFT) and amorphous (RIGHT) SiO₂ [4-5]</i>	4
1.2:	<i>Physical properties of glass-forming melts as a function of temperature</i>	5
2.1:	<i>Schematic of elastic neutron / X-ray diffraction with neutron / X-ray of initial parameters (E_i, k_i) scattered off of the sample with 2θ angle from the initial path with final parameters of E_f and k_f. Momentum transfer vector Q is obtained from the wave vectors k as shown in the figure on the right. Scattered neutron wave / X-ray into a solid angle of ϕ (from y-axis) and 2θ (from z-axis)</i>	10
2.2:	<i>GEneral Materials GEM diffractometer at ISIS, RAL, Oxford UK.</i>	11
2.3:	<i>b values for some isotopes of the elements of the periodic table.</i>	13
2.4:	<i>The effect of correcting the effective density on the absorption correction in $I(Q)$ for each bank.</i>	15
2.5:	<i>The effect of correcting the effective density on the total correlation function $T(r)$.</i>	15
2.6:	<i>The effect of bank angles on resonance range</i>	16
2.7:	<i>Q-dependence of $f(Q)$ in neutron and X-ray diffractions.</i>	18
2.8:	<i>$T^N(r)$ and $T^X(r)$ for PbTe₅O₁₁.</i>	18
3.1:	<i>Differential thermal analysis curve typical of a glass showing glass transition temperatures T_g, crystallisation temperatures T_x and T_c, and melting temperature T_m.</i>	23
3.2:	<i>Stokes, Rayleigh, and anti-Stokes transitions in Raman spectroscopy.</i>	24
3.3:	<i>Reduction of the Raman spectra to remove the Boson peak at low wavenumber.</i>	25
3.4:	<i>X-ray diffraction process according to Bragg's law.</i>	26
3.5:	<i>Zeeman splitting and quadrupolar interaction of ¹¹B isotope in B.</i>	28
3.6:	<i>Magic-angle spinning (54.73°) MAS NMR setup.</i>	29
3.7:	<i>Typical NMR spectrum for ¹¹B in borogermanate glass.</i>	30

4.1:	<i>The basic [TeO₄] unit as in α-TeO₂ crystal. Te (gold) is bonded to O (red) atoms with two short equatorial bonds (<2.00 Å) (grey cylinder) and two long axial bonds (<2.00 Å) (striped cylinder). E is the stereo-chemically active lone-pair of electrons of the Te atom</i>	32
4.2:	<i>Simulated total correlation function T(r) of α-TeO₂, b-TeO₂, and γ-TeO₂ crystals. T(r) for Te-O and O-O pairs are shown in solid red and dotted blue lines respectively. The sum of all pairs is the thicker black line. The T(r) for Te-Te starts at >3 Å. Lorch modification function is used for simulating the T(r).</i>	34
4.3:	<i>Simulated T(r) for the lithium tellurite crystals showing the total (Null Li) correlation function (thick black), Te-O pair correlation (red), Li-O pair correlation (dashed blue), and O-O pair correlation (dotted green). T(r) for (Nat Li) Li-O shows a negative distribution due to the value of average scattering length for the Li at the natural abundance (-1.90).</i>	35
4.4:	<i>Partial Te-O pair distributions in TeO₂, Li₂Te₂O₅, and Li₂TeO₃ crystals for each Te site. The distances can be parameterised with 2 peaks (3 for α-Li₂Te₂O₅) according to the definition of short(r1), long(r2), and longer(2.35) bonds as shown by the vertical lines.</i>	36
4.5:	<i>T(r) for Li-O pair in the lithium tellurite crystals. Average n_{LiO} of 4 is represented by the peak at ~2 Å. The peak at ~2.7 Å is the next nearest Li-O distance found in α-Li₂Te₂O₅.</i>	39
4.6:	<i>Simulated T(r) for Li-O pairs in lithium tellurite crystal for individual Li sites</i>	41
4.7:	<i>Simulated T(r) for the lead tellurite crystals, selected for comparison with the glass structure. Te-O pair (red area), Pb-O pair (blue area), and O-O pair (green dotted).</i>	43
4.8:	<i>Te environments in tellurite, lithium tellurite, and lead tellurite crystals. r_{TeO} is compared to the short and long bonds of 1.879 and 2.121 Å found in α-TeO₂ (vertical lines). The evolution of the longer long bond of Te-O is a function of composition, regardless of the modifier cation type.</i>	44
4.9:	<i>Simulated T(r) for Te-O pairs in the selected lead tellurite crystals. Orange area marks the sum of Te-O peaks due to Te-O pairs within the first coordination shell.</i>	45
4.10:	<i>Partial T(r) for each Te site in PbTe₅O₁₁.</i>	45
4.11:	<i>Simulated T(r)_{PbO} for the lead tellurite crystals. Orange area is the sum of the average n_{PbO} of about 8.</i>	49
4.12:	<i>Partial T(r)_{PbO} simulated using thermal parameters from the crystal structure and a value similar to the experimental results.</i>	51
4.13:	<i>[TeO_{4/2}] ↔ [TeO_{2/2}O] equilibria. Units taken from McLaughlin et al. [26]</i>	52

4.14:	Upper and lower limits of second oxide M_aO_b in binary M_aO_b - TeO_2 glasses [27]	52
4.15:	$[TeO_{4/2}] \leftrightarrow [TeO_{3/2}O^-]$ equilibrium for $2Li^+ + O^{2-} + 2[TeO_4] \leftrightarrow 2([TeO_4]^- Li^+)$. McLaughlin et al. [26]	53
4.16:	$[TeO_{3/2}O^-] \leftrightarrow [TeO_{1/2}O^{2-}]$ equilibrium. Units taken from McLaughlin et al. [26]	53
4.17:	Transformation of $[TeO_4]$ unit to $[TeO_3]$ unit via intermediate $[TeO_{3+1}]$ unit. $[TeO_4]$ unit is represented by the TeO_2 polyhedron in α - TeO_2 crystal. This intermediate unit is drawn with the longest bond in scale as found in α - $Li_2Te_2O_5$ (longest $r > 2.2$ Å). The resonance structure is not shown in the $[TeO_3]$ unit. This unit is represented by a TeO_3 polyhedron found in Li_2TeO_3 .	54
4.18:	The fractions of $[TeO_3]$, $[TeO_4]$, $NBO(O2)$, and $BO(O1)$ units as a function of n_{TeO} as derived in Eqn 4.4 The dotted shows the fractions of the units found in the roller-quenched pure TeO_2 glass corresponding to the n_{TeO} value of 3.68 [24].	55
4.19:	The average n_{TeO} model for TeO_2 glass based on K_2O - TeO_2 glasses. For $x < 14.3$ mol%, n_{TeO} is constant at 3.68. This is based on the n_{TeO} value of 3.68 which was experimentally obtained for pure TeO_2 glass. 14.3 mol% is the deviation point determined by the fractions of $[TeO_3]$ and $[TeO_4]$ units from n_{TeO} . For $x > 14.3$ mol%, n_{TeO} is best fitted with the b value of 1 [28], revealing 25% of the bond valence contribution from O2 (bridging oxygen) sites.	57
4.20:	Figure 4.20: n_{TeO} values for the alkali (Li_2O and K_2O), divalent (PbO and ZnO) and trivalent (B_2O_3 and Al_2O_3) tellurites.	58
5.1:	Phase diagram for the Li_2O - TeO_2 system [2]. There is a eutectic composition at about 22.5 and a peritectic at 30 mol% Li_2O . Two lithium tellurite phases ($Li_2Te_2O_5$ and Li_2TeO_3) are shown in the figure. The 5 glass compositions in this study are marked by the dotted lines.	62
5.2:	(a) The measured densities for the Li_2O - TeO_2 glasses: natural glasses (blue, left-pointed triangle) and null glasses (red, right-pointed triangle) compared to SciGlass data (grey circle) and pure amorphous TeO_2 from Barney et al. [3]. (b) Molar volumes of the glasses (symbols as in (a)) compared with the SciGlass data. Error bars for the natural and null glasses are within the points shown.	63
5.3:	Calculated number density for constituent atoms as a function of Li_2O composition for both natural and null glasses (red triangles). The number density plots for O and Te atoms in the glasses show the deviational behaviour compared with the crystals (linear fit, dashed black line).	64
5.4:	Figs. (a) to (f) show the thermal analysis curves for $xLi_2O \cdot (1-x)TeO_2$ glasses for $x = 10, 15, 20, 25, 30$ and 35^* mol% showing the heating curve (black, top) and cooling curve (red, bottom) lines for each glass composition. $*x = 35$ mol% is a glass partially-crystallised with $Li_2Te_2O_5$. The glasses were heated at a rate of 10 °C/min and Newtonian cooled. (g) Stack plot of heating curves showing two compositional regions of similar crystallisation behaviour; lower Li_2O compositions, $x = 10, 15$, and 20 mol% with just one exothermic peak, and higher	66

Li₂O compositions, x = 25, and 30 mol% with three exothermic peaks. x = 35 mol% is made up of mostly Li₂Te₂O₅ crystal phase (33.33 mol% of Li₂O). Close resemblance between x = 30 and 35 mol% reflects the proximity of the x = 30 mol% glass to the α/β -Li₂Te₂O₅ phase field.

- 5.5: *The values of T_g for the glasses at different nominal compositions. T_g can be linearly fitted with two lines to highlight the intersection at $x \sim 15$ mol%, similar to the behaviour observed in the density values. Inset shows the glass stability, $T_x - T_g$. The data are fitted with a spline interpolation showing the behaviour of the glass stability as a function of Li₂O content with a maximum stability towards devitrification at $x \sim 20$ mol%. This is supported by the cooling curve for this glass in Fig 5.4 where negligible crystallisation was observed upon cooling. Black circles are the T_g values for the Li₂O-TeO₂ glasses prepared using silica crucible for splat-quenching method and a roller-quenched series. The red circles are the T_g values from the glasses prepared using a similar environment as for the studied glass; using a platinum crucible and splat quenching method.* 67
- 5.6: *Graphical representation of ⁶Li and ⁷Li isotopic percentages in the samples of 1(mineral spodumene), 2(natural glass), 3(null glass), 4(enriched glass), and 5(enriched glass with glass and crystal inclusions). Similar isotope distribution in glassy and glassy/crystalline state is confirmed from SIMS analysis on samples 4 and 5. NB – the spread in values for spodumene indicates the progress of the set-up process.* 69
- 5.7: *Raman spectra for the Li₂O-TeO₂ glasses. The y-axes are (a) normalised measured intensity, (b) normalised reduced intensity. (a) was normalised to the maximum intensity, (b) was reduced by elimination of the Boson peak [15] and (c) is the area-normalised reduced intensity in the region of interest encompassing the Te-O vibrations.* 69
- 5.8: *(a) Comparison of the Raman peak manifold shape from the 10 mol% and 30 mol% glasses with the Raman spectra of the related crystals. (b) Peak de-convolution of the Te-O vibrations according to the peak assignment as in Table 5.6* 71
- 5.9: *(a) showing the peak areas from the fits for each composition and (b) showing the n_{TeO} calculated.* 72
- 5.10: *Distinct scattering ($i(Q)$) and total correlation function ($T(r)$) for the null lithium tellurite glasses. An offset is used between each plot for clarity. $i(Q)$ with a Q maximum value of 35 \AA^{-1} (a) was Fourier-transformed to $T(r)$ (b) for each glass composition.* 74
- 5.11: *Distinct scattering, $i(Q)$, and total correlation function, $T(r)$, for the natural lithium tellurite glasses. An offset is used between each plot for clarity. $i(Q)$ with a Q maximum value of 35 \AA^{-1} (a) was Fourier-transformed to $T(r)$ (b) for each glass composition.* 74
- 5.12: *$T(r)/w_{TeO}$ and $T(r)/w_{O2}$ for the null glasses, stacked and compared with amorphous TeO₂ for each x giving a qualitative comparison of the evolution of the* 75

tellurium-oxygen environment in glasses on addition of Li_2O to $\alpha\text{-TeO}_2$. $T(r)$ for the glasses are weighted to the coefficient of $(2-\delta_{ij})c_i b_i b_j$. * $\alpha\text{-TeO}_2$ data taken from Barney et al.[3]

- 5.13: (a) Te-O and O-O distances, and the magnitude of lone-pair vectors found in $\alpha\text{-TeO}_2$, $\beta\text{-TeO}_2$, $\gamma\text{-TeO}_2$, $\alpha\text{-Li}_2\text{Te}_2\text{O}_5$, $\beta\text{-Li}_2\text{Te}_2\text{O}_5$, and Li_2TeO_3 crystal phases; (b) Comparison of $T(r)$ for $\alpha\text{-TeO}_2$ (green solid line) to the simulated $T(r)$'s for the TeO_2 polymorphs [Barney et al., to be published]. 77
- 5.14: Approximation of $^{\text{Null}}T(r)$ to $\gamma\text{-TeO}_2$ and $\beta\text{-Li}_2\text{Te}_2\text{O}_5$. $T(r)_{\text{Te-O}}$ partials for the glasses, $\gamma\text{-TeO}_2$ crystal, and $\beta\text{-Li}_2\text{Te}_2\text{O}_5$ crystals are shown in open circle, blue, and dashed green respectively. Simulated $T(r)_{\text{Te-O}}$ for the glasses (red), simulated from the mixture of the crystals. 78
- 5.15: Peak fitting of the correlation function for $x = 10$ mol% (null $\text{Li}_2\text{O}\text{-TeO}_2$ glass) with three (arbitrary) Gaussians convoluted with the Lorch modification function [22]. For simplicity, O-O distribution is represented by a Gaussian of which also contains longer Te-O distances 79
- 5.16: Average tellurium to oxygen coordination number (n_{TeO}) as a function of Li_2O content, obtained by integration, compared to the values obtained in $\text{K}_2\text{O}\text{-TeO}_2$ glasses [3]. The error for the average $n_{\text{TeO}}(\text{Li})$ is shaded in grey. 80
- 5.17: The selection of the average n_{TeO} for $x < 15$ mol% (plateau region) and its effect on the average n_{TeO} fit quality for $x > 15$ mol% (post-plateau region). 82
- 5.18: The TeO_2 Model for $\text{Li}_2\text{O}\text{-TeO}_2$ system for plateau ($x < 15$ mol%) and post-plateau ($x > 15$ mol%) regions. 84
- 5.19: The number of required Li-O bonds in both plateau and post-plateau regions and the contribution from O1 (O1a, O1b, O1c) and O2 type of oxygen atoms as a function of R unit of Li_2O in 1 unit of TeO_2 . 85
- 5.20: n_{LiO} in various glass formers. Legend: a [34], b[35], c[36], d[40], e[37], and f[38]. Ref: a, b, c, and f were obtained by isotope substitution neutron diffraction, d was obtained by molecular dynamics and e was obtained by the combination of natural neutron diffraction combined with molecular dynamics. 87
- 5.21: $T(r)$ of null (black) and natural (red) glasses and the difference (blue) representing the lithium partial correlation functions. 88
- 5.22: Difference plots stacked with fits. Dotted lines are the $T(r)$ for Li-O partials, red and green peaks are the fitted peaks, and black lines are the residuals of the fit. The red peak contributes to the n_{LiO} value of 4. 89
- 5.23: n_{LiO} obtained by means of peak fitting with two Gaussians at 2.00 and 2.25 Å. Higher n_{LiO} observed in $x = 10, 15$, and 20 mol% Li_2O is due to the contribution from the peak at 2.25 Å (r_{LiO} as seen in $\beta\text{-Li}_2\text{Te}_2\text{O}_5$ phase) Error bars are large due to poor signal to noise ratio because of the ^6Li absorption. 90

5.24:	Comparison of r_{LiO} found in various lithium tellurite crystals as well as in Li_2O . Slight shift is observed.	90
6.1:	Phase diagram for the $PbO-TeO_2$ system reproduced from Stavrakieva et al.[1].	96
6.2:	(a) shows the measured densities for the $PbO-TeO_2$ glasses based on nominal composition (red upward pointed triangle) and based on EDX analysis (blue downward pointed triangle) compared to the SciGlass data (open circle). (b) shows the calculated molar volumes of the glasses (symbols as in (a)) compared with the SciGlass data. Error bars for the glasses are within the points shown. (c), (d), and (e) show the calculated number densities for constituent atoms, symbol as in (a). Black filled circles are values from the crystal phases ($\gamma-TeO_2$, $PbTe_5O_{11}$, $Pb_2Te_3O_8$, $PbTeO_3$) with the dashed line being the line of best fit. (1), (2), and (3) in (c) reveal groups of O number density which may result from different preparation environments and/or structural differences.	98
6.3:	High energy X-ray diffraction patterns for $xPbO-(100-x)TeO_2$ glasses for $x = 10, 12.5, 15, 17.5, 20(a)$ and 25 mol%. Significant crystallisation is seen in 20(a) and 25 mol% PbO samples. Negligible crystallisation is seen in 10 mol% PbO sample (spots ringed in red).	100
6.4:	1D plots of high energy X-ray diffraction spectra for $xPbO-(100-x)TeO_2$ glasses for (a) $x = 10$ and 25 mol% compared to published data for $PbTe_3O_7$ from PanAnalytical software database and (b) stack plot of $x = 10, 12.5, 15, 17.5, 20(a)$ and 25 mol%	101
6.5:	(a) experimentally obtained Raman spectra (normalised); (b) reduced and area-normalised Raman spectra showing the region of interest encompassing the $Te-O$ vibrations; (c) Raman peak deconvolution of contributions from $[TeO_4]$ and $[TeO_3]$ units; (d) area of the peaks in (c) as a function of x ; and (e) average n_{TeO} obtained compared to the values from Sekiya et. al. [17] $x = 20$ represents 20(a) mol% of PbO	103
6.6:	(a) shows the distinct scattering function $i(Q)$ for $PbO-TeO_2$ glasses with 10, 12.5, 15, 17.5, and 20(b) mol% PbO and (b) shows the total correlation function $T^N(r)$ obtained by taking the Fourier transforms of the functions in (a) with a Q_{max} value of 35 \AA^{-1}	105
6.7:	(a) shows the distinct scattering function $i(Q)$ for $PbO-TeO_2$ glasses with 10, 12.5, 15, 17.5, and 20(a) mol% PbO and (b) shows the total correlation function $T^x(r)$ obtained by taking the Fourier transforms of the functions in (a) with a Q^{max} value of 20 \AA^{-1}	105
6.8:	The sums of fit and the residuals from the simultaneous fitting of the X-ray and neutron diffraction data.	106
6.9:	Comparison of the total $T(r)$ (weighted to the $Te-O$ pair weighting factors) to highlight the $Te-O$ pair environment in the glasses with respect to the pure TeO_2 glass.	107

6.10:	<i>Comparison of the weighted $T(r)$ of 15PbO-85TeO₂ to pure TeO₂ glass and of 17.5PbO-82.5TeO₂ to Null20Li₂O-80TeO₂ glasses to show the plateau and post-plateau similarities respectively. Individual Te-O peaks represent the 17.5PbO sample.</i>	107
6.11:	<i>The residual of $T(r)$ 20PbO-80TeO₂ – $T(r)$ Null20Li₂O-80TeO₂ glasses, showing the “PbO” peak. The data for the 20PbO(b) sample are used.</i>	108
6.12:	<i>Fitted Te-O peaks for 17.5PbO-82.5TeO₂ glass from NXFit</i>	109
6.13:	<i>The determination of b value for PbO-TeO₂ glasses</i>	112
6.14:	<i>The average n_{TeO} for PbO-TeO₂ glasses, compared with Li₂O-TeO₂ and K₂O-TeO₂ glasses</i>	113
6.15:	<i>The number of bonds in the plateau and post-plateau regions for $b = 2.1$, and $b = 1.15$.</i>	114
6.16:	<i>The average PbO coordination number, n_{PbO}, reported in various binary lead glasses. Ref: d [22], b [19], e [26], f [24], a [20], c [21], h [2] and g [25].</i>	115
6.17:	<i>PbO distance, r_{PbO}, reported for various binary lead glasses as in Fig. 6.15 and references therein. The distances are as expected from Brese and O’Keefe [27]</i>	115
6.18:	<i>Figure 6.18: PbO and OO peaks from NXFit in 17.5PbO-82.5TeO₂ and PbTe₅O₁₁.</i>	116
6.19:	<i>Fitted peaks for 17.5PbO-82.5TeO₂ glass from NXFit</i>	117
6.20:	<i>The distances of PbO and OO in PbTe₅O₁₁ from 2.4 to 3.1 Å</i>	117
6.21:	<i>Contribution of short r_{OO} (O8) in an edge-sharing connection in PbTe₅O₁₁.</i>	118
6.22:	<i>Contribution of short r_{OO} (O9) in an edge-sharing connection in PbTe₅O₁₁.</i>	118
6.23:	<i>Typical corner-wise TeO₂ network connectivity in the glasses where the r_{OO} is about 2.6 Å.</i>	118
6.24:	<i>Similarity of $T(r)_{\text{TeO}}$ in pure TeO₂ glass, PbTe₅O₁₁, and PbO-TeO₂ glasses</i>	120
6.25:	<i>Individual TeO environment for 5 Te sites in PbTe₅O₁₁</i>	121
7.1:	<i>Superstructural borate units [27]</i>	126
7.2:	<i>Figure 7.2: n_{BO} in alkali borates and the borate model, $n_{\text{BO}} = 3 + x/(100-x)$, n_{BO} values for Li, Na, K, Rb, and Cs were taken from [8]. The thick dashed line represents initial $[\text{BO}_4]^-$ formation (Eqn. 7.1)</i>	126

7.3:	<i>Raman spectra for lithium and potassium borate glasses, taken from Dwivedi and Khanna [25]</i>	127
7.4:	<i>n_{BO} in alkali germanates, a[31], b[35], c[32, 34],d[33] and the germanate model [21]</i>	129
7.5:	<i>Raman spectra for lithium and potassium germanate [17].</i>	130
7.6:	<i>Optimised bridging oxygen environments in binary borogermanate glasses [41].</i>	131
7.7	<i>Ternary plot for nominal glass compositions in this study</i>	133
7.8:	<i>K/Ge ratio from EDX and nominal composition</i>	134
7.9:	<i>The density value and its derivatives for the binary borogermanate glasses</i>	135
7.10:	<i>Density plot for lithium and potassium borogermanate glasses</i>	137
7.11:	<i>Molar volume plot for lithium and potassium borogermanate glasses</i>	138
7.12:	<i>Number density plot for B and Ge in lithium and potassium borogermanate glasses</i>	139
7.13:	<i>Number density plot for O in lithium and potassium borogermanate glasses</i>	139
7.14:	<i>Number density plot for Li and K in lithium and potassium borogermanate glasses</i>	140
7.15:	<i>a) Raman spectra of pure GeO_2 glass (solid black line) and binary borogermanate glasses (solid colour lines) with their simulated spectra from pure GeO_2 and pure B_2O_3 glasses (dashed lines); (b), (c), and (d) are the same spectra divided into 3 regions: 100-360, 300-600, and 600-900 cm^{-1} to highlight the region of interest for Ge-O and B-O vibrations.</i>	141
7.16:	<i>Assignment of borate and germanate vibrations in lithium borogermanate glasses</i>	142
7.17:	<i>The Raman spectra of the lithium borogermanate glasses.</i>	143
7.18:	<i>LBG Raman spectra compared to LG, taken from Henderson [17].</i>	144
7.19:	<i>Raman spectra for potassium borogermanate glasses, compared to potassium germanate glasses</i>	145
7.20:	<i>Vibrations of B-O associated with NBO in KBG glasses</i>	146
7.21:	<i>The lithium [1] and sodium [2] borosilicate models for n_{BO}</i>	148

7.22:	<i>The reedmergnerite group, taken from [27]</i>	148
7.23:	<i>The mechanism of alkali distribution in borosilicate network</i>	149
7.24:	<i>^{11}B MAS NMR spectra for vitreous B_2O_3 and binary borogermanate glasses</i>	150
7.25:	<i>^{11}B NMR spectra for the lithium and potassium borogermanate glasses</i>	151
7.26:	<i>Comparison of the n_{BO} for the LBG glasses to the lithium borosilicate model [1]</i>	152
7.27:	<i>Comparison of the n_{BO} for the KBG glasses to the sodium borosilicate model</i>	154
7.28:	<i>^{11}B NMR spectra for $\text{M}_2\text{O}-\text{BO}_{1.5}-\text{GeO}_2$ ($\text{M}=\text{Li}$ (dashed blue, 14.15 T) and K (solid pink, 14.1 T))</i>	155
7.29:	<i>Total correlation function $T(r)$ and distinct scattering $i(Q)$ for lithium borogermanate glasses</i>	157
7.30:	<i>Total correlation function $T(r)$ and distinct scattering $i(Q)$ for potassium borogermanate glasses</i>	158
7.31:	<i>Parameterisation of the B-O peak corresponding to $[\text{BO}_3]$ and $[\text{BO}_4]$ units</i>	159
7.32:	<i>n_{BO} and n_{GeO} for LBG glasses from various methods</i>	161
7.33:	<i>n_{BO} and n_{GeO} for KBG glasses from various methods</i>	161
7.34:	<i>$T(r)$ of LBG and KBG glasses fitted with a peak corresponding to a $[\text{GeO}_4]$ to highlight the necessity of more peak(s) corresponding to a higher coordinated $[\text{GeO}_{4+}]$ unit.</i>	162
7.35:	<i>Comparison of the $T(r)_{\text{GeO}}$ for LBG and KBG glasses highlighting the area, hence n_{GeO} difference.</i>	163
7.36:	<i>n_{GeO} and n_{BO} agreement in LBG glasses</i>	164
7.37:	<i>n_{GeO} and n_{BO} agreement in KBG glasses</i>	165
7.38:	<i>$T(r)$-Nat, $T(r)$-Null, and $T(r)$-Difference for the selected samples of 20 mol% Li_2O for each B series</i>	165
7.39:	<i>$T(r)$-Difference for the selected samples of 20 mol% Li_2O for each B series with Li-O peaks</i>	166
7.40:	<i>Li site (1/1) found in approximated LiBGeO_4 crystal phase [60].</i>	167
7.41:	<i>Average n_{LiO} in $20\text{Li}_2\text{O}-x\text{BO}_{1.5}-(80-x)\text{GeO}_2$ for $x = 10, 20$, and 30 mol%</i>	167

8.1:	<i>Molar volume and number density for constituent atoms in $\text{Li}_2\text{O}-\text{TeO}_2$ and $\text{PbO}-\text{TeO}_2$ glasses. Red dashed line is a guide-to-the-eye fit, connecting the glasses and the pure-TeO_2 glass ($\alpha\text{-TeO}_2$).</i>	172
8.2:	<i>n_{TeO} for $\text{Li}_2\text{O}-\text{TeO}_2$, $\text{K}_2\text{O}-\text{TeO}_2$, and $\text{PbO}-\text{TeO}_2$ glasses</i>	173
8.3:	<i>Glass compositions of $\text{M}_2\text{O}-\text{BO}_{1.5}-\text{GeO}_2$ for $\text{M} = \text{Li}$ and K in this study</i>	175

Acknowledgement

First and foremost, I would like to express my gratitude to my supervisor, Dr. Diane Holland. Without her, this would not be possible. Truly, from the bottom of my heart, there are no words I could use to describe my biggest gratitude to her.

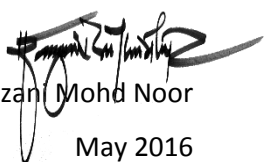
Secondly, I would like to thank my co-supervisors; Dr. Alex Hannon, Dr. Emma Barney, and Dr. Oliver Alderman for all the help with neutron and X-ray diffraction analysis, and Dr. Mark Newton with the Raman (and EPR) instrumentation. I would also like to thank Prof. Ray Dupree and Dr. Tom Kemp for the help with nuclear magnetic resonance, Dr. Chris Benmore (and Dr. Oliver Alderman) for the synchrotron X-ray diffraction data from APS, Argonne National Lab, USA, Dr. David Walker for the X-ray diffraction facility, Dr. Richard Morris for the secondary ion mass spectroscopy (SIMS) analysis, Dr. Ian Farnan for the mineral for SIMS analysis, Mr Dave Hammond for the thermogravimetry analysis, Mr. Steve York for the energy dispersive X-ray facility.

The Department of Physics, University of Warwick, STFC's Rutherford Appleton Laboratory, Advantage West Midlands, European's Society of Glass Technology, Universiti Teknologi Malaysia, and Ministry of Higher Education of Malaysia are thanked for their contribution to this research (facilities, opportunities, and financial)

Finally, not forgetting my friends and housemates, whom I shall not forget to mention, Luke, Kye, Alifah, Ari, Midi, Wan, Pian, Shira, Afiq, Shairani, Zahid, and also a special shout-out to Ms. Susan Tatlock, the postgraduate Physics coordinator for such an excellent support.

Declaration

I declare that the work presented in this thesis is my own except where stated otherwise, and was carried out entirely at the University of Warwick, during the period of May 2012 to May 2016, under the supervision of Dr. Diane Holland. The research reported here has not been submitted, either wholly or in part, in this or any other academic institution for admission to a higher degree. It is anticipated that further part of this work will be submitted for publication in due course.



Faizani Mohd Noor
May 2016

Abstract

The structures of lithium and lead tellurite glasses ($\text{Li}_2\text{O}-\text{TeO}_2$ and $\text{PbO}-\text{TeO}_2$) are studied using the combinations of neutron diffraction, isotope substitution neutron diffraction, and synchrotron X-ray diffraction. Additional complementary methods such as density measurement, thermal analysis and Raman spectroscopy show that the tellurite networks in lithium and lead tellurite glasses exhibit similar behaviour as a function of composition. From the diffraction data, real-space interatomic information on the glasses was extracted. The local environments of Te remain largely unchanged in both glasses if the second content is less than 15 mol%, as reported earlier for $\text{K}_2\text{O}-\text{TeO}_2$. For Li_2O or PbO contents greater than 15 mol%, however, the average Te-O coordination number changes with composition and differently for the two oxides. A TeO_2 Model, which has been successfully applied to $\text{K}_2\text{O}-\text{TeO}_2$ glasses, is extended to Li^+ and Pb^{2+} . By comparing the total correlation functions of the glasses to relevant crystal phases, the short-range parameters of the crystals can be used to optimise the model for Li^+ and Pb^{2+} and explain the value of the average coordination number of Te. The environments of Li^+ and Pb^{2+} were extracted using isotope substitution neutron diffraction (Li) and complementary neutron-X-ray diffraction (Pb). In the glasses studied (10, 15, 20, 25 and 30 mol% Li_2O and 10, 12.5, 15, 17.5 and 20 mol% PbO), both Li^+ and Pb^{2+} behave as modifiers with the average $n_{\text{LiO}} = 4 - 5$ and $n_{\text{PbO}} = 8$ with the distances r_{LiO} and r_{PbO} comparable to crystal phases of similar composition.

The structures of lithium and potassium borogermanate glasses are studied using the combinations of neutron diffraction, isotope substitution neutron diffraction, and ^{11}B MAS NMR. From the complementary methods such as density measurement, and Raman spectroscopy, changes are seen to occur in both borate and germanate networks. From ^{11}B NMR, the average B-O coordination number, n_{BO} , in lithium borogermanate glasses is different from n_{BO} in potassium borogermanate glasses of the same stoichiometry and resembles the behaviour of Li^+ and K^+ in borosilicate glasses, as described by the Zhong's lithium borosilicate model and Dell and Bray's sodium borosilicate model. From neutron diffraction data (null isotope neutron diffraction for lithium borogermanate), the average Ge-O coordination number n_{GeO} is extracted and, like n_{BO} , n_{GeO} in lithium borogermanate is different from potassium borogermanate. In the former, n_{GeO} increases as a function of Li_2O , whilst in the latter, n_{GeO} shows a maximum at about 20% K_2O . For Li^+ , the average Li-O coordination number n_{LiO} can be obtained using the difference technique (using diffraction data from samples made with natural and null-scattering lithium isotopes). For the limited samples examined, n_{LiO} was found to have a value of 4 to 5 with two distinct Li-O distances which can be assigned to $\text{Li}-\text{O}_\text{B}$ and $\text{Li}-\text{O}_\text{Ge}$ distances.

Abbreviations

BV	Bond valence
EDX	Energy dispersive X-ray
BO	Bridging oxygen
EXAFS	Extended x-ray absorption fine structure
FWHM	Full Width at Half Maximum
GEM	General Materials (diffractometer)
ISND	Isotope substitution neutron diffraction
LP	Lone-pair
MAS	Magic Angle Spinning
NBO	Non-bridging oxygen
ND	Neutron diffraction
NMR	Nuclear Magnetic Resonance
RMS	Root mean square
RS	Raman spectroscopy
SIMS	Secondary ion mass spectroscopy
TO	Terminal oxygen
XRD	X-ray Diffraction

Chapter 1 – Introduction

1.1 Thesis introduction

1.1.1 Introduction

This thesis is entitled “*Advanced Techniques for Extracting Structural Information from Neutron Diffraction of Glasses*”. Its aim is to study the structure of complex oxide glasses by means of diffraction (neutron and/or X-ray) techniques and to apply various contrast techniques (null and natural isotope neutron diffraction (ND) difference technique, neutron and X-ray diffraction complementary technique, and isostructural neutron diffraction technique). These contrast techniques simplify the data obtained and thereby extract information about specific atom environments. Other techniques, such as nuclear magnetic resonance (NMR) and Raman scattering (RS), are also used as complementary probes of the glass structure.

1.1.2 Objectives

In this study, two series of binary tellurite glasses ($\text{Li}_2\text{O}-\text{TeO}_2$ and $\text{PbO}-\text{TeO}_2$), and two series of ternary alkali borogermanate glasses ($\text{Li}_2\text{O}-\text{B}_2\text{O}_3-\text{GeO}_2$ and $\text{K}_2\text{O}-\text{B}_2\text{O}_3-\text{GeO}_2$) are studied.

In the binary tellurite glasses, the focus of the study is to probe the environments of Te(IV) atom in terms of:

- a) The change in the Te environment as a function of the composition of the second oxide of Li_2O (univalent, alkali metal oxide, typical modifier), or PbO (divalent, heavy metal oxide, typical intermediate) and deduce a TeO_2 model for each case.
- b) The stereochemical activity of the lone-pair (LP) cation on Te (one $5s^2$ lone-pair) in the presence of the second oxide of Li_2O (with no lone-pair) or PbO (with one $6s^2$ lone-pair).

This involves the:

- I. Study of the environment of Te and Li in $\text{Li}_2\text{O}-\text{TeO}_2$ glasses using isotope substitution neutron diffraction (ISND) technique, which is to:
 - a. Measure the average Te–O and Li–O coordination numbers, n_{TeO} and n_{LiO} .
 - b. Measure the average Te–O and Li–O bond distances, r_{TeO} and r_{LiO} .
 - c. Probe the $[\text{TeO}_n]$ and $[\text{LiO}_n]$ species/units present in the glasses.

- d. Compare with the TeO_2 Model for alkali metal oxides.
- II. Study of the environment of Te and Pb in $\text{PbO}-\text{TeO}_2$ glasses using a combination of neutron and X-ray diffraction techniques, which is to:
- a. Measure the average Te–O and Pb–O coordination numbers, n_{TeO} and n_{PbO} .
 - b. Measure the average Te–O and Pb–O bond distances, r_{TeO} and r_{PbO} .
 - c. Probe the $[\text{TeO}_n]$ and $[\text{PbO}_n]$ species/units present in the glasses.
 - d. Compare with the TeO_2 Model for alkali metal oxides.

In the ternary borogermanate ($\text{M}_2\text{O}-\text{B}_2\text{O}_3-\text{GeO}_2$, $\text{M} = \text{Li}$, and K) glasses, the focus of the study is to probe the environments of B and Ge in a mixed glass former system in terms of:

- a) The effect of different alkali metal (Li and K) on the B environment in the ternary borogermanate glasses.
- b) The effect of different B environment on the Ge environment in both $\text{M} = \text{Li}$ and K systems.

This involves the study of alkali borogermanate ($\text{M}_2\text{O}-\text{B}_2\text{O}_3-\text{GeO}_2$, $\text{M} = \text{Li}$ and K) glasses using the combination of standard neutron diffraction, isotope substitution neutron diffraction and ^{11}B nuclear magnetic resonance techniques, which is to:

- a. Measure the average B–O coordination number, n_{BO} for $\text{M} = \text{K}$ and Li
- b. Measure the average Ge–O coordination number, n_{GeO} for $\text{M} = \text{K}$ and Li
- c. Measure the average B–O bond distance, r_{BO} for $\text{M} = \text{K}$ and Li
- d. Measure the average Ge–O distance, r_{GeO} for $\text{M} = \text{K}$ and Li
- e. Probe the $[\text{BO}_n]$ and $[\text{GeO}_n]$ species present in the glasses for $\text{M} = \text{K}$ and Li
- f. Deduce a B_2O_3 (in ternary borogermanate) model for $\text{M} = \text{K}$ and Li
- g. Deduce a GeO_2 (in ternary borogermanate) model for $\text{M} = \text{K}$ and Li
- h. Compare with the alkali borosilicate models

1.1.3 Thesis structure

Chapter 1 discusses the introduction of the thesis, including the objectives of the study, and the thesis structure. A brief introduction of the glass theory and the glass systems of interest in this study (tellurite and borogermanate) is also included.

The theory of the main probe used in this study (diffraction) is discussed in Chapter 2. Two sources of diffraction (neutron and X-ray) are considered. The chapter also discusses

the specific approaches used in this study, for instance, the null neutron diffraction technique, the isostoichiometric technique, and the neutron and X-ray complementary diffraction technique. The methods for extracting structural information from the diffraction data are discussed, which includes interpretation in terms of short range analysis of the glass structure.

Chapter 3 discusses the methods used in acquiring and processing the data in this study. The methods include density measurement, thermal analysis, Raman scattering, neutron and X-ray diffraction, as well as nuclear magnetic resonance.

Chapter 4 describes the local environments in pure TeO_2 , $\text{Li}_2\text{O}-\text{TeO}_2$ and $\text{PbO}-\text{TeO}_2$ crystals, in terms of average distances and coordination numbers as a function of composition and type of modifier. Important approximation parameters are obtained from these crystal structures which are later used in the glass short-range structure analysis. The literature on tellurite glass structure is then reviewed. This includes the structure of pure TeO_2 glass and alkali tellurite glasses. The mechanism of TeO_2 network changes as a function of a modifier is also discussed, which later serves as a basis for understanding the $\text{Li}_2\text{O}-\text{TeO}_2$ and $\text{PbO}-\text{TeO}_2$ glasses. The chapter later describes the lone-pair activity of Te in pure TeO_2 , lithium TeO_2 , and lead TeO_2 crystals.

Chapter 5 describes the preparation of the null and natural lithium tellurite glass samples and their general characterisations, including determination of the isotopic ratio of $^6\text{Li}/^7\text{Li}$. Raman scattering is used to identify species in the glasses and derive a semi-quantitative estimate of the average Te-O coordination number n_{TeO} . In the neutron diffraction section, the total correlation functions $T(r)$ for the null glasses are used to obtain the r_{TeO} distribution and average n_{TeO} as a function of the modifier Li_2O content, x , which are compared with pure TeO_2 and the related lithium tellurite crystals to highlight the differences and similarities in both Te and O environments. As will be described in the chapter, the average $n_{\text{TeO}}(x)$ values obtained are discussed based on two regions, plateau ($x < 15$ mol%) and post-plateau ($x > 15$ mol%). The lithium environment is obtained from the natural – null difference $T(r)$.

Chapter 6 describes the preparation method of the $\text{PbO}-\text{TeO}_2$ glass samples and their general characterisation. Raman scattering is used to identify species in the glasses and the information used to derive a semi-quantitative estimate of n_{TeO} . The neutron total correlation functions $T^{\text{N}}(r)$ for the glasses are compared with $T^{\text{N}}(r)$ for pure TeO_2 (glass and crystal phases) and $\text{PbTe}_5\text{O}_{11}$ crystal to highlight the differences and similarities in Te, Pb, and O environments. Using both $T^{\text{N}}(r)$ and the X-ray diffraction total correlation function,

$T^x(r)$, the Te-O distance distributions and average n_{TeO} are extracted as a function of the modifier PbO content, x . The average $n_{\text{TeO}}(x)$ values are again discussed based on two regions, plateau ($x < 15$ mol%) and post-plateau ($x > 15$ mol%). The lead environment is later considered in conjunction with the tellurium environment to obtain a consistent description of the glass structure.

Chapter 7 presents preliminary results and discussion for alkali borogermanate glasses (lithium and potassium). Density analysis is initially used to observe the anomalous change (if any) in the borate-germanate glass network and the trend is compared with the alkali borate and germanate glasses. Raman scattering is used to compare the vibrations of various species present in the ternary alkali borogermanate glasses with respect to the binary borate and germanate glasses. The difference in the vibrations (species) formed in the lithium and potassium borogermanate glasses are also discussed to infer that the changes occur in both borate and germanate network. From ^{11}B MAS NMR analysis on these two samples, B environments in lithium and potassium borogermanate glasses are revealed follow the lithium and sodium borosilicate models by Zhong *et al.* [1] and Dell and Bray [2], respectively.

Chapter 8 concludes the study on these glass systems based on the knowledge obtained and recommends some contexts for further study.

1.2 Glass definition: Structure and kinetics

The strict definition of a glass is, a material (solid) that has no long-range order (non-crystalline/amorphous) and exhibits a glass transition temperature [3].

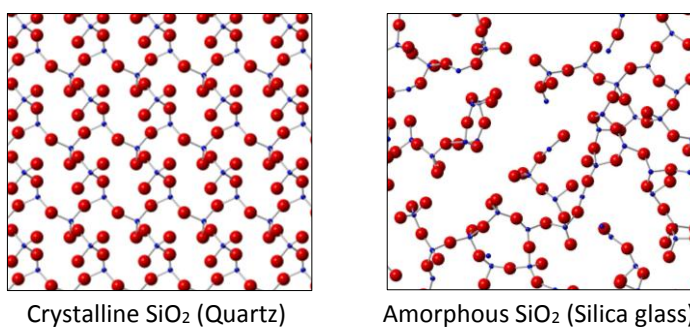


Figure 1.1: 3-dimensional ~ 5 Å thick slices of crystalline (LEFT) and amorphous (RIGHT) SiO₂ [4-5].

From the definition, structurally, a glass is regarded as a solid, which lacks long-range order but possesses short-range order, as shown in Fig. 1.1. In both crystalline and amorphous SiO₂, a silicon atom (blue) is coordinated to 4 oxygen atoms (red) in a tetrahedral shape. In crystalline SiO₂, both short and long-range orders are present whereas in

amorphous SiO_2 , only the short-range order of the tetrahedral $[\text{SiO}_4]$ unit is preserved while disorder is introduced in terms of connectivity and bond angle distribution.

Goldschmidt stated that glasses with formula R_nO_m form more easily when the ratio of the ionic radius of R to O is from 0.2 to 0.4. This mostly corresponds to R coordinated to O in tetrahedral units, as in SiO_2 and GeO_2 . This idea was later expanded by Zachariasen [6] who stated that: (1) oxygen cannot be connected to more than 2 cations, (2) the coordination of the cation is small, 3-4, (3) oxygen polyhedra must share corners, not edges or faces, and (4) for a continuous random network, at least 3 corners must be shared. These characteristics, in general, imply that glass formation is more likely to happen for open structures with a low packing density of polyhedra. These rules can be used to identify the role of oxides in glass network formation: glass network former (conventional or conditional), glass modifier, or intermediate between these two. Apart from his structural theory of glass formation, Zachariasen also stated that to form glasses, the melt must be cooled under proper conditions.

This leads to the kinetic theory of glass formation. In theory, any material can be made into a glass if the melt can be held in a supercooled state (maintaining its liquid form below the melting point). This can be done by preventing nucleation and crystal growth during the cooling process. One of the ways of doing this is by rapidly quenching a melt. The kinetics of glass formation diagram is shown in Fig. 1.2.

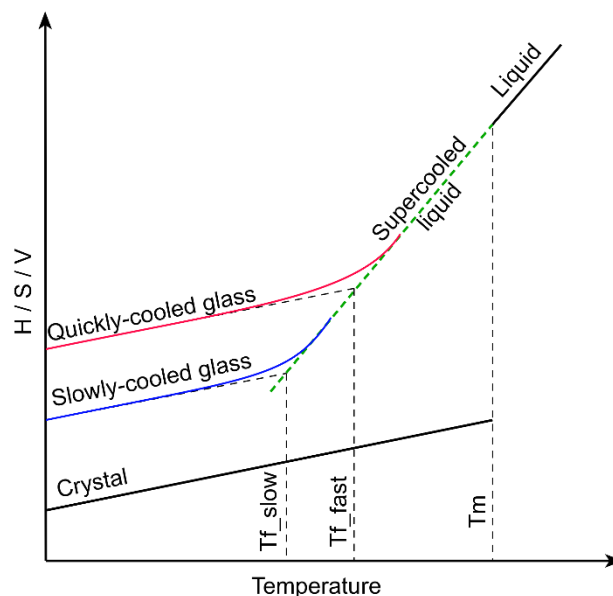


Figure 1.2: Physical properties of glass-forming melts as a function of temperature.

In the figure, if the melt is held at T_m long enough so the molecules can rearrange and the disorder, S decreases to a specific value at a certain enthalpy, H or volume, V, solid

crystalline phase of that melt would form. To form the glass, the melt should be quickly cooled. The glass molecules are “frozen” at the fictive temperature T_f . Higher T_f (consequently higher T_g) would mean higher entropy, enthalpy, or volume (structure resembles more the liquid phase rather than the crystal). The concept of T_f was introduced by Tool [7] and is often used synonymously with the T_g term, even though they are defined differently. T_g is the experimentally measured glass transition temperature, a temperature where its instantaneous viscosity is about 10^{12} Pa s whilst T_f is the actual temperature of the metastable supercooled liquid above the glass transition range (instantaneous temperature of the melt).

An important parameter, when describing or probing glass structure, is the range. For the short range, the parameters are the polyhedral units $[RO_n]$ present, the average coordination number n_{RO} , bond length r_{RO} , and associated bond angles. These parameters can be obtained by experiment and simulation. The parameters for the intermediate range (including neighbouring polyhedra) such as connectivity, bond angle, and bond torsion angle are more difficult to determine experimentally but can be obtained by simulation. In a glass, there is no long-range order.

1.3 Oxide glass structures

1.3.1 Tellurite glasses

Glasses are widely used in daily life because of the specific qualities they possess (transparency, hardness, thermal, optoelectronic, *etc.*). In communication applications, increasing traffic demand of information transmission is more likely to be supported by light transmission using optical fibre than by the current conventional electrical transmission. Most optical fibres are drawn from silicate glass because it is cheap, chemically stable and the forming technology is straightforward. However, the transmission window of silica glass fibre is limited; it is used at 1550 nm but, at wavelengths greater than 2000 nm (in the mid-infrared region) it becomes opaque, unlike tellurite glass [8-9]. The mid-infrared region is particularly interesting for various applications including material processing, spectroscopy, medicine, military and communications [10]. Tellurite glass is a better candidate than silica glass not only because of its wider transmission range but also higher linear and nonlinear refractive indices, and lower dispersion [11]. In order to successfully engineer tellurite glass fibres with the desired properties, a thorough understanding of the structural and chemical origins of these properties is crucial. The high nonlinearity of the glass has been attributed to (a) the polarisability of the $[TeO_4]$ unit (where tellurium is coordinated to 4 oxygen atoms in

a trigonal bipyramidal arrangement) [12] ; (b) the empty 5d orbital in Te [13-15] ; and (c) the presence of the lone-pair of electrons in Te [16]. Part of this thesis examines the changes to the local environment of tellurium with a change in the modifier content. The results will then be used to try to explain the effect of tellurium environment on its high nonlinearity.

1.3.2 Borogermanate glasses

Like tellurite glasses, borogermanate glasses also possess desired critical properties (such as density and refractive index) suitable for uses in waveguide systems [17]. These properties depend on the structure of the glass, mainly from the constituent borate and germanate networks.

In pure borate glass, the structure is made up of $[\text{BO}_3]$ units [18]. The addition of alkali oxide will transform $[\text{BO}_3]$ to $[\text{BO}_4]^-$ until a saturation point at ~ 30 mol% [19-20]. Beyond this point, further addition of alkali oxide creates $[\text{BO}_3]^-$ with non-bridging oxygen NBO. From the point of view of the average boron-oxygen coordination number n_{BO} , this will, therefore, increase the n_{BO} to a maximum value at ~ 30 mol% and later decrease n_{BO} [3, 21]. In accordance with the behaviour of n_{BO} , anomalies in the physical properties of the glasses are observed [22-23]. In alkali borate glasses, many borate superstructural units are formed and destroyed, which are used to successfully describe the borate anomaly [3].

In alkali germanate glasses, as a function of alkali content, a germanate anomaly in the physical properties is also observed [23-24]. This anomaly is caused by the conversion of $[\text{GeO}_4]$ units to charged higher coordinated $[\text{GeO}_5]^-$ or $[\text{GeO}_6]^{2-}$ units [25]. Similarly with the borate anomaly, further addition of alkali content converts the higher coordinated units and forms $[\text{GeO}_4]^-$ with an NBO and the glass structure will experience an overall decrease in the average Ge-O coordination number [26-27].

The structure of ternary borogermanate glasses is complicated because boron and germanium can have more than one stable coordination. Therefore, this could cause unexpected changes in the structural/superstructural species formed in the glass. This thesis examines the borate and/or germanate anomaly in ternary lithium and potassium borogermanate glasses and compares the results with related models.

1.4 References

1. Zhong, J., Wu, X., Liu, M. L., Bray, P. J. *Journal of Non-Crystalline Solids* 1988, 107, 81-87.
2. Dell, W. J., Bray, P. J., Xiao, S. Z. *Journal of Non-Crystalline Solids* 1983, 58, 1-16.
3. Shelby, J. E., *Introduction to Glass Science and Technology*, 2nd Ed., 2005.

4. Le Roux, S., Petkov, V. Interactive Structure Analysis of Amorphous and Crystalline Systems (ISAACS) Program. <http://isaacs.sourceforge.net/index.html>.
5. Le Roux, S., Petkov, V. *Journal of Applied Crystallography* 2010, **43**, 181-185.
6. Zachariasen, W. H. *Journal of the American Chemical Society* 1932, **54**, 3841-3851.
7. Tool, A. Q. *Journal of the American Ceramic Society* 1946, **29**, 240-253.
8. Kitamura, R., Pilon, L., Jonasz, M. *Applied Optics* 2007, **46**, 8118-8133.
9. Modest, M. F., *Radiative Heat Transfer (Third Edition)*; Academic Press: Boston, 2013, p 904.
10. *Nat Photon* 2012, **6**, 407-407.
11. Jha, A., Richards, B., Jose, G., Teddy-Fernandez, T., Joshi, P., Jiang, X., Lousteau, J. *Progress in Materials Science* 2012, **57**, 1426-1491.
12. Suehara, S., Thomas, P., Mirgorodsky, A., Merle-Méjean, T., Champarnaud-Mesjard, J., Aizawa, T., Hishita, S., Todoroki, S., Konishi, T., Inoue, S. *Physical Review B* 2004, **70**, 205121.
13. Lines, M. *Physical Review B* 1991, **43**, 11978.
14. Lines, M. *Physical Review B* 1990, **41**, 3383.
15. Blanchandin, S., Thomas, P., Marchet, P., Champarnaud-Mesjard, J., Frit, B. *Journal of Alloys and Compounds* 2002, **347**, 206-212.
16. Porter, Y., Ok, K. M., Bhuvanesh, N., Halasyamani, P. S. *Chemistry of Materials* 2001, **13**, 1910-1915.
17. Sigaev, V. N., Lotarev, S. V., Orlova, E. V., Stefanovich, S. Y., Pernice, P., Aronne, A., Fanelli, E., Gregora, I. *Journal of Non-Crystalline Solids* 2007, **353**, 1956-1960.
18. Soper, A. K. *Journal of Physics: Condensed Matter* 2011, **23**, 365402.
19. Prabakar, S., Rao, K., Rao, C. In *¹¹B NMR Spectra and Structure of Boric Oxide and Alkali Borate Glasses*, Proceedings of the Royal Society of London A: Mathematical, Physical and Engineering Sciences, The Royal Society: 1990; pp 1-15.
20. Zhong, J., Bray, P. J. *Journal of Non-Crystalline Solids* 1989, **111**, 67-76.
21. Kroeker, S., Aguiar, P. M., Cerquiera, A., Okoro, J., Clarida, W., Doerr, J., Olesiuk, M., Ongie, G., Affatigato, M., Feller, S. A. *Physics and Chemistry of Glasses-European Journal of Glass Science and Technology Part B* 2006, **47**, 393-396.
22. Kapoor, S., Bola George, H., Betzen, A., Affatigato, M., Feller, S. *Journal of Non-Crystalline Solids* 2000, **270**, 215-222.
23. Feller, S., Lower, N., Affatigato, M. *Physics and Chemistry of Glasses* 2001, **42**, 240-246.
24. Yiannopoulos, Y. D., Varsamis, C. P. E., Kamitsos, E. I. *Journal of Non-Crystalline Solids* 2001, **293-295**, 244-249.
25. Hannon, A. C., Di Martino, D., Santos, L. F., Almeida, R. M. *Journal of Non-Crystalline Solids* 2007, **353**, 1688-1694.
26. Ueno, M., Misawa, M., Suzuki, K. *Physica B+ C* 1983, **120**, 347-351.
27. Hannon, A. C., Di Martino, D., Santos, L. F., Almeida, R. M. *Journal of Physical Chemistry B* 2007, **111**, 3342-3354.

Chapter 2 – Diffraction

2.1 Introduction

This chapter discusses the theory of diffraction which is the main method used in this structural study of glasses. Both neutron and X-ray diffraction are discussed, including the theory and practice of null neutron diffraction and isostoichiometric neutron diffraction. In addition, the theory and practice of the complementary method of neutron and X-ray diffraction are discussed. Some of the practical problems regarding neutron resonance and absorption are described. The chapter is then concluded by discussing the quantification of the structural information obtained from the diffraction experiments.

2.2 Diffraction theory: Neutron and X-ray

Diffraction is a powerful method for probing atomic or molecular structure in materials. Neutron diffraction has the advantage of the neutral charge of the neutron which allows it to penetrate deeper into an atom and interact with the nucleus, compared to X-rays which interact with the electron cloud of the atom. In elastic scattering, neutrons / X-rays are scattered by the sample at an angle of 2θ and the momentum transfer vector Q is obtained from the initial and final wave vectors, k , of the neutron / X-ray as shown in Fig. 2.1. In the figure (3D diagram for the collision), ϕ and 2θ are the angles between the scattered beam to the y-axis (y-plane, blue) and z-axis (z-plane, orange), respectively. The solid angle in Fig. 2.1 is given by

$$d\Omega = \sin 2\theta \, d2\theta \, d\phi \quad (2.1)$$

Total cross section σ over the solid angle Ω is the differential cross section $I(Q)$ and is defined as

$$I(Q) = \frac{d\sigma}{d\Omega}(Q) = \int_{-\infty}^{\infty} \frac{d\sigma}{d\Omega d\omega} d\omega = I^s(Q) + i(Q) \quad (2.2)$$

Where ω is the angular momentum of the energy transferred ($E = \hbar\omega$), $I^s(Q)$ is the self-scattering, and $i(Q)$ is the distinct scattering and $I^s(Q)$ and $i(Q)$ are represented as

$$I^s(Q) = \sum_i^n c_i \overline{f_i^2(Q)} (1 + P_i(Q, \theta, T, \dots)) \quad (2.3)$$

$$i(Q) = \sum_i^n \sum_j^n c_i c_j f_i(Q) f_j(Q) (S_{ij}(Q) - 1) \quad (2.4)$$

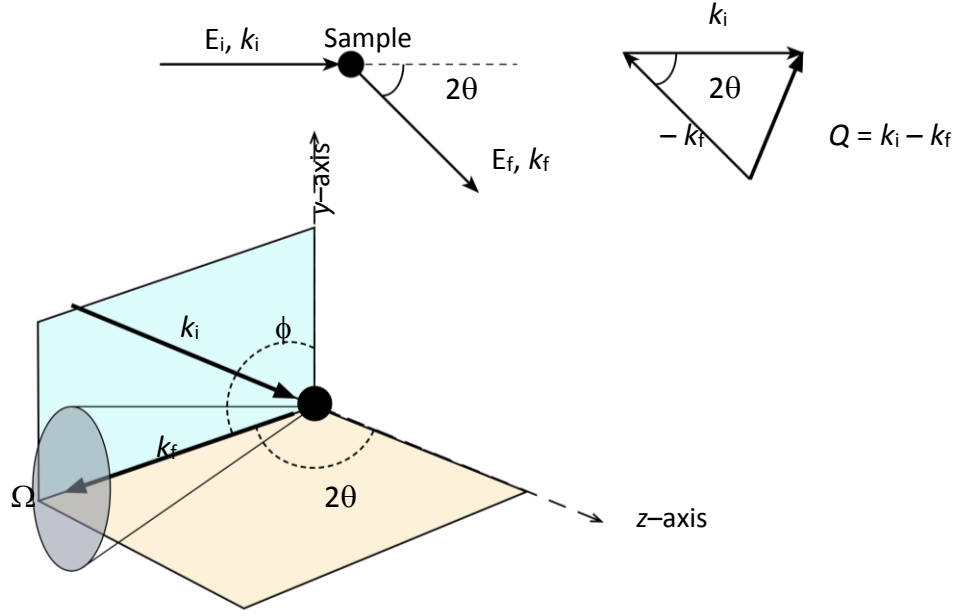


Figure 2.1: Schematic of elastic neutron / X-ray diffraction with neutron / X-ray of initial parameters (E_i, k_i) scattered off of the sample with 2θ angle from the initial path with final parameters of E_f and k_f . Momentum transfer vector Q is obtained from the wave vectors k as shown in the figure on the right. Scattered neutron wave / X-ray into a solid angle of ϕ (from y-axis) and 2θ (from z-axis)

Where P_i is the Placzek [1] corrections as a function of Q , θ , T , and etc, and $f_i(Q)$ is either the atomic form factor (for X-ray) or the coherent neutron scattering length (for neutron) for the element i as in

$$\begin{aligned} X\text{-ray} & ; f_i(Q) = \sum_{j=1}^4 a_j \exp(-b_j Q^2) + c \\ \text{Neutron} & ; f_i(Q) = \bar{b}_i \end{aligned} \quad (2.5)$$

Where a , b , and c are in the X-ray case the parameters from the *International Tables for Crystallography* (1992), Vol. C [2] whilst b in the neutron case is the coherent neutron scattering length [3]. Eqn 2.3 is calculated and Eqn. 2.4 is obtained experimentally from the GEM diffractometer [4]. The structure factor term $S_{ij}(Q)$ as $S_{ij}(Q)-1$ as in (Eqn. 2.4) is defined as

$$S_{ij}(Q) - 1 = 4\pi\rho_o \int_0^\infty r^2 (g_{ij}(r) - 1) \frac{\sin(rQ)}{rQ} dr \quad (2.6)$$

which contains the real-space function $g_{ij}(r)$ and can be obtained by taking the Fourier transform of (Eqn. 2.6). The term $g_{ij}(r) - 1$ in Eqn. 2.6 is given in (Eqn. 2.7) and used to determine the coordination number of atom i by j as in (Eqn. 2.8)

$$g_{ij}(r) - 1 = \frac{1}{2\pi^2\rho_o} \int_0^\infty Q^2 (S_{ij}(Q) - 1) \frac{\sin(rQ)}{rQ} dQ \quad (2.7)$$

$$n_{ij}(r_1, r_2) = 4\pi c_j \rho_0 \int_{r_1}^{r_2} r^2 g_{ij}(r) dr = \frac{c_j}{c_i} n_{ji}(r_1, r_2) \quad (2.8)$$

This equation later reduces to Eqn 2.9 for neutron diffraction.

$$n'_{ij} = \frac{\bar{r}_{ij} A_{ij}^N}{(2 - \delta_{ij}) c_i \bar{b}_i \bar{b}_j} \quad (2.9)$$

where A_{ij}^N is the area in $T^N(r)$ arising from the i - j pair. The more common expression, the total correlation function $T(r)$ (Eqn. 2.10), is used in this chapter. It is a parameter containing all atom pair distribution functions, and is obtained by taking a Fourier transform of Eqn. 2.6

$$T(r) = T^0(r) + \frac{2}{\pi} \int_0^\infty Q i(Q) M(Q) \sin(rQ) dQ \quad (2.10)$$

Where $T^0(r)$ is the average density contribution to the calculated correlation function

$$T^0(r) = 4\pi r \rho_0 \left(\sum_i c_i \bar{b}_i \right) \quad (2.11)$$

Where ρ_0 is the density (units per cubic Å).

The neutron diffraction data were obtained using the GEneral Materials Diffractometer, GEM [5] at ISIS Oxford. GEM has the capability of taking high momentum transfer values, which lead to high real-space resolution (60 Å^{-1}) and, therefore, accurate coordination numbers. It has 8 detector banks covering a wide range of 2θ from 1.2° to 171.4° as shown in Fig. 2.2.

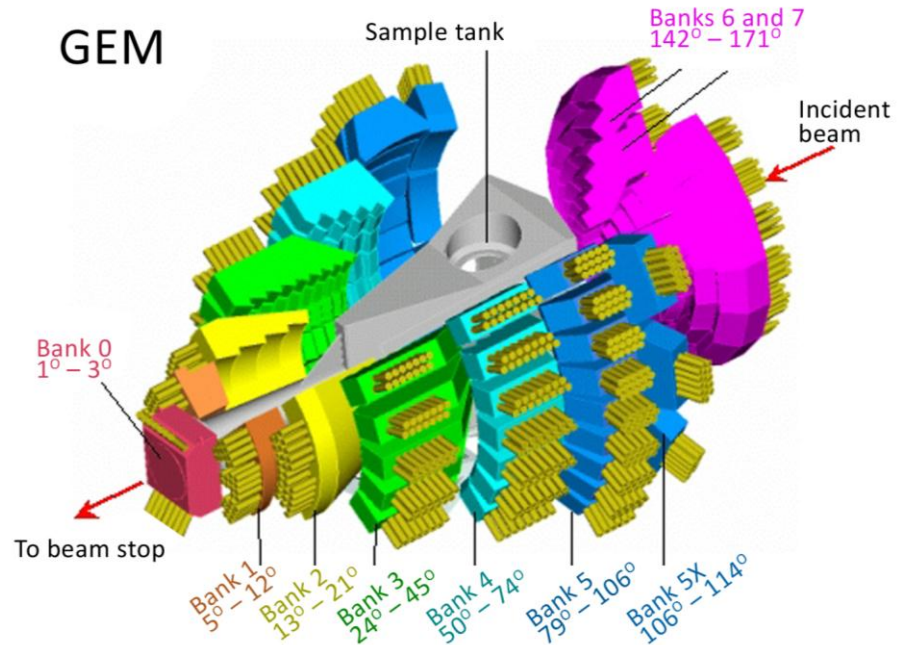


Figure 2.2: GEneral Materials GEM diffractometer at ISIS, RAL, Oxford UK.

Glass samples, in the form of fragments from 1 to 3 mm across, were packed in an 8.3 mm internal diameter, cylindrical vanadium can with either 40 microns or 25 microns thick walls, with the packing density from 40 to 50 %. A total current of about 1500 microamps for each sample was collected to give good signal-to-noise ratio. Data were corrected and normalised for multiple scattering, inelasticity, as well as absorption correction using measurements made on the empty instrument, empty vanadium can, and vanadium (or latterly vanadium-niobium) rod using the GudrunN program [6]. For systems containing tellurium atoms, Q_{\max} was limited to 35 \AA^{-1} to avoid the ^{123}Te resonance at about 2.2 eV whereas for the other systems it was extended to 40 \AA^{-1} .

2.3 Diffraction techniques

2.3.1 Introduction

This section discusses the methods of extracting structural information from neutron and / or X-ray diffraction data. These cover null neutron diffraction, isostoichiometric neutron diffraction, and complementary neutron and X-ray diffraction.

2.3.2 Null neutron diffraction technique

2.3.2.1 Neutron scattering length, b

The $T(r)$ term in Eqn 2.10 for neutron diffraction can also be identified as a sum of all partial correlation functions for i - j pair of atoms as in

$$T^N(r) = \sum_{ij} c_i \overline{b_i b_j} t_{ij}(r) \quad (2.12)$$

Here, a parameter b (which is a complex number) is introduced and is defined as

$$\Psi = -\frac{b}{r} e^{ikr} \quad (2.13)$$

Where Ψ is the S -wave function (spherically symmetrical) of the scattered neutrons and b is the unique coherent neutron scattering length of any nucleus which can be a positive or a negative value.

In order to understand the origin of the negative scattering length, the neutron interaction with the nucleus (nuclear potential) has to be discussed. Depending on the isotope (Fermi pseudopotential depth and other parameters), during a collision, neutrons could be scattered positively or negatively. Having a positive scattering length value would mean that the neutrons will be subjected to the repulsive potential of the nucleus, making it impenetrable. Therefore, the scattered wave will experience a negative phase shift because

scattered neutron waves will have its phase shifted by 180° from the incident wave when scattered by a hard (impenetrable) sphere. Conversely, a negative scattering length would mean that the incident neutrons will experience an attractive potential and will yield a positive phase shift. The choice of the minus sign in this equation is to ensure that most isotopes will have a positive b value [7].

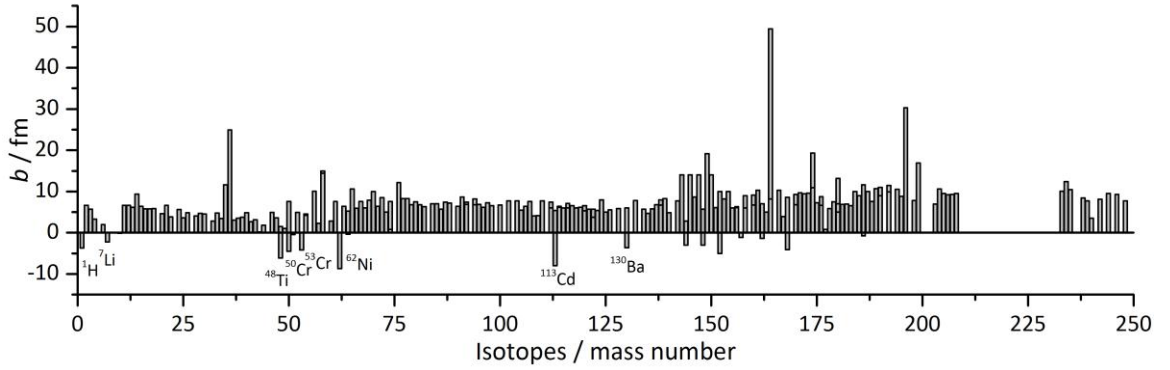


Figure 2.3: b values for some isotopes of the elements of the periodic table.

A suitable combination of positive and negative scattering isotopes of an element can therefore produce effectively null neutron scattering. The scattering length values for certain isotopes are shown in Fig 2.3.

2.3.2.2 Null neutron diffraction

Systematic studies on lithium tellurite glasses using null-scattering isotope substitution neutron diffraction have not previously been reported. By combining the appropriate proportions of ^7Li ($b = -2.22$ barns) and ^6Li ($b = 2.00$ barns) the average scattering length of lithium atoms \bar{b}_{Li} can be adjusted to zero and lithium partial correlation functions are removed from the total correlation function $T(r)$ leaving only tellurium and oxygen partials in the total correlation function. $T(r)$ is the sum of all the partial correlation function and can be expanded as;

$$\begin{aligned} T^N(r) = & c_{\text{Te}} \overline{b_{\text{Te}} b_{\text{Te}}} t_{\text{TeTe}}(r) + c_{\text{Te}} \overline{b_{\text{Te}} b_{\text{O}}} t_{\text{TeO}}(r) + c_{\text{Te}} \overline{b_{\text{Te}} b_{\text{Li}}} t_{\text{TeLi}}(r) + \\ & c_{\text{O}} \overline{b_{\text{O}} b_{\text{Te}}} t_{\text{OTe}}(r) + c_{\text{O}} \overline{b_{\text{O}} b_{\text{O}}} t_{\text{OO}}(r) + c_{\text{O}} \overline{b_{\text{O}} b_{\text{Li}}} t_{\text{OLi}}(r) + \\ & c_{\text{Li}} \overline{b_{\text{Li}} b_{\text{Te}}} t_{\text{LiTe}}(r) + c_{\text{Li}} \overline{b_{\text{Li}} b_{\text{O}}} t_{\text{LiO}}(r) + c_{\text{Li}} \overline{b_{\text{Li}} b_{\text{Li}}} t_{\text{LiLi}}(r) \\ = & T^{\text{Natural}}(r) \end{aligned} \quad (2.14)$$

In null samples, the average coherent neutron scattering length for lithium, \bar{b}_{Li} is approximately zero and Eqn 2.14 can be reduced to;

$$T^{\text{Null}}(r) = c_{\text{Te}} \overline{b_{\text{Te}} b_{\text{Te}}} t_{\text{TeTe}}(r) + (c_{\text{Te}} + c_{\text{O}}) \overline{b_{\text{Te}} b_{\text{O}}} t_{\text{TeO}}(r) + c_{\text{O}} \overline{b_{\text{O}} b_{\text{O}}} t_{\text{OO}}(r) \quad (2.15)$$

which contains only tellurium and oxygen pairwise combinations. In lithium tellurite glasses, r_{TeO} does not overlap with either r_{OO} or r_{TeTe} . This means that the Li partials can be easily extracted from the total correlation function, $T^N(r)$ by taking the difference between $T^{natural}(r)$ and $T^{null}(r)$

$$T^{Nat-Null}(r) = -(c_O + c_{Li})(\bar{b}_O \bar{b}_{Li} t_{LiO}(r) + c_{LiLi} \bar{b}_{Li}^2 t_{LiLi}(r) - c_{Li} \bar{b}_{Li} \bar{b}_{Te} t_{LiTe}(r)) \quad (2.16)$$

which contains only lithium and oxygen pairwise correlation functions and short r_{LiO} does not overlap with longer r_{LiTe} in the total $T(r)$. $-c_{LiX} \bar{b}_{Li} \bar{b}_X t_{LiX}(r)$ is equivalent to $-T_{LiX}(r)$. The negative sign indicating a negative area in the total correlation function arising from the negative value of b_{Li} in natural abundance Li.

2.3.2.3 Neutron absorption and resonances

Two of the problems when dealing with thermal neutron diffraction are neutron absorption and resonance in certain nuclei, for instance in Li(^6Li), B(^{10}B), and Te(^{123}Te). ^6Li and ^{10}B are atoms that have high neutron absorption cross-section. ^{10}B has an absorption cross section value of 3835 barns and for ^6Li it is 940 barns [3]. In the case of B containing samples, the problem is reduced (but not eliminated) by using ^{11}B -enriched samples (typically >99 %). ^6Li however is used deliberately to create a null neutron scattering sample as discussed, therefore the neutron absorption is problematic in samples containing ^6Li isotope.

Neutrons of lower energy (low Q value) have the greater probability of being captured by the nucleus because they have lower momentum. As a consequence of this, the problem with absorption can be seen from the baseline of $I(Q)$ at lower Q values as seen in Fig. 2.4 especially the red curve (ρ_{eff_1}) as well and can be translated to the negative peak in the low r region in $T(r)$ as in Fig. 2.5. Corrections can be performed by adjusting the DCS value (can be done by changing the effective density value and/or the composition of the glass). The DCS level can be defined as:

$$DCS \text{ level} = \frac{\sum_i c_i \langle b_i^2 \rangle}{4\pi} \quad (2.17)$$

Where c_i and b_i are the concentration and neutron scattering values of atom/nuclei i in the beam. The concentration c depends on density ρ and composition x . For the analyses performed in this study, for convenience, glass nominal composition is used and only the (effective packing) density is optimised accordingly. In samples containing Te, however, the average DCS value is meaningless due to the large resonance peaks of ^{123}Te . In this study, the nominal glass composition is used and the effective density (depends on the packing efficiency in the sample can) is changed accordingly to mitigate the problem with the

absorption. This is justified by the non-uniform size of the glass bits packed into the container. As seen in the figure, changing (in this case, increasing) the effective density value, the problem due to the absorption is reduced greatly.

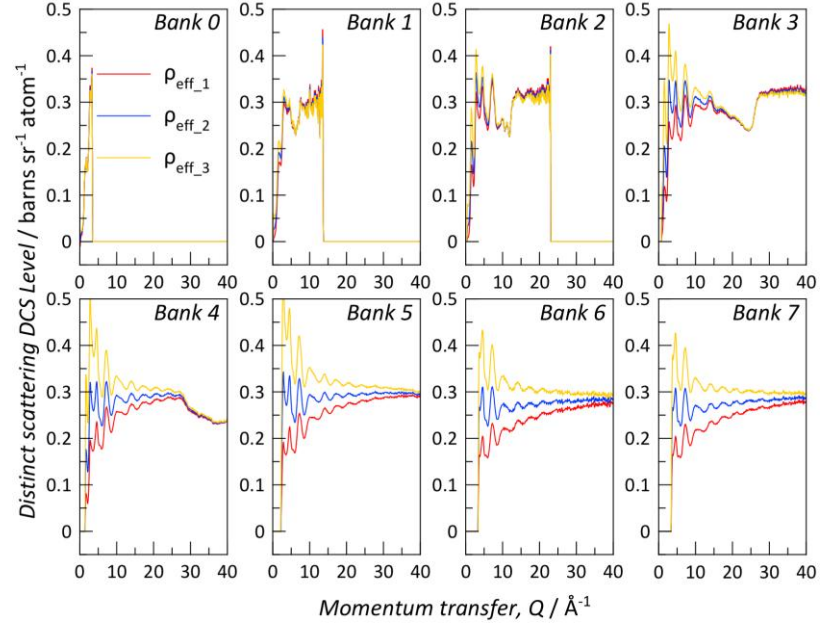


Figure 2.4: The effect of correcting the effective density on the absorption correction in $I(Q)$ for each bank. ρ_{eff_1} is the measured effective (packing) density whilst ρ_{eff_2} and ρ_{eff_3} are adjusted effective packing densities.

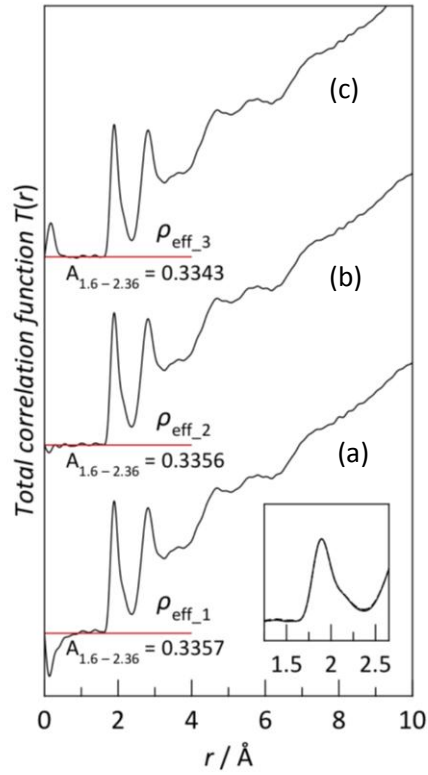


Figure 2.5: The effect of correcting the effective density on the total correlation function $T(r)$.

Samples with neutron absorbing isotopes will usually show negative peaks near $r = 0$ in the $T(r)$ as Fig. 2.5. As seen in the figure, the negative peaks are reduced as a function of the effective density used where (a) was processed using the (under-estimate) calculated effective density, (b) was processed using optimally estimated (increase of about $\sim 20\%$) effective density and (c) was processed using an overly estimated (increase of about $\sim 50\%$) effective density. The structural information from the $T(r)$ is however, robust to analysis error. As seen in the inset of the figure and the integral area under the curve ($1.6 - 2.36 \text{ \AA}$), the $T(r)$ obtained in the region of interest ($r > 1.5 \text{ \AA}$) is fairly unaffected by the correction. Absorption correction (in the effective density value) was however still done to obtain a cleaner $T(r)$.

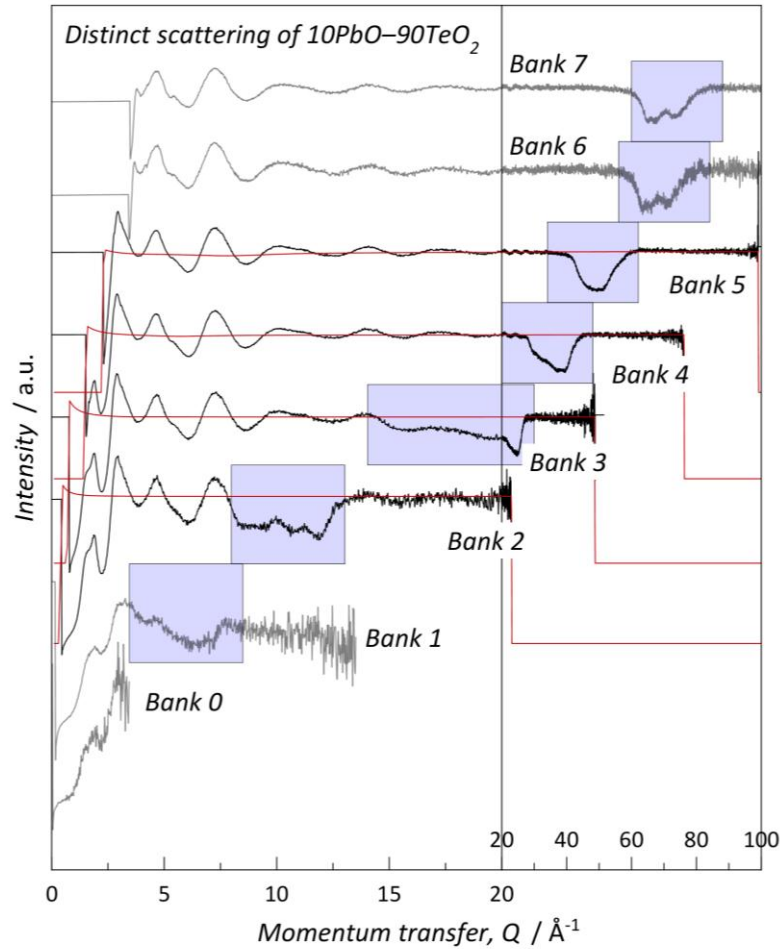


Figure 2.6: The effect of bank angles on resonance range.

Another problem with neutron diffraction is neutron resonance. In this process, neutrons are also captured, but at a certain energy, rather than at the low energy. ^{128}Te for example has a neutron resonance at about 2.2 eV [8]. From the GEM, the data are collected

over 180° using 8 banks positioned at different angle θ . This therefore will mean that the 2.2 eV absorption will produce a decrease in the scattered intensity in $I(Q)$ at different Q positions depending on the angle θ of the bank as shown in Fig. 2.6 (blue shaded squares), according to this equation

$$Q = \frac{4\pi}{\lambda} \sin\theta \quad (2.18)$$

The implication of this resonance energy is the limitation of the Q_{\max} value which can be used, which will affect the resolution of $T(r)$. ISIS's GEM is a state of the art instrument that is capable of taking high resolution data to up to $Q_{\max} = 40 \text{ \AA}^{-1}$ in SiO_2 , GeO_2 , and B_2O_3 systems for example. However, this range is reduced to 35 \AA^{-1} in TeO_2 systems due to this resonance problem. In this study, only banks 2 to 5 were used in merging because bank 0 to 1 contain little information. In theory, by including banks 6 to 7, a higher Q_{\max} value could be used because the resonance is out of the range of interest, however, to avoid unnecessary noise, these banks were not included in the merging.

2.3.3 Isostoichiometric neutron technique

In a series of binary oxide systems (for example, $\text{Li}_2\text{O}-\text{TeO}_2$, $\text{Na}_2\text{O}-\text{TeO}_2$, and $\text{K}_2\text{O}-\text{TeO}_2$) where the Te environment in each system is iso-structural (similar at the same content of R_2O ($\text{R} = \text{Li}, \text{Na}, \text{and K}$)), the environment of Li, Na, and K can be extracted by removing the contribution of the Te environment from each system. This method is called the iso-stoichiometric neutron diffraction technique. Using this method, Barney *et al.* [9] have successfully extracted the environment of Li, Na, and K in $x = 10$, and 20 mol% $\text{R}_2\text{O}-\text{TeO}_2$ glasses. In the case of glass structure analysis, the method is best used where the glass network is *independent* of the modifier cation type but can also be useful where network differences are minor.

2.3.4 Neutron and X-ray complementary technique

In general, the distinct scattering $i(Q)$ which contains the experimentally obtained structural information is defined as

$$i(Q) = \sum_i^M \sum_j^M c_i c_j f_i(Q) f_j(Q) (S_{ij}(Q) - 1) \quad (2.19)$$

Where the form factor, $f(Q)$, is defined differently in the case of neutron or X-ray diffraction, as follows

$$\begin{aligned}
\text{Neutron; } f_i(Q) &= b_i \\
\text{X-ray; } f_i(Q) &= \sum_{i=1}^4 a_i e^{-b_i Q^2} + c
\end{aligned}
\tag{2.20}$$

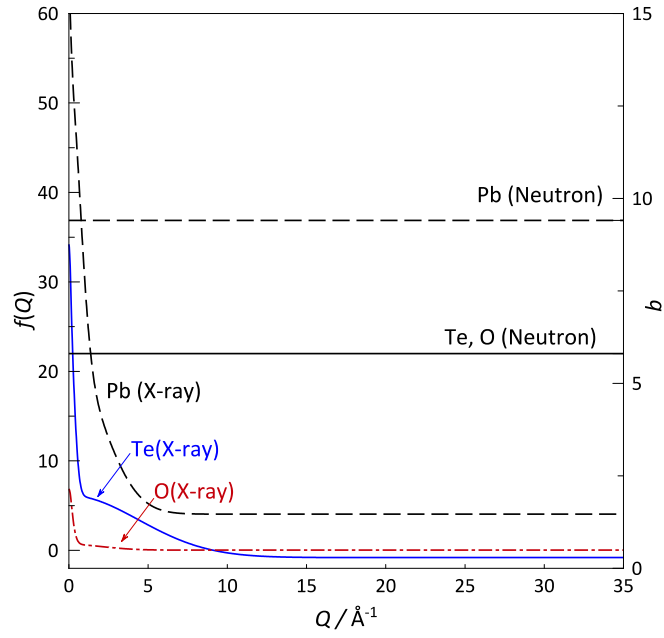


Figure 2.7: Q -dependence of $f(Q)$ in neutron and X-ray diffractions for Pb, Te, and O.

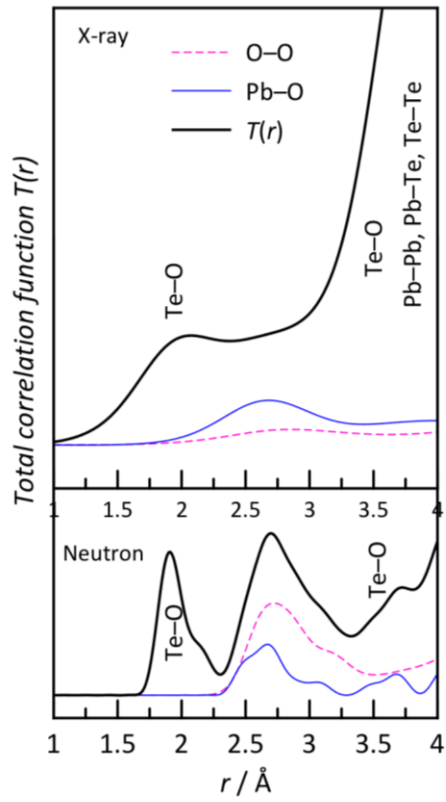


Figure 2.8: $T^N(r)$ and $T^X(r)$ for $\text{PbTe}_5\text{O}_{11}$.

In the case of neutron diffraction, the form factor is the scattering length constant b , whilst in the case of X-ray it is a function dependent on Q . The difference in magnitude of the form factors provides contrast in the $T(r)$ obtained specific to certain atomic pairs. The magnitude of the contrast in a system containing Pb, Te, and O, for example is shown in Fig. 2.7. It can be seen that the $f(Q)$ for the O atom in X-ray diffraction is negligible whilst the value in neutron diffraction is not. Consequently, the partial $T(r)$ for the O-O pair is negligible in X-ray diffraction. In the study of most glasses, the O-O distance overlaps with most modifier-oxygen, R-O, distances. For a simple illustration, Fig. 2.8 compares the simulated $T^N(r)$ and $T^X(r)$ for the $\text{PbTe}_5\text{O}_{11}$ crystal. From the comparison, the Pb-O distance is clearly revealed in the system. Due to the different nature of neutron and X-ray interactions in the sample as discussed, the $i(Q)$ for neutron and X-ray obtained are weighted differently as below.

$$i^N(Q) = \sum_i^M \sum_j^M c_i c_j b_i b_j (s_{ij}(Q) - 1)$$

$$i^X(Q) = \frac{\sum_i^M \sum_j^M c_i c_j f_i(Q) f_j(Q) (s_{ij}(Q) - 1)}{\left(\sum_i^M c_i f_i(Q) \right)^2} \quad (2.21)$$

Consequently, the $T(r)$ for each case is defined differently as follows.

$$T^N(r) = 4\pi r n_0 \left(\sum_i c_i \bar{b}_i \right) + \frac{2}{\pi} \int_0^\infty Q i^N(Q) M(Q) \sin(rQ) dQ$$

$$T^X(r) = 4\pi r n_0 + \frac{2}{\pi} \int_0^\infty Q i^X(Q) M(Q) \sin(rQ) dQ \quad (2.22)$$

Where $M(Q)$ is the Lorch modification function [10], used to reduce the termination ripples due to the truncation effect from the Fourier Transform.

2.4 Direct structural information from total correlation function

2.4.1 Peak position and shape

The total correlation function is made up of a sum of well-defined delta functions. Due to static and dynamic disorders, the spike-shape delta functions are therefore broadened resulting in Gaussian peak shapes [11]. Therefore, the peak, convoluted with a sinc function to compensate for the termination ripples from the Fourier transform, would contain the width, shape, and position reflecting the real atomic probability distribution.

In B_2O_3 glasses for example, by using the bond-valence calculation [12], the B-O peak can be resolved into two distances (by using Gaussian peaks) appropriate for B atom

coordinated to 3 and 4 oxygen atoms. In GeO_2 glasses, the presence of the higher coordinated $[\text{GeO}_{4+}]$ units can be seen in the $T(r)$ [13]. In these two cases, the peak parameterisation is simple due to the symmetric distribution of the distance which reflects the nature of bonding in the glasses. In more complex systems, for example TeO_2 glass where Te-O distance distribution present is asymmetric, the peak parameterisation is rather difficult as the asymmetry could arise from multiple symmetrical function peaks and/or one or more asymmetrical distribution peak. For simplicity, the asymmetric Te – O distance distribution is often represented by an arbitrary combination of Gaussians [14].

2.4.2 Peak integrated intensity

For a well-defined peak where the $T(r)$ consists of only the partial correlation function for i-j atom pair, the coordination number of atom i to atom j, and vice versa can be calculated by integrating the area of the peak (Eqn. 2.9). This parameter is one of the most important parameters when quantifying a glass structure since it describes directly the local environment of a specific atom.

2.5 References

1. Placzek, G. *Physical Review* 1952, 86, 377.
2. Wilson, A. J. C. *International Tables for X-ray Crystallography*, Vol. C, Table 9.5. 1.1 1992.
3. Sears, V. F. *Neutron News* 1992, 3, 26-37.
4. Hannon, A. *Encyclopedia of Spectroscopy and Spectrometry* 2004, 1479-1492.
5. Hannon, A. C. *Nuclear Instruments and Methods in Physics Research Section A: Accelerators, Spectrometers, Detectors and Associated Equipment* 2005, 551, 88-107.
6. Soper, A. *Rutherford Appleton Laboratory Technical Report* 2011.
7. Bacon, G. E., *Neutron Diffraction*, 3rd Ed.; Clendon Press, 1975, p 636.
8. Heindl, C., Ruderman, I. *Physical Review* 1951, 83, 660.
9. Barney, E. R., Hannon, A. C., Holland, D., Umesaki, N., Tatsumisago, M. *Journal of Non-Crystalline Solids* 2015, 414, 33-41.
10. Lorch, E. *Journal of Physics C: Solid State Physics* 1969, 2, 229.
11. Egami, T., Billinge, S. J. L., *Underneath the Bragg Peaks: Structural Analysis of Complex Materials*, 2003; Vol. 7, p 57.
12. Brese, N., O'Keefe, M. *Acta Crystallographica Section B: Structural Science* 1991, 47, 192-197.
13. Hoppe, U., Kranold, R., Weber, H.-J., Hannon, A. *Journal of Non-Crystalline Solids* 1999, 248, 1-10.
14. Barney, E. R., Hannon, A. C., Holland, D., Umesaki, N., Tatsumisago, M., Orman, R. G., Feller, S. *Journal of Physical Chemistry Letters* 2013, 4, 2312-2316.

Chapter 3 – Experimental and analytical techniques

3.1 Introduction

This chapter describes the theory and working principles for each of the experimental techniques used for data acquisition in this study. The data analysis procedures, in terms of the corrections made to the data and the interpretation of the results, are also included. In characterising a glass structure, these methods are typically used in combination with one or more others to derive short-range information which is often compared with the corresponding crystal structures [1-3]: density measurement [4], thermal analysis [5-7], Raman spectroscopy [8-13], conventional laboratory X-ray diffraction [5, 14-15], energy dispersive X-ray spectroscopy [16], secondary ion mass spectroscopy [17], neutron diffraction [1, 18-24], high energy X-ray diffraction [18, 25-26], and nuclear magnetic resonance [23, 27-29]. Details of neutron diffraction were covered in Chapter 2 and the remaining techniques are described briefly in this chapter.

3.2 Glass–crystal structure comparison

The crystallographic information (cif) files used in this study were obtained from the Royal Society of Chemistry's National Chemical Database Service [30]. The neutron and X-ray (partial and total) correlation functions were simulated from the cif files using the XTAL program [31]. In a glass, where the system is metastable, the internal energy of the glass is likely to be minimised by having cations in a similar environment to that in the related crystal [32]. Therefore, the short-range environment of the experimental total correlation function, $T(r)$ can be comparable to the simulated crystal $T(r)$. As will be discussed in Chapter 4, the short-range parameters of the tellurite crystals (TeO_2 , lithium tellurite, and lead tellurite) can be used to partially describe the short-range environment in the lithium and lead tellurite glasses. The crystal structure of potassium borogermanate glasses is discussed briefly in conjunction with the neutron diffraction analysis in Chapter 7.

3.3 Density measurement

The density values were measured using a helium gas pycnometer, model Micro-meritics Accupyc II 1340 Helium Pycnometer at the Department of Physics, the University of Warwick. The gas pycnometer measures the volume ($V \text{ cm}^3$) of a sample using the gas displacement method as dictated by the Boyle's Law volume-pressure relationship which

states that “for a fixed mass of gas, at a constant temperature, the product (pressure x volume) is a constant”:

$$PV = nRT \quad 3.1$$

Where P is the pressure (atm), V is the volume (cm^3), n is the number of moles (mol), R is the gas universal constant ($82.06 \text{ cm}^3 \text{ atm K}^{-1} \text{ mol}^{-1}$), and T is the temperature (K). By using a known mass input ($m \pm 0.001 \text{ g}$), the density ($\rho \text{ g cm}^{-3}$) is calculated from this relationship:

$$\rho = m / V \quad 3.2$$

The setup has a capability of measuring sample volume with an accuracy of $\pm 0.001 \text{ cm}^3$. A gas chamber of 3.5 cm^3 was used for all the samples. The volume of the sample was measured in a pre-calibrated helium gas chamber until 5 measurements were consistent within a certain error. The known density of a vitreous SiO_2 rod ($2.20 \pm 0.01 \text{ g cm}^{-3}$) was measured in each session to check the accuracy of the readings.

The density values measured were averaged (typically 2 samples, 5 measurements for each sample) and the error was calculated from their standard deviation. The density values were used to derive the molar volume ($V_m \text{ cm}^3 \text{ mol}^{-1}$), and the number density ($N \text{ atoms cm}^{-3}$) as in Eqn. 3.3 and 3.4. The density value is used to estimate the composition of the glasses by comparison with the values obtained from the SciGlass database [33], whilst its derivatives (Eqn 3.3 and 3.4) are used to study contributions from constituent units/atoms present in the glass. Feller *et al.* [4] directly related the glass structures of borates, silicates, germanates, vanadates, and thiborates glasses with the trend in average coordination number change.

$$V_m = MW / \rho \quad 3.3$$

$$N_i = N_A \rho c_i / MW \quad 3.4$$

$$MW = \sum_{i=1}^n c_i A_i \quad 3.5$$

Where V_m is the molar volume, MW (g mol^{-1}) is the molecular weight of the glass, ρ (g cm^{-3}) is the density of the glass, N_i (atoms cm^{-3}) is the number density for atom i , N_A is the Avogadro's number ($6.022 \times 10^{23} \text{ atoms mol}^{-1}$), c_i is the fraction of atom i in the glass, and A_i is the mass number of atom i .

3.4 Thermal analysis [34-35]

Thermal events in the glasses were identified using a differential thermal analyser (DTA), model Stanton Redcroft DTA 673-4 at the Department of Physics, the University of Warwick. The DTA measures the temperature of the sample with respect to the reference material as

a function of temperature. About 100 mg of powdered glass was placed in a platinum-rhodium crucible and heated in static air at 10 °C/min to about 100 °C above the liquidus for each glass. The sample was then allowed to cool to room temperature. Alumina Al_2O_3 is used as a reference standard due to its high melting point (2050 °C) and stability over the temperature range used (room temperature to 1500 °C available). An increase in sample temperature with respect to the reference would denote that heat is released from the sample (exothermic) and a decrease in the temperature would mean that the heat is being absorbed by the sample (endothermic reaction). The change of temperature is then recorded as a function of temperature. A typical sequence of thermal events in a glass is shown in Fig. 3.1. Various thermodynamic events in the glass were extracted: glass transition temperature (T_g), crystallisation onset temperature (T_x), crystallisation peak temperature (T_c), and melting temperature (T_m). This information can be used to confirm the glass amorphicity, the phases present during the thermal reaction, and to estimate the glass stability towards devitrification (temperature window between T_x and T_g ; $T_x - T_g$). Like density, T_g can also be used to probe for structural changes by using topological constraint theory [36]. Barney *et al.* [22] used the T_g values of alkali tellurite glasses to describe the glass structures.

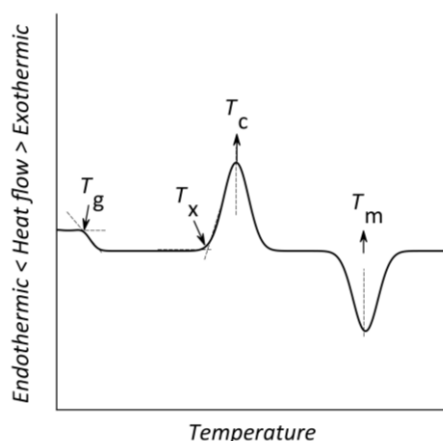


Figure 3.1: Differential thermal analysis curve typical of a glass showing glass transition temperatures T_g , crystallisation temperatures T_x and T_c , and melting temperature T_m .

3.5 Raman spectroscopy [37]

Raman spectra of the glasses (intensity as a function of wavenumber / Raman shift ($\tilde{\nu}$) in cm^{-1}) were obtained using a Raman InVia Microscope, equipped with a 514 and 532 nm laser source courtesy of the Diamond Research Group, Milburn House, the University of Warwick. Raman spectroscopy measures the energy (frequency) of a molecule that is in inelastic interaction with the laser beam. As seen in Fig. 3.2, there are 3 types of collision: Stokes,

Rayleigh, and Anti-Stokes. In the Stokes and Rayleigh processes, the molecule is excited from the ground state S_G to a virtual state. In the Stokes process, the excited molecule relaxes into an excited state S_E , however, in the Rayleigh process, it relaxes back to the ground state S_G (and is, therefore, elastic). In the anti-Stokes process, a molecule in an excited state S_E is stimulated to transition to a virtual level, then, relaxes to the ground state S_G . Under ambient conditions, (the case for all the Raman spectra in this study), most molecules are in the ground state S_G , hence, the frequencies detected are within the Stokes region. A Rayleigh peak at 19455 cm^{-1} or 18796 cm^{-1} (corresponding to 514 nm or 532 nm laser sources respectively) is blocked by a filter, though the maximum wavenumber recorded in this study was only 3000 cm^{-1} .

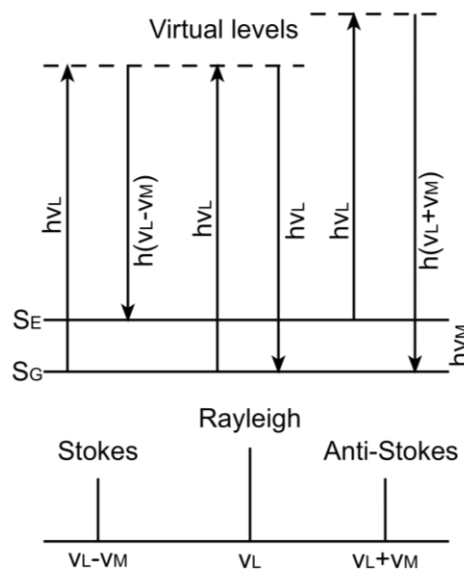


Figure 3.2: Stokes, Rayleigh, and anti-Stokes transitions in Raman spectroscopy.

In (Raman) spectroscopy, the Raman shift or wavenumber $\tilde{\nu}$ is defined as the frequency divided by the speed of light. This is particularly convenient when measuring the atomic / molecular spectra where the wavenumber is the reciprocal of its wavelength.

$$\tilde{\nu}(m^{-1}) = \frac{\tilde{\nu}(s^{-1})}{c(m s^{-1})} = \frac{1}{\lambda(m)} \quad 3.6$$

Each vibration of a pair of bonded atoms produces (depending on selection rules) a unique Raman shift ($\tilde{\nu}$) corresponding to its moment of inertia that can be used to fingerprint the molecular species present in the sample by referencing the frequency of the species to the frequency of a known similar species found in a reference material. The spectrometer was operated at a laser power of about 10 mW to avoid any thermal damage to the glass sample. The beam was focused on bulk samples for 5 acquisitions for each spot. Data were collected

for a minimum of 5 spots with the precision of at least 4 out of 5 spectra being identical once normalised. Raman spectra were collected from a minimum of $\sim 200 \text{ cm}^{-1}$, (limited by the notch filter) to a high wavenumber ($\sim 3000 \text{ cm}^{-1}$). A baseline for each spectrum was subtracted by a (exponential) spline within this region. The spectrum of a glass is characterised by the Boson peak at low wavenumber (to up to 500 cm^{-1}) which arises due to phonon vibration in the glass as described by Bose-Einstein statistics. The Boson peak is often fitted with a Rayleigh peak and is known as a Rayleigh wing. In the glasses where the region of interest is close to / included within the Boson peak, the spectrum has to be reduced to remove the Boson peak for accurate quantification. The reduction factor used is defined as

$$I_{\text{reduced}}(\tilde{\nu}) = \left(\frac{1}{(\tilde{\nu}_L - \tilde{\nu})^4} \right) \tilde{\nu} \left(\frac{1}{\exp\left(\frac{\hbar \tilde{\nu}}{k_B T}\right) - 1} + 1 \right) I_{\text{experimental}}(\tilde{\nu}) \quad 3.7$$

Where ν_L is the frequency of the laser, $(\tilde{\nu}_L - \tilde{\nu})^{-4}$ is the usual correction for the wavelength dependence of the scattered intensity and $n(\tilde{\nu}, T) = [\exp(\hbar \tilde{\nu} / k_B T) - 1]^{-1}$ is the mean number for phonon occupation, \hbar is the Planck's constant divided by 2π , $\tilde{\nu}$ is the Raman wavenumber, k_B is the Boltzmann constant, and T is the temperature. The description of the low-frequency region treatment regarding the Bose-Einstein statistics is discussed herein [10]. After the spectrum is baseline-corrected and reduced, it is normalised to the total area under the curve. The spectrum is then fitted with Gaussian peaks assigned to certain species present in the glass. The area of each peak was calculated and the average coordination number of ij pair of atoms were calculated based on the ratio of the peaks associated with the different species. Fig. 3.3 illustrates the reduction process.

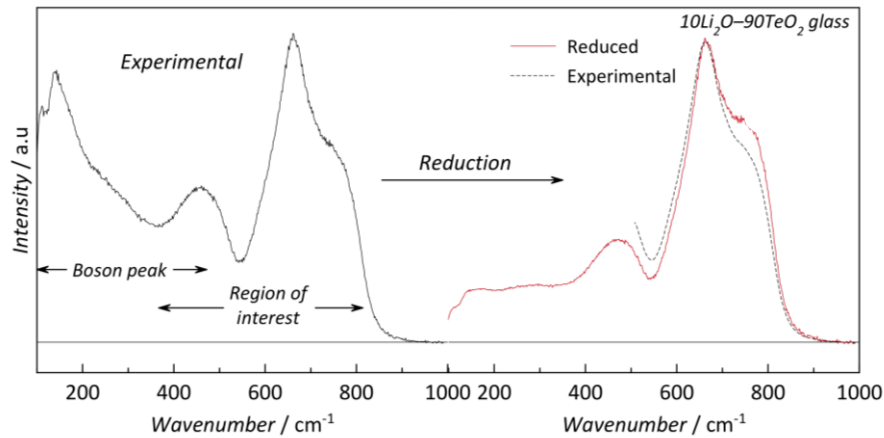


Figure 3.3: Reduction of the Raman spectra to remove the Boson peak at low wavenumber.

3.6 X-ray powder diffraction

A powder X-ray diffractometer model Bruker D5005 with Cu K α X-ray wavelength of 0.154 nm at the Department of Physics, the University of Warwick was used to obtain the diffraction patterns of the samples in this study. The diffractometer measures the intensity ($I(2\theta)$) of the diffracted X-ray beam according to Bragg's law as in Eqn 3.8 and shown in Fig. 3.4.

$$2d \sin \theta = n\lambda \quad 3.8$$

Where d is the d -spacing between planes, 2θ is the diffraction angle (an angle between the diffracted and transmitted beams), λ is the X-ray wavelength, and n is the order of reflection (usually 1).

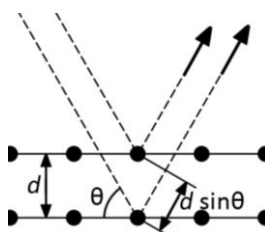


Figure 3.4: X-ray diffraction process according to Bragg's law.

The X-ray beam is reflected at the 2θ angle as a function of the d -spacing and the intensity of the reflected beam is collected. The X-ray diffraction pattern is compared to a the built-in powder diffraction database (PanAnalytical XRD software) and the ICSD crystal database [30]. The glass samples were powdered and compacted in a sample holder of diameter ~ 2.5 cm. The X-ray diffraction pattern was collected for 2θ angle between 5° and 90° taken with 0.02° steps. The amorphicity of the glass samples was confirmed by the presence of the broad halo peak, and in the case of partially crystallised samples, the crystal phase present in the glass was determined.

3.7 Energy dispersive X-ray spectroscopy

Elemental analysis of the samples was carried out using a field emission gun scanning electron microscope, FEGSEM (Zeiss SUPRA 55-VP) at 20 kV, courtesy of the Microscopy Group, Department of Physics, the University of Warwick, with help from Mr Steve York. Pulverised glass sample was dabbed onto a sticky carbon pad on a metal holder. This provides sufficient conductivity to avoid surface charging of the sample. Measurements were taken from 6 different spots for 100 s of exposure for each spot. The relative amounts of elements in the sample are quantified by the detection of the characteristic X-rays

emitted by elements after ZAF (Z: atomic number, A: X-ray absorption, and F: X-ray fluorescence) correction was performed using the EDAX Genesis software to correct the background-subtracted integrated intensities.

3.8 Secondary ion mass spectroscopy SIMS

For SIMS analysis, a depth profiler model Atomika 4500 was used, courtesy of Dr Richard Morris. SIMS analysis was done to verify the isotopic abundances of ^6Li : ^7Li and ^{10}B : ^{11}B isotopes in the glass samples. For the Li isotope measurement, a mineral spodumene $\text{LiAl}(\text{SiO}_3)_2$ courtesy of Dr Ian Farnan of the University of Cambridge was used to optimise the SIMS condition for the measurements. SIMS determines the relative abundance of elements/isotopes in a sample by bombarding its surface with a primary ion beam and separating the ejected secondary ions according to their masses and then measuring them. In depth profiling, the secondary ions are emitted from below the initial surface. To measure the relative abundance of ^6Li and ^7Li in $^{\text{Nat}}\text{Li}_2\text{O}-\text{TeO}_2$ and $^{\text{Null}}\text{Li}_2\text{O}-\text{TeO}_2$, and ^{10}B and ^{11}B in $\text{K}_2\text{O}-\text{B}_2\text{O}_3-\text{GeO}_2$, 3 scans per sample using an O_2^+ primary ion beam at 1 keV and 20 nA were taken within the suitable mass ranges; 5 to 9 a.m.u for ^6Li and ^7Li , and 9 to 12 a.m.u for ^{10}B and ^{11}B . The incident angles and the scan sizes are 30° and 400 microns, and 45° and 200 microns for the lithium and boron systems respectively. As for the depth profiling analysis, all parameters were kept similar except for the primary beam current and scan size for the lithium system which were changed to 80 nA and 350 microns, respectively. The samples were depth-profiled for about 35 minutes ignoring the signals for the first 10 minutes to avoid any SIMS transient effects. From the profiles obtained, the average count of mass for each isotope was determined to find the relative isotope abundance. The relative abundances of ^6Li and ^7Li were used to confirm the null average neutron scattering length of the null samples and, for the ^{10}B and ^{11}B , it was used to improve the neutron diffraction data processing by correcting the absorption due to the ^{10}B isotope.

3.9 Synchrotron X-ray diffraction [38]

The high energy X-ray total scattering data were collected at the Argonne National Laboratory APS Beamline 6-ID-D by Dr Chris Benmore (Magnetic Materials Group, Advanced Photon Source, Argonne, Chicago USA) and Dr Oliver Alderman (Materials Development Inc Chicago). An X-ray wavelength of 0.14349 Å (86.406 keV), just below the 88keV Pb K-edge, was used on the lead tellurite ($\text{PbO}-\text{TeO}_2$) glass samples. The synchrotron was in continuous top-up mode during the data collection and therefore normalisation was only required to

the exposure time, not the monitor counts. The glass samples were ground to a fine powder in an agate pestle and mortar, in air, on the day of the experiment to avoid water attack. The powdered sample was loaded into 1mm inner diameter Kapton tubes (wall thickness of ~100 microns) and held vertically in the sample changer. An area detector of Tl-doped CsI scintillator, with the dimensions of 2048 x 2048 pixels, where each pixel has 200 micron x 200 micron square, and 500 microns deep was used. A programme called Fit2D [39] was used to average out and integrate the diffraction data. Corrections were then applied to the output for the absorption of the scattered beam between the sample and the detector, and the detector's oblique angle of incidence. The output was then processed using GudrunX (variation of GudrunN [40], for X-ray) with the standard procedures in Gudrun as described in Chapter 2.

3.10 Nuclear magnetic resonance (NMR) [41]

In NMR, a population of nuclear spins becomes distributed between a series of energy levels whose degeneracy has been removed by placing the sample in a magnetic field (B , typically 1 to 20 T). The energy levels depend on characteristics of the nucleus which must possess a magnetic moment (nuclear spin $I > 0$). The number of levels ($2I + 1$) is determined by the nuclear spin I , which has a value $3/2$ for ^{11}B , the nucleus of interest to this study; the extent of their (Zeeman) splitting ($\gamma\hbar B$) depends on the strength of the magnetic field and on the gyromagnetic ratio, γ , of the nucleus (Fig. 3.5). This energy separation can be equated to the Larmor frequency, $\omega_L = \gamma B$. For $I > 1/2$, the separations of the energy levels are also modified by the quadrupolar interaction.

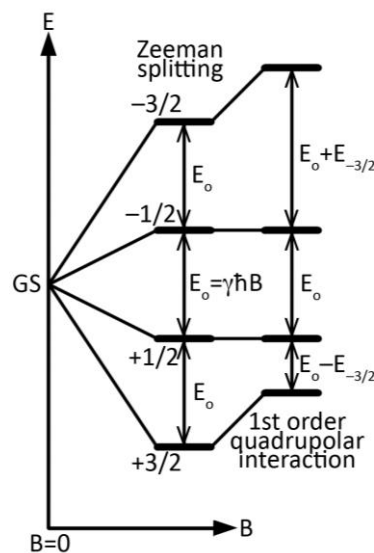


Figure 3.5: Zeeman splitting and quadrupolar interaction of ^{11}B isotope in B .

The distribution of the nuclear spins is then perturbed by application of an ω rf pulse for a few microseconds and, as the distribution re-equilibrates, the change in magnetisation which occurs (the free induction decay, FID) is measured. The NMR spectrum is then obtained by taking a Fourier transform of the FID which converts the time domain of the signal to the frequency domain. The resulting spectrum is plotted as intensity against chemical shift, δ , which is defined as: $\delta = (\nu_{\text{sample}} - \nu_{\text{ref}})/\nu_{\text{ref}}$ where ν_{sample} and ν_{ref} are the frequencies of the sample and of a reference material which is either the recognised standard for that nucleus (primary standard) or a material which is easier to obtain/use (secondary standard) but whose chemical shift with respect to the primary standard is well known and can be corrected for. The chemical shift is an indicator of the extent to which the applied field B is modified locally by the chemical environment in comparison with the local environment in the primary reference. It gives information about the number and type of nearest and next-nearest neighbours of a nucleus. The ability to obtain this local information on a specific nucleus is of particular value in a glass. However, this depends on being able to resolve the contributions to the spectrum from different sites, which in turn requires the elimination/reduction of various broadening mechanisms. Many of these can be largely eliminated by the use of magic-angle spinning (MAS) where a rotor containing the powdered sample is spun rapidly (typically 5 to 30 kHz and even up to 100 kHz) around its cylindrical axis which is set at the magic-angle θ to the applied field (Fig. 3.6) where θ takes the value 54.73° such that the expression $3\cos^2\theta - 1$ goes to zero.

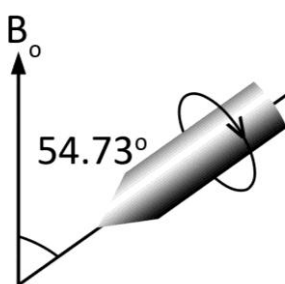


Figure 3.6: Magic-angle spinning (54.73°) MAS NMR setup.

^{11}B NMR spectra were collected using a 14.1 T Bruker Avance II+ 600 MHz spectrometer tuned to 192.3 MHz using a Bruker 4 mm probe (lithium borogermanate system) or a 14.15 T Varian spectrometer using a 4 mm Varian T3 probe tuned to 193.1 MHz with magic angle spinning (MAS) frequency 12 kHz in both cases. BPO_4 was used as a secondary reference material with chemical shift -3.3 ppm with respect to the primary reference boron trifluoride ether (BTE). Fig. 3.7 shows a typical ^{11}B NMR spectrum; the contributions from boron coordinated to 3 and 4 neighbours can be clearly seen. The area of $[\text{BO}_3]$ is scaled by a factor

of 1.04 to compensate for loss of intensity into the sidebands. The average coordination number for boron is then calculated based on the integrated peak intensities. The coordination number $n_{BO} = 3 + N_4$ where

$$N_4 = \frac{\text{Area}[\text{BO}_4]}{(1.04 * \text{Area}[\text{BO}_3]) + \text{Area}[\text{BO}_4]} \quad 3.9$$

The $[\text{BO}_4]$ peak is narrow and symmetric because the $[\text{BO}_4]$ unit is near-spherically symmetric and hence has only a small field gradient. The $[\text{BO}_3]$ unit is only axially symmetric and hence has a significant field gradient which interacts with the quadrupole moment of the ^{11}B nucleus leading to a broad, complex lineshape.

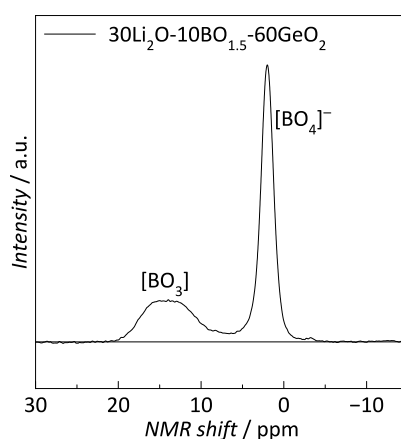


Figure 3.7: Typical NMR spectrum for ^{11}B in borogermanate glass.

3.11 References

1. Barney, E. R., Hannon, A. C., Holland, D., Umesaki, N., Tatsumisago, M., Orman, R. G., Feller, S. *Journal of Physical Chemistry Letters* 2013, 4, 2312-2316.
2. Scholze, H., *Glass: Nature, Structure, and Properties*; Springer Science & Business Media, 2012.
3. Leadbetter, A., Wright, A. *Journal of Non-Crystalline Solids* 1972, 7, 23-36.
4. Feller, S., Lower, N., Affatigato, M. *Physics and Chemistry of Glasses* 2001, 42, 240-246.
5. Taniguchi, T., Inoue, S., Mitsuhashi, T., Nukui, A. *Journal of Applied Crystallography* 2000, 33, 64-70.
6. Araujo, E., Idalgo, E., Moraes, A., Souza Filho, A., Mendes Filho, J. *Modern Physics Letters B* 2010, 24, 527-537.
7. Avramov, I., Guinev, G., Rodrigues, A. *Journal of Non-Crystalline Solids* 2000, 271, 12-17.
8. Sekiya, T., Mochida, N., Ohtsuka, A., Tonokawa, M. *Journal of Non-Crystalline Solids* 1992, 144, 128-144.
9. Tatsumisago, M., Lee, S.-K., Minami, T., Kowada, Y. *Journal of Non-Crystalline Solids* 1994, 177, 154-163.
10. Hehlen, B., Courtens, E., Vacher, R., Yamanaka, A., Kataoka, M., Inoue, K. *Physical Review Letters* 2000, 84, 5355.
11. Champarnaud-Mesjard, J., Blanchandin, S., Thomas, P., Mirgorodsky, A., Merle-Mejean, T., Frit, B. *Journal of Physics and Chemistry of Solids* 2000, 61, 1499-1507.

12. Soltay, L., Henderson, G. *Physics and Chemistry of Glasses-European Journal of Glass Science and Technology Part B* 2005, 46, 381-384.
13. Kalampounias, A. G., Boghosian, S. *Vibrational Spectroscopy* 2012, 59, 18-22.
14. Bates, S., Zografi, G., Engers, D., Morris, K., Crowley, K., Newman, A. *Pharmaceutical Research* 2006, 23, 2333-2349.
15. Suryanarayana, C., Norton, M. G., *X-Ray Diffraction: A Practical Approach*; Springer Science & Business Media, 2013.
16. Romero, M., Rincón, J. M. *Journal of the American Ceramic Society* 1999, 82, 1313-1317.
17. Smets, B., Lommen, T. *Physics and Chemistry of Glasses* 1982, 23, 83-7.
18. Takaishi, T., Takahashi, M., Jin, J., Uchino, T., Yoko, T. *Journal of the American Ceramic Society* 2005, 88, 1591-1596.
19. Cormier, L., Calas, G., Beuneu, B. *Journal of Non-Crystalline Solids* 2007, 353, 1779-1784.
20. Majérus, O., Cormier, L., Calas, G., Soper, A. *Physica B: Condensed Matter* 2004, 350, 258-261.
21. Niida, H., Uchino, T., Jin, J., Kim, S., Fukunaga, T., Yoko, T. *Journal of Chemical Physics* 2001, 114.
22. Barney, E. R., Hannon, A. C., Holland, D., Umesaki, N., Tatsumisago, M. *Journal of Non-Crystalline Solids* 2015, 414, 33-41.
23. Barney, E., Hannon, A., Holland, D., Winslow, D., Rijal, B., Affatigato, M., Feller, S. *Journal of Non-Crystalline Solids* 2007, 353, 1741-1747.
24. Alderman, O. L., Hannon, A. C., Holland, D., Umesaki, N. *Journal of Non-Crystalline Solids* 2014, 386, 56-60.
25. Alderman, O., Ferlat, G., Baroni, A., Salanne, M., Micoulaut, M., Benmore, C., Lin, A., Tamalonis, A., Weber, J. *Journal of Physics: Condensed Matter* 2015, 27, 455104.
26. Petkov, V., Billinge, S., Shastri, S., Himmel, B. *Physical Review Letters* 2000, 85, 3436.
27. Hung, I., Howes, A., Parkinson, B., Anupöld, T., Samoson, A., Brown, S. P., Harrison, P., Holland, D., Dupree, R. *Journal of Solid State Chemistry* 2009, 182, 2402-2408.
28. Howes, A., Vedishcheva, N., Samoson, A., Hanna, J. V., Smith, M. E., Holland, D., Dupree, R. *Physical Chemistry Chemical Physics* 2011, 13, 11919-11928.
29. Roderick, J., Holland, D., Howes, A., Scales, C. *Journal of Non-Crystalline Solids* 2001, 293, 746-751.
30. In *National Chemistry Database Service*, Royal Society of Chemistry: 2016.
31. Hannon, A., *Xtal: A Program for Calculating Interatomic Distances and Coordination Numbers for Model Structures*; Rutherford Appleton Laboratory, 1993.
32. Zachariasen, W. H. *Journal of the American Chemical Society* 1932, 54, 3841-3851.
33. In *SciGlass Professional 7.3*, ITC Inc.: 2008.
34. Wendlandt, W. W., *Thermal Methods of Analysis*; Wiley-Interscience. New York, 1974.
35. Brown, M. E., Gallagher, P. K., *Handbook of Thermal Analysis and Calorimetry: Recent Advances, Techniques and Applications*; Elsevier, 2011; Vol. 5.
36. Gupta, P. K., Mauro, J. C. *Journal of Chemical Physics* 2009, 130, 094503.
37. Colthup, N., *Introduction to Infrared and Raman Spectroscopy*; Elsevier, 2012.
38. Koch, M., Bordas, J. *Nuclear Instruments and Methods in Physics Research* 1983, 208, 461-469.
39. Hammersley, A. *European Synchrotron Radiation Facility Internal Report* 1997, 68.
40. Soper, A. *Rutherford Appleton Laboratory Technical Report* 2011.
41. Duer, M. J., *Solid State NMR Spectroscopy: Principles and Applications*; John Wiley & Sons, 2008.

Chapter 4 – Tellurites

4.1 Introduction

This chapter describes the cation M environments in TeO_2 , lithium tellurite (IV) and lead (II) tellurite (IV) crystals, in terms of average M-O distances (r_{MO}) and average M-O coordination numbers (n_{MO}). Important local environment information is obtained from these crystal structures to be used in the glass short-range structure analysis. The literature on tellurite glass structure is then reviewed and the mechanism by which the tellurite network changes as a function of modifier content is discussed. This later serves as a basis for tellurite glass structural models, including the tellurite model (for pure tellurite glass), and the alkali tellurite model (based on potassium tellurite glasses), and a description of aluminium tellurite and boron tellurite glasses. The chapter concludes with a summary of the Te, Li, and Pb environments in crystals and the likely implications for the glasses.

4.2 TeO_2 crystal structures

4.2.1 α , β , γ , and δ polymorphs of TeO_2

There are 4 known TeO_2 crystal polymorphs: α - TeO_2 , β - TeO_2 , γ - TeO_2 and δ - TeO_2 . The alpha phase (tetragonal, paratellurite) is the most stable form. This phase transforms into the beta phase (orthorhombic, tellurite) at high pressure [1-2]. This beta phase also irreversibly transforms to the alpha phase at high temperature (600 °C) [3]. The other two phases are metastable phases found during re-crystallisation of rich TeO_2 -containing glasses [4-8].

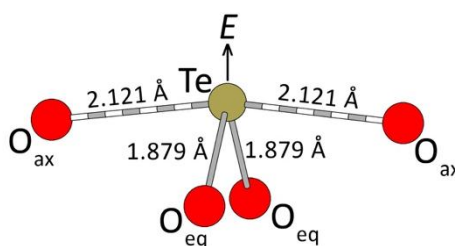


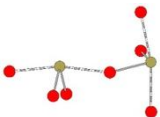
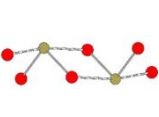
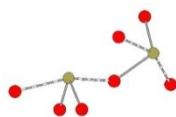
Figure 4.1: The basic $[\text{TeO}_4]$ unit as in α - TeO_2 crystal. Te (gold) is bonded to O (red) atoms with two short equatorial bonds ($<2.00 \text{ \AA}$) (grey cylinder) and two long axial bonds ($<2.00 \text{ \AA}$) (striped cylinder). E is the stereo-chemically active lone-pair of electrons of the Te atom.

Crystal structure data are available for α - TeO_2 [9], β - TeO_2 [3], and γ - TeO_2 [4], but not δ - TeO_2 . However, Gulenko *et al.* [10] studied its structure (when synthesised with small modifier content, i.e., 5 – 10 mol%) by neutron diffraction and simulation. The structural unit of α - TeO_2 is shown in Fig. 4.1.

4.2.2 Tellurium (IV) environment

In α , β , and γ -TeO₂ phases, the average Te-O coordination number (n_{TeO}) is 4 for $r_{\text{TeO}} < 2.2$ Å and there is only 1 Te site in each phase. The tellurium atom (Te) in α -TeO₂ (Fig 4.1) is connected to 4 bridging oxygen atoms (BO) in a distorted trigonal bipyramidal (tbp) geometry. There are two short equatorial Te-O_{eq} bonds (1.879 Å) and two longer axial Te-O_{ax} bonds (2.121 Å) in the polyhedron. The distortion is caused by the steric effect of the stereochemically active lone-pair of electrons (E) which occupies the third equatorial site of the polyhedron. The symmetry (present in the α -TeO₂ phase) is absent in both β -TeO₂ and γ -TeO₂ phases with the presence of 2 non-equal short and 2 non-equal long bonds as shown in Table 4.1. In δ -TeO₂, Gulenko *et al.* [10] used molecular dynamics simulation to show the presence of [TeO₃] units with one terminal oxygen TO (Te=O) atom in addition to the [TeO₄] units which implies that the average n_{TeO} in δ -TeO₂ is less than 4.

Table 4.1: The short range order parameters as observed in α -TeO₂, β -TeO₂, γ -TeO₂, and δ -TeO₂ phases. All oxygen atoms shown are bridging oxygen ($O_{n/2}$) atoms. Long (> 2 Å) axial bonds are represented by the striped cylinder and shorter equatorial bonds are represented by the solid cylinder. The TeO₂ connectivity in γ -TeO₂ is similar to α -TeO₂ but with a different torsion angle. r_{max} is defined by the upper limit of the first coordination sphere from the $T(r)$ as in Fig. 4.2

	α -TeO ₂	β -TeO ₂	γ -TeO ₂	δ -TeO ₂
Structural unit	TeO _{4/2}	TeO _{4/2}	TeO _{4/2}	[TeO ₄] and [TeO ₃]
Average n_{TeO} ($r_{\text{TeO_max}}=2.36$ Å)	$n_{\text{TeO}} = 4$	$n_{\text{TeO}} = 4$	$n_{\text{TeO}} = 4$	$n_{\text{TeO}} < 4$
Te site	1	1	1	N/A
Short bond / Å	1.879, 1.879	1.879, 1.972	1.859, 1.946	N/A
Long bond / Å	2.121, 2.121	2.070, 2.196	2.019, 2.197	N/A
TeO ₂ connectivity	Corner	Edge	Corner	N/A
				

TeO₂ polyhedra in α -TeO₂ and γ -TeO₂ are corner-sharing whilst face-sharing occurs in β -TeO₂. γ -TeO₂ is a metastable form but its structure is more similar to that of the stable α -TeO₂ and not to β -TeO₂ which is a high pressure / temperature polymorph. The close similarity of the structures of pure TeO₂ glass and γ -TeO₂ is evident in thermal analysis of TeO₂ glasses where pure TeO₂ glass transforms to γ -TeO₂ on heating [11]. Based on this, the local environments in TeO₂ glass are therefore likely to be similar to those of γ -TeO₂ as will later be discussed. The simulated neutron total correlation functions ($T(r)$) for all of the phases are shown in Fig. 4.2. The Te-O separations ($r_{\text{TeO}} < 2.4$ Å, in all the phases, appear to consist of two distributions centred at ~ 1.85 - 1.95 Å and ~ 2.1 - 2.2 Å. The peak width of the

second distribution is seen to decrease as a function of the crystal stability ($\alpha > \beta > \gamma$). The oxygen-oxygen (r_{OO}) distributions in α -TeO₂ and β -TeO₂ are similar, and can be approximated as a single peak centred at ~ 2.8 Å. In γ -TeO₂ however, there is a shorter r_{OO} at ~ 2.5 Å. This short distance plays an important role in indicating the stereo-chemical activity of the Te lone-pair as will be discussed later in this thesis.

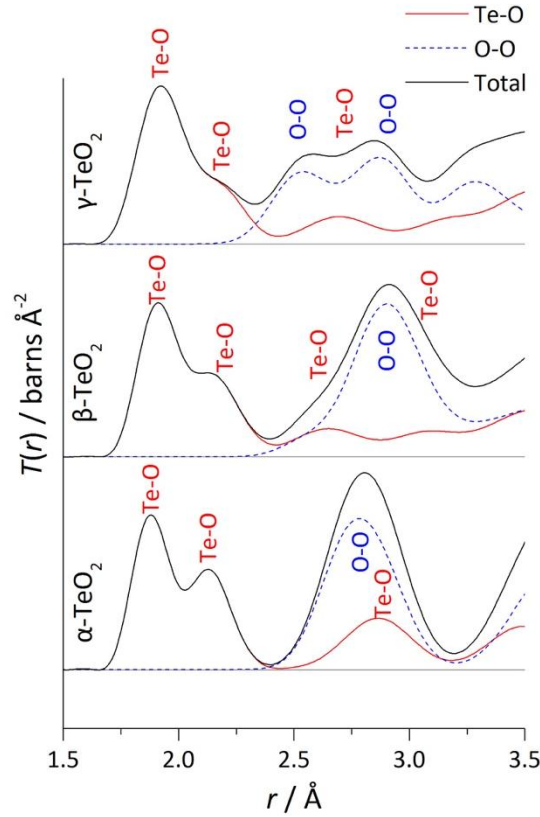


Figure 4.2: Simulated total correlation function $T(r)$ of α -TeO₂, β -TeO₂, and γ -TeO₂ crystals. $T(r)$ for Te-O and O-O pairs are shown in solid red and dotted blue lines respectively. The sum of all pairs is the thicker black line. The $T(r)$ for Te-Te starts at > 3 Å. Lorch modification function is used for simulating the $T(r)$.

4.3 Lithium tellurite crystals

4.3.1 General structure

There are 3 known lithium tellurite (Te(IV)) crystals: α -Li₂Te₂O₅ [12], β -Li₂Te₂O₅ [12] (high temperature phase [13]), and Li₂TeO₃ [14]. α -Li₂Te₂O₅ and β -Li₂Te₂O₅ (33.33 mol% of Li₂O) contain four-coordinated distorted trigonal bi-pyramidal tbp [TeO₃₊₁] units. Subscript: 3+1 means 3 short bonds ($r < 2.0$) and 1 longer bond ($2.0 < r < 2.2$). The unit is similar to the trigonal bi-pyramidal shape of the [TeO₄] unit found in TeO₂ crystals but with one Te-O bond extended. Li₂TeO₃ (50 mol% Li₂O) contains only three-coordinated trigonal pyramidal tp [TeO₃]²⁻ units. [TeO₃₊₁] polyhedra in α -Li₂Te₂O₅ are connected via corners, similar to α -TeO₂, whereas, in β -Li₂Te₂O₅, they are connected via both corners and edges. Li atoms are

arranged in distorted tetrahedral $[\text{LiO}_4]$ units in all of the crystals within the r_{LiO} limit of 2.60 Å and the next nearest oxygen atom is at ~ 2.70 Å which is found only in $\alpha\text{-Li}_2\text{Te}_2\text{O}_5$. These short range structural parameters are summarised in Table 4.2.

Table 4.2: Local order structural parameters in the lithium tellurite crystals.

	$\alpha\text{-Li}_2\text{Te}_2\text{O}_5$	$\beta\text{-Li}_2\text{Te}_2\text{O}_5$	Li_2TeO_3
Structural units	Distorted tbp $[\text{TeO}_{3+1}]$, distorted tetrahedral $[\text{LiO}_4]$ and $[\text{LiO}_{4+1}]$	Distorted tbp $[\text{TeO}_{3+1}]$ and distorted tetrahedral $[\text{LiO}_4]$	Trigonal pyramidal tp $[\text{TeO}_3]^{2-}$ and distorted tetrahedral $[\text{LiO}_4]$
Average n_{xo} ($r_{\text{TeO_max}}=2.36$ Å, $r_{\text{LiO_max}}=2.60$ Å)	$n_{\text{TeO}} = 4$ $n_{\text{LiO}} = 4$	$n_{\text{TeO}} = 4$ $n_{\text{LiO}} = 4$	$n_{\text{TeO}} = 3$ $n_{\text{LiO}} = 4$
Te sites	2	2	1
Li sites	2	2	2
TeO ₂ connectivity	Corner	Corner, edge	None (All non-bridging O)

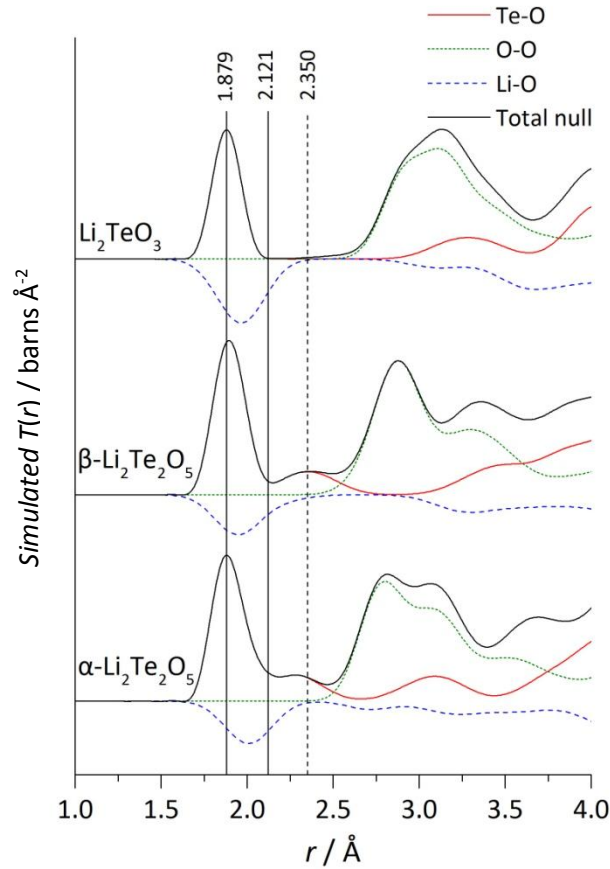


Figure 4.3: Simulated $T(r)$ for the lithium tellurite crystals showing the total (Null Li) correlation function (thick black), Te-O pair correlation (red), Li-O pair correlation (dashed blue), and O-O pair correlation (dotted green). $T(r)$ for (Nat Li) Li-O shows a negative distribution due to the value of average scattering length $\langle b \rangle$ for the Li at the natural abundance (-1.90).

Fig. 4.3 shows the simulated null $T(r)$ for the lithium tellurite crystals (null scattering is described in Chapter 2, Section 2.3.2). The contribution due to the $[\text{TeO}_{3+1}]$ units is clearly seen in the $T(r)_{\text{TeO}}$ for $\alpha\text{-Li}_2\text{Te}_2\text{O}_5$ and $\beta\text{-Li}_2\text{Te}_2\text{O}_5$ (the peak at 1.879 Å comprises the “3” short bonds, and the peak at 2.350 Å comprises the longer “+1” bond). In Li_2TeO_3 there is only 1 peak at 1.879 Å denoting the presence of solely three-coordinated units (the $[\text{TeO}_3]^{2-}$ resonance unit would have an r_{TeO} value of 1.8706 Å, from the bond valence calculation [15]). The Li-O partials show no clear difference between the crystals giving only 1 (negative) peak at ~ 2 Å. This corresponds to all $[\text{LiO}_4]$ units found in the crystals regardless of the average n_{TeO} .

4.3.2 Tellurium (IV) environment

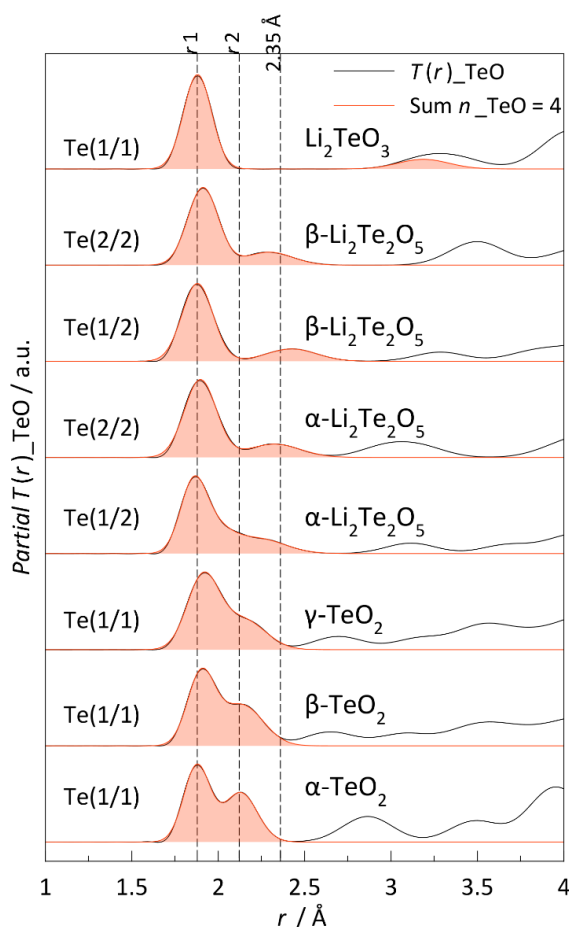


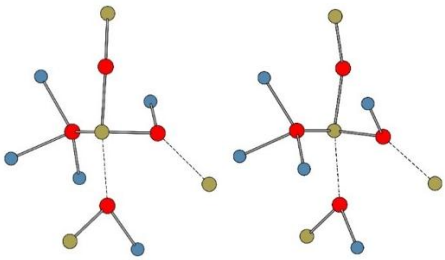
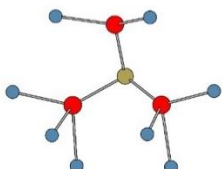
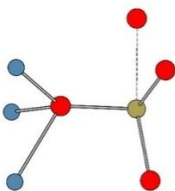
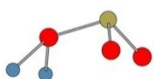
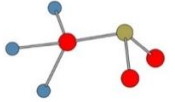
Figure 4.4: Partial Te-O pair distributions in TeO_2 , $\text{Li}_2\text{Te}_2\text{O}_5$, and Li_2TeO_3 crystals for each Te site. The distances can be parameterised with 2 peaks (3 for $\alpha\text{-Li}_2\text{Te}_2\text{O}_5$) according to the definition of short(r_1), long(r_2), and longer(2.35) bonds as shown by the vertical lines.

Comparing the Te environments in the TeO_2 , $\alpha\text{-Li}_2\text{Te}_2\text{O}_5$, $\beta\text{-Li}_2\text{Te}_2\text{O}_5$, and Li_2TeO_3 crystals, the most striking feature observed is the evolution of the long axial Te-O bond. Fig. 4.4 shows

the simulated ‘partial’ $T(r)$ for each Te site, arranged according to the Li_2O content and the polymorphic stability. High temperature polymorphs (β phases of the crystals) have longer “long” r_{TeO} bonds compared to their respective α phases while the “short” r_{TeO} bonds remain approximately unchanged. The same trend is observed as a function of composition with more $[\text{TeO}_4]$ units being transformed into $[\text{TeO}_{3+1}]^-$ until at 50 mol% of Li_2O , where all units are $[\text{TeO}_3]^{2-}$ units. This trend gives a good indication of how the Te environment might change with composition in the glassy state.

4.3.3 Non-bridging oxygen environments

Table 4.3: Te–NBO environments in alkali tellurite crystals. (O – red; Te – gold; Li – blue)

	$\alpha\text{-Li}_2\text{Te}_2\text{O}_5$ and $\beta\text{-Li}_2\text{Te}_2\text{O}_5$	Li_2TeO_3
Te site(s)	 $\text{TeO}_{3/2}\text{O}^-$	 TeO_3^{2-} $\text{TeO}(\text{O}^-)_2$
Te–NBO	 $\text{Te}-\text{O}^-(\text{O1b})$ $(\text{Te}-\text{O1b})$	 $\text{Te}=\text{O} \leftrightarrow \text{Te}^+-\text{O}^-$ $(\text{Te}-\text{O1c})$  $\text{Te}-\text{O}^- \leftrightarrow \text{Te}=\text{O}$ $(\text{Te}-\text{O1c})$

The tellurium - non-bridging oxygen (Te–NBO) environments in $[\text{TeO}_4]^-$ and $[\text{TeO}_3]^{2-}$ units in lithium tellurite crystals, $\text{Li}_2\text{Te}_2\text{O}_5$ and Li_2TeO_3 , respectively (Table 4.3) have different Te–NBO distances. The $[\text{TeO}_4]^-$ unit in $\text{Li}_2\text{Te}_2\text{O}_5$ can be more accurately represented by

$\text{TeO}_{3/2}\text{O}^-$ (3 BOs and 1 NBO) whereas the $[\text{TeO}_3]^{2-}$ unit in Li_2TeO_3 is $\text{TeO}(\text{O}^-)_2$ (3 NBOs: a resonance between 2 NBO and 1 double bond oxygen). For simplicity, the NBOs in $[\text{TeO}_4]^-$ and $[\text{TeO}_3]^-$ are represented as O1b and O1c, respectively. The nomenclature of these units is explained in Appendix A. The bond parameters of the Te-O1b and Te-O1c, derived from the crystal structures, are shown in Table 4.4. The average $r_{\text{Te-O1b}}$ is shorter than $r_{\text{Te-O1c}}$ by 0.034 Å which lowers the Te–O bond valence and consequently affects the average number of Li atoms which can be provided with coordination: on average, 2.48 lithium atoms bond to O1b and 2.77 lithium atoms to O1c. The average number of lithium atoms around the NBO shown in Table 4.5 is calculated based on the bond distances of Te–O pairs in each crystal phase for the cases of $n_{\text{LiO}} = 4, 4.5$, and 5 (relevant to later results).

4.3.4 Lithium environment

In lithium tellurite crystals, a lithium atom is coordinated to an average of 4 oxygen atoms in a distorted tetrahedral $[\text{LiO}_4]$ unit (cut-off value of 2.5 Å, defined by the upper limit of the first coordination sphere as shown in the $T(r)$ in Fig. 4.5). From Fig. 4.5, the Li–O distances range from 1.92 to 2.21 Å. For 4-coordinated Li, the principal Li–O distance in all the crystal phases can be fitted with a Gaussian at 1.96 Å (from bond valence calculation, the value is 1.98 Å [15]).

Table 4.4: Bond parameters of Te–O and Li–O pairs in lithium tellurite crystals.

Crystal	$r(\text{Te-O1b}) / \text{\AA}$	$r(\text{O1b-Li}) / \text{\AA}$		
		Li1	Li2	Li3
$\alpha\text{-Li}_2\text{Te}_2\text{O}_5$	1.841	1.974	2.041	2.041
	1.850	1.942	2.006	2.018
$\beta\text{-Li}_2\text{Te}_2\text{O}_5$	1.849	1.960	1.969	1.922
	1.856	1.930	1.943	2.217
Average	1.849 Å (1.41 v.u.)	1.997 Å (0.24 v.u.)		
	$r(\text{Te-O1c}) / \text{\AA}$	$r(\text{O1c-Li}) / \text{\AA}$		
		Li1	Li2	Li3
Li_2TeO_3	1.929	1.932	1.993	2.003
	1.848	1.896	1.975	2.024
	1.871	1.995	1.938	-
Average	1.883 Å (1.29 v.u.)	1.970 Å (0.26 v.u.)		

Higher coordinated Li is not uncommon, as 5 and 6 coordinated Li is also observed in other crystals [16]. However, in the $\alpha\text{-Li}_2\text{Te}_2\text{O}_5$ phase, one Li site has 1 additional O atom at 2.727 Å (0.03 v.u.). If this oxygen is considered as bonding, the unit can be labelled as $[\text{LiO}_{4+1}]$ unit.

However, this distance is not included in the first coordination sphere as clearly seen in Fig. 4.5, which shows the $T(r)$ for the Li-O pairs in the tellurite crystals.

Table 4.5: Average number of Li atoms bonded to O1a, O1b, and O1c for the cases of $n_{\text{LiO}} = 4, 4.5$, and 5, and the calculated values from the crystal phases

NBO site	Average n_{LiO}	Average Li atoms	Case
O1b	4	2.36	I
	4.5	2.66	II
	5	2.95	III
	Crystal site	2.48	-
O1c	4	2.84	IV
	4.5	3.20	V
	5	3.55	VI
	Crystal site	2.77	-
O1a <i>Te=O</i> (<i>Te</i> – terminal oxygen, 1.5 v.u.)	4	2.00	VII
	4.5	2.25	VIII
	5	2.50	IX
	Crystal site	-	-

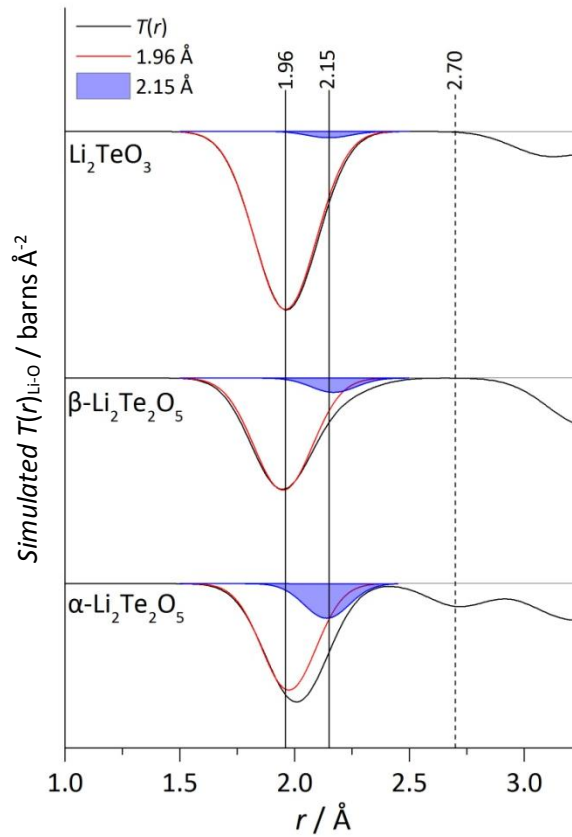


Figure 4.5: $T(r)$ for Li-O pair in the lithium tellurite crystals. Average n_{LiO} of 4 is represented by the peak at ~ 2 Å. The peak at ~ 2.7 Å is the next nearest Li-O distance found in $\alpha\text{-Li}_2\text{Te}_2\text{O}_5$

The area from the Li-O peak for each crystal gives an average lithium coordination number of 4 (cut-off 2.6 Å). As seen in the figure, the average Li-O distances in the crystals are similar

at about 2 Å. This average distance can be parameterised with two peaks: one fixed at 1.96 Å to represent the tetrahedral Li-O distance; and the second peak at 2.15 Å, arbitrarily positioned to enable a fit the total Li-O peak. The area of the second peak at 2.15 Å is an indirect measure of the degree of asymmetry in the tetrahedral [LiO₄] unit. The r_{LiO} distribution in $\alpha\text{-Li}_2\text{Te}_2\text{O}_5$ is more distorted than that in $\beta\text{-Li}_2\text{Te}_2\text{O}_5$. However, since it contains contributions from 2 Li sites in the crystals, it may not reflect the actual Li site in the crystal. Individual Li site parameters will be discussed later in this section.

Table 4.6: Running bond valence sum for Li-O bonds in the lithium tellurite crystals.

	From site	To site	Distance, r / Å	BV / v.u.	Running sum BV / v.u.
$\alpha\text{-Li}_2\text{Te}_2\text{O}_5$	Li(1)	O	1.974	0.25	0.25
			2.006	0.23	0.49
			2.008	0.23	0.72
			2.040	0.21	0.93
	Li(2)	O	2.621	-	-
				-	-
				-	-
				-	-
				-	-
				-	-
				-	-
$\beta\text{-Li}_2\text{Te}_2\text{O}_5$	Li(1)	O	1.922	0.29	0.29
			1.938	0.28	0.57
			1.960	0.26	0.83
			2.217	0.13	0.97
	Li(2)	O	2.724	-	-
				-	-
				-	-
				-	-
				-	-
				-	-
Li_2TeO_3	Li(1)	O	1.896	0.31	0.31
			1.955	0.27	0.58
			1.993	0.24	0.82
			2.004	0.23	1.05
	Li(2)	O	2.553	-	-
				-	-
				-	-
				-	-
				-	-
				-	-

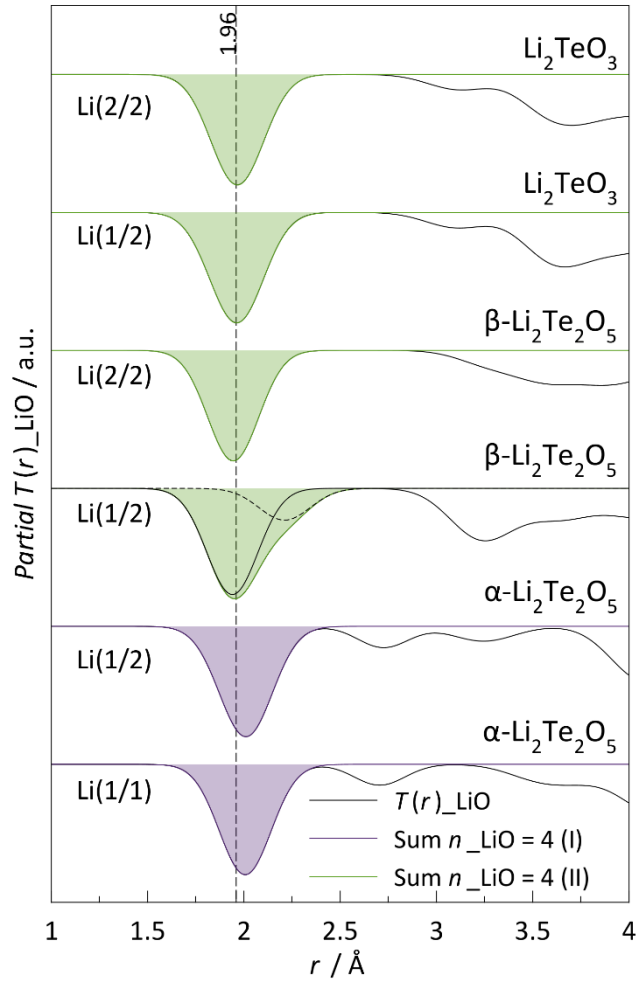


Figure 4.6: Simulated $T(r)$ for Li–O pairs in lithium tellurite crystal for individual Li sites

The contribution of bond valence from O atoms to Li is shown in Table 4.6. The limit of r_{LiO} is often taken to be less than the shortest r_{LiLi} . The total bond valence for Li ranges from 0.93 to 1.10 based on the r_{LiO} in the table, with 4 bonding oxygen atoms. The bond valence sum is however slightly lower in $\alpha\text{-Li}_2\text{Te}_2\text{O}_5$ unless the fifth oxygen atom at 2.726 Å is considered giving the sum of 0.96 instead of 0.93. The simulated $T(r)$ for the individual Li sites are shown in Fig. 4.6. The shape of the Li–O distance distribution for all Li sites in $\alpha\text{-Li}_2\text{Te}_2\text{O}_5$ and Li_2TeO_3 are similar but with different centre of the peak. Whilst the Li2 site in $\beta\text{-Li}_2\text{Te}_2\text{O}_5$ has a similar distribution and peak centre as the Li sites in Li_2TeO_3 , the Li1 site is remarkably different due to the longer r_{LiO} at 2.217 Å. The average n_{LiO} is however still 4. The Li1 site ($\beta\text{-Li}_2\text{Te}_2\text{O}_5$) is therefore a suitable visualisation of the distorted tetrahedral $[\text{LiO}_4]$ unit and possibly the Li environment in lithium tellurite glasses. This is in accordance with the general knowledge that the structure of a glass is more similar to that of the high temperature crystal polymorph of the same composition rather than the stable crystal polymorph.

4.4 Lead tellurite crystals

4.4.1 General structure

There are 3 lead tellurite crystals within the composition range of these studies: $\text{PbTe}_5\text{O}_{11}$ [17], $\text{Pb}_2\text{Te}_3\text{O}_8$ [18], and PbTeO_3 [19]. These crystal phases are selected from the literature based on the (smallest) R-value. Compared to lithium tellurite crystals, the Te environments in lead tellurites are more complex. In $\text{PbTe}_5\text{O}_{11}$ (16.67 mol% PbO) and $\text{Pb}_2\text{Te}_3\text{O}_8$ (40 mol% PbO), there are 5 and 4 Te sites respectively, comprising both $[\text{TeO}_4]$ and $[\text{TeO}_3]$ units. In PbTeO_3 (50 mol% PbO), there are 3 $[\text{TeO}_3]$ sites. In lithium tellurite crystals, $[\text{TeO}_3]$ units only exist at 50 mol% Li_2O with intermediate $[\text{TeO}_{3+1}]$ units being found at 33.33 mol% Li_2O , whereas in lead tellurite, the $[\text{TeO}_3]$ units exist in lead tellurite crystal with PbO content of as low as 16.67 mol%.

Table 4.7: Local order structural parameters in lead tellurite crystals. *the next $r_{\text{Te-O}}$ is at 2.644 Å.

	$\text{PbTe}_5\text{O}_{11}$	$\text{Pb}_2\text{Te}_3\text{O}_8$	PbTeO_3
Structural units	Distorted tbp $[\text{TeO}_4]$, tp $[\text{TeO}_3]$, and distorted $[\text{PbO}_8]$ units	Distorted tbp $[\text{TeO}_{3+1}]$, $[\text{TeO}_4]$, tp $[\text{TeO}_3]$, distorted $[\text{PbO}_7]$ and $[\text{PbO}_8]$ units	Trigonal pyramidal tp $[\text{TeO}_{3+1}]$, distorted $[\text{PbO}_5]$ and $[\text{PbO}_7]$ units
Average coordination number, n_{XO}	$n_{\text{TeO}} = 3.70$ (max 2.35 Å) $n_{\text{PbO}} = 6.35$ (max 3.00 Å) $n_{\text{PbO}} = 8.00$ (max 3.30 Å)	$n_{\text{TeO}} = 2.93$ (max 2.35 Å) $n_{\text{PbO}} = 3.19$ (2.44 Å)	$n_{\text{TeO}} = 3.00$ (max 2.35 Å) $n_{\text{PbO}} = 1.95$ (2.27 Å)
Te sites	5	4	3
Pb sites	1	2	3
TeO_2 connectivity	Corner and edge	Corner	None*

In lithium tellurites, the average n_{LiO} is 4 in all compositions; in lead tellurites, Pb-O polyhedra with 2 to 8 oxygen atoms are present, leading to differences in average n_{PbO} . The short-range order parameters of the lead tellurite crystals are shown in Table 4.7. The cut-off values are shown in parentheses. From the table, for example, $n_{\text{TeO}} = 3.70$ (max 2.35 Å) means that 3.70 was obtained by integration, with the max r of 2.35 Å and $n_{\text{PbO}} = 1.95$ (2.27 Å) mean that 1.95 was obtained by the area of a peak with the r value of peak value is 2.27 Å. Integration is often used when the peak of interest is not well resolved. With increasing PbO content, both average n_{TeO} and n_{PbO} decrease within the selected cut-off distances. At 40 and 50 mol% PbO, Pb^{2+} has an average coordination number typical of a glass network former whereas it resembles a modifier in 16.67mol% lead tellurite crystal.

Fig. 4.7 shows the total correlation functions for the lead tellurite crystals of $\text{PbTe}_5\text{O}_{11}$ [17], $\text{Pb}_2\text{Te}_3\text{O}_8$ [18], and PbTeO_3 [19]. The Te environment shows the same trend (evolution of the longer long bond) as a function of modifier content as previously discussed

in the lithium tellurite crystals. The Pb environment is more variable but, in general, the average r_{PbO} (and consequently n_{PbO}) decreases with increasing PbO content. The O-O distance however is seen to be roughly similar in all the three phases. From a glass structural point of view, the lower average n_{PbO} value at higher compositions means that if the melt of that particular composition could be quenched into a glass, Pb would behave as a glass former rather than a modifier. O-O pairs in these crystals also show a wide distribution as seen in the figure.

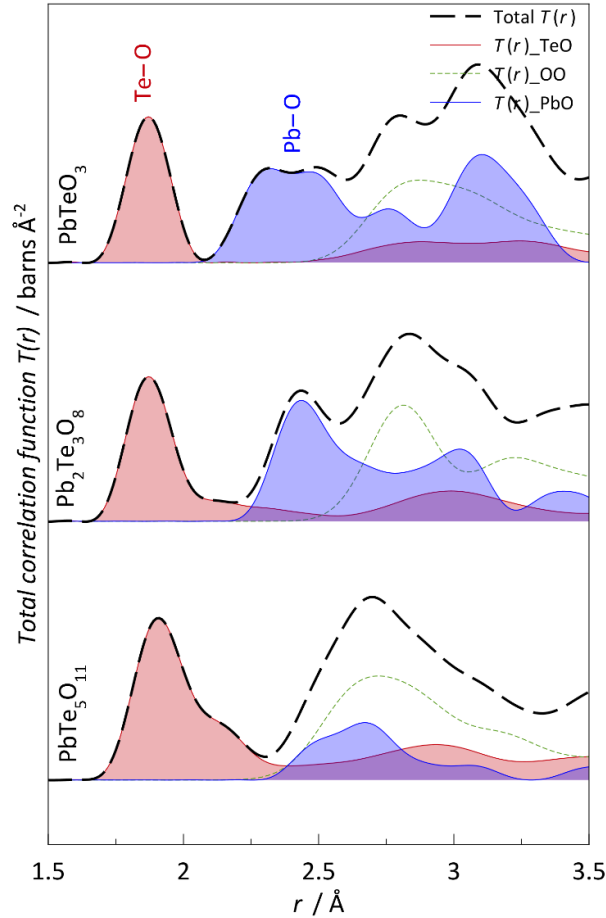


Figure 4.7: Simulated $T(r)$ for the lead tellurite crystals, selected for comparison with the glass structure. Te-O pair (red area), Pb-O pair (blue area), and O-O pair (green dotted).

4.4.2 Tellurium (IV) environment

As shown in Fig. 4.8, the Te environment in the 16.67 mol% PbO tellurite crystal, $\text{PbTe}_5\text{O}_{11}$, is very similar to $\gamma\text{-TeO}_2$. Based on the similarity of the Te environment in $\text{PbTe}_5\text{O}_{11}$ and $\gamma\text{-TeO}_2$, $\text{PbTe}_5\text{O}_{11}$ could be a suitable crystal structure for comparison with the lead tellurite glasses. However $\text{PbTe}_5\text{O}_{11}$ was not mentioned in slowly cooled PbO- TeO_2 glasses which yield $\gamma\text{-TeO}_2$, $\text{Pb}_2\text{Te}_3\text{O}_8$, and PbTeO_3 [20]. Fig. 4.9 shows the tellurium environment in the lead tellurite crystals. In general, as previously mentioned, n_{TeO} decreases as a function of PbO content. In

PbTe₅O₁₁, the average n_{TeO} value is 3.70 (as represented by the orange coloured area). Having this average n_{TeO} value of less than 4 indicates that in this crystal phase, there are [TeO₄] and [TeO₃] units. In Pb₂Te₃O₈, the first Te–O coordination shell gives an average n_{TeO} value of 2.93, or 3.50 if the second coordination shell is included, while in PbTeO₃, the average n_{TeO} value is 3.00 with an average distance reflecting the resonance Te–O distance in a [TeO₃]²⁻ unit.

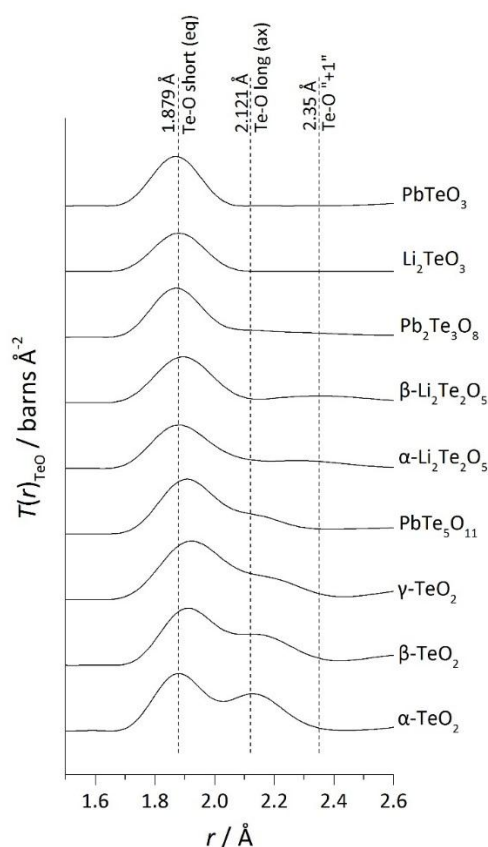


Figure 4.8: Te environments in tellurite, lithium tellurite, and lead tellurite crystals. r_{TeO} is compared to the short and long bonds of 1.879 and 2.121 Å found in α -TeO₂ (vertical lines). The evolution of the longer long bond of Te-O is a function of composition, regardless of the modifier cation type.

Table 4.8 shows the running bond valence sum for Te-O bonds in each site of all the crystal phases related to this study. From the table, the Te-O bond valence sum for Te(IV) in [TeO₄] and [TeO₃] units range from 3.95 to 4.27 v.u. The average Te-O bond valence in PbTe₅O₁₁, Pb₂Te₃O₈, and PbTeO₃ is 4.08, 4.21, and 4.20 v.u, respectively. Closer examination of each tellurium site is important in order to understand all the possible Te-O polyhedral environments in lead tellurite glasses. Collectively, there are 11 Te sites in these crystals, however, only the sites from PbTe₅O₁₁ are considered due to its formation in devitrified glass, and its composition being similar to the glasses in this study. The partial simulation of each Te site in PbTe₅O₁₁ is as shown in Fig. 4.10. As seen in the figure, the Te1, Te4, and Te5 sites are the [TeO₄] type (TeO_{2short} + 2long), similar to the unit in α -TeO₂, whereas the Te2 and

Te3 sites are the $[\text{TeO}_{3+1}]$ type, similar (but slightly longer distance of the long “+1” bond) to the units in the $\beta\text{-Li}_2\text{Te}_2\text{O}_5$ phase.

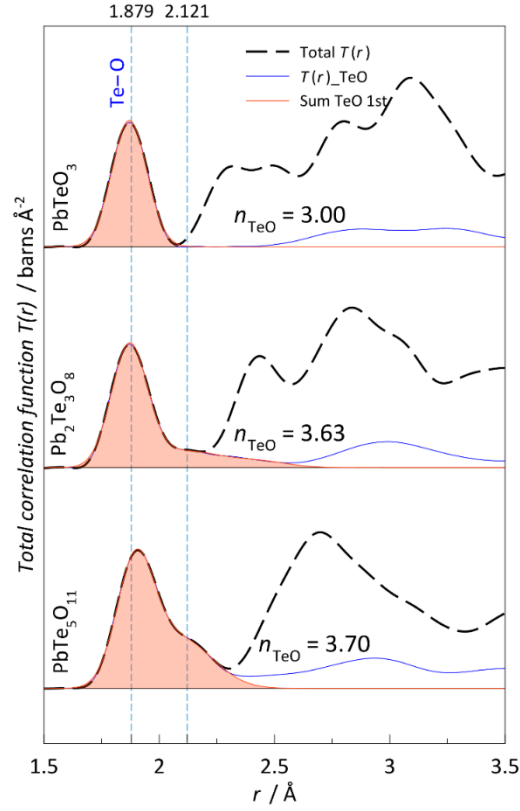


Figure 4.9: Simulated $T(r)$ for Te–O pairs in the selected lead tellurite crystals. Orange area marks the sum of Te–O peaks due to Te–O pairs within the first coordination shell.

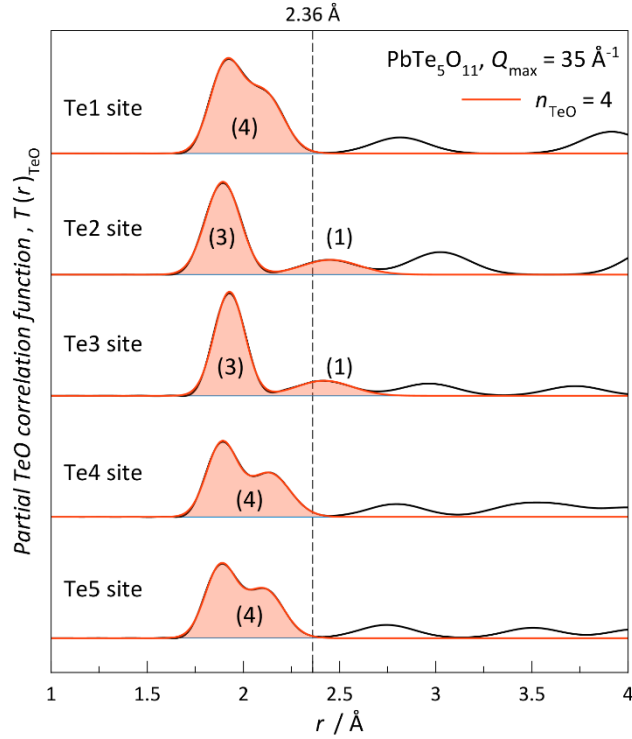


Figure 4.10: Partial $T(r)$ for each Te site in $\text{PbTe}_5\text{O}_{11}$.

Table 4.8: Bond valence calculation of the Te–O bonds in lead tellurite crystals.

Crystal	Te site	$r / \text{\AA}$	BV / v.u.	Running BV sum
PbTe₅O₁₁	Te1	1.875	1.3902	1.3902
		1.937	1.1764	2.5666
		2.100	0.7580	3.3246
		2.117	0.7224	4.0470
	Te2	1.835	1.5502	1.5502
		1.890	1.3357	2.8859
		1.956	1.1127	3.9986
		2.445	0.2976	4.2962
	Te3	1.908	1.2709	1.2709
		1.913	1.2566	2.5275
		1.964	1.0942	3.6217
		2.411	0.3265	3.9482
	Te4	1.865	1.4291	1.4291
		1.904	1.2847	2.7138
		2.080	0.7988	3.5126
		2.177	0.6149	4.1276
	Te5	1.854	1.4722	1.4722
		1.901	1.2973	2.7695
		2.105	0.7460	3.5155
		2.107	0.7428	4.2583
PbTe₃O₈	Te1	1.852	1.4806	1.4806
		1.852	1.4806	2.9612
		2.160	0.6437	3.6048
		2.160	0.6437	4.2485
	Te2	1.859	1.4532	1.4532
		1.859	1.4532	2.9064
		1.883	1.3616	4.2680
		1.856	1.4643	1.4643
	Te3	1.868	1.4156	2.8799
		2.008	0.9712	3.8511
		2.338	0.3983	4.2494
		2.984	0.0694	4.3188
	Te4	1.857	1.4615	1.4615
		1.900	1.3001	2.7616
		1.900	1.3001	4.0617
		2.798	0.1147	4.1763
PbTeO₃	Te1	1.870	1.4114	1.4114
		1.875	1.3891	2.8005
		1.887	1.3480	4.1485
		2.745	0.1324	4.2810
		2.934	0.0794	4.3604
	Te2	1.859	1.4536	1.4536
		1.879	1.3768	2.8304
		1.883	1.3620	4.1923
		2.762	0.1264	4.3187
	Te3	1.848	1.4951	1.4951
		1.860	1.4489	2.9440
		1.899	1.3050	4.2490
		2.912	0.0843	4.3333

4.4.3 Non-bridging oxygen environments

Table 4.9: Bond parameters of Te–O and Pb–O pairs in lead tellurite crystals.

	Crystal		$r(\text{Te-O1b}) / \text{\AA}$	$r(\text{O1b-Pb}) / \text{\AA}$				
				Te	Pb1	Pb2	Pb3	Pb4
[TeO ₄]	Te–O–(Pb)	Pb ₂ Te ₃ O ₈	1.852 (Te1)	–	2.374	–	–	–
			1.852 (Te1)	–	2.374	–	–	–
	$\Sigma\text{BV}_\text{O}=1.89$		$\text{BV}_{\text{O-Te}}=1.40$		0.54			
	#Te–O–(Pb,Te)	PbTe ₅ O ₁₁	1.875 (Te1)	2.411	2.739	–	–	–
			1.908 (Te3)	2.080	2.710	–	–	–
			2.411 (Te3)	1.875	2.739	–	–	–
			2.177 (Te4)	1.901	3.078	–	–	–
			2.080 (Te4)	1.908	2.710	–	–	–
			1.901 (Te5)	2.177	3.078	–	–	–
	$\Sigma\text{BV}_\text{O}=1.90$		1.25	0.52	0.14			
	Te–O–(Pb,Pb)	PbTe ₅ O ₁₁	1.854 (Te5)	–	2.509	2.634	–	–
	1.97		1.39		0.34	0.24		
	#Te–O–(Pb,Pb,Te)	Pb ₂ Te ₃ O ₈	2.338 (Te3)	1.900	2.732	2.859		
	$\Sigma\text{BV}_\text{O}=2.08$		0.38	1.23	0.19	0.28		
	Te–O–(Pb,Pb,Pb)	PbTe ₅ O ₁₁	1.865 (Te4)	–	2.472	2.648	2.884	
		Pb ₂ Te ₃ O ₈	1.856 (Te3)	–	2.470	2.556	2.934	
			1.868 (Te3)	–	2.372	2.636	3.032	
	$\Sigma\text{BV}_\text{O}=2.13$		1.36		0.41	0.26	0.10	
[TeO ₃]	Te–O–(Pb)	Pb ₂ Te ₃ O ₈	1.859 (Te2)	–	2.440	–	–	–
			1.859 (Te2)	–	2.440	–	–	–
		PbTeO ₃	1.869 (Te1)	–	2.750	–	–	–
			1.879 (Te2)	–	2.294	–	–	–
	$\Sigma\text{BV}_\text{O}=1.70$		1.34		0.36			
	Te–O–(Pb,Pb)	PbTeO ₃	1.887 (Te1)	–	2.335	2.528	–	–
			1.875 (Te1)	–	2.245	3.022	–	–
			1.859 (Te2)	–	2.758	3.057	–	–
			1.883 (Te2)	–	2.264	2.628	–	–
			1.848 (Te3)	–	2.471	2.813	–	–
			1.860 (Te3)	–	2.504	3.062	–	–
	$\Sigma\text{BV}_\text{O}=1.90$		1.34		0.42	0.14		
	#Te–O–(Pb,Pb,Te)	Pb ₂ Te ₃ O ₈	1.900 (Te4)	2.338	2.732	2.859	–	–
			1.900 (Te4)	2.338	2.732	2.859	–	–
	$\Sigma\text{BV}_\text{O}=1.93$		1.23	0.38	0.19	0.13		
	Te–O–(Pb,Pb,Pb)	PbTeO ₃	1.899 (Te3)	–	2.371	2.471	2.960	–
	$\Sigma\text{BV}_\text{O}=2.21$		1.23		0.50	0.38	0.10	
	Te–O–(Pb,Pb,Pb,Pb)	Pb ₂ Te ₃ O ₈	1.857 (Te4)	–	2.439	3.069	3.069	3.080
	$\Sigma\text{BV}_\text{O}=1.96$		1.46		0.41	0.08	0.08	0.07

Table 4.9 shows the bond distances and bond valence values of Te–O bonds obtained from the related crystal structures. These parameters are categorised into two: related to O1b connected to a [TeO₄] unit, and related to O1c connected to a [TeO₃] unit. From the table, the bond valence for Te–O1b has values of 1.40, 1.39, and 1.36 v.u. whilst Te–O1c has values

of 1.34, 1.34, 1.23, and 1.32 v.u. (not including those marked with superscript #, because the O is a bridging oxygen; connected to another Te). For convenience, these values are rounded to 1 decimal place and averaged out as shown in Table 4.10. As previously discussed for the Te-O1b and Te-O1c in the lithium tellurites, these numbers could be used to partially characterise the short range order in the lead tellurite glasses (Chapter 6)

Table 4.10: Bond parameters of Te–O1b, Te–O1c, and Te–O2 in lead tellurite crystals.

		<i>rTeO (bv)</i>
[TeO ₄]	Te–O–(Pb)	1.85 (1.4)
	Te–O–(Pb,Te)	1.89 (1.3)
	Te–O–(Pb,Pb)	1.85 (1.4)
	Te–O–(Pb,Pb,Te)	1.90 (1.2)
	Te–O–(Pb,Pb,Pb)	1.86 (1.4)
	Average Te–O(O1b)	1.4
	Te–O(O2)	1.3
[TeO ₃]	Te–O–(Pb)	1.87 (1.3)
	Te–O–(Pb,Pb)	1.87 (1.3)
	Te–O–(Pb,Pb,Te)	1.90 (1.2)
	Te–O–(Pb,Pb,Pb)	1.90 (1.2)
	Te–O–(Pb,Pb,Pb,Pb)	1.88 (1.5)
	Average Te–O(O1c)	1.3
	Te–O(O2)	1.2
Te–O–(<i>n</i> Te) <i>n</i> ≥ 1		–

4.4.4 Lead (II) environment

Fig. 4.11 shows the simulated partial $T(r)_{\text{PbO}}$ for PbTe₅O₁₁, Pb₂Te₃O₈, and PbTeO₃ crystal phases. The total $T(r)$ are shown as the dashed line, the partial $T(r)$ for PbO pairs are shown in blue line and the area shaded in orange represents the contribution of PbO pair for the total average PbO coordination number of about 8. The actual number calculated is shown in the figure. The blue dashed lines represent the distance for the average Pb–O coordination number (labelled in the top parentheses) calculated based on the bond-valence parameters by Brese and O’Keefe [15]. The line labelled *r*-cutoff (8) represents the cutoff radius where the integral of the $T(r)_{\text{PbO}}$ gives the average n_{PbO} value of 8. As seen in the figure, the PbO distance decreases as a function of PbO content. In PbTe₅O₁₁, the partial $T(r)_{\text{PbO}}$ has a principal peak centred at a value corresponding to the average n_{PbO} value of 8. In Pb₂Te₃O₈, the partial $T(r)$ could be parameterised with a minimum of 2 peaks where the first peak is centred at a distance corresponding to the average n_{PbO} value of 5. In PbTeO₃, the presence of even shorter PbO distances (corresponding to the average n_{PbO} = 3) is obvious. A general trend is seen that in the crystalline form, as more PbO is added to the TeO₂, the shortest PbO distance decreases to corresponding to n_{PbO} value of 8 to 5 and 3. In glasses, this trend

would describe the behaviour of Pb^{2+} as being a modifier, intermediate, and a glass former respectively.

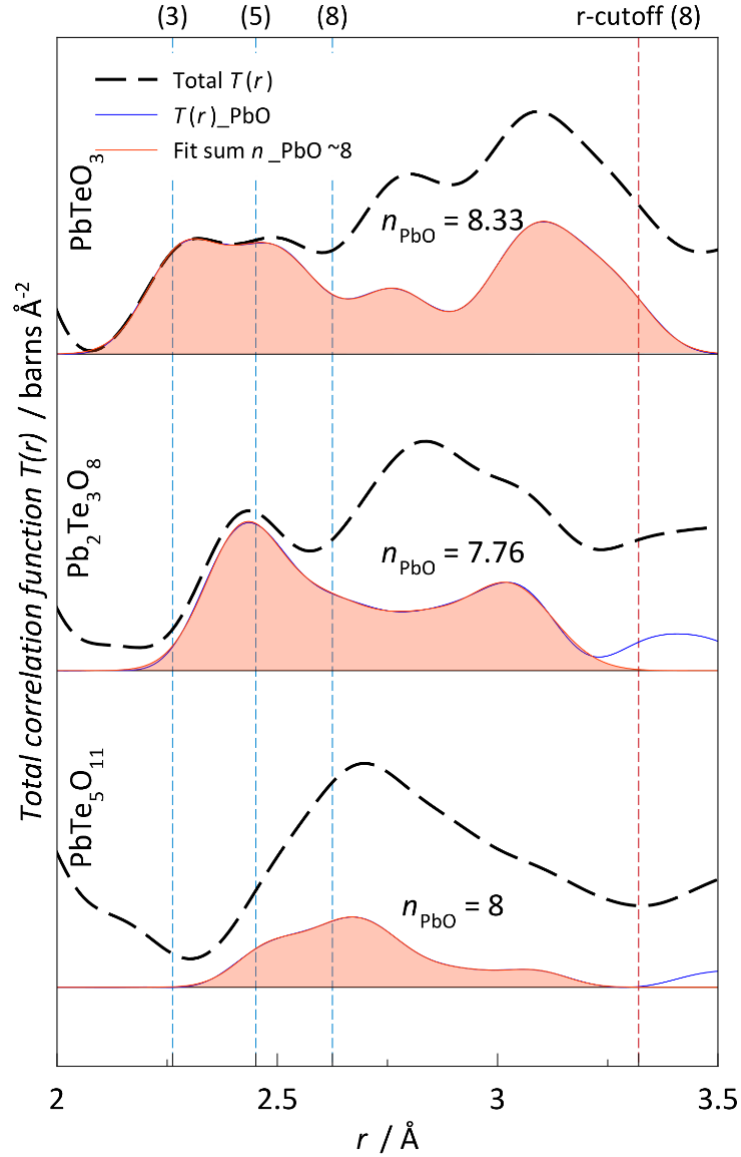


Figure 4.11: Simulated $T(r)$ Pb-O for the lead tellurite crystals. Orange area is the sum of the average n_{PbO} of about 8.

Table 4.11 shows the Pb-O bond distances and bond valence sums of the crystal phases. For $\text{PbTe}_5\text{O}_{11}$, there is only 1 Pb site present and the $[\text{PbO}_8]$ polyhedron is made up of 4 short and 4 long Pb-O bond distances. In this crystal, the bond valence sum for Pb is less than 2. The selection of short and long Pb-O bond limit is subjective since Pb-O distance distribution is highly asymmetrical. For convenience, all PbO polyhedra in the crystals are mostly all 8-coordinated within about 3.3 Å.

From the calculated bond valence values, in total listed in Table 4.11 (marked bold), the values are not all 2. This is because the bond valence approximation for Pb^{2+} is less

accurate, due to its lone pair of electrons which causes the PbO distances to be highly distorted.

Table 4.11: Bond parameter for Pb-O pair in lead tellurite crystals.

Crystal	Pb site	$r / \text{\AA}$	BV / v.u.	Running sum BV
PbTe ₅ O ₁₁	Pb1	2.471	0.3787	0.3787
		2.509	0.3420	0.7207
		2.634	0.2439	0.9646
		2.647	0.2354	1.2000
		2.710	0.1988	1.3988
		2.739	0.1839	1.5827
		2.883	0.1244	1.7071
		3.078	0.0735	1.7806
PbTe ₃ O ₈	Pb1	2.3716	0.4958	0.4958
		2.4395	0.4127	0.9084
		2.4698	0.3802	1.2887
		2.6359	0.2427	1.5313
		2.8588	0.1329	1.6642
		2.9342	0.1084	1.7726
		3.032	0.0832	1.8558
		3.0688	0.0753	1.9311
	Pb2	2.3736	0.4931	0.4931
		2.4386	0.4137	0.9068
		2.5555	0.3016	1.2084
		2.5555	0.3016	1.5100
		2.7323	0.1870	1.6970
		2.7323	0.1870	1.8840
		3.0795	0.0732	1.9572
		3.3414	0.0361	1.9933
PbTeO ₃	Pb1	2.372	0.4959	0.4959
		2.471	0.3790	0.8749
		2.504	0.3471	1.2220
		2.628	0.2483	1.4703
		2.813	0.1503	1.6205
		2.960	0.1011	1.7217
		3.057	0.0778	1.7995
		3.108	0.0677	1.8672
		3.151	0.0603	1.9275
		3.855	0.0090	1.9365
	Pb2	2.294	0.6111	0.6111
		2.335	0.5475	1.1586
		2.528	0.3246	1.4832
		2.758	0.1745	1.6577
		3.062	0.0768	1.7345
		3.108	0.0678	1.8023
		3.125	0.0648	1.8671
		3.238	0.0476	1.9147
	Pb3	2.245	0.6988	0.6988
		2.264	0.6640	1.3628
		2.471	0.3792	1.7420
		2.750	0.1783	1.9203
		3.022	0.0855	2.0058
		3.231	0.0486	2.0544

Fig. 4.12 shows the simulated partial $T(r)_{\text{PbO}}$ for Pb sites in $\text{PbTe}_5\text{O}_{11}$ and $\text{Pb}_2\text{Te}_3\text{O}_8$. For simulation of alkali tellurite crystals, the thermal parameters for Te-O and M-O pairs (M = Li, Na, and K) were obtained from *Barney et al.* [21]. For lead tellurite crystals, the thermal parameter for Te-O is available in the literature [21], but not for Pb-O pairs. Therefore, the value of RMS bond length variation $\langle u \rangle$ (0.2) as calculated by XTAL from the crystallographic (cif file) was used. As shown by the black line, due to the large value used, the partial $T(r)_{\text{PbO}}$ is highly broadened to the point where the Pb-O peak for $\text{PbTe}_5\text{O}_{11}$ can be fitted with just one Gaussian. Peaks for $\text{Pb}_2\text{Te}_3\text{O}_8$ however are still resolvable into multiple Gaussians. The shape of the $T(r)$ Pb-O from simulation however can be simulated with a much lower value (0.05), so that the shape of simulated $T(r)$ is similar to that observed by experiment (Chapter 6, Section 6.5, using the difference technique with the null lithium tellurite neutron data).

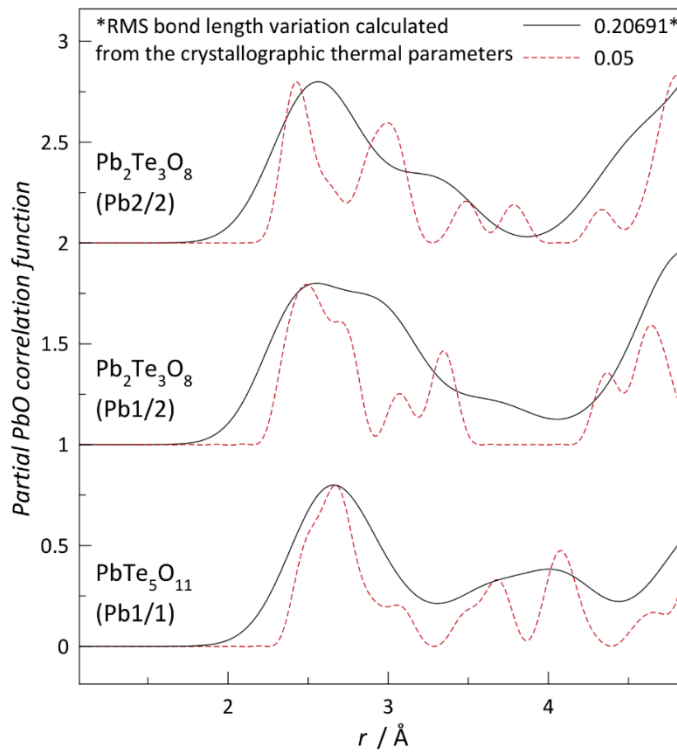


Figure 4.12: Partial $T(r)$ PbO simulated using thermal parameters from the crystal structure and a value similar to the experimental results.

4.5 Glass structures and models

4.5.1 Pure TeO_2 glass

Traditionally, the pure TeO_2 glass network is thought to resemble the α - TeO_2 crystal, i.e. consisting only of corner-sharing $[\text{TeO}_4]$ polyhedral units connected by $-\text{Te}_{\text{ax}}\text{O}_{\text{eq}}-\text{Te}-$ bridges (average $n_{\text{TeO}} = 4$) (ax = axial, eq = equatorial) as in Fig. 4.1 [22]. This is analogous to the relationship between SiO_2 and GeO_2 crystals and their pure glasses. n_{TeO} values of

tellurite glasses with low modifier contents were measured, using neutron diffraction, to be close to 4 in K_2O-TeO_2 [23]. These values were thought to decrease linearly from $n_{TeO} = 4$ in pure TeO_2 as modifier is added where the $[TeO_4]$ units change to $[TeO_3]$ via the intermediate unit $[TeO_{3+1}]$, as previously discussed. However, the value of n_{TeO} in pure TeO_2 glass was recently experimentally measured by Barney *et al.* [24] who found a value of 3.68 instead of 4.00. This suggests that there are $[TeO_3]$ units already present in TeO_2 glass. Based on a Raman study, Tatsumisago *et al.* [25] suggested that, in the melt, $[TeO_3]$ and $[TeO_4]$ units could be in equilibrium according to the model shown in Fig. 4.13.

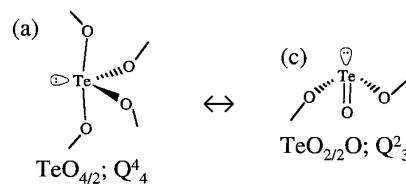


Figure 4.13: $[TeO_{4/2}] \leftrightarrow [TeO_{2/2}O]$ equilibria. Units taken from McLaughlin *et al.* [26].

Therefore, when molten TeO_2 is quenched fast enough (roller-quenching), some of the $[TeO_3]$ units may be retained in the glass amongst the $[TeO_4]$ units found in stable TeO_2 crystals. The structure of pure TeO_2 glass can be compared to the δ - TeO_2 crystal phase which has both $[TeO_4]$ and $[TeO_3]$ units with non-bridging oxygen atoms [10]. The terminal oxygen atoms (non-bridging, and non-charged, later described as O1a type of oxygen) associated with the $[TeO_3]$ units present in pure TeO_2 glass can provide additional coordination sites for modifier cations added to the glass, at least at lower concentrations. This will increase the critical modifier oxide content where further $[TeO_3]$ units with non-bridging oxygen atoms need to be created.

4.5.2 Tellurite glasses

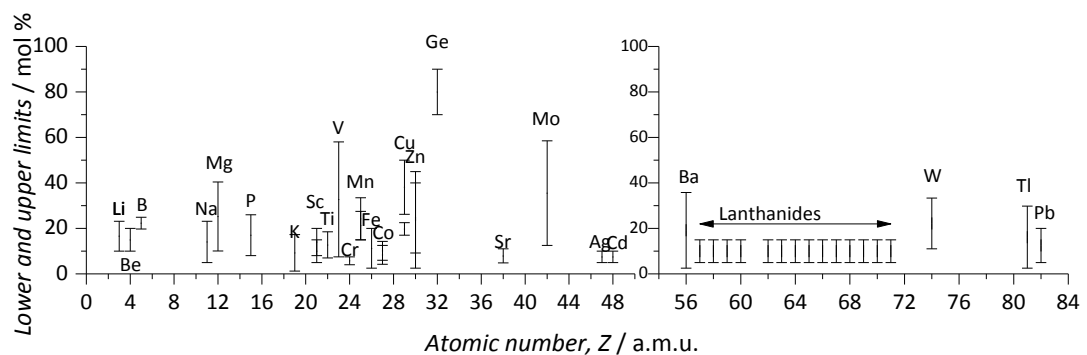


Figure 4.14: Upper and lower limits of second oxide M_aO_b in binary $xM_aO_b-(100-x)TeO_2$ glasses [27].

Fig. 4.14 shows the lower and upper content limits of the second oxides which have been studied in binary TeO_2 glasses. Group I elements have a range of 5 to 20 mol% but this increases for some transition elements.

4.5.3 Te-O bond breaking processes

In the presence of a modifying oxide M_aO_b , the $\text{Te}_{\text{eq}}\text{O}_{\text{ax}}\text{-Te}$ bridge is broken in order to create non-bridging oxygen atoms to accommodate the M^+ cations. This process is similar to the creation of non-bridging oxygen atoms in SiO_2 -based glasses. The process is illustrated for the case of lithium tellurite glasses in Fig. 4.15 where one $[\text{TeO}_4]^-$ unit is produced for each Li^+ unit present in the glasses.

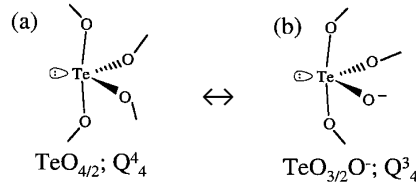


Figure 4.15: $[\text{TeO}_{4/2}] \leftrightarrow [\text{TeO}_{3/2}\text{O}^-]$ equilibrium for $2\text{Li}^+ + \text{O}^{2-} + 2[\text{TeO}_4] \leftrightarrow 2([\text{TeO}_4]^- \text{Li}^+)$. McLaughlin et al. [26].

As shown in Fig. 4.15, the bridge breaking process introduces non-bridging oxygen atoms without changing the tellurium coordination number. In a situation where the modifier cation coordination cannot be satisfied by the number of non-bridging oxygen atoms present, a further means of creating non-bridging atoms is achieved by the mechanism involving charged units which involves the transformation of the $[\text{TeO}_4]^-$ to $[\text{TeO}_3]^-$ as shown in Fig. 4.16. As this process transforms $[\text{TeO}_4]$ to $[\text{TeO}_3]$ units, the average n_{TeO} of the system will decrease.

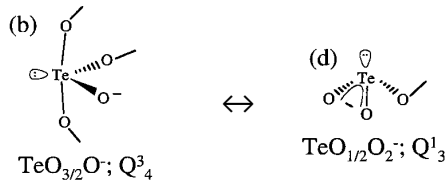


Figure 4.16: $[\text{TeO}_{3/2}\text{O}^-] \leftrightarrow [\text{TeO}_{1/2}\text{O}_2^-]$ equilibrium. Units taken from McLaughlin et al. [26].

During these transformation processes, $[\text{TeO}_4]$ changes to $[\text{TeO}_3]$ via $[\text{TeO}_{3+1}]$, units as in Fig. 4.17, which may be similar to those found in TeO_2 , $\text{Li}_2\text{Te}_2\text{O}_5$, and Li_2TeO_3 .

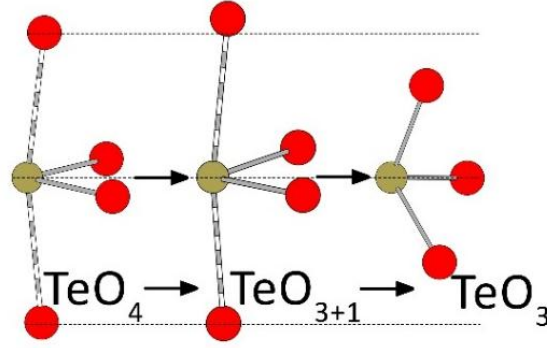


Figure 4.17: Transformation of $[TeO_4]$ unit to $[TeO_3]$ unit via intermediate $[TeO_{3+1}]$ unit. $[TeO_4]$ unit is represented by the TeO_2 polyhedron in α - TeO_2 crystal. This intermediate unit is drawn with the longest bond as found in α - $Li_2Te_2O_2$ (longest $r > 2.2 \text{ \AA}$). The resonance structure is not shown in the $[TeO_3]$ unit. This unit is represented by a TeO_3 polyhedron found in Li_2TeO_3 .

4.6 TeO_2 structural models [28]

4.6.1 Pure TeO_2 glass

The model derivation is taken from the work of Dr Emma Barney, Dr Diane Holland, and Dr Alex Hannon [28]. In TeO_2 there are 2 O atoms *for every* Te atom.

$$n_{TeO} \cdot c_{Te} = n_{OTe} \cdot c_O \quad (4.1)$$

where n_{ij} is the average coordination number of atom i to atom j, and c_i is the atomic fraction of atom i. n_{OTe} can be calculated for known n_{TeO} (experimental), using c_{Te} ($=1/3$), and c_O ($=2/3$). Assuming that the only species present are 3-coordinated Te (Te_3), 4-coordinated Te (Te_4), oxygen bonded to 1 Te (O_1) and oxygen bonded to 2 Te (O_2), n_{OTe} can be represented by:

$$n_{OTe} = \frac{(2 * N_{O2}) + (1 * N_{O1})}{N_O} \quad (a)$$

$$n_{OTe} = 1 + \frac{N_{O2}}{N_O} \quad (b) \quad (4.2)$$

$$n_{OTe} = 2 - \frac{N_{O1}}{N_O} \quad (c)$$

Rearranging Eqn. 4.2 (a), the fractions of O_2 and O_1 units can be calculated for known n_{TeO} . In pure TeO_2 glass ($c_{Te} = 1/3$ and $c_O = 2/3$), the experimental n_{TeO} of 3.68 leads to an average n_{OTe} value of 1.84 (from Eqn 4.1), which gives the O_1 and O_2 fractions units as 0.16 and 0.84, respectively. Using similar relationships, the fractions of Te_3 and Te_4 can be calculated as

$$n_{TeO} = \frac{(3 * N_{Te3}) + (4 * N_{Te4})}{N_{Te}} \quad (a)$$

$$n_{TeO} = 4 - \frac{N_{Te3}}{N_{Te}} \quad (b) \quad (4.3)$$

$$n_{TeO} = 3 + \frac{N_{Te4}}{N_{Te}} \quad (c)$$

The fractions of various units are shown in Fig. 4.18 as a function of the average n_{TeO} . It is seen that in a system of $n_{\text{TeO}} = 3.68$, there are 33% of Te3 units, 67% of Te4 units, 13 % of O1 unit and 83% of O2 units. In fractions, these units can be represented as:

$$\text{Pure TeO}_2 \text{ glass} = \frac{1}{3} \text{Te}_3 + \frac{2}{3} \text{Te}_4 + \frac{1}{3} \text{O}_1 + \frac{5}{3} \text{O}_2 \quad (4.4)$$

The n_{TeO} obtained by simulation studies [29-30] including $[\text{TeO}_3]$, $[\text{TeO}_4]$, and $[\text{TeO}_5]$ units give similar values to experiment [24] if $[\text{TeO}_5]$ is excluded (unobserved in known Te-O and Li-Te-O crystals). The fractions of all the units in Eqn 4.4 are unique to the n_{TeO} value of 3.68 and affect the threshold modifier content (Fig. 4.18). The number of non-bridging oxygen (NBO) and the average boron-oxygen coordination number n_{BO} in borate systems [31] are affected by the cooling rate (hence T_g and T_f). Therefore the value n_{TeO} could depend on the melting and quenching processes. The model of Barney *et al.* is derived for a roller quenched glass sample.

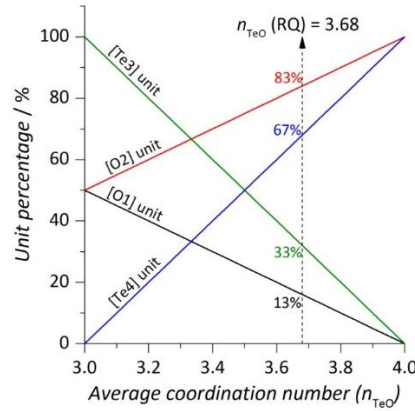


Figure 4.18: The fractions of $[\text{TeO}_3]$, $[\text{TeO}_4]$, NBO(O2), and BO(O1) units as a function of n_{TeO} as derived in Eqn 4.4 The dotted shows the fractions of the units found in the roller-quenched pure TeO_2 glass corresponding to the n_{TeO} value of 3.68 [24].

4.6.2 Alkali tellurite glasses

When N' units of K_2O are added to N units of TeO_2 ($N'/(N'+N) = x$ mol% of K_2O), the bridge breaking process will decrease the number of O2 units by N' and increase the number of O1 type by $2N'$ and give the number of units present according to the equation:

$$\begin{aligned} & N \text{ unit of } \text{TeO}_2 + N' \text{ unit of } \text{K}_2\text{O} \\ &= \left[\frac{N}{3} \right] \text{Te}_3 + \left[\frac{2N}{3} \right] \text{Te}_4 + \left[\frac{N}{3} + 2N' \right] \text{O}_1 + \left[\frac{5N}{3} - N' \right] \text{O}_2 + [2N'] \text{K} \end{aligned} \quad (4.5)$$

K^+ has a preferred coordination number of 6 and therefore a K–O bond will have a bond valence of 1/6: a K^+ ion needs a total of 6 K–O bonds to fully complete its bond valence requirement. From related known crystal structures, O1–Te has a bond valence of 1.5 v.u., [24] leaving the remaining 0.5 v.u. on O1 available to provide 3 K–O bonds ($0.5 / (1/6)$). From these conditions, all bonds are used up when when (\leftrightarrow indicates “are balanced by”)

$$6(\text{number of K units}) \leftrightarrow 3(\text{number of O1 units}) \quad (4.6)$$

and by substituting the values of K and O1 units from Eqn 4.5 into Eqn 4.6, the maximum N' unit of K_2O that can be incorporated before any $[TeO_4]$ units need be transformed to $[TeO_3]$ units is obtained as in Eqn 3.4. This corresponds to 14.28 mol% of K_2O indicating that from 0 to 14.28 mol% of K_2O , n_{TeO} remains constant at 3.68.

$$N'/N = 1/6 \equiv 14.28 \text{ mol\%} \quad (4.7)$$

In the case of Li_2O-TeO_2 glasses, the coordination number of Li^+ (n_{LiO}) is expected to be 4 (though see Section 5.4.5), giving the condition for exhaustion of pre-existing $[TeO_3]$ as $4(\text{number of Li units}) \leftrightarrow 2(\text{number of O1 units})$ which leads to the same composition as in Eqn. 3.4. This composition is specific to the ratio of units obtained from the average n_{TeO} value of 3.68, it should be noted that different average n_{TeO} value leads to different fractions of O1 and consequently a different composition at N'/N . The model is true based on the assumptions that there are only Te_4 , Te_3 , O2, and O1 units present and that K, and any M in general, is bonded to only O1. This threshold composition is called the deviation composition (x_D) for simplicity. The average n_{TeO} is therefore constant (3.68) up to this x_D (14.28 mol%) for the case of K_2O-TeO_2 . At x_D ($N'/N = 1/6$), the total units in the glass are:

$$\begin{aligned} & NTeO_2 + \left(\frac{N}{6}\right)K_2O \\ &= \left[\frac{N}{3}\right]Te_3 + \left[\frac{2N}{3}\right]Te_4 + \left[\frac{N}{3} + 2\left(\frac{N}{6}\right)\right]O_1 + \left[\frac{5N}{3} - \left(\frac{N}{6}\right)\right]O_2 + \left[2\left(\frac{N}{6}\right)\right]K \end{aligned} \quad (4.8)$$

Adding 1 unit of K_2O will produce another 2 units of O1 from the bridge-breaking process. However 2 K^+ ions need a total of 12 K–O1 bonds to satisfy their bond valences, therefore, the simple bridge-breaking process produces insufficient O1 sites to satisfy the bond valence of the modifier cations. Therefore, $[TeO_4]$ units need to be transformed to $[TeO_3]$ unit by the process of bond-breaking to create more NBO atoms. In general, by adding M further K_2O units, Mb Te–O bonds are broken in addition to the normal bridge breaking process (b is the number of bonds being broken during transformation of $[TeO_4]$ to $[TeO_3]$ units, which can be determined experimentally). Hence the total number of Te_4 units will decrease by Mb and the total number of Te_3 units will increase by Mb and Eqn. 4.8 becomes

$$\begin{aligned} & NTeO_2 + \left[\left(\frac{N}{6}\right) + M\right]K_2O \\ &= \left[\frac{N}{3} + Mb\right]Te_3 + \left[\frac{2N}{3} - Mb\right]Te_4 \\ &+ \left[\frac{N}{3} + 2\left(\frac{N}{6}\right) + Mb\right]O_1 + \left[\frac{5N}{3} - \left(\frac{N}{6}\right) - Mb\right]O_2 \\ &+ \left[2\left(\frac{N}{6}\right) + 2M\right]K \end{aligned} \quad (4.9)$$

and from Eqn. 4.9, n_{TeO} of the system becomes

$$n_{\text{TeO}} = \frac{11}{3} - \frac{Mb}{N} \quad (4.10)$$

and the total K_2O content M' would be

$$M' = \frac{\frac{N}{6} + M}{\frac{7}{6} + M} 100 \text{ mol\%} \quad (4.11)$$

Rearranging Eqn. 4.11, the further unit added M can be expressed as

$$M = \frac{N(7M' - 100)}{6(100 - M')} \quad (4.12)$$

and putting Eqn. 4.12 into 4.10, n_{TeO} of the system as a function of K_2O content beyond the maxima would be

$$n_{\text{TeO}} = \frac{11}{3} - \frac{b(7M' - 100)}{6(100 - M')} \quad (4.13)$$

From the definition in Eqn. 4.9, for every unit of K_2O added, N_{O_1} increases by $2 + b$ where 2 and b come from the bridge-breaking and bond-breaking processes respectively. A b value of 1 generates values of n_{TeO} which are close to the experimental values of n_{TeO} (Fig. 4.19).

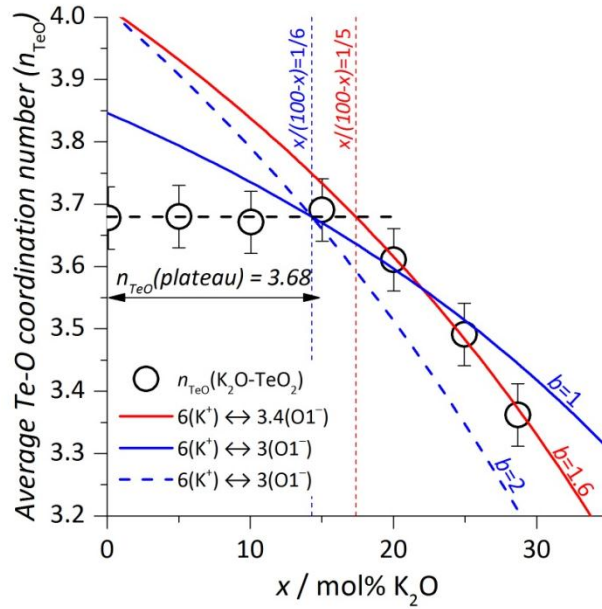


Figure 4.19: The average n_{TeO} model for TeO_2 glass based on $\text{K}_2\text{O}-\text{TeO}_2$ glasses. For $x < 14.3$ mol%, n_{TeO} is constant at 3.68. This is based on the n_{TeO} value of 3.68 which was experimentally obtained for pure TeO_2 glass. 14.3 mol% is the deviation point determined by the fractions of $[\text{TeO}_3]$ and $[\text{TeO}_4]$ units from n_{TeO} . For $x > 14.3$ mol%, n_{TeO} is fitted with the b value of 1 [28], revealing 25% of the bond valence contribution from O2 (bridging oxygen) sites.

This would mean the number of N_{O_1} increases by $(2+b) = 3$ hence providing $3(2+b) = 9$ $\text{K}-\text{O}_1$ bonds. This is insufficient since 2 K^+ needs 12 $\text{K}-\text{O}_1$ bonds. This suggests that the remaining bonds must be contributed by O2 sites. The average n_{TeO} model beyond x_D can also be

formulated by fitting the data points and the value of b (1.6) obtained would be closer to ideal (2). This however would indicate that the bond valence for Te–O1 is different than calculated.

Model for K

$$n_{\text{TeO}(K)} = \begin{cases} 3.68 & ; x < 14.3 \text{ mol\%} \\ 3.68 - \frac{(x - 14.3)b}{100 - x} & ; x > 14.3 \text{ mol\%}; b = 1 \end{cases} \quad (4.14)$$

Where M is the further K_2O unit added above 14.3 mol% and N is the total unit of TeO_2 .

4.6.3 Non-alkali tellurites

In aluminium tellurite and tellurium borate glasses, the average n_{TeO} decreases linearly without the presence of the plateau and post plateau regions observed in the alkali tellurite glasses. In these particular systems, Al^{3+} and B^{3+} exist as glass formers with shorter cation-oxygen distance. The shorter cation-oxygen bonds will have larger bond valence requirement, limiting the number of bonds which can be provided by O1-Te. In pure TeO_2 glass, there are various O sites.

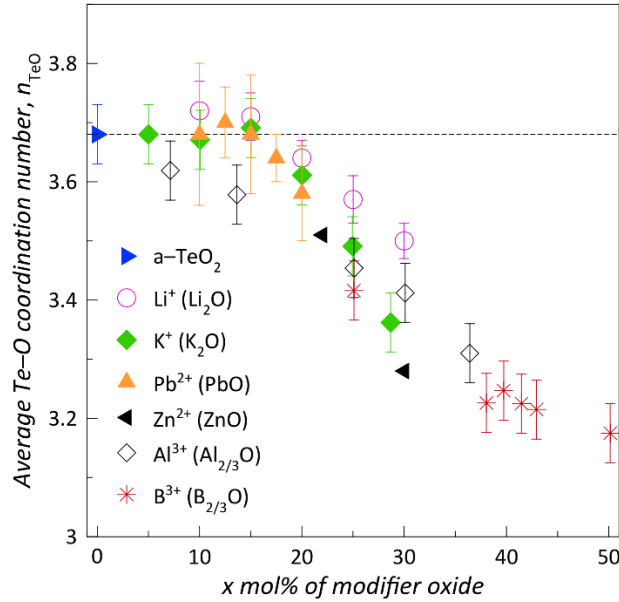


Figure 4.20: n_{TeO} values for the alkali (Li_2O and K_2O), divalent (PbO and ZnO) and trivalent (B_2O_3 and Al_2O_3) tellurites.

The coordination change of Te is driven by the availability of the O sites for bonding with the second oxide cation. In alkali tellurites where the second oxide cation behaves as a modifier (similar longer cation-oxygen distance), there is no preferential oxygen site for bonding, hence the oxygen cages could be filled with a more flexible (bonding-wise) modifier

cations. In the case where the second oxide is a glass former, the flexibility of the TeO_2 network is constrained by the glass former oxide network in contrast to the situation observed in alkali TeO_2 glasses where the network is highly dominated by TeO_2 . It is therefore possible that a glass former/intermediate, n_{TeO} will not produce the plateau region in the average n_{TeO} value (see Fig 3.24 for the behaviour of Al^{3+} (Barney *et al.*, to be published) and B^{3+} [32]).

4.7 References

1. Busca, G., *Heterogeneous Catalytic Materials: Solid State Chemistry, Surface Chemistry and Catalytic Behaviour*; Elsevier, 2014.
2. Worlton, T., Beyerlein, R. *Physical Review B* 1975, 12, 1899.
3. Beyer, H. *Zeitschrift für Kristallographie-Crystalline Materials* 1967, 124, 228-237.
4. Champarnaud-Mesjard, J., Blanchandin, S., Thomas, P., Mirgorodsky, A., Merle-Mejean, T., Frit, B. *Journal of Physics and Chemistry of Solids* 2000, 61, 1499-1507.
5. Mirgorodsky, A., Merle-Méjean, T., Champarnaud, J.-C., Thomas, P., Frit, B. *Journal of Physics and Chemistry of Solids* 2000, 61, 501-509.
6. Blanchandin, S., Marchet, P., Thomas, P., Champarnaud-Mesjard, J., Frit, B., Chagraoui, A. *Journal of Materials Science* 1999, 34, 4285-4292.
7. Blanchandin, S. Etude Cristallochimique De Quelques Phases Cristallisées Et Vitreuses Appartenant Aux Systemes $\text{TeO}_2\text{-WO}_3$ Et $\text{TeO}_2\text{-Nb}_2\text{O}_5\text{-Bi}_2\text{O}_3$. Université de Limoges, 2000.
8. Dutreilh-Colas, M. Nouveaux Matériaux Pour L'optique Non Linéaire: Synthèse Et Étude Structurale De Quelques Phases Cristallisées Et Vitreuses Appartenant Aux Systèmes $\text{TeO}_2\text{-Ti}_2\text{O-Ga}_2\text{O}_3$ Et $\text{TeO}_2\text{-Ti}_2\text{O-PbO}$. Université de Limoges, 2001.
9. Thomas, P. *Journal of Physics C: Solid State Physics* 1988, 21, 4611.
10. Gulenko, A. Etude Structurale Du Verre De TeO_2 Et De La Variété Désordonnée $\text{TeO}_2\text{-}\Delta$ Par Dynamique Moléculaire. Université de Limoges, 2014.
11. Sidel, S., Santos, F., Gordo, V., Idalgo, E., Monteiro, A., Moraes, J. C. S., Yukimitu, K. *Journal of Thermal Analysis and Calorimetry* 2011, 106, 613-618.
12. Cachau-Herreillat, D., Norbert, A., Maurin, M., Philippot, E. *Journal of Solid State Chemistry* 1981, 37, 352-361.
13. Taniguchi, T., Inoue, S., Mitsunashi, T., Nukui, A. *Journal of Applied Crystallography* 2000, 33, 64-70.
14. Folger, F. *Zeitschrift für anorganische und allgemeine Chemie* 1975, 411, 103-110.
15. Brese, N., O'Keefe, M. *Acta Crystallographica Section B: Structural Science* 1991, 47, 192-197.
16. Wenger, M., Armbruster, T. *European Journal of Mineralogy* 1991, 387-400.
17. Oufkir, A., Dutreilh, M., Thomas, P., Champarnaud-Mesjard, J., Marchet, P., Frit, B. *Materials Research Bulletin* 2001, 36, 693-703.
18. Champarnaud-Mesjard, J.-C., Thomas, P., Colas-Dutreilh, M., Oufkir, A. *Zeitschrift für Kristallographie. New Crystal Structures* 2001, 216, 185-186.
19. Zavodnik, V. E., Ivanov, S. A., Stash, A. I. *Acta Crystallographica Section E: Structure Reports Online* 2008, 64.
20. Kaur, A., Khanna, A., Pesquera, C., González, F., Sathe, V. *Journal of Non-Crystalline Solids* 2010, 356, 864-872.
21. Barney, E., Hannon, A., Holland, D., Umesaki, N., Tatsumisago, M. *Journal of Non-Crystalline Solids* 2015, 414, 33-41.

22. Barney, E., Hannon, A., Holland, D. *Journal of Physical Chemistry C* 2012, **116**, 3707-3718.
23. Hoppe, U., Gugov, I., Bürger, H., Jónvári, P., Hannon, A. *Journal of Physics: Condensed Matter* 2005, **17**, 2365.
24. Barney, E. R., Hannon, A. C., Holland, D., Umesaki, N., Tatsumisago, M., Orman, R. G., Feller, S. *Journal of Physical Chemistry Letters* 2013, **4**, 2312-2316.
25. Tatsumisago, M., Lee, S.-K., Minami, T., Kowada, Y. *Journal of Non-Crystalline Solids* 1994, **177**, 154-163.
26. McLaughlin, J. C., Tagg, S., Zwanziger, J. *Journal of Physical Chemistry B* 2001, **105**, 67-75.
27. El-Mallawany, R. A., *Tellurite Glasses Handbook: Physical Properties and Data*; CRC press, 2011.
28. Alex Hannon, Emma Barney, Holland, D., TeO₂ Structural Model 2016.
29. Gulenko, A., Masson, O., Berghout, A., Hamani, D., Thomas, P. *Physical Chemistry Chemical Physics* 2014, **16**, 14150-14160.
30. Pietrucci, F., Caravati, S., Bernasconi, M. *Physical Review B* 2008, **78**, 064203.
31. Wu, J., Stebbins, J. F. *Journal of Non-Crystalline Solids* 2010, **356**, 2097-2108.
32. Barney, E. R., Hannon, A. C., Holland, D. *Physics and Chemistry of Glasses-European Journal of Glass Science and Technology Part B* 2009, **50**, 156-164.

Chapter 5 – Lithium tellurite (IV) glasses

5.1 Introduction

This chapter describes the preparation method of the null and natural glass samples and the general characterisations that include density measurement, thermal analysis, and secondary ion mass spectroscopy. These initial characterisations are used to confirm the glass nominal composition, the amorphicity (as well as the crystal phases present during heat treatment), and the isotopic ratio of $^6\text{Li}/^7\text{Li}$ of the glasses, respectively. Subsequently, Raman scattering is used to probe the presence of various units or species in the glasses and the information is used to derive a semi-quantitative estimate of the average Te-O coordination number n_{TeO} . In the neutron diffraction section, the total correlation functions $T(r)$ for the null and natural glasses are presented. The null $T(r)$'s are compared with pure TeO_2 and the related lithium tellurite crystals to highlight the differences and similarities in both Te and O environments. From the related crystals, the Te-O distances are extracted and used to parameterise the Te-O interatomic distance r_{TeO} in the glasses. From the parameterisation, the average n_{TeO} is calculated as a function of the modifier Li_2O content, x . The average $n_{\text{TeO}}(x)$ values obtained are discussed based on two regions, plateau ($x < 15$ mol%) and post-plateau ($x > 15$ mol%). The lithium environment is later considered in conjunction with the tellurium environment to obtain a consistent description of the glass structure. The chapter is concluded by summarising the experimental method and general findings, followed by presentation of the short and intermediate range structural information deduced from the study (species/unit presents, average coordination number and distances).

5.2 Sample preparation and general characterisation

5.2.1 Sample preparation

Lithium tellurite glasses, with nominal composition $x\text{Li}_2\text{O} \cdot (100-x)\text{TeO}_2$ for $x = 10, 15, 20, 25$, and 30 mol%, were prepared in two series; natural (using Li_2CO_3 at natural Li isotope abundance and reagent grade TeO_2) and null (using null Li_2CO_3 , i.e., an appropriate mixture of natural and ^6Li -enriched Li_2CO_3 , and reagent grade TeO_2). Details of the null neutron scattering formulations are discussed in Section 2.3.2.2. Each 10 g batch of glass was appropriately weighed and intimately mixed in a pestle and mortar before being heated from room temperature to 800 °C at 10 °C/min in a Pt/Rh or Pt/Au crucible and then held at

that temperature for 30 minutes to homogenise the melt. The melting temperature was chosen to be approximately 100 °C above the highest liquidus in the composition range (Fig. 5.1) and was fixed for all the samples to provide a similar thermal history. The melt was then quenched by immersing the crucible base in water at room temperature.

*Table 5.1: Glasses appearance by visual observation. The $x = 35$ mol% glass sample was made to confirm no amorphous material is obtained at this composition using this method. ^aMade using a Pt/Rh crucible, ^bMade using a Pt/Au crucible. *Made in a small batch of approximately 1 g for the purpose of Raman analysis.*

Nominal composition / mol%	Appearance	
	Natural glasses	Null glasses
5	Crystalline ^a , Amorphous*	N/A
10	Amorphous ^b (with separable crystalline bits ^a)	Amorphous ^b
15	Amorphous ^{a,b}	Amorphous ^b
20	Amorphous ^a	Amorphous ^b
25	Amorphous ^a	Amorphous ^b
30	Amorphous ^b (with separable crystalline bits ^a)	Amorphous ^b
33	Amorphous with crystalline inclusions ^{a*}	N/A
35	Crystalline ^a	N/A

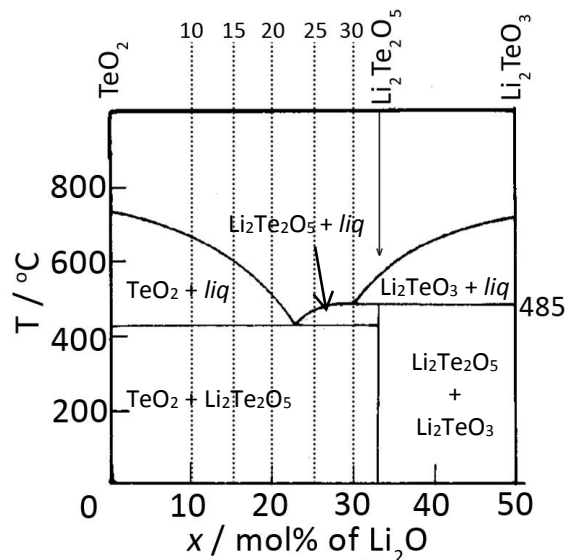


Figure 5.1: Phase diagram for the $\text{Li}_2\text{O}-\text{TeO}_2$ system [2]. There is a eutectic composition at about 22.5 and a peritectic at 30 mol% Li_2O . Two lithium tellurite phases ($\text{Li}_2\text{Te}_2\text{O}_5$ and Li_2TeO_3) are shown in the figure. The 5 glass compositions in this study are marked by the dotted lines.

The glasses were judged to be amorphous by visual inspection (later confirmed by neutron diffraction). The physical appearance of the glasses is as summarised in Table 5.1. As seen in the table, glasses with compositions at the higher and lower Li_2O contents have crystalline inclusions in them when made using the Pt/Rh crucible, but not when made using the Pt/Au non-wetting crucible. It should be noted that the Pt/Au crucible has a slightly thinner wall than the Pt/Rh crucible which will increase the heat transfer rate, helping to avoid

crystallisation. The formation of crystalline inclusions in the glasses at the lower and higher limits is consistent with the limits of glass formation range as reported in the literature (SciGlass database [1]).

5.2.2 Density measurement

The measured density values are reported in Table 5.2. Fig. 5.2(a) compares the density values for both natural and null glasses, as a function of Li_2O content (mol%), with those obtained from the SciGlass database [1]. As indicated in Table 5.2, the difference between the natural and null glass molecular weights, due to different $^6\text{Li}/^7\text{Li}$ isotope contents, is small (about 0.1 to 0.2 %) and is negligible since the mass contribution comes mostly from the heavier Te atoms (the mass difference between $^{\text{Nat}}\text{Li}_2\text{O}$ and $^{\text{Null}}\text{Li}_2\text{O}$ is 2%). The differences in the experimental densities are within the experimental error of up to $\sim 0.03 \text{ g cm}^{-3}$.

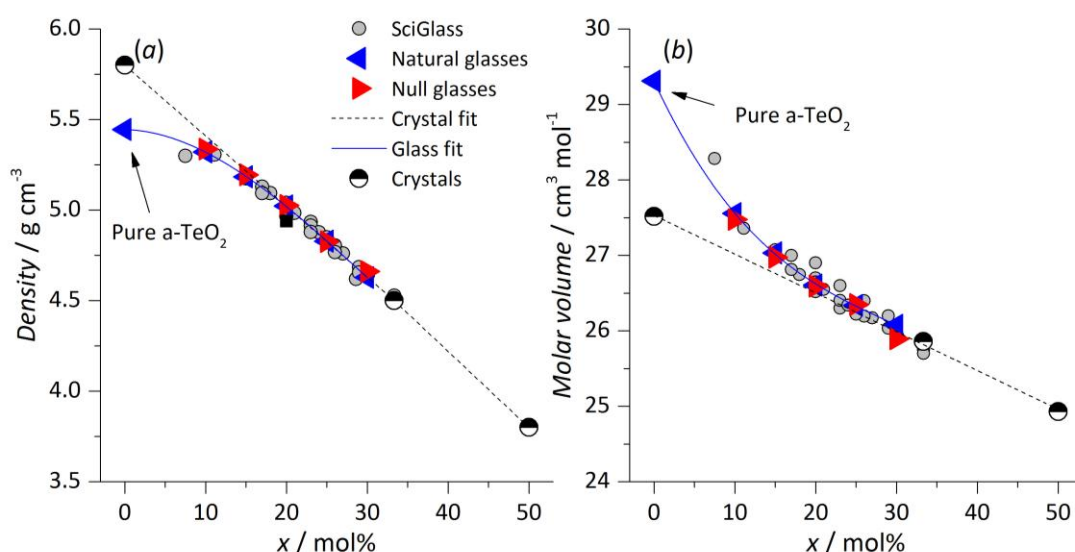


Figure 5.2: (a) The measured densities for the $\text{Li}_2\text{O}-\text{TeO}_2$ glasses: natural glasses (blue, left-pointed triangle) and null glasses (red, right-pointed triangle) compared to SciGlass data (grey circle) and pure amorphous TeO_2 from Barney et al. [3] (b) Molar volumes of the glasses (symbols as in (a)) compared with the SciGlass data. Error bars for the natural and null glasses are within the points shown.

In general, the density decreases almost linearly as a function of Li_2O content as the heavier TeO_2 is replaced by lighter Li_2O . However, the curve of the glass (data) fit in Fig. 5.2(a) diverges from the linear crystal (data) fit. The density values can be fitted with two linear equations intersecting at $x \approx 15 \text{ mol\%}$. The rate of decrease for $x < 15 \text{ mol\%}$ region is less than for $x > 15 \text{ mol\%}$. The measured densities are consistent with the values compiled in SciGlass for the same system, indicating that the glass compositions used in this study are close to the nominal compositions. Fig. 5.2(b) shows the molar volume of the glasses as a

function of x . In general, as more Li_2O is added, the molar volume decreases, meaning that, the glass molecular structure experiences an overall shrinkage associated with the formation of one or more structural moieties with smaller volume occupation per mole or which occupy pre-existing empty space in the network.

The molar volume versus composition plot also shows the same behaviour as observed in the density plot. For $x < 15$ mol%, the rate of change is greater than for the $x > 15$ mol%. A better impression of the actual packing of atoms is gained by examining number density plots for the system. These are shown in Fig. 5.3. That for Li atom is linearly related to x , however the plots for Te and O atoms show a change in slope at ~ 15 mol%, indicating that it is the tellurite network which is undergoing a change at this composition, consistent with the neutron diffraction analysis as will be discussed later. However, a coordination number change for Te atom cannot be concluded solely from the density data, since Te-O polyhedra could change shape and volume without a change in the coordination number.

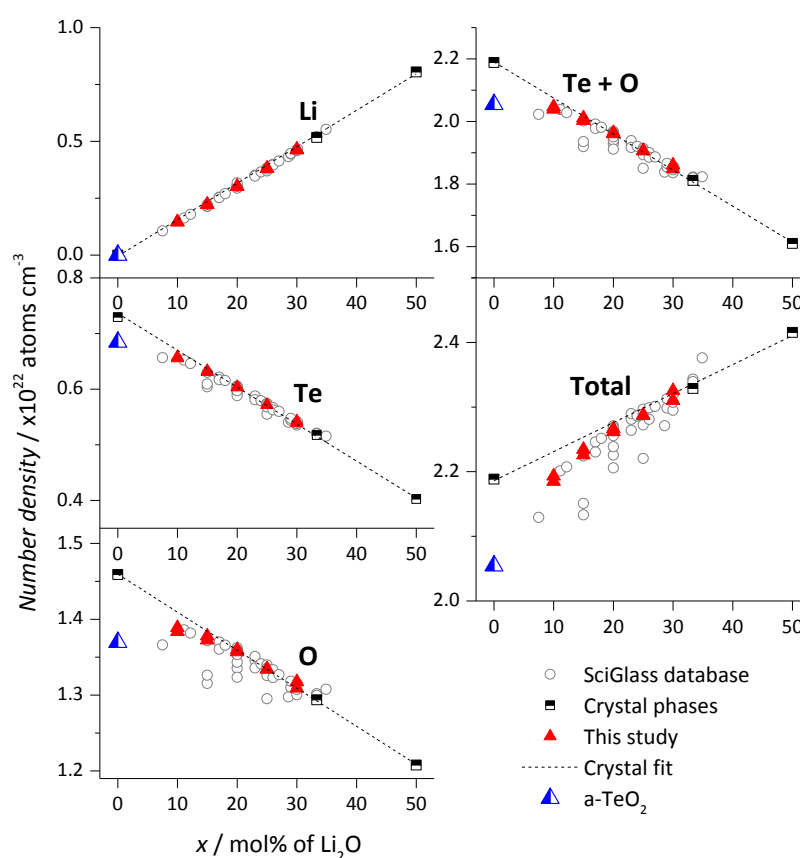


Figure 5.3. Calculated number density for constituent atoms as a function of Li_2O composition for both natural and null glasses (red triangles). The number density plots for O and Te atoms in the glasses show the deviational behaviour compared with the crystals (linear fit, dashed black line).

Comparison of the behaviour of the glass density, molar volume, and number density values, as a function of Li_2O content (Fig. 5.2 and Fig. 5.3), with that observed for the corresponding

lithium tellurite crystal phases (γ -TeO₂, Li₂Te₂O₅ and Li₂TeO₃) shows that the change in gradient reflects the deviation of the tellurite network structure of the glass from the 3D repeating structure of crystalline TeO₂. The overall decrease in both density and molar volume with increasing Li₂O content reflects the small size and mass of the lithium ion.

Table 5.2: Molecular weight MW, density ρ , and molar volume MV values for natural and null xLi₂O-(100-x)TeO₂ glasses

x Li ₂ O (mol%)	MW ^{Nat} (g mol ⁻¹)	MW ^{Null} (g mol ⁻¹)	ρ^{Nat} (g cm ⁻³)	ρ^{Null} (g cm ⁻³)	MV ^{Nat} (cm ³ mol ⁻¹)	MV ^{Null} (cm ³ mol ⁻¹)
10	146.63	146.54	5.32	5.34	27.6	27.5
15	140.14	140.01	5.18	5.20	27.0	27.0
20	133.65	133.48	5.02	5.03	26.6	26.6
25	127.17	126.95	4.83	4.83	26.3	26.3
30	120.68	120.41	4.63	4.66	26.1	25.9

5.2.3 Thermal analysis

Fig 5.4 shows the DTA heating and cooling curves for the (natural) lithium tellurite glasses between room temperature and 700 °C. The glasses with $x = 10, 15$, and 20 mol% Li₂O show similar, simple heating curves with one exothermic and one endothermic peak in addition to the T_g "step". The glasses with $x = 25$ and 30 mol% show more complex curves with three exothermic peaks, plus one endothermic peak for $x = 25$ and two endothermic peaks for $x = 30$. The curve for $x = 35$ is included as a comparison of the thermal events occurring in the partially devitrified sample.

On heating, after the glass network relaxes into the supercooled liquid state, thermodynamics will drive the liquid state to crystallise according to its current local structure. Since there is just one exothermic crystallisation peak observed for $x = 10, 15$, and 20 mol% of Li₂O (from this point forward called the lower Li₂O contents), and three peaks were observed for $x = 25$ and 30 (from this point forward called the higher Li₂O contents), this suggests that the glass structures in the lower Li₂O contents group are closely related, and similarly for the higher Li₂O contents group, based on their readiness to crystallise similarly as heat is applied. In order to minimise the internal energy, tellurium atoms in Li₂O-TeO₂ glass would likely adopt their short-range order environments as in tellurium-oxygen and/or lithium-tellurium-oxygen crystal phases, e.g., α -TeO₂, β -TeO₂, γ -TeO₂, α -Li₂Te₂O₅, β -Li₂Te₂O₅, and/or Li₂TeO₃ [4].

A crystallisation kinetics study on a lower Li₂O contents sample ($x = 20$ mol%) [5] revealed the formation of γ -TeO₂, α -TeO₂, and α -Li₂Te₂O₅. An earlier study on a higher Li₂O contents sample ($x = 30$ mol%) [6] found that an unknown lithium tellurite crystal (LTX) was formed, which later transformed to α -Li₂Te₂O₅ phase and then into β -Li₂Te₂O₅ phase. At the

same temperature where LTX formed, pure TeO_2 glass also formed, which then later transformed into $\alpha\text{-TeO}_2$. This study reported no formation of the $\gamma\text{-TeO}_2$ crystal phase. Studies [7-9] on crystallisation of vitreous TeO_2 found that the $\gamma\text{-TeO}_2$ phase was formed first followed by the transformation into $\alpha\text{-TeO}_2$. It can be inferred that, in $\text{Li}_2\text{O}\text{-TeO}_2$ glass, metastable $\gamma\text{-TeO}_2$, $\alpha\text{-TeO}_2$, and $\text{Li}_2\text{Te}_2\text{O}_5$ are therefore closely related to the glass structure for both (higher and lower) groups but with different crystallisation kinetics, these being determined by the activation energy needed to rearrange local structure. This is consistent with the crystal phases as labelled in the phase diagram (Fig. 5.1). $\alpha\text{-Li}_2\text{Te}_2\text{O}_5$ is more stable than $\beta\text{-Li}_2\text{Te}_2\text{O}_5$ with the latter being the high temperature phase which is closer to glass phase [10]. Particular emphasis will be placed on $\gamma\text{-TeO}_2$, $\alpha\text{-TeO}_2$, and $\beta\text{-Li}_2\text{Te}_2\text{O}_5$ when discussing the glass structure though without ignoring the other phases, e.g., $\beta\text{-TeO}_2$, $\beta\text{-Li}_2\text{Te}_2\text{O}_5$ and Li_2TeO_3 .

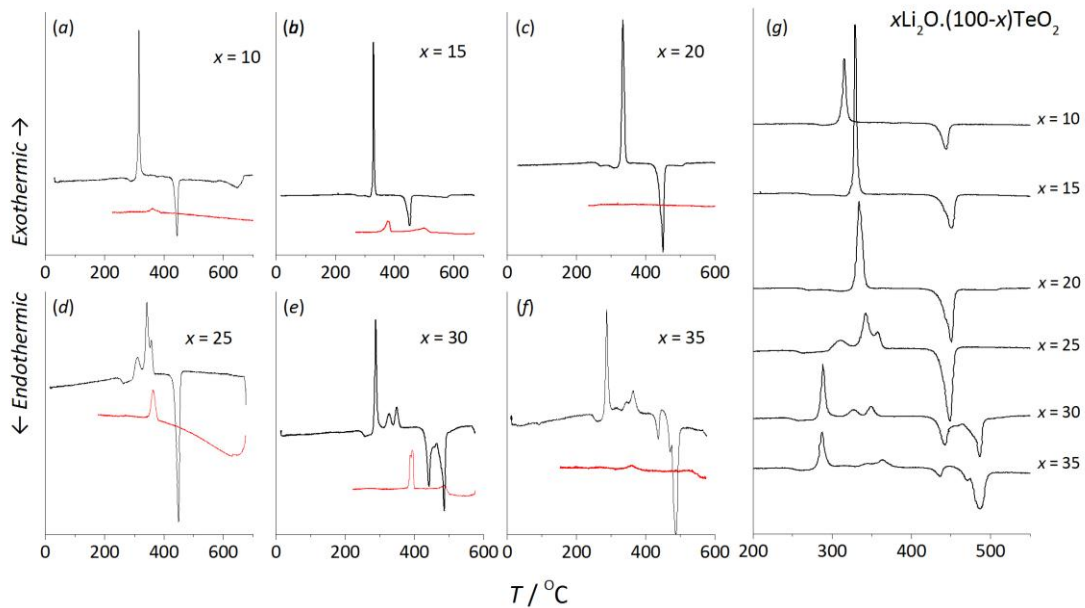


Figure 5.4: Figs. (a) to (f) show the thermal analysis curves for $x\text{Li}_2\text{O} \cdot (100-x)\text{TeO}_2$ glasses for $x = 10, 15, 20, 25, 30$ and 35^* mol% showing the heating curve (black, top) and cooling curve (red, bottom) lines for each glass composition. $^*x = 35$ mol% is a glass partially-crystallised with $\text{Li}_2\text{Te}_2\text{O}_5$. The glasses were heated at a rate of $10\text{ }^\circ\text{C}/\text{min}$ and Newtonian cooled. (g) Stack plot of heating curves showing two compositional regions of similar crystallisation behaviour; lower Li_2O compositions, $x = 10, 15$, and 20 mol% with just one exothermic peak, and higher Li_2O compositions, $x = 25$, and 30 mol% with three exothermic peaks. $x = 35$ mol% is made up of mostly $\text{Li}_2\text{Te}_2\text{O}_5$ crystal phase ($33.33\text{mol}\%$ of Li_2O). Close resemblance between $x = 30$ and 35 mol% reflects the proximity of the $x = 30$ mol% glass to the $\alpha/\beta\text{-Li}_2\text{Te}_2\text{O}_5$ phase field.

The glass transition temperatures (T_g) and crystallisation temperatures (T_x) are extracted from the DTA curves and tabulated as in Table 5.3 and shown in Fig 5.5. The T_g values are compared to those obtained from the SciGlass database [1] and, in general, they show a similar trend (decreasing, as a function of x). As T_g is partially related to the cooling

rate [11-13], the T_g in the figure can be grouped into two (higher and lower T_g) groups to represent rapidly cooled and slowly cooled glasses, respectively. The T_g values measured by Tatsumisago *et al.* [11] are higher than those prepared in similar melting environment but different cooling rate. Apart from that, T_g is also a function of bond strength [14].

Table 5.3: Temperatures, T_g , T_x , and T_c extracted from the differential thermal analysis curve as well as calculated glass stability (towards devitrification) parameter for each glass

$x /$ mol%	Glass transition temperature, $T_g /$ $^{\circ}\text{C}$	Crystallisation temperature					Glass stability, $T_x - T_g$
		Onset, $T_x / ^{\circ}\text{C}$	Peak, $T_c / ^{\circ}\text{C}$				
			T_{C1}	T_{C2}	T_{C3}	T_{C4}	
10	275	308	315	-	-	-	32
15	262	318	328	-	-	-	56
20	254	324	334	-	-	-	69
25	249	294	310	341	357	-	45
30	244	279	288	327	349	-	35
35	243	279	287	317	345	363	36

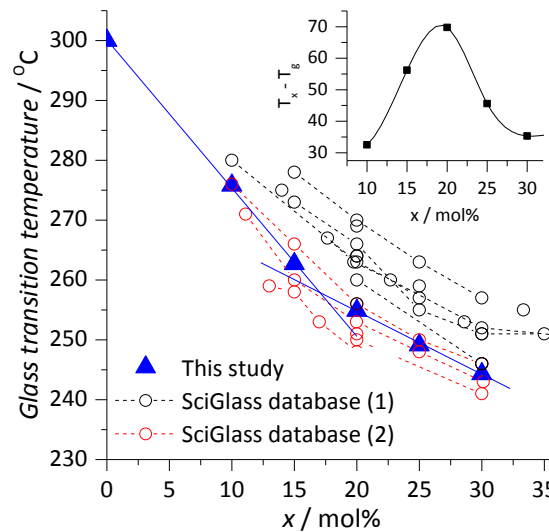


Figure 5.5: The values of T_g for the glasses at different nominal compositions. T_g can be linearly fitted with two lines to highlight the intersection at $x \sim 15$ mol%, similar to the behaviour observed in the density values. Inset shows the glass stability, $T_x - T_g$. The data are fitted with a spline interpolation showing the behaviour of the glass stability as a function of Li_2O content with a maximum stability towards devitrification at $x \sim 20$ mol%. This is supported by the cooling curve for this glass in Fig 5.4 where negligible crystallisation was observed upon cooling. Black circles are the the T_g values for the $\text{Li}_2\text{O}-\text{TeO}_2$ glasses prepared using silica crucible for splat-quenching method and a roller-quenched series. The red circles are the T_g values from the glasses prepared using a similar environment as for the studied glass; using a platinum crucible and splat quenching method.

A general trend is observed from the database with glasses prepared in silica crucibles having T_g values higher than those prepared in platinum/gold crucibles at a similar cooling rate. This is possibly due to contamination by SiO_2 from the crucible. T_g is partly a measure of disorder as it is a temperature at which the supercooled liquid ‘freezes’ to form the glass.

Glasses in which the molecules are ‘locked’ at higher energies (temperature) are probably more disordered (having the molecular arrangement more similar to the liquid state compared to the solid state). The glass stability towards devitrification parameter is taken as the temperature gap between T_g and the onset crystallisation temperature and is shown as the inset in Fig. 5.5. The glass with $x = 20$ mol% is the most stable towards devitrification as also evidenced by the Newtonian cooling curve where no crystallisation peak is seen.

Table 5.4: Melting environments of the same glass system taken from the SciGlass database

	Melting environments		T_g group	Cooling method
	Crucible	$T_m / ^\circ\text{C}$		
Tatsumisago '94	Silica/Platinum	700-900	Higher	RQ
Heo '92	Silica	800-850	Higher	SQ
Zhang '92	Silica	750-850	Higher	SQ
Inoue '92	Platinum	650-750	Lower	SQ
Lee '94	Platinum	800	Lower	SQ
Mochida '78	Gold	700-900	Lower	SQ

RQ is roller-quenched, and SQ is splat quenched.

5.2.4 Secondary ion mass spectroscopy

To ensure that the glass samples which should contain null lithium isotope are of the correct isotopic composition, secondary ion mass spectroscopy (SIMS) analysis was done on the null samples and also on the natural and enriched $\text{Li}_2\text{O}-\text{TeO}_2$ glasses courtesy of Dr Richard Morris of the Department of Physics. The enriched $\text{Li}_2\text{O}-\text{TeO}_2$ glasses were made using only ^6Li -enriched Li_2CO_3 as a part of the SIMS study to verify the $^6\text{Li}/^7\text{Li}$ isotope ratio and this glass was not used in the neutron diffraction study. The SIMS setup was optimised using the mineral spodumene, $\text{LiAl}(\text{SiO}_3)_2$, courtesy of Dr Ian Farnan of the University of Cambridge. A glass sample with $x = 20$ mol% Li_2O was chosen to represent the series and the results are presented in Table 5.5 and Fig. 5.6.

Table 5.5: Isotopic ratios of ^6Li and ^7Li isotopes in the natural, enriched, and null lithium glasses and natural lithium aluminosilicate mineral crystal. The glass samples (2, 3, 4, and 5) of $x = 20$ mol% were selected for the SIMS analysis. Sample 4 represents clear glass whereas sample 5 represents the cloudy glass with small crystalline regions of the same composition.

Sample	% ^6Li	% ^7Li	$\langle b \rangle$
$\text{LiAl}(\text{SiO}_3)_2$ (1)	8.6 ± 0.6	91.4 ± 0.6	-1.857
$x^{\text{Nat}}\text{Li}_2\text{O}-\text{TeO}_2$ (2)	7.5 ± 0.1	92.5 ± 0.1	-1.904
$x^{\text{Null}}\text{Li}_2\text{O}-\text{TeO}_2$ (3)	52.4 ± 0.2	47.6 ± 0.2	-0.008
$x^{\text{Enr}}\text{Li}_2\text{O}-\text{TeO}_2$ (4)	95.0 ± 0.3	5.0 ± 0.3	1.789
$x^{\text{Enr}}\text{Li}_2\text{O}-\text{TeO}_2$ (5)	95.1 ± 0.2	4.9 ± 0.2	1.793

From the analysis, the natural and enriched glasses have the quoted abundance value of $^6\text{Li}/^7\text{Li}$, i.e., 7.5% ^6Li and 92.5% ^7Li , and 95% ^6Li and 5% ^7Li within the errors respectively. The null glass was also confirmed to be null with 52.4% ^6Li and 47.6 % ^7Li having a total neutron scattering value, $\langle b \rangle$ of -0.008 to 3 decimal places, i.e. effectively zero.

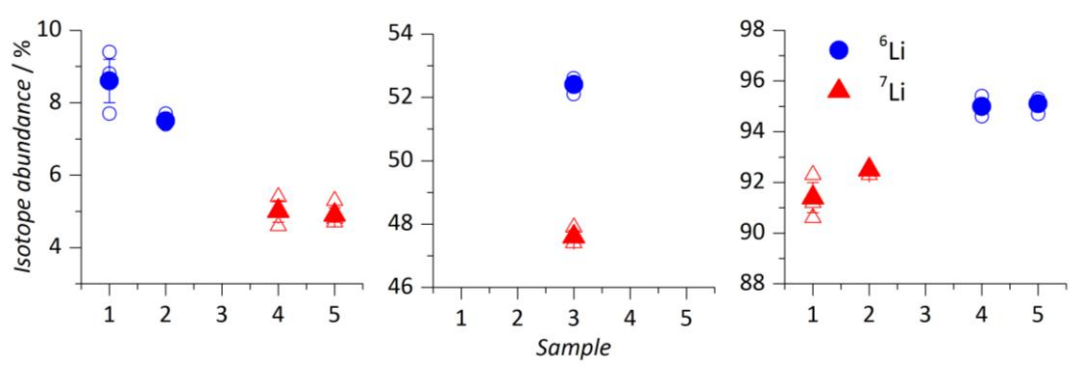


Figure 5.6: Graphical representation of ^6Li and ^7Li isotopic percentages in the samples of 1(mineral spodumene), 2(natural glass), 3(null glass), 4(enriched glass), and 5(enriched glass with glass and crystal inclusions). Similar isotope distribution in glassy and glassy/crystalline state is confirmed from SIMS analysis on samples 4 and 5. NB – the spread in values for spodumene indicates the progress of the set-up process.

5.3 Raman spectroscopy

Figs 5.7 (a) and (b) show the measured and reduced intensities respectively of the Raman spectra from 100 cm^{-1} to 1000 cm^{-1} . The reduced Raman spectra were obtained by multiplying the experimental intensity with the correction factors for the wavelength-dependent scattered intensity and temperature-dependent mean number for phonon occupation in the glass as discussed in Section 3.5. The reduction was done so that the main features of the Te–O vibrations in the glass can be highlighted for study.

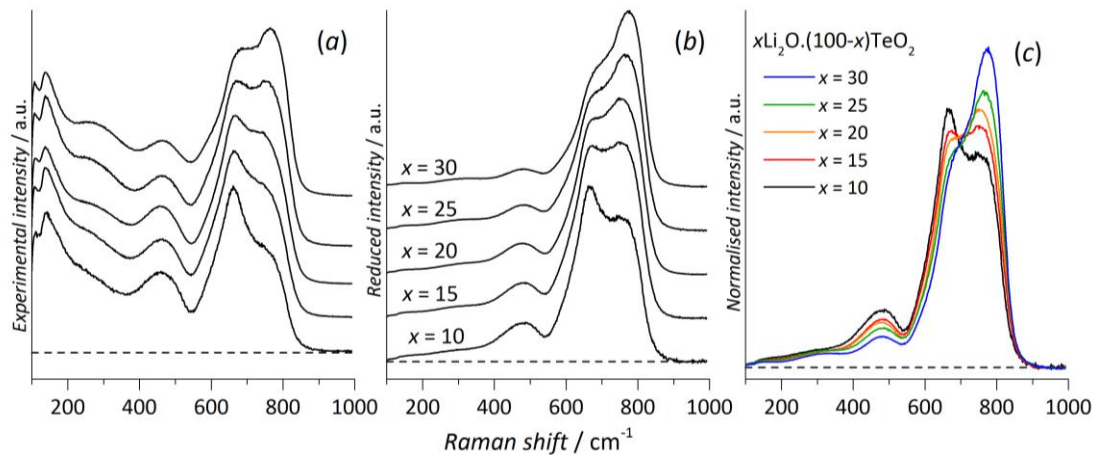


Figure 5.7: Raman spectra for the $\text{Li}_2\text{O}-\text{TeO}_2$ glasses. The y-axes are (a) normalised measured intensity, (b) normalised reduced intensity. (a) was normalised to the maximum intensity, (b) was reduced by elimination of the Boson peak [15] and (c) is the area-normalised reduced intensity in the region of interest encompassing the Te-O vibrations.

The Raman spectra show a broad continuous peak manifold from approximately 500 to 900 cm^{-1} , characteristic of Te–O vibrations as typically observed in tellurite glasses [15-16] encompassing the vibrations in various Te environments, e.g., 3, 3+1, and 4 coordinated Te. As Li_2O content is increased, a major change was observed in the shape of the manifold, i.e., the peak at 600 cm^{-1} decreased whilst the peak at about 800 cm^{-1} increased (Fig. 5.7 (c)). In the literature, the region from 500 to 900 cm^{-1} is typically resolved into 4 peaks assigned to the vibrational modes of either a 4-coordinated pseudo-trigonal bipyramidal (tbp) unit or a 3-coordinated trigonal pyramidal (tp) unit as shown in Table 5.6 [15-16]. These peaks were determined from the vibration modes of $[\text{TeO}_3]$, $[\text{TeO}_{3+1}]$ and $[\text{TeO}_4]$ units in various TeO_2 polymorphs [17] and $\text{M}_2\text{O}-\text{TeO}_2$ crystals ($\text{M} = \text{Li}, \text{Na}, \text{K}, \text{Rb}, \text{Cs}, \text{ and } \text{Tl}$) [16]. The Raman shifts covering the lower wavenumbers in the broad peak (620 to 670 cm^{-1}) for the $[\text{TeO}_4]$ unit are derived from the paratellurite ($\alpha\text{-TeO}_2$) crystal whereas the higher region is attributed to two peaks from 720 to 780 cm^{-1} for the $[\text{TeO}_3]$ units found in M_2TeO_3 crystal phases.

Table 5.6: Peak assignment for Raman vibration of Te-O species in TeO_2 glasses

Raman shift / cm^{-1}	Mode of vibration	Assignment
430 490	Bending	-Te–O–Te- or -O–Te–O-
626 667	Stretching	$[\text{TeO}_4]$ tbp
720 771	Stretching	$[\text{TeO}_3]$ tp

As previously discussed in Section 5.2.3, the thermal analysis shows that the lower Li_2O contents ($x = 10, 15$, and 20 mol% of Li_2O) and higher Li_2O contents ($x = 25$ and 30 mol% of Li_2O) undergo different crystallisation behaviour, suggesting that they have a different local glass structure. This is reflected in the Raman spectra by the change in the relative peak heights at about 650 cm^{-1} and 780 cm^{-1} . Since the peak at 650 cm^{-1} is attributed to the $[\text{TeO}_4]$ unit found in $\alpha\text{-TeO}_2$, and the 780 cm^{-1} is attributed to the $[\text{TeO}_3]$ unit found in Li_2TeO_3 , the Raman spectra suggest that for the lower contents group, the short-range order in the glasses more closely resembles those structures with $[\text{TeO}_4]$ units such as $\alpha\text{-TeO}_2$ and $\gamma\text{-TeO}_2$ as shown in Fig. 5.8(a). The peak at 780 cm^{-1} is only found in $\alpha\text{-Li}_2\text{Te}_2\text{O}_5$, $\beta\text{-Li}_2\text{Te}_2\text{O}_5$ and Li_2TeO_3 where there are $[\text{TeO}_{3+1}]$ and $[\text{TeO}_3]$ units present. It could therefore be inferred that, in general, $[\text{TeO}_4]$ units (short-range order similar as in $\alpha\text{-TeO}_2$ and $\gamma\text{-TeO}_2$) transform to $[\text{TeO}_3]$ (as in Li_2TeO_3 or TeO_2 in liquid state) [18] via intermediate $[\text{TeO}_{3+1}]$ units (as found in $\alpha\text{-Li}_2\text{Te}_2\text{O}_5$) with increasing Li_2O content. From the DTA analysis in the previous section, it was shown that, in this particular order, $\text{Li}_2\text{O}-\text{TeO}_2$ glasses crystallise to form TeO_2 crystal

(from metastable γ -phase transforming to stable α -phase) and $\text{Li}_2\text{Te}_2\text{O}_5$ (from α -phase to high temperature β -phase) as shown in Fig 5.8(a). From this, it can also be inferred that these glasses have a short range structure comparable to γ - TeO_2 . This is also supported by the similarity of the Raman spectra of the pure TeO_2 glass and the Li_2O - TeO_2 glasses with low Li_2O contents. The region of interest in the Raman spectra for the Te–O vibrations can be resolved into 4 peaks as given in Table 5.6, where the peaks at the two lowest (626 and 667 cm^{-1}) and two highest (720 and 771 cm^{-1}) energies are assigned to the stretching modes of the $[\text{TeO}_4]$ and $[\text{TeO}_3]$ units, respectively and the peak at about 490 cm^{-1} is attributed to the bending modes of $-\text{Te}-\text{O}-\text{Te}-$ bridges and not included in determining the average coordination number of Te in the glass [16]. From the fits shown in Fig. 5.8(b), the central Raman shift and area of individual peaks were extracted and the average Te-O coordination number for each glass composition was calculated and listed in Table 5.7. Similar peak widths were used for the individual peaks in the figure. The sum of the fits gives good agreement with the experimental spectra. The average Raman shifts of the peaks from the fits are consistent with the expected values from the literature [15-16].

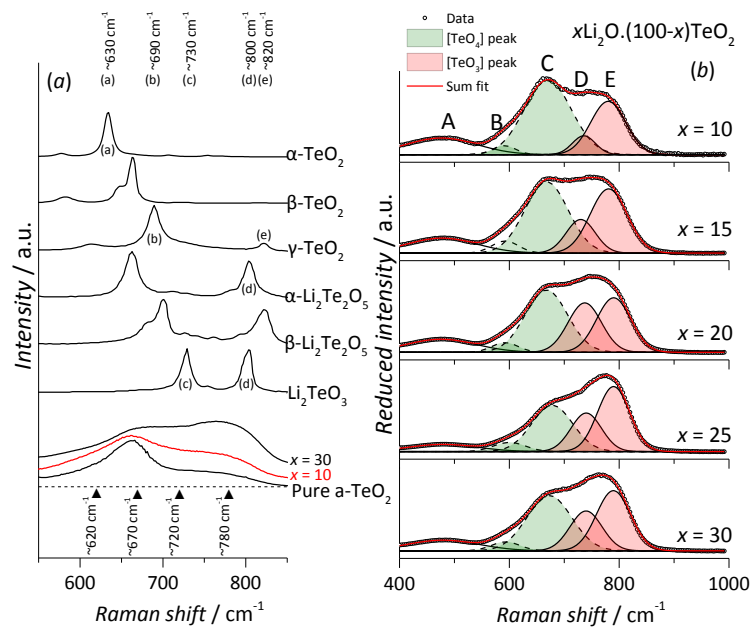


Figure 5.8: (a) Comparison of the Raman peak manifold shape from the 10 mol% and 30 mol% glasses with the Raman spectra of the related crystals. (b) Peak de-convolution of the Te-O vibrations according to the peak assignment as in Table 5.6

The peak area contributed by the vibrations from $-\text{Te}-\text{O}-\text{Te}-$ or $-\text{O}-\text{Te}-\text{O}-$ bridges seems to decrease as more Li_2O is added, because more bridges are broken by the Li^+ ions (creation of non-bridging oxygen atoms). In the case of $[\text{TeO}_4]$ units, the area for Peak B (593 cm^{-1}) remains roughly constant at a very low value but Peak C (671 cm^{-1}) shows a steady decrease

across the compositions denoting the transformation of $[\text{TeO}_4]$ units to other unit(s). The peaks contributed by the $[\text{TeO}_3]$ units show rather a random pattern as represented by Peak D (736 cm^{-1}) and Peak E (786 cm^{-1}) (Fig 5.9(a)). Peak D (736 cm^{-1}) has a maximum area at $x = 20 \text{ mol\%}$ meanwhile Peak E (786 cm^{-1}) has the maximum area at about $x = 15 \text{ mol\%}$.

Table 5.7: Peak parameters obtained from fitting of the Raman spectra

x / mol%	Central Raman shift $\pm 1 / \text{cm}^{-1}$						Area $\pm 1 / \%$				
	10	15	20	25	30	Av $\pm \sigma$	10	15	20	25	30
Peak A	476	477	475	479	479	477 ± 2	27	24	21	17	11
Peak B	590	592	591	593	600	593 ± 7	16	24	19	19	22
Peak C	670	667	667	672	678	671 ± 7	26	23	19	18	14
Peak D	735	730	737	739	740	736 ± 6	8	18	30	23	21
Peak E	780	780	790	789	789	786 ± 4	18	23	18	20	20
Average n_{TeO} ($\pm 0.2 \text{ max}$)							3.62	3.51	3.45	3.45	3.40

Based on this, it could be inferred that, as Li_2O is added to the TeO_2 network, $-\text{Te}-\text{O}-\text{Te}-$ bridges are broken to accommodate the Li^+ ions and at the same time transforming the $[\text{TeO}_4]$ unit to a $[\text{TeO}_3]$ unit via the intermediate $[\text{TeO}_{3+1}]$ unit. In general, if the $\alpha\text{-TeO}_2$ model of $\alpha\text{-TeO}_2$ is accepted, the average coordination number of tellurium to oxygen, n_{TeO} will therefore decrease from a value close to 4 at $x = 0 \text{ mol \%}$ to a value close to 3 at $x = 50 \text{ mol \%}$ as shown in Fig 5.9 (b). However, the average n_{TeO} obtained from the Raman data, once extrapolated to $x = 0 \text{ mol\%}$ intercepts at 3.68, the value which was experimentally measured by neutron diffraction for n_{TeO} of the pure TeO_2 glass [3].

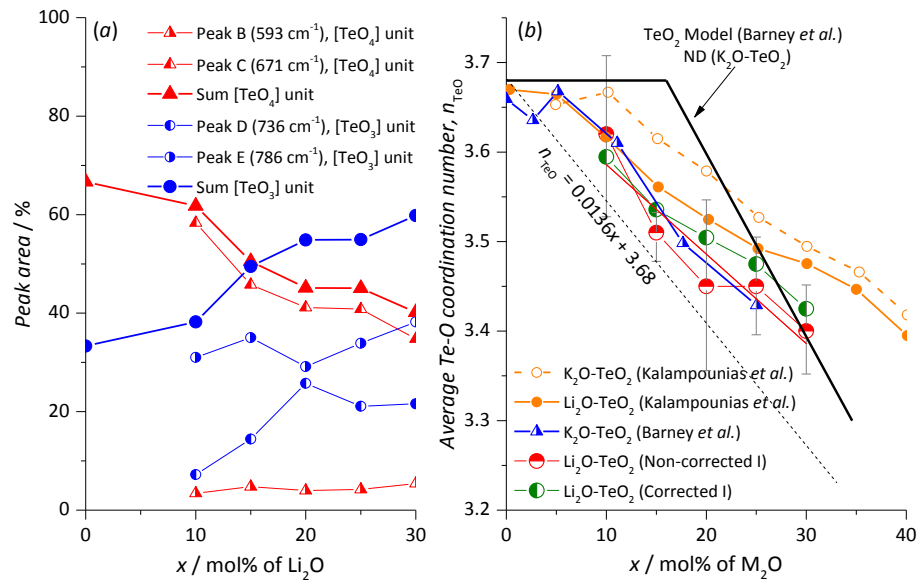


Figure 5.9: (a) showing the peak areas from the fits for each composition and (b) showing the n_{TeO} calculated.

In Fig. 5.9 (b), the average n_{TeO} decreases almost linearly as a function of x . Contrary to the TeO_2 Model (solid black line), the constant average n_{TeO} for x less than 15 mol% is not observed. The Raman average n_{TeO} values in this study were obtained by two means; using corrected-intensity (Fig. 5.7(b)) and using non-corrected-intensity (Fig. 5.7(a)). As seen in Fig. 5.9(b), the correction produces little effect on the average n_{TeO} values obtained (within the error). The average n_{TeO} value for the $\text{Li}_2\text{O}-\text{TeO}_2$ (this study) and $\text{K}_2\text{O}-\text{TeO}_2$ [3] show similar behaviour compared to the values reported by Kalampounias *et al.* [15]. They follow a similar trend with composition, with the absence of the constant average n_{TeO} plateau shown by the average neutron n_{TeO} data used by the TeO_2 Model. In Raman scattering analysis, similar Te–O vibrational modes (approximate bond distance) in $\alpha\text{-TeO}_2$ and $\beta\text{-TeO}_2$ appear at two different Raman shifts because of the localisation of the vibrations [16] since the $[\text{TeO}_4]$ units are shared corner-wise and edge-wise in $\alpha\text{-TeO}_2$ and $\beta\text{-TeO}_2$ respectively. The effect of localisation is also observed between $\alpha\text{-Li}_2\text{Te}_2\text{O}_5$ and $\beta\text{-Li}_2\text{Te}_2\text{O}_5$. This adds to the difficulty of analysing Raman spectra quantitatively in a glass (where there are various species of $[\text{TeO}_4]$, $[\text{TeO}_{3+1}]$, and $[\text{TeO}_3]$ with different bond distances and connectivity), but qualitatively, it can be stated that, as a function of a modifier, the $[\text{TeO}_4]$ units are transformed into the $[\text{TeO}_3]$ units.

5.4 Neutron diffraction

5.4.1 Null and natural samples

Figs 5.10(a) and 5.11(a) show the distinct scattering, $i(Q)$, data from the null and natural samples respectively. As discussed in Chapter 2, the presence of the ^{123}Te resonance limits Q_{max} to 35 \AA^{-1} for Fourier transformation and neutron absorption by ^6Li reduces the signal-to-noise ratio. Figs 5.10(b) and 5.11(b) show the total scattering, $T(r)$, for both null and natural glasses. The $T(r)$ plots for the null glasses (Fig. 5.11(b)) contain solely the tellurium and oxygen partials, since the lithium partials have been eliminated as a consequence of the $^{\text{Null}}\text{Li}$ zero average neutron scattering length, $\langle b \rangle = 0$ as discussed in Section 2.3.2.2. The first peak in $T(r)$ shows the asymmetric distribution of first neighbour tellurium-oxygen distances in TeO_2 glasses and the second peak contains a complex manifold of oxygen-oxygen correlations superimposed on longer tellurium-oxygen distances. The negative $T(r)$ for the lithium partials (due to the negative $\langle b \rangle$ value of $^{\text{Nat}}\text{Li}$) is contained in the first peak with the asymmetric Te-O distance distribution.

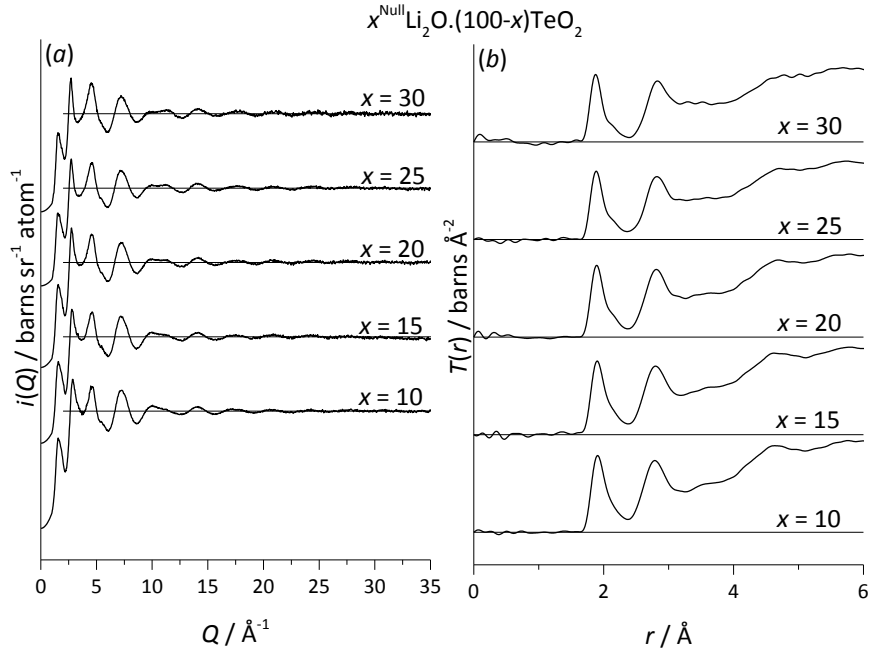


Figure 5.10: Distinct scattering ($i(Q)$) and total correlation function ($T(r)$) for the null lithium tellurite glasses. An offset is used between each plot for clarity. $i(Q)$ with a Q maximum value of 35 \AA^{-1} (a) was Fourier-transformed to $T(r)$ (b) for each glass composition.

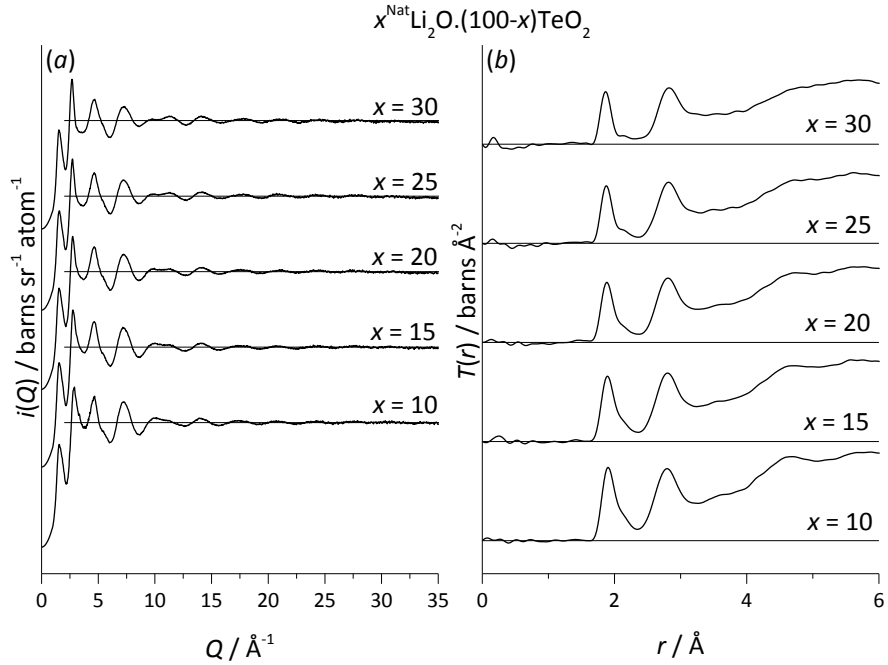


Figure 5.11: Distinct scattering, $i(Q)$, and total correlation function, $T(r)$, for the natural lithium tellurite glasses. An offset is used between each plot for clarity. $i(Q)$ with a Q maximum value of 35 \AA^{-1} (a) was Fourier-transformed to $T(r)$ (b) for each glass composition.

5.4.2 Comparison with a-TeO₂ and relevant crystal phases

The $T(r)$'s in Fig 5.12(a) and Fig 5.12(b) are normalised by the tellurium-oxygen and oxygen-oxygen pair weighting factors (w_{TeO} and w_{OO}) to focus on the short-range tellurium-oxygen and oxygen-oxygen environments, respectively (to up to 2.36 Å). w_{ij} for atoms i and j is given by

$$w_{ij} = (2 - \delta_{ij})c_i b_i b_j \quad 5.1$$

where δ_{ij} , c , and b are the Kronecker delta ($\delta_{ij} = 1$ for $i = j$, and $\delta_{ij} = 0$ for $i \neq j$), atomic fraction, and average neutron scattering length, respectively. These normalised $T(r)/w_{\text{TeO}}$ and $T(r)/w_{\text{OO}}$ plots of the null glasses for $x = 10, 15, 20, 25, 30$ mol% are each compared to the $T(r)$ of pure TeO₂ glass to highlight the difference in the tellurium and oxygen environments in the glasses with respect to the pure TeO₂ glass.

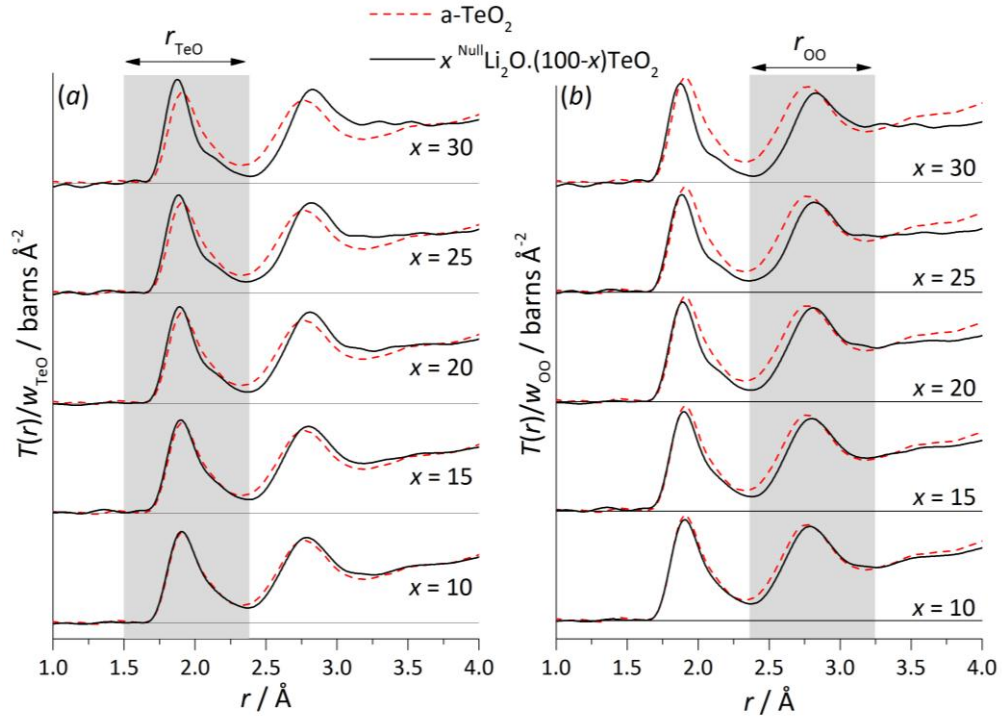


Figure 5.12: $T(r)/w_{\text{TeO}}$ and $T(r)/w_{\text{OO}}$ for the null glasses, stacked and compared with amorphous TeO₂ for each x giving a qualitative comparison of the evolution of the tellurium-oxygen environment in glasses on addition of Li₂O to a-TeO₂. $T(r)$ for the glasses are weighted to the coefficient of $(2 - \delta_{ij})c_i b_i b_j$. *a-TeO₂ data taken from Barney et al. [3].

As was previously concluded from analysis of their Raman spectra, the $x = 10, 15$, and 20 mol% glasses are thought to be more similar to pure TeO₂ glass (a-TeO₂) and the other compositions to β -Li₂Te₂O₅. However, as seen in Fig 5.12 (a), only the $x = 10$ and possibly 15 mol% Li₂O glasses have short range tellurium environments similar to those found in pure TeO₂ glass and hence could also be compared to γ -TeO₂. For the $x = 25$ and 30

mol% glass $T(r)$, in each plot, the area contributed by the shorter Te-O bond distance(s) is larger than in α -TeO₂ and the distributions are similar to that found in the high temperature β -Li₂Te₂O₅ phase [10], whilst for $x = 20$ mol%, the short-range of Te-O bond distance distribution is in between these two groups. This suggests that the short-range Te environments in these glasses are similar to γ -TeO₂ and β -Li₂Te₂O₅ but in different proportions, depending on composition, with γ -TeO₂ being the most in $x = 10$ mol% and the least in $x = 30$ mol%. This is consistent with the finding that, upon cooling from the melt, lithium tellurite glasses first crystallise into two crystal forms; γ -TeO₂ and Li₂Te₂O₅ (α and β phases) [5-6, 18], as well as from the Li₂O–TeO₂ binary phase diagram (Fig. 5.1).

The comparison of the oxygen environments in the glasses to those in γ -TeO₂ is however more complicated due to the stronger steric effect of the Te lone-pair in γ -TeO₂ compared to the other polymorphs, which causes r_{OO} to be shorter in γ -TeO₂ as shown in Fig 5.13 (a) where the magnitude of the lone-pair vector is the largest compared to other crystal phases relevant to this study. The lone-pair vector is defined as;

$$|\mathbf{E}| = -|\mathbf{r}| = -|\mathbf{r}_{Te-O(x)} + \mathbf{r}_{Te-O(x)} + \mathbf{r}_{Te-O(x)}| \quad 5.2$$

The shorter r_{OO} distance in γ -TeO₂ can be seen in its $T(r)$ at about 2.5 Å (Fig. 5.13 (b)). In Fig. 5.12(b), the leading edges of the weighted $T(r)$ for the glasses shift to higher r with increasing x . This short O-O distance is apparent in both α -TeO₂ and γ -TeO₂ (this region contains no Te-O peaks) and corresponds to the O_{eq}-O_{ax} distance shortened due to the steric effect of the lone pair LP, which is most active in γ -TeO₂ and probably in α -TeO₂ glass (Fig. 5.13 (a)). The lone pair activity, measured by the magnitude of the lone pair vector $|\mathbf{E}|$, depends on Te-O distance (r) and the angles (θ) between each each Te-O bond. In the crystals, both r and θ can be obtained and the lone pair activity can be studied. In the glasses however, not enough information can be extracted to study the lone-pair activity since r can only be estimated (whilst θ can only be obtained by simulation). From the point of view of r , the decrease of the O-O peak contribution at 2.5 Å is merely a reflection of the change of the [TeO₄] geometry upon transformation to a [TeO₃] unit.

As mentioned in Section 5.4.2, upon cooling from the melt, the lithium tellurite glasses crystallise into two crystal phases; γ -TeO₂ and Li₂Te₂O₅ (α -phase) therefore the structure of the glasses might be close to that of these crystals. Fig. 5.14 shows a comparison of the $T(r)$ for the null glasses with the $T(r)$ of γ -TeO₂ and β -Li₂Te₂O₅. β -Li₂Te₂O₅ is chosen over α -Li₂Te₂O₅ because it is the high temperature polymorph [10] and therefore likely to have a structure more similar to the glasses. These $T(r)$'s were simulated using XTAL [19] using the atomic displacement parameters herein [20]. The leading edge for $T(r)$ of the null glasses for the lower Li₂O contents is similar to that in γ -TeO₂ and, as more Li₂O is added,

it moves to fit the leading edge of $T(r)_{\text{Te-O}}$ in $\beta\text{-Li}_2\text{Te}_2\text{O}_5$. This supports the Raman and DTA results regarding the formation of these two crystal structures and the proximity of the glass structures to them. These $T(r)$'s were then scaled according to the equation

$$x\text{Li}_2\text{O} \cdot (100-x)\text{TeO}_2 \rightarrow x(\beta\text{-Li}_2\text{Te}_2\text{O}_5) + (100-3x)(\gamma\text{-TeO}_2) \quad 5.3$$

Reasonable fits were achieved for the shorter average distances but not for the longer Te-O distances. This is expected since it should be noted that the longer ($> 2 \text{ \AA}$) Te-O average

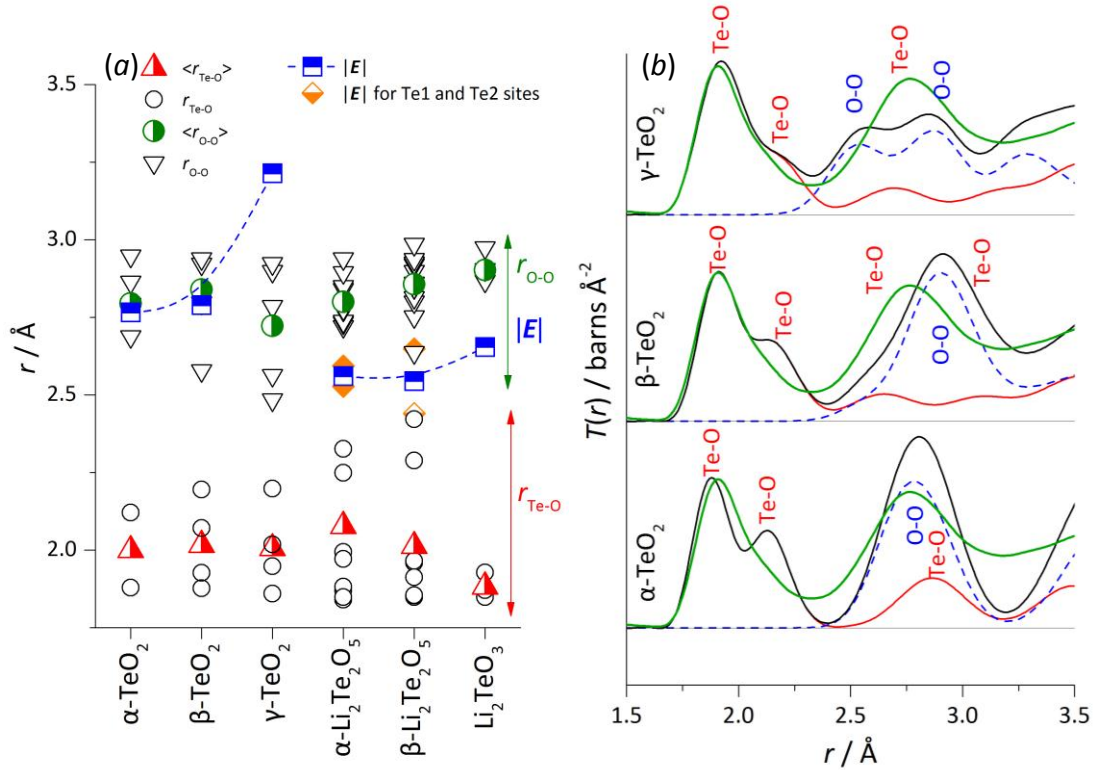


Figure 5.13: (a) Te-O and O-O distances, and the magnitude of lone-pair vectors found in $\alpha\text{-TeO}_2$, $\beta\text{-TeO}_2$, $\gamma\text{-TeO}_2$, $\alpha\text{-Li}_2\text{Te}_2\text{O}_5$, $\beta\text{-Li}_2\text{Te}_2\text{O}_5$, and Li_2TeO_3 crystal phases; (b) Comparison of $T(r)$ for $\alpha\text{-TeO}_2$ (green solid line) to the simulated $T(r)$'s for the TeO_2 polymorphs [Barney et al., to be published].

distance in the glasses (with maximum 30 mol% modifier) is much shorter than the value in $\beta\text{-Li}_2\text{Te}_2\text{O}_5$ (with the value of 33.33 mol% modifier) (Note: The average long r_{TeO} distance increases from $\alpha\text{-TeO}_2$ (2.125 \AA) to $\beta\text{-TeO}_2$ (2.135 \AA) to $\gamma\text{-TeO}_2$ (2.142 \AA) to $\alpha\text{-Li}_2\text{Te}_2\text{O}_5$ (2.197 \AA) to $\beta\text{-Li}_2\text{Te}_2\text{O}_5$ (2.353 \AA) and then it goes way beyond 3 \AA in Li_2TeO_3)

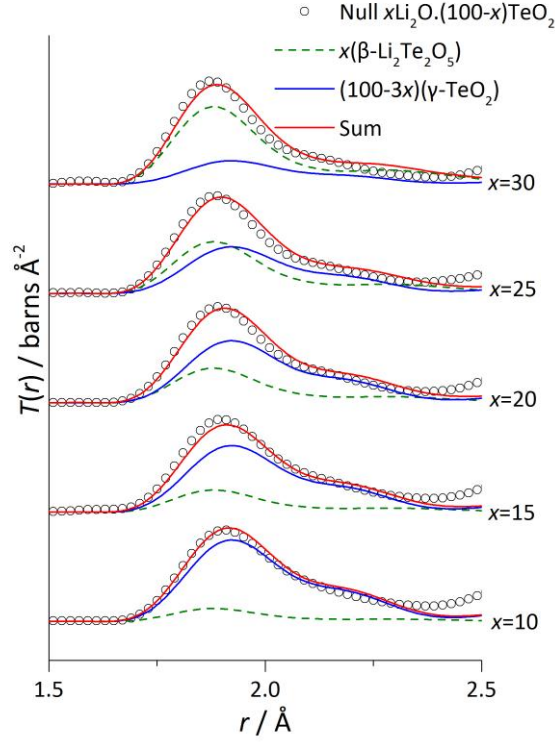


Figure 5.14: Approximation of $^{Null}T(r)$ to γ -TeO₂ and β -Li₂Te₂O₅. $T(r)_{Te-O}$ partials for the glasses, γ -TeO₂ crystal, and β -Li₂Te₂O₅ crystals are shown in open circle, blue, and dashed green respectively. Simulated $T(r)_{Te-O}$ for the glasses (red), simulated from the mixture of the crystals.

5.4.3 Parameterising complex Te-O distances

When measuring the average n_{TeO} of the glasses using integration, the difficulty in determining a proper cut-off radius for the first coordination sphere of tellurium to oxygen arises. This is due to the asymmetric distribution of tellurium-oxygen distances and the overlap between the upper limit of the first Te-O coordination sphere and the lower limit of the second Te-O coordination sphere which is enveloped within the oxygen-oxygen distance distribution centred at about 2.8 Å. In pure TeO₂ glass, Barney *et al.* arbitrarily fitted the first peak using the leading edge, took the residual from the first peak, and then fitted a second peak from the leading edge of the residual. The residual from the first and second peaks were fitted simultaneously with two Lorch-modified Gaussians to represent a third Te-O peak and the combined O-O peaks [3].

Fig. 5.15 shows an example of the fitting process for the 10^{Null}Li₂O-90TeO₂ sample. The same process was applied for the rest of the samples. The fitting, by manual alteration of parameters, uses three Lorch-modified Gaussian peaks to represent 3 arbitrary Te-O distances. In the figure, the cut-off radius for the third peak was at 2.36 Å, consistent with the value found in crystalline TeO₂. These same three Te-O peaks can be used to fit the $T(r)$ for the lower Li₂O contents ($x = 10$ and 15 mol%) because the environment of tellurium in

these glasses (i.e. the $r = 1.70$ to 2.25 Å region) seems largely unchanged compared to the $T(r)$ from the amorphous TeO_2 . The three and four-coordinated tellurium species in these glasses are present in the same approximate proportions as they are in pure TeO_2 glass. This is consistent with the TeO_2 Model which states that, at these compositions, there are enough terminal oxygens present to satisfy the bond valence requirement of the modifier cations without the need for transforming a $[\text{TeO}_4]$ unit to a $[\text{TeO}_3]$ unit to create a non-bridging oxygen [3].

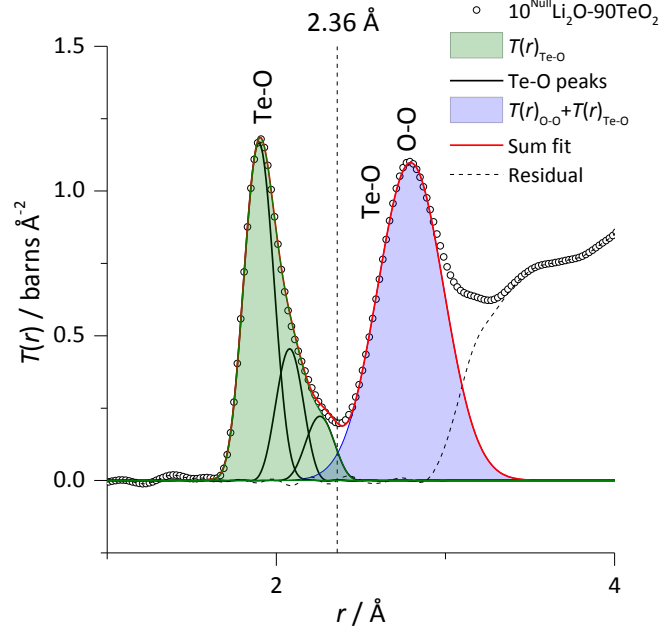


Figure 5.15: Peak fitting of the correlation function for $x = 10$ mol% (null $\text{Li}_2\text{O}-\text{TeO}_2$ glass) with three (arbitrary) Gaussians convoluted with the Lorch modification function [21]. For simplicity, O-O distribution is represented by a Gaussian of which also contains longer Te-O distances.

The change in the tellurium environment, as a result of adding Li_2O , is evident from the change of the peak shape of the Te-O correlation showing systematic increase in the proportion of shorter Te-O distances (centred at 1.82 Å) and decrease in the proportion of longer distances (centred at 2.02 Å) with respect to the amorphous TeO_2 total correlation function. The shorter and longer distances are consistent with the distances of the three and four coordinated tellurium species found in Li_2TeO_3 (1.85 Å, 1.87 Å, and 1.93 Å) or $\alpha\text{-Li}_2\text{Te}_2\text{O}_5$ (1.84 Å, 1.85 Å, 1.87 Å, 1.88 Å, and 1.97 Å) and $\gamma\text{-TeO}_2$ (1.86 Å, 1.95 Å, 2.02 Å, and 2.20 Å) respectively. This suggests that, when modifier is added and the bond valence of the modifier cation is unsatisfied, the 2.02 Å long bond (in $\gamma\text{-TeO}_2$) in four coordinated tellurium is broken leaving a three-coordinated tellurium with a shorter 1.82 Å bond (as in $\text{Li}_2\text{Te}_2\text{O}_5$ or Li_2TeO_3). The formation of the three-coordinated tellurium was also reported in sodium tellurite (^{125}Te NMR) [22] and potassium tellurite (neutron diffraction) [3] glasses. We have

previously established that, at low Li_2O contents, the TeO environment in those compositions is very similar to each other up to $r = 2.33 \text{ \AA}$. This r -cut-off is in fact, the minimum point of $T(r)$ between the first and second coordination peaks in pure TeO_2 glass. The minimum points are however at slightly longer distances in Li_2O - TeO_2 glasses, ranging from 2.36 to 2.37 \AA . This is consistent with the trend observed in the evolution of the long r from $[\text{TeO}_4]$, to $[\text{TeO}_3]$ via $[\text{TeO}_{3+1}]$ units in lithium tellurite crystals (Section 4.3.2). In other words Li_2O is affecting the Te environment by increasing its average long TeO distance.

The value of average n_{TeO} is obtained by integration of $T(r)$ since fewer errors are introduced into the process. However, the distribution of Te-O distances in the first coordination shell (area marked green in Fig. 5.15) overlaps with the average O-O distance distribution and the longer Te-O distance distribution (in second coordination shell) giving rise to uncertainty in determining $r_{\text{cut-off}}$ for the integral limit. The peak at $r \sim 2.8 \text{ \AA}$ is often fitted with one symmetric Gaussian to represent one broad average oxygen-oxygen distance distribution (which also includes the second coordination sphere Te-O distances) and information obtained from this peak was used to refine the cut-off radius for integration. As seen in Fig. 5.15, the integral limit is set at 2.36 \AA . In Fig 5.16, the trend in average n_{TeO} values obtained for the melt-quenched lithium tellurite glasses is consistent with the model based on a series of roller-quenched potassium tellurite glasses [3]; the average n_{TeO} is constant for $x \leq 15 \text{ mol\%}$ and decreases linearly for $x > 15 \text{ mol\%}$ as a function of x . However the value of the average n_{TeO} in the lithium tellurite glasses is slightly (but measurably) greater than that reported in the potassium tellurite glasses.

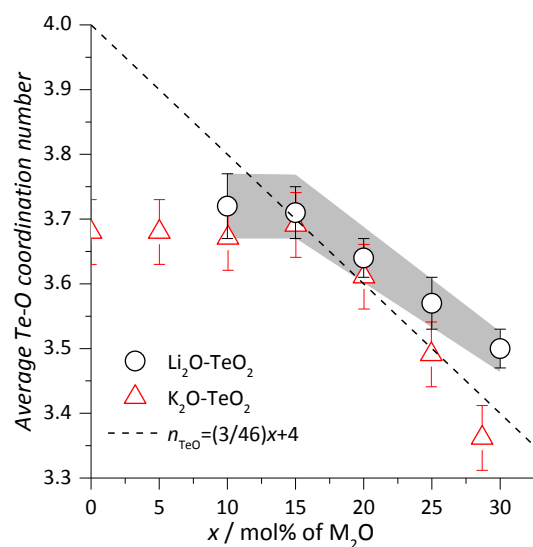


Figure 5.16: Average tellurium to oxygen coordination number (n_{TeO}) as a function of Li_2O content, obtained by integration, compared to the values obtained in K_2O - TeO_2 glasses [3]. The error for the average $n_{\text{TeO}}(\text{Li})$ is shaded in grey.

According to the TeO_2 Model (assuming only three and four-coordinated tellurium species present in the system), the value of the average n_{TeO} in a- TeO_2 of 3.68(4) corresponds to about one-third ($32 \pm 6\%$) of three-coordinated tellurium and two-thirds ($68 \pm 6\%$) of four coordinated tellurium. This value does not change until x is about 15 mol%. In the lithium tellurite glasses the aforementioned constant average n_{TeO} for $x \leq 15$ mol% is 3.70(4), which is within the error of 3.68(5). This value however, corresponds to a slightly different percentages of 30% of three-coordinated tellurium atoms and 70% of four-coordinated tellurium atoms. A difference in the average n_{TeO} values may possibly be explained by reference to the Raman study on lithium tellurite glasses by Tatsumisago [18] which concluded that the proportion of three-coordinated tellurium units increases with temperature and for a lithium tellurite in the liquid state, three-coordinated tellurium units are present at a much higher proportion, relative to the four-coordinated tellurium units, compared with glass of the same composition. The more slowly cooled, melt-quenched lithium tellurite samples of the current study show greater reversion of $[\text{TeO}_3]$ to $[\text{TeO}_4]$ and hence a higher value of the average n_{TeO} . The effect of quenching rate on the coordination number is also reported in other glass systems [23-25].

5.4.4 Extension of the TeO_2 model

In the $\text{K}_2\text{O}-\text{TeO}_2$ model, the O1 unit represents an oxygen atom bonded to one tellurium atom, regardless of (a) whether it is a charged NBO or a neutral terminal TO atom and (b) the nature of the tellurium environment, i.e. $[\text{TeO}_4]$ or $[\text{TeO}_3]$ polyhedron. For example the O1 in $\text{TeO}_{3/2}\text{O}^-$, $\text{TeO}_{1/2}\text{OO}^-$, $\text{TeO}_{2/2}\text{O}$, and $\text{TeO}_{1/2}(\text{O}^{2-})$ are treated as similar and having the same bond valency of 1.5 v.u. – a value consistent with $\text{K}_2\text{Te}_4\text{O}_9$ and K_2TeO_3 ($\text{TeO}_{3/2}\text{O}^-$, and $\text{TeO}_{1/2}\text{OO}^-$) and gaseous TeO_2 (for the $\text{TeO}_{2/2}\text{O}$ unit).

Table 5.8: Approximated bond parameters of Te-O1 in the lithium tellurite glasses as in related phases of liquid TeO_2 and lithium tellurite crystals.

Unit	Bond	Te-O bond valence / v.u	Average number of bonds to Li		Taken from
			For $n_{\text{LiO}} = 4$	For $n_{\text{LiO}} = 5$	
O2	--Te--O--Te--	-	-	-	-
O1a	--Te=O	1.5	2	2.5	Gaseous TeO_2 [26-27]
O1b	--Te--O $^-$	1.4	2.36	3	$[\text{TeO}_4]$ in $\text{Li}_2\text{Te}_2\text{O}_5$ [10]
O1c	--Te=O	1.3	2.84	3.5	$[\text{TeO}_3]$ in Li_2TeO_3 [28]

In lithium tellurites (as discussed in Chapter 4) however, the Te-O1 bond lengths (and hence the bond valence) do differ in $[\text{TeO}_4]^-$ and $[\text{TeO}_3]^-$ units and therefore 3 types of O1 must be considered: O1a, similar to O1 as in the $\text{K}_2\text{O}-\text{TeO}_2$ Model, attributed to the terminal oxygen

(Te=O) present in pure TeO₂ glass which is retained from the melt; O1b, an NBO bonded to a Te in [TeO₄]⁻ as found in Li₂Te₂O₅ crystals; and O1c, a resonance of NBO↔TO type of oxygen atom, bonded to a Te in [TeO₃]²⁻ as found in Li₂TeO₃ crystal, as summarised in Table 5.8. Adjusting the bond valence values of Te-O1 accordingly, can affect the average number of modifying cation (in this case Li⁺) around each of them.

5.4.4.1 Plateau region: $x < 15$ mol%

In Fig. 5.17, by closely examining the plateau region, the average n_{TeO} value for $x < 15$ mol% could either be 3.68 (blue), 3.70 (red), or 3.71 (green) depending on which datapoints are used for the linear fitting. The average n_{TeO} value of 3.68(4), (blue) corresponds to the fit of a-TeO₂ and xK₂O.(1-x)TeO₂ ($x = 5, 10$, and 15 mol%) glasses (Fig. 5.16); the average n_{TeO} value of 3.70(4) (red) corresponds to the fit of a-TeO₂ and xLi₂O.(1-x)TeO₂ ($x = 10$ and 15 mol%) glasses; and the average n_{TeO} value of 3.71(4) (green) corresponds to the fit of xLi₂O.(1-x)TeO₂ ($x = 10$ and 15 mol%).

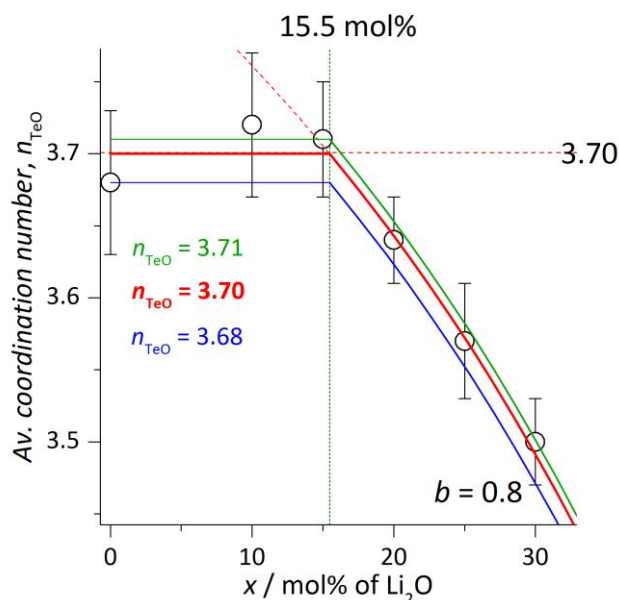


Figure 5.17: The selection of the average n_{TeO} for $x < 15$ mol% (plateau region) and its effect on the average n_{TeO} fit quality for $x > 15$ mol% (post-plateau region).

Since the average n_{TeO} (plateau) affects the fractions of the Te3, Te4, O1(O1a, O1b, and O1c), and O2 units present in the glasses (Section 4.6.1), the selected average n_{TeO} value would also affect the determination of the deviation composition (x_D). The agreement between x_D and the quality of the average n_{TeO} fit for $x > 15$ mol% can be used to estimate the reliability of the chosen average n_{TeO} value for $x < 15$ mol% region.

For all the fits, the x_D (composition in mol% at $N'/N = 0.18$ ($0.18\text{Li}_2\text{O}-1\text{TeO}_2$)) is achieved when all O1a, and O1b are used up for providing coordination to Li, as discussed in Section 4.6.2. x_D is obtained at 15.5 mol% of Li_2O (Section 4.6.2) as shown in Fig. 5.17. x_D is used in determining the average n_{TeO} fit for $x > 15$ mol% according to this equation

$$n_{\text{TeO}}(x \text{ post} - \text{plateau}) = n_{\text{TeO}}(x \text{ plateau}) - \left[b^* \left(\frac{x}{100-x} - \frac{x_D}{100-x_D} \right) \right] \quad 5.4$$

As seen in the figure, the average $n_{\text{TeO}} = 3.70$ gives the most reasonable fits for both regions of $x < 15$ and $x > 15$ mol% whereas the average $n_{\text{TeO}} = 3.68$ does not agree with the experimental data for both regions. The average n_{TeO} for the $\text{Li}_2\text{O}-\text{TeO}_2$ glasses for $x < 15$ mol% is therefore selected to be 3.70(4). This value is within the experimental error of the value of 3.68(4) which was reported in the TeO_2 Model. However, if it is taken as being correct, the value of n_{TeO} in a system with R unit of Li_2O and 1 unit of TeO_2 ($R\text{Li}_2\text{O}-1\text{TeO}_2$) of 3.70 corresponds to

$$\begin{aligned} \text{In glass with } R\text{Li}_2\text{O and } 1\text{TeO}_2 \text{ units} = \\ 0.3 \text{ units of Te3} + 0.7 \text{ units of Te4} + \\ 0.3 \text{ units of O1a} + 2R \text{ units of O1b} + \\ (1.7-R) \text{ units of O2} + 2R \text{ units of Li} \end{aligned} \quad 5.5$$

and, according to these fractions of $[\text{TeO}_4]$ and $[\text{TeO}_3]$ units, the maximum value of x before any $[\text{TeO}_4]$ unit need be converted to $[\text{TeO}_3]$ would be about 15.5 mol% ($R = 0.18$). This is based on the assumption that the deviation composition is achieved when

$$4(\text{units of Li}) \leftrightarrow 2(\text{units of O1a}) + 2.36(\text{units of O1b}) \quad 5.6$$

"All bonds are used up in the system when (LEFT SIDE) 1 Li^+ is coordinated to 4 oxygen atoms and (RIGHT SIDE) Each of the O1a and O1b units are connected to an average of 2 and 2.36 Li^+ ions respectively)

i.e. where a lithium is coordinated to 4 oxygen atoms, and the terminal oxygen (O1a) and non-bridging oxygen in $[\text{TeO}_4]^-$ unit (O1b) types of oxygen can, on average, coordinate 2 and 2.36 lithium atoms respectively (Table 5.8). This is based on the bond valence calculation of the O1 type of oxygen found in $\alpha\text{-Li}_2\text{Te}_2\text{O}_5$ and $\beta\text{-Li}_2\text{Te}_2\text{O}_5$.

As seen in Eqn 5.6, it is assumed that only O1 type of oxygen is providing coordination to Li^+ for the deviation composition x_D to be at such value. Bonding to O2 type of oxygen is not uncommon as evidenced in the lithium tellurite crystals of $\alpha\text{-Li}_2\text{Te}_2\text{O}_5$ and $\beta\text{-Li}_2\text{Te}_2\text{O}_5$, therefore a more appropriate representation of the equality in Eqn 5.6 is

$$4(\text{units of Li}) \leftrightarrow 2(\text{units of O1a}) + 2.36(\text{units of O1b}) + p(\text{units of O2}) \quad 5.7$$

where p is the average number of Li atoms bonded to O2 type of oxygen. The constant p can be determined experimentally from the post-plateau $n_{\text{TeO}}(x)$ ($x = 20, 25$, and 30 mol%).

5.4.4.2 Post-plateau region: $x > 15$ mol%

The deviation composition of 15.5 mol% of Li_2O corresponds to the value of $R \approx 0.18$ ($R\text{Li}_2\text{O}-1\text{TeO}_2$). Therefore, at any composition in the plateau region, the total nominal composition of the system would be

$$(0.18 + M)\text{Li}_2\text{O}-1\text{TeO}_2 \quad 5.8$$

where M is the further unit of Li_2O added to the glass network. The M term in x corresponding to $x\text{Li}_2\text{O}-(100-x)\text{TeO}_2$ is

$$M = \frac{x}{100-x} - 0.18 \quad 5.9$$

In addition to the existing $[\text{TeO}_n]$ units present as in Eqn. 5.5, every addition of M Li_2O unit increases the $[\text{TeO}_3]$ units by Mb and decreases the $[\text{TeO}_4]$ units by Mb as in

$$N_{\text{Te}} = [0.3 + Mb]_{N_{\text{Te}3}} + [0.7 - Mb]_{N_{\text{Te}4}} \quad 5.10$$

And from this, n_{TeO} can be simplified as

$$n_{\text{TeO}} = 3.70 - Mb \quad 5.11$$

As shown in Fig. 5.18, a b value of 0.8 fits the experimental data. This can be compared with the value of $b = 1$ used by Barney *et al.* [3] in discussing the potassium tellurite glasses. From Eqn 5.6, the number of bonds which O1 could take can be written as

$$N_{\text{O}1} \leftrightarrow 2*(0.3)_{\text{O}1a} + 2.36*(2)_{\text{O}1b} + 2.84*(Mb)_{\text{O}1c} \quad 5.12$$

The factor of 2.84 represents the average number of lithium atoms bonded to the O1c, derived from the bond valence calculation of O1c found in Li_2TeO_3 as discussed in Section 4.3.4. The fit of the average n_{TeO} values for $x > 15$ mol% from Eqn. 5.12 is shown in Fig. 5.18

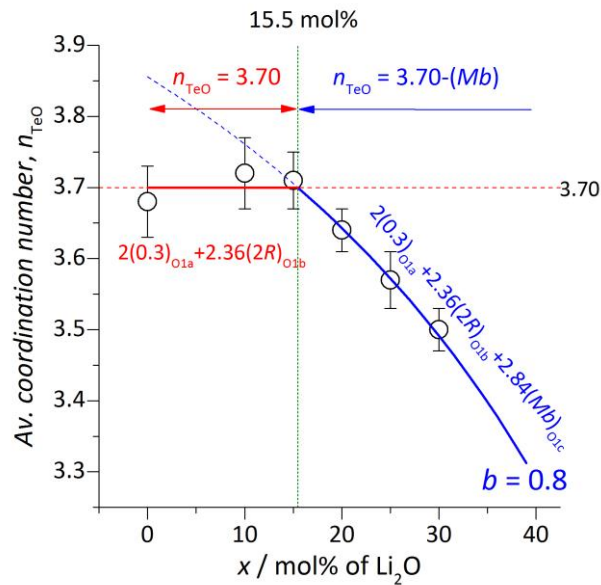


Figure 5.18: The TeO_2 Model for $\text{Li}_2\text{O}-\text{TeO}_2$ system for plateau ($x < 15$ mol%) and post-plateau ($x > 15$ mol%) regions.

Eqn 5.13 describes the average $n_{\text{TeO}}(x)$ for $\text{Li}_2\text{O}-\text{TeO}_2$ system. The average n_{TeO} is divided into two regions: plateau ($x < 15.5$ mol%) and post-plateau ($x > 15.5$ mol%). 15.5 mol% is called the deviation composition, x_D , the composition where the number of available Li-O bonds from O1 type of oxygen matches the number of required bonds for Li atoms. In the plateau region, $n_{\text{TeO}}(x)$ is constant at the value of 3.70 whilst in the post-plateau region, $n_{\text{TeO}}(x)$ changes as a function of x and a constant b ($b = 0.8$).

$$n_{\text{TeO}}(x) = \begin{cases} 3.70 & ; 0 < x < 15.5 \text{ mol\%} \\ 3.70 - \left(\frac{x}{100-x} - 0.18 \right) b & ; x > 15.5 \text{ mol\%, } b = 0.8 \end{cases} \quad 5.13$$

Where $(x/(100-x) - 15.5 \text{ mol\%})$ is M minus the further number of units added after x_D (15.5 mol%), and total unit of TeO_2 is always unity in the system. According to Eqn 5.12, the number of available Li-O bonds would be $2.36(2) + 2.84(0.8) = 6.992$ Li-O bonds which is still insufficient since the total number of required bonds is 8 Li-O bonds. This indicates that some contribution of bonds from O2 is required.

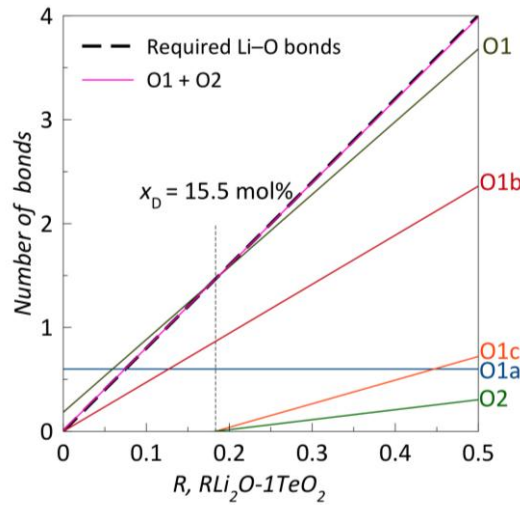


Figure 5.19: The number of required Li-O bonds in both plateau and post-plateau regions and the contribution from O1 (O1a, O1b, O1c) and O2 type of oxygen atoms as a function of R unit of Li_2O in 1 unit of TeO_2 .

In Fig. 5.19, in the plateau region, the number of bonds available for bonding to lithium from O1a and O1b ($\text{O1} = \text{O1a} + \text{O1b}$) exceeds the number of required bonds. This means that there is sufficient O1 sites for bonding with Li^+ ion without the necessity to create more O1 sites. At 15.5 mol%, the O1 line and the “required Li-O bonds” line intercept, indicating that at this composition, the number of bonds provided by O1 sites matches the number of the required bonds for the Li^+ ions. After this composition, the number of available bonds is no longer sufficient, hence O1c must be created by transformation of $[\text{TeO}_4]^- \rightarrow [\text{TeO}_3]^-$ units. This causes the average n_{TeO} to decrease beyond 15.5 mol%. The average n_{TeO} values experimentally obtained are consistent with a b value of 0.8, b being the rate of

transformation of $[\text{TeO}_4]^-$ to $[\text{TeO}_3]^-$ unit. This value is, however, still not sufficient to supply the number of bonds, meaning that the remainder must come from O2. In the plateau region it is not possible to mathematically determine the presence of this O2 species since O1b is highly excessive from the bridge-breaking process which occurs upon the introduction of Li_2O into the TeO_2 network. Therefore it is assumed that, up to 15.5 mol%, 59% of the bonds come from O1b and 41 % come from O1a (assumed based on the known contribution of bonds at 15.5%). Beyond this composition, the percentage of each unit starts to vary accordingly as O1c units are created. However the number of available bonds from O1c is insufficient therefore Li has to be bonded to O2. Taking the difference between the number of bonds required and the available bonds from O1, the contribution from O2 type of oxygen is obtained as follows

$$8R_{\text{Li}} \leftrightarrow 2(0.3)_{\text{O1a}} + 2.36(2R)_{\text{O1b}} + 2.84(Mb)_{\text{O1c}} + 1.02(Mb)_{\text{O2}} \quad 5.14$$

Where for every \underline{R} unit of Li_2O added, 2×4 Li-O bonds are required"

This equation suggests that the number of bonds from O2 is a function of b , as in O1c. This would therefore mean that, in $x < 15$ mol%, O2 provides no contribution, hence the p constant as in Eqn. 5.7 is zero. Since $M = R - 0.18$ units then, from Eqn. 5.14, it can be said that the third and fourth terms contribute no value for $x < 15.5$ mol% and only contribute for $x > 15.5$ mol%. The number of available Li-O bonds in both regions can be represented as in Eqn. 5.15

$$\text{Li-O bonds} = \begin{pmatrix} 2(0.3)_{\text{O1a}} + 2.36(2R)_{\text{O1b}} & ; \quad 0 < x < 15.5 \text{ mol\%} \\ 2(0.3)_{\text{O1a}} + 2.36(2R)_{\text{O1b}} + 2.84(Mb)_{\text{O1c}} + 1.02(Mb)_{\text{O2}} & ; \quad x > 15.5 \text{ mol\%, } b = 0.8 \end{pmatrix} \quad 5.15$$

Where $R = x / (100 + x)$ and $M = R - 0.18$

5.4.5 Lithium environment

The lithium ion, Li^+ , takes various coordination numbers in crystals: 3, 4, 5, 6, and 8 (within 2.7 Å, arbitrarily chosen). Whilst $n_{\text{LiO}} = 4$ is the most common coordination number (generally tetrahedral, with mean Li-O distance of 1.96(3) Å), the higher coordination of 5 is seen in LiBO_2 [29]. Lithium has a weak disposition to form its preferred coordination polyhedron and often adopts the coordination number governed by the environment of the neighbouring groups with higher order of rigidity [30]. In zeolites, where there are various oxygen cages of different sizes, Li is free to adopt its preferred 4-coordination [30].

From Raman scattering studies, alkali metals have been reported to behave differently in SiO_2 and GeO_2 glass systems where Li has greater preference for associating with $\text{Q}^{(2)}$ species in germanates (where n_{GeO} changes with x rather than in silicates (where

n_{SiO} is maintained at 4 regardless of x) [31-33]. This simply suggests that the environment of a modifier cation is influenced by the environment of the glass former cation.

As shown in Fig. 5.20, in SiO_2 , n_{LiO} values were reported to be between 2.16 and 4 within 1.97 Å, [34-36] the lower n_{LiO} was reported by Hannon *et al.* suggesting clustering of Li in the silicate network [36]. In B_2O_3 systems, n_{LiO} values were reported to be between 4.2 and 4.9 with two distances of 1.97 and 2.03 Å and the Li atom was suggested to be in a distorted tetrahedral site [34, 37-39]. In phosphate glasses, n_{LiO} values were obtained by molecular dynamics and reported to be between 4 and 5 [40]. The average n_{LiO} has not been determined experimentally in tellurite glasses and is usually assumed to be 4 to enable the extraction of n_{TeO} [41-44]. M = Li, Na, and K were reported to have respective n_{MO} values of 4, 5, and 6 by Barney *et al.* for $x < 20$ mol% $x\text{M}_2\text{O} \cdot (100-x)\text{TeO}_2$ systems where Te was found to have a constant coordinaton number [20].

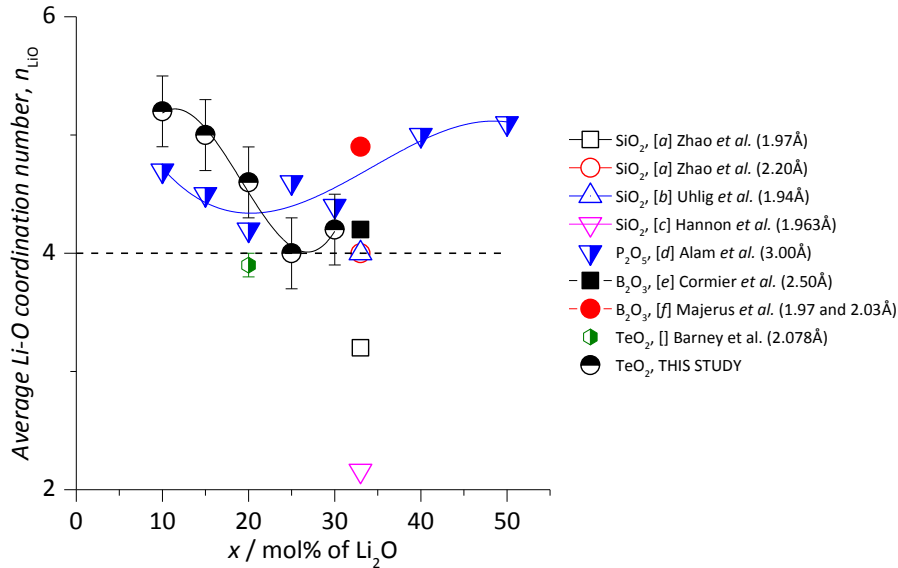


Figure 5.20: n_{LiO} in various glass formers. Legend: a [34], b[35], c[36], d[40], e[37], and f[38]. Ref: a, b, c, and f were obtained by isotope substitution neutron diffraction, d was obtained by molecular dynamics and e was obtained by the combination of natural neutron diffraction combined with molecular dynamics. Spline fits are included as guides to the eye.

Figure 5.11 shows the total correlation functions $T(r)$ for the natural glasses which contain lithium partials (of negative intensity with the exception of t_{LiLi}). The first Li-O partial is clearly seen by the reduction in total $T(r)$ intensity at about 2 Å. Correlation functions for the null glasses do not contain any information on the lithium environment, natural glasses however preserve this information and the lithium environment can be obtained by taking the difference between these two sets of data.

Fig. 5.21 shows the plot of $T(r)$ for both null and natural samples for all compositions with their respective difference plot (nat – null), which corresponds to the partial correlation function of lithium-oxygen in $\text{Li}_2\text{O}-\text{TeO}_2$ glasses.

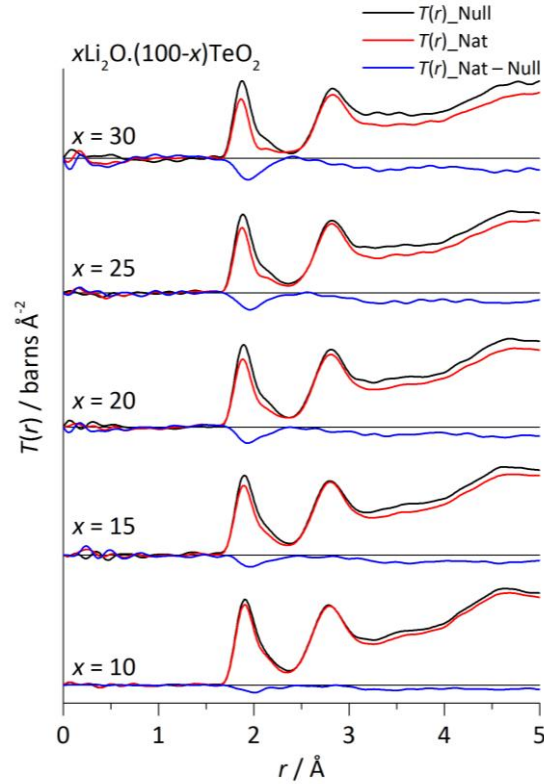


Figure 5.21: $T(r)$ of null (black) and natural (red) glasses and the difference (blue) representing the lithium partial correlation functions.

The region of interest including the Li-O distances is shown in Fig 5.22. The $T(r)_{\text{Li,O}}$ obtained can be fitted with two Gaussians covering the range from $r = 1.5$ to as high as 2.5 Å. Fit quality is guided by the residual's consistency with the noise in the signal. The peak parameters of the fit are shown in Table 5.9 along with the values for n_{LiO} obtained by integration of the two peaks, which are also plotted in Fig. 5.23.

Table 5.9: Peak parameters for Li-O pair correlation functions

x /mol%	Peak 1				Peak 2				n_{LiO}
	$r / \text{\AA}$	BV / v.u.	$\langle u_{\text{LiO}} \rangle^{1/2}$ / Å	n_{LiO}	$r / \text{\AA}$	BV / v.u.	$\langle u_{\text{LiO}} \rangle^{1/2}$ / Å	n_{LiO}	
10	1.982(2)	0.25	0.278(4)	3.94	2.291(4)	0.11	0.177(7)	1.24	5.18
15	1.968(3)	0.26	0.254(5)	3.94	2.224(8)	0.13	0.202(14)	1.11	5.05
20	1.954(3)	0.27	0.257(5)	3.96	2.184(7)	0.14	0.135(13)	0.62	4.58
25	1.976(3)	0.25	0.317(5)	3.99	2.385(31)	0.08	0.100(60)	0.08	4.07
30	1.954(2)	0.27	0.297(3)	3.99	2.195(10)	0.14	0.122(18)	0.18	4.17
Average	1.967(13)	0.26	0.281(27)	3.96(3)	2.233(53)	0.13	-	-	-

The value of n_{LiO} generally decreases as a function of Li_2O content in the glass; for $x = 10$, and 15 mol% of Li_2O , n_{LiO} is constant at $\sim 5.0(5)$, at 20 mol% it decreases to $n_{\text{LiO}} = \sim 4.5(5)$ and becomes $\sim 4.0(5)$ at $x = 25$, and 30 mol% of Li_2O . As seen in the figure, the first peak in all compositions, can be fitted with a principal peak (red peak, fixed position) centred at about 1.967(13), to contribute to the n_{LiO} value of 4. This distance is consistent with the mean $r_{\text{LiO}} = 1.979 \text{ \AA}$ for tetrahedral $[\text{LiO}_4]$ as observed in $\text{Li}_2\text{Te}_2\text{O}_5$ (α and β phases) and Li_2TeO_3 crystals Fig. 5.24.

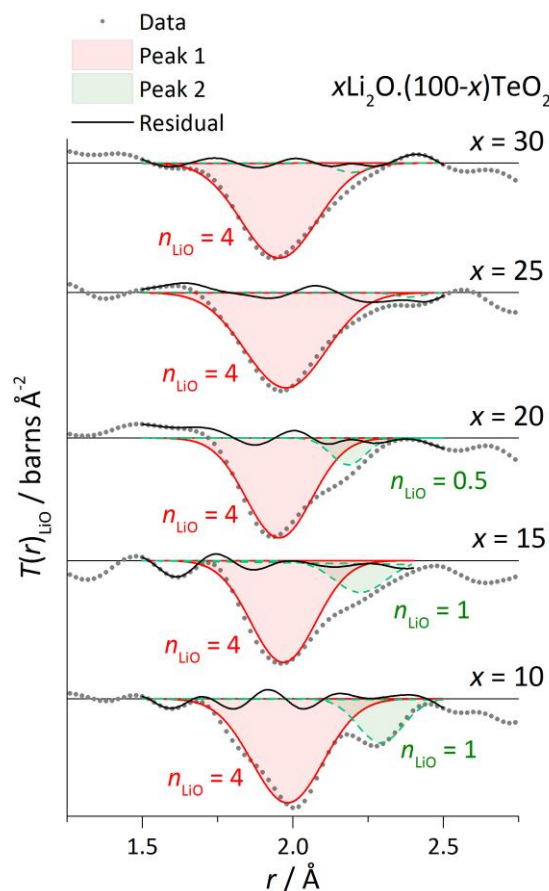


Figure 5.22: Difference plots stacked with fits. Dotted lines are the $T(r)$ for Li, O partials, red and green peaks are the fitted peaks, and solid black lines are the residuals of the fit. The red peak contributes to the n_{LiO} value of 4. n_{LiO} was obtained from the area of the $\text{Li}-\text{O}$ peak(s).

In the lower Li_2O compositions ($x = 10$, 15, and 20 mol%), there is a significant contribution from another peak at an average value of about 2.223(6) \AA (Table 5.9). The position of the second peak decreases slightly as x increases (for $x = 10$, 15, and 20 mol%). The average distance (2.223 \AA) does not correspond to $n_{\text{LiO}} = 5$ (2.061 \AA), however it is found in the 4-coordinated $\text{Li}-\text{O}$ polyhedron in the β - $\text{Li}_2\text{Te}_2\text{O}_5$ phase ($\sim 2.25 \text{ \AA}$). This indicates that at low Li_2O contents, the Li environment (up to the second coordination sphere) may be similar to that found in β - $\text{Li}_2\text{Te}_2\text{O}_5$.

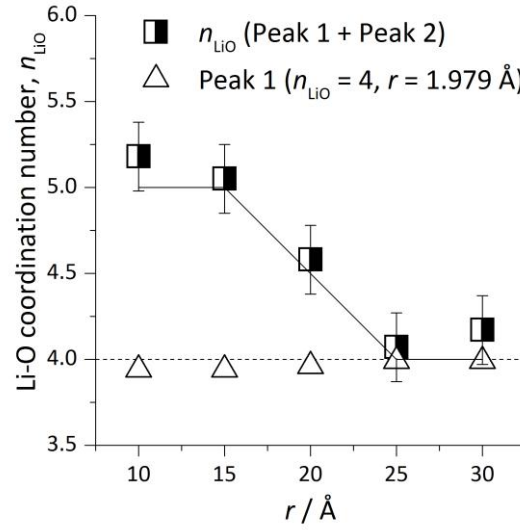


Figure 5.23: n_{LiO} obtained by means of peak fitting with two Gaussians at 2.00 and 2.25 Å. Higher n_{LiO} observed in $x = 10, 15$, and 20 mol% Li_2O is due to the contribution from the peak at 2.25 Å (r_{LiO} as seen in $\beta\text{-Li}_2\text{Te}_2\text{O}_5$ phase) Error bars are large due to poor signal to noise ratio because of the ^6Li absorption.

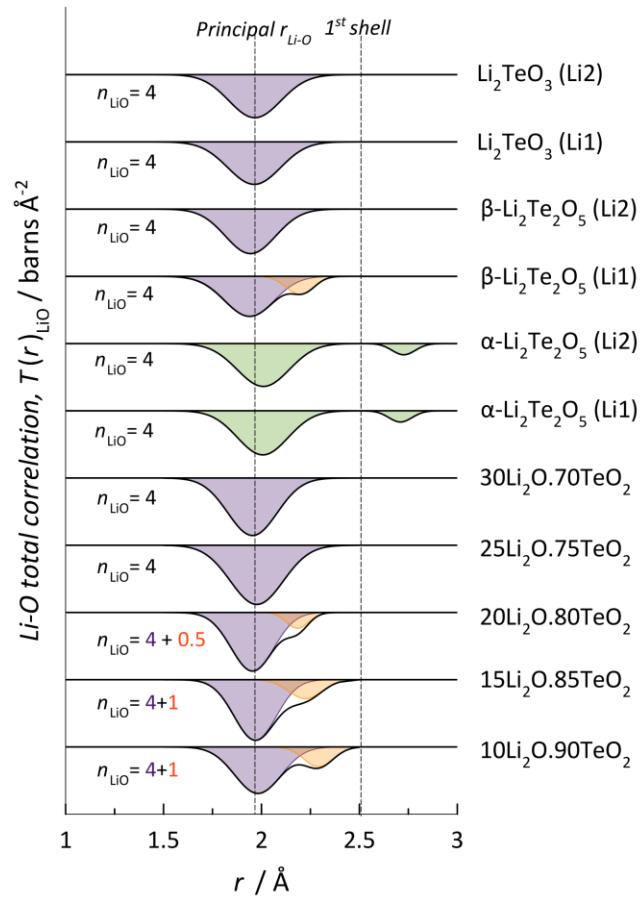


Figure 5.24: Comparison of r_{LiO} found in various lithium tellurite crystals as well as in Li_2O . Slight shift is observed.

The peak however is not seen in the higher Li_2O content group (compositionally more similar to Li_2TeO_3 crystal phase). This may support the previous inference that the glass structure is

similar to $\gamma\text{-TeO}_2$ and $\beta\text{-Li}_2\text{Te}_2\text{O}_5$. This second peak contributes values of approximately 1, 1, and 0.5 to n_{LiO} in $x = 10, 15$, and 20 mol% of Li_2O respectively. More accurate representation of $n_{\text{LiO}} = 5$ would be $4 + 1$ and $4 + 0.5$ for 4.5 (i.e. a mixture of 4 and $4+1$). (NB - 6-coordination is dominant for Li in Te(VI) crystals – i.e. lithium tellurates). The rather large error associated with n_{LiO} (± 0.5) results from taking the difference between two datasets where the signal-to-noise ratio is compromised by both the presence of the Te resonance and the neutron absorption due to ^6Li (which is particularly troublesome for the null scattering samples).

5.5 Conclusions

Two series of lithium tellurite glasses, $x\text{Li}_2\text{O} \cdot (100-x)\text{TeO}_2$ for $x = 10, 15, 20, 25$, and 30 mol% were prepared with natural and null lithium and these glass compositions were confirmed to be consistent with the nominal values by comparing the experimental density values with the ones in the literature. The average neutron scattering lengths of the null lithium tellurite glasses were calculated from compositions obtained using SIMS. A change in Te local environment can be inferred from the deviation in the property versus composition plots for density, molar volume and number density at ~ 15 mol% Li_2O .

Differential thermal analysis revealed two compositional regions of crystallisation for (a) $x = 10, 15$, and 20 mol% and (b) $x = 25$, and 30 mol%). Literature reports of crystallisation studies on $x = 20$ and 30 mol%, representing a member from each group, indicate crystallisation to give $\gamma\text{-TeO}_2 \rightarrow \alpha\text{-TeO}_2$, and $\beta\text{-Li}_2\text{Te}_2\text{O}_5$ respectively. Both $\gamma\text{-TeO}_2$ and $\alpha\text{-TeO}_2$ have only $[\text{TeO}_4]$ units and $\beta\text{-Li}_2\text{Te}_2\text{O}_5$ has only the TeO_{3+1} unit; an intermediate unit in the transformation of TeO_4 to TeO_3 (as found in Li_2TeO_3). The readiness of these glasses to form these phases indicates that they share similar local environments to the crystals formed. Therefore, in the lower Li_2O content glasses, the TeO_4 species of $\alpha\text{-TeO}_2$ or $\gamma\text{-TeO}_2$ dominate whilst, in the higher Li_2O contents group, the lower co-ordinated TeO_{3+1} as in $\alpha\text{-Li}_2\text{Te}_2\text{O}_5/\beta\text{-Li}_2\text{Te}_2\text{O}_5/\text{Li}_2\text{TeO}_3$ becomes more important. This is also supported by the similarity of the Raman peak manifolds of the lower Li_2O glasses to $\gamma\text{-TeO}_2$ and $\alpha\text{-TeO}_2$, and the higher Li_2O glasses to $\alpha\text{-Li}_2\text{Te}_2\text{O}_5$ and Li_2TeO_3 . Based on the total area of peaks assigned to Te-O vibrations from TeO_4 , compared to peaks from TeO_3 , the average coordination of number of tellurium to oxygen $^{\text{Raman}}n_{\text{TeO}}$ was obtained and found to decrease linearly as a function of Li_2O content and, extrapolation to $x = 0$ mol% gave an n_{TeO} value close to that reported for amorphous TeO_2 [3]. However, the $^{\text{Raman}}n_{\text{TeO}}$ behaviour as a function of Li_2O content did not replicate that observed for the K_2O system reported in that study. Raman

scattering is not necessarily directly quantitative and therefore cannot determine n_{TeO} with the precision obtainable from neutron diffraction.

Null lithium isotope neutron diffraction was employed to measure n_{TeO} accurately in the glasses. It was found that the Te environment in the lower lithium-content tellurite glasses are similar to the pure TeO_2 glass, whereas in the higher content, the shorter r_{TeO} corresponding to $[\text{TeO}_3]$ units becomes more apparent. This alone suggests that there is a change from $[\text{TeO}_4]$ to $[\text{TeO}_3]$ unit in the glasses as Li_2O is added. The $T(r)$ of $\gamma\text{-TeO}_2$ and $\beta\text{-Li}_2\text{Te}_2\text{O}_5$ were combined to achieve a reasonable approximation of the Te environments in the glasses as a mixture of those found in the crystals.

The average n_{TeO} values found are largely consistent with the model proposed by Barney *et al.* [3]; i.e. constant n_{TeO} for $x < 15$ mol% and decreasing linearly beyond this composition. However the values of n_{TeO} obtained are slightly higher than reported for the K_2O system. The TeO_2 Model assumes n_{TeO} is independent of the modifier ion size but it would appear that TeO_2 glasses modified by small Li^+ cations contain less $[\text{TeO}_3]$ than the equivalent K^+ glass for the same modifier content. One alternative factor that may contribute to this is the rate at which the glass was quenched. The $\text{Li}_2\text{O}\text{-TeO}_2$ glasses reported here were quenched relatively slowly (cooling of the crucible base), compared to the roller-quenched $\text{K}_2\text{O}\text{-TeO}_2$ glasses. Therefore the $\text{Li}_2\text{O}\text{-TeO}_2$ glass structure had more time to reorganize from that of the melt (reportedly containing more $[\text{TeO}_3]$).

For $x > 15$ mol%, the rate of transformation $[\text{TeO}_4]^-$ to $[\text{TeO}_3]^-$ was seen to be slower in the presence of Li_2O rather than K_2O . Li, being smaller in size, hence having smaller average coordination number than K, ($n_{\text{LiO}} < n_{\text{KO}}$), could mean that Li^+ is more mobile in the glass networks and could satisfy its bond valence requirement with less necessity for conversion of $[\text{TeO}_4]^-$ units to $[\text{TeO}_3]^-$ units to provide oxygen atoms for bonding.

Using the natural-null difference neutron diffraction technique, the average n_{LiO} was extracted from the glasses. The lithium-oxygen distribution in each composition has one principal peak at about 1.97 Å (close to the average Li-O distance in tetrahedral $[\text{LiO}_4]$) and contributing 4.0(5) to the average n_{LiO} . In the lower Li_2O contents ($x = 10, 15$, and 20) a secondary Li-O peak at about an average value of 2.23 Å increases the total average n_{LiO} to 5, 5, and 4.5 for $x = 10, 15$, and 20, respectively. The average position of the secondary peak is similar to an Li1-O distance of the high temperature $\beta\text{-Li}_2\text{Te}_2\text{O}_5$ crystal phase. In general, Li in small quantities ($x < 15$ mol%) in $\text{Li}_2\text{O}\text{-TeO}_2$ glasses has a local structure similar to $\beta\text{-Li}_2\text{Te}_2\text{O}_5$ with 2 resolved r_{LiO} peaks at 1.97 and 2.23 Å ($n_{\text{LiO}} > 4$) whereas in larger quantities ($x > 15$)

mol%) there is only one r_{LiO} peak at about 1.97 Å ($n_{\text{LiO}} = 4$) such as found in the Li_2TeO_3 crystal phase.

The quality of the $\text{Li}_2\text{O}-\text{TeO}_2$ neutron diffraction data is reduced by the ^6Li neutron absorption and ^{128}Te resonance phenomenon at 2.2 eV which lower the signal-to-noise ratio and limit Q_{max} to 35 Å⁻¹, hence lowering the resolution of $T(r)$. These limitations reduce the possibility of resolving the Te-O distance in the $[\text{TeO}_3]$ unit. To be able to do so would help us to parameterise the complex asymmetric Te-O distances better and to understand the changes during $[\text{TeO}_4] \leftrightarrow [\text{TeO}_4]^-$ and $[\text{TeO}_4]^- \leftrightarrow [\text{TeO}_3]^-$ transformation processes.

5.6 References

1. In *SciGlass Professional 7.3*, ITC Inc.: 2008.
2. Narayanan, R. A. *Physical Review B* 2001, 64, 134207.
3. Barney, E. R., Hannon, A. C., Holland, D., Umesaki, N., Tatsumisago, M., Orman, R. G., Feller, S. *Journal of Physical Chemistry Letters* 2013, 4, 2312-2316.
4. Zachariasen, W. H. *Journal of the American Chemical Society* 1932, 54, 3841-3851.
5. Araujo, E., Idalgo, E., Moraes, A., Souza Filho, A., Mendes Filho, J. *Modern Physics Letters B* 2010, 24, 527-537.
6. Taniguchi, T., Inoue, S., Mitsunashi, T., Nukui, A. *Journal of Applied Crystallography* 2000, 33, 64-70.
7. Chagraoui, A., Ramzi, Z., Tairi, A., Mandil, A., Talibouridah, M., Ajebli, K., Abboud, Y. *Journal of Materials Processing Technology* 2009, 209, 3111-3116.
8. Chagraoui, A., Chakib, A., Mandil, A., Tairi, A., Ramzi, Z., Benmokhtar, S. *Scripta Materialia* 2007, 56, 93-96.
9. Chagraoui, A., Tairi, A., Ajebli, K., Bensaid, H., Moussaoui, A. *Journal of Alloys and Compounds* 2010, 495, 67-71.
10. Cachau-Herreillat, D., Norbert, A., Maurin, M., Philippot, E. *Journal of Solid State Chemistry* 1981, 37, 352-361.
11. Tatsumisago, M., Minami, T., Kowada, Y., Adachi, H. *Physics and Chemistry of Glasses* 1994, 35, 89-97.
12. Moynihan, C. T., Easteal, A. J., BOLT, M. A., Tucker, J. *Journal of the American Ceramic Society* 1976, 59, 12-16.
13. Moynihan, C. T., Easteal, A. J., Wilder, J., Tucker, J. *Journal of Physical Chemistry* 1974, 78, 2673-2677.
14. Gibbs, J. H., DiMarzio, E. A. *The Journal of Chemical Physics* 1958, 28, 373-383.
15. Kalampounias, A. G., Boghosian, S. *Vibrational Spectroscopy* 2012, 59, 18-22.
16. Sekiya, T., Mochida, N., Ohtsuka, A., Tonokawa, M. *Journal of Non-Crystalline Solids* 1992, 144, 128-144.
17. Siebert, H. *Zeitschrift für anorganische und allgemeine Chemie* 1954, 275, 225-240.
18. Tatsumisago, M., Lee, S.-K., Minami, T., Kowada, Y. *Journal of Non-Crystalline Solids* 1994, 177, 154-163.
19. Hannon, A., *Xtal: A Program for Calculating Interatomic Distances and Coordination Numbers for Model Structures*; Rutherford Appleton Laboratory, 1993.
20. Barney, E., Hannon, A., Holland, D., Umesaki, N., Tatsumisago, M. *Journal of Non-Crystalline Solids* 2015, 414, 33-41.
21. Lorch, E. *Journal of Physics C: Solid State Physics* 1969, 2, 229.
22. Holland, D., Bailey, J., Ward, G., Turner, B., Tierney, P., Dupree, R. *Solid State Nuclear Magnetic Resonance* 2005, 27, 16-27.

23. Wu, J., Stebbins, J. F. *Journal of Non-Crystalline Solids* 2013, 362, 73-81.
24. Stebbins, J. F., Dubinsky, E. V., Kanehashi, K., Kelsey, K. E. *Geochimica et Cosmochimica Acta* 2008, 72, 910-925.
25. Wu, J., Stebbins, J. F. *Journal of Non-Crystalline Solids* 2010, 356, 2097-2108.
26. Zazorin, E., Zharskii, I., Pinaev, G., Kupreev, V., Spiridonov, V. *Journal of Structural Chemistry* 1974, 15, 588-590.
27. Konings, R., Booij, A., Kovacs, A. *Chemical Physics Letters* 1998, 292, 447-453.
28. Folger, F. *Zeitschrift für anorganische und allgemeine Chemie* 1975, 411, 103-110.
29. Kirfel, A., Will, G., Stewart, R. *Acta Crystallographica Section B: Structural Science* 1983, 39, 175-185.
30. Wenger, M., Armbruster, T. *European Journal of Mineralogy* 1991, 387-400.
31. Henderson, G., Soltay, L., Wang, H. *Journal of Non-Crystalline Solids* 2010, 356, 2480-2485.
32. Soltay, L., Henderson, G. *Physics and Chemistry of Glasses-European Journal of Glass Science and Technology Part B* 2005, 46, 381-384.
33. Soltay, L. G., Henderson, G. S. *The Canadian Mineralogist* 2005, 43, 1643-1651.
34. Zhao, J., Gaskell, P., Cluckie, M., Soper, A. *Journal of Non-Crystalline Solids* 1998, 232, 721-727.
35. Uhlig, H., Hoffmann, M. J., Lamparter, H. P., Aldinger, F., Bellissent, R., Steeb, S. *Journal of the American Ceramic Society* 1996, 79, 2833-2838.
36. Hannon, A. C., Vessal, B., Parker, J. M. *Journal of Non-Crystalline Solids* 1992, 150, 97-102.
37. Cormier, L., Calas, G., Beuneu, B. *Journal of Non-Crystalline Solids* 2007, 353, 1779-1784.
38. Majérus, O., Cormier, L., Calas, G., Soper, A. *Physica B: Condensed Matter* 2004, 350, 258-261.
39. Cormier, L., Gaskell, P., Calas, G., Zhao, J., Soper, A. *Physical Review B* 1998, 57, R8067.
40. Alam, T., Liang, J.-J., Cygan, R. *Physical Chemistry Chemical Physics* 2000, 2, 4427-4432.
41. Shimizugawa, Y., Maeseto, T., Suehara, S., Inoue, S., Nukui, A. *Journal of Materials Research* 1995, 10, 405-410.
42. Niida, H., Uchino, T., Jin, J., Kim, S., Fukunaga, T., Yoko, T. *Journal of Chemical Physics* 2001, 114.
43. McLaughlin, J., Tagg, S., Zwanziger, J., Haefner, D., Shastri, S. *Journal of Non-Crystalline Solids* 2000, 274, 1-8.
44. McLaughlin, J. C., Tagg, S., Zwanziger, J. *Journal of Physical Chemistry B* 2001, 105, 67-75.

Chapter 6 – Lead(II) tellurite(IV) glasses

6.1 Introduction

This chapter describes the preparation method of the glass samples and the general characterisation methods that include density measurement, energy dispersive X-ray analysis, and X-ray diffraction. These initial procedures are used to confirm the glass nominal composition, the amorphicity, and the identity of any crystal phase(s) in the samples. Subsequently, Raman scattering is used to probe the presence of various units or species in the glasses and the information used to derive a semi-quantitative estimate of the average Te-O coordination number n_{TeO} . In the neutron diffraction section, the total correlation functions $T^N(r)$ for the glasses are presented. These are compared with the $T^N(r)$ for pure TeO_2 (glass and crystal phases) and the $T^N(r)$ for $\text{PbTe}_5\text{O}_{11}$ crystal to highlight the differences and similarities in Te, Pb, and O environments. Using both $T^N(r)$ and the X-ray diffraction total correlation function, $T^X(r)$, the Te-O distances are extracted. Later, the average n_{TeO} is calculated as a function of the modifier PbO content, x . The average $n_{\text{TeO}}(x)$ values obtained are discussed based on two regions, plateau ($x < 15$ mol%) and post-plateau ($x > 15$ mol%). The lead environment is later considered in conjunction with the tellurium environment to obtain a consistent description of the glass structure. The chapter is concluded by summarising the general findings, followed by presentation of the short and intermediate range structural information deduced from the study (species/unit presents, average coordination number and distances).

6.2 Sample preparation and experimental details

Lead tellurite glasses, with nominal compositions $x\text{PbO} \cdot (100-x)\text{TeO}_2$ for $x = 5, 7.5, 10, 12.5, 15, 17.5, 20(a), 20(b)$, and 25 mol%, were prepared using reagent grade Pb_3O_4 (Aldrich, 99%) and TeO_2 (Alfa Aesar 99%). Both 20(a) and 20(b) glass samples have crystal inclusions (as later revealed from diffraction experiments) with the latter having less in quantity. Each 15 g batch of glass was appropriately weighed and intimately mixed in an agate pestle and mortar before being heated from room temperature to a melting temperature, T_m , of 800 °C at 10 °C/min in a non-wetting Pt/5Au crucible. The T_m was chosen to be about 100 °C above the liquidus (of the sample with the highest value) and was fixed to maintain a similar melting history for each glass melt. The melts were then held at temperature for 30 minutes

for homogenisation and later quenched by immersing the crucible base in water at room temperature.

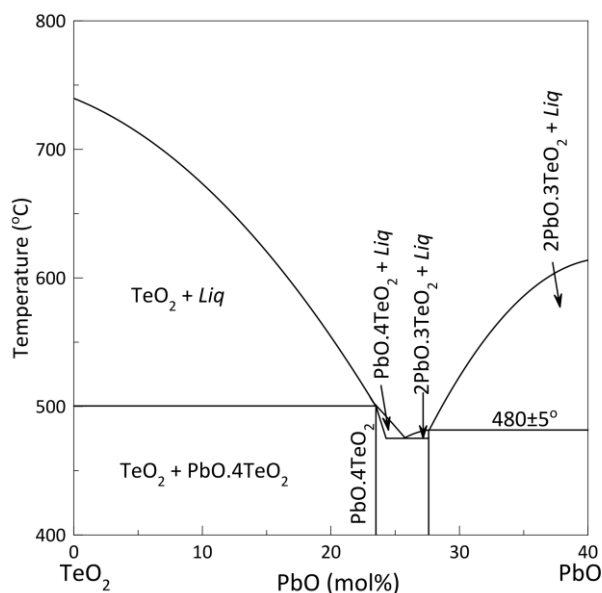


Figure 6.1: Phase diagram for the PbO-TeO₂ system reproduced from Stavrakieva et al.[1].

A Cu K_α X-ray powder diffractometer (Bruker D5000) (Section 3.6) was used to collect the X-ray diffraction patterns of selected glass samples ($x = 15, 20(a), 20(b),$ and 25 mol% $x\text{PbO}-(100-x)\text{TeO}_2$) to check the amorphicity and identify any crystal phase(s) present in the glasses. Additional information on crystallinity was obtained from the neutron diffraction and high-energy X-ray diffraction experiments.

A Micromeritics AccuPyc 1330 gas pycnometer, using He glass, was used to measure the density of the glass samples ($x = 10, 12.5, 15, 17.5, 20(a),$ and 25 mol% $x\text{PbO}-(100-x)\text{TeO}_2$). Glass molar volume and number density were then calculated as discussed in detail in Section 3.3.

A Zeiss Supra55-VP Scanning Electron Microscope (SEM) operated at an accelerating voltage of 10 kV (Section 3.7) was used to determine the Pb and Te atomic percentages of the glass samples ($x = 10, 12.5, 15, 17.5,$ and $20(a)$ mol% $x\text{PbO}-(100-x)\text{TeO}_2$). Details of the data processing are given in Section 3.7.

A Renishaw inVia Raman Microscope, equipped with a 514.5 nm Ar⁺ laser source (Section 3.5) was used to collect the Raman spectra of the glass samples ($x = 5, 7.5, 10, 15, 20(a),$ and 25 mol% $x\text{PbO}-(100-x)\text{TeO}_2$). The details of the general Raman data acquisition and processing are described in Section 3.5.

High resolution neutron diffraction data were obtained at ISIS (RAL, UK) using the GEM diffractometer (Section 2.2) on the glass samples $x = 10, 12.5, 15, 17.5, 20(a), 20(b)$ and

25 mol% $x\text{PbO} \cdot (100-x)\text{TeO}_2$. 8 – 10 g of $\text{PbO}-\text{TeO}_2$ glass samples were packed into V-cans with 40 – 50 % packing. Total beam-time exposure for the samples was from 800 – 1300 μA as shown in Table 6.1. The exposure is higher in the 10 mol% PbO glass in order to compensate for the lower S/N ratio in the high Te content glass due to the Te neutron resonance.

Table 6.1: Neutron beam exposure time for $\text{PbO}-\text{TeO}_2$ glass samples

Glass sample (mol% PbO)	Exposure (μA)
10	1300
12.5	1050
15	1050
17.5	1050
20(a)	800
20(b)	1050
25	800

High energy, total X-ray scattering data were collected by Dr Oliver Alderman and Dr Chris Benmore at the Advanced Photon Source, Argonne National Laboratory, USA using the APS Beamline 6-ID-D with an X-ray wavelength of 0.14349\AA (86.406 keV, just below the 88keV Pb K-edge) (Section 3.9). The $x\text{PbO} \cdot (100-x)\text{TeO}_2$ glasses of $x = 10, 12.5, 15, 17.5, 20(a)$, and 25 mol% were ground to a fine powder in an agate pestle and mortar, in air, and were loaded into 1 mm inner diameter Kapton tubes (wall thickness 100 microns). An area X-ray detector (TI-doped CsI scintillator, 2048×2048 pixels, each pixel $200\text{ }\mu\text{m} \times 200\text{ }\mu\text{m}$ square, and $500\text{ }\mu\text{m}$ deep) was used. The diffraction patterns obtained were processed as discussed in Section 3.9.

6.3 Results - General characterisation

6.3.1 Sample quality

Table 6.2 compares the nominal glass compositions with those obtained using EDX. In all the samples, a uniform mass loss equivalent to about 1 mol% PbO was measured, with a slightly higher mass loss being measured in the 20(a) mol% PbO glass. These losses are consistent, within the error, with those observed in $\text{PbO}-\text{GeO}_2$ glasses which were melted at a higher temperature [2].

6.3.2 Density

Table 6.2 shows the density values as well as the molar volumes and number densities for the constituent atoms derived from the density values.

Table 6.2: Glass compositions and density values for PbO-TeO₂ glasses.

Composition /x mol% PbO			Density / g cm ⁻³	Molar volume / cm ³ mol ⁻¹	Number density / atoms cm ⁻³		
Nominal	EDX	Loss			Pb	Te	O
10.0	9.1(3)	0.9	5.920(1)	28.04	7.41 x10 ²⁰	6.67 x10 ²¹	1.407 x10 ²²
12.5	11.6(2)	0.9	5.997(1)	27.94	9.37 x10 ²⁰	6.56 x10 ²¹	1.406 x10 ²²
15.0	13.7(2)	1.3	6.077(1)	27.83	1.14 x10 ²¹	6.45 x10 ²¹	1.404 x10 ²²
17.5	16.4(3)	1.1	6.161(1)	27.71	1.35 x10 ²¹	6.35 x10 ²¹	1.404 x10 ²²
20.0(a)	18.6(4)	1.4	6.246(1)	27.59	1.56 x10 ²¹	6.24 x10 ²¹	1.403 x10 ²²

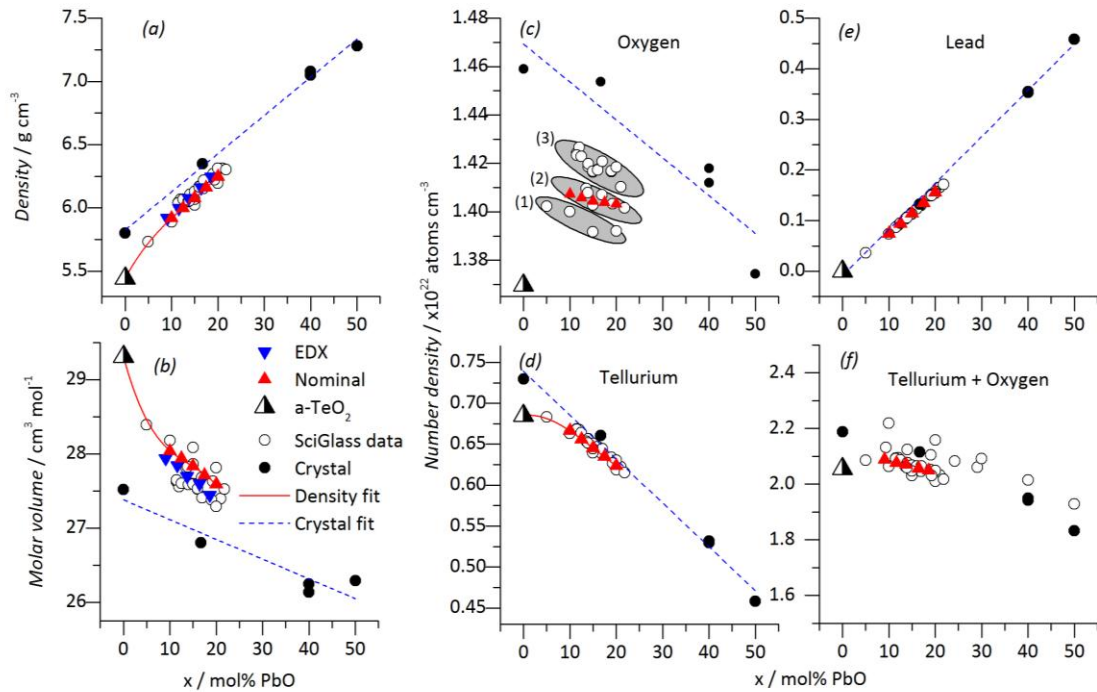


Figure 6.2: (a) shows the measured densities for the PbO-TeO₂ glasses based on nominal composition (red upward pointed triangle) and based on EDX analysis (blue downward pointed triangle) compared to the SciGlass data (open circle). (b) shows the calculated molar volumes of the glasses (symbols as in (a)) compared with the SciGlass data. Error bars for the glasses are within the points shown. (c), (d), and (e) show the calculated number densities for constituent atoms, symbol as in (a). Black filled circles are values from the crystal phases (γ -TeO₂, PbTe₅O₁₁, Pb₂Te₃O₈, PbTeO₃) with the dashed line being the line of best fit. (1), (2), and (3) in (c) reveal groups of O number density which may result from different preparation environments and/or structural differences.

Fig. 6.2(a) shows the density values as a function of both nominal and EDX compositions and compares them with the value from the SciGlass database [3], pure TeO₂ glass [4], PbTe₅O₁₁ [5], Pb₂Te₃O₈ [6-7] and PbTeO₃ [8]. The glass density increases as TeO₂ is

replaced by heavier PbO molecules, and the data points for the nominal composition PbO-TeO₂ glasses and for pure TeO₂ glass are fitted to a polynomial function in order to highlight the deviation from $x = 0$ to $x \sim 10$ mol% of PbO. The measured values agree with the values obtained from the SciGlass database suggesting that the glass composition in the study is close to the nominal value.

Fig. 6.2(b) shows the molar volume values of the glasses, calculated from the density values in Fig. 6.2(a). The number density plots are shown in Fig. 6.2(c), (d), and (e) for oxygen, tellurium, and lead atoms respectively. Pb number density shows a linear increase with x which is almost coincident with that for the crystal phases of γ -TeO₂, PbTe₅O₁₁, Pb₂Te₃O₈, and PbTeO₃; Te number density, however, shows deviation from the crystal fit. This trend is the same as observed in Li₂O-TeO₂ glasses, which reflects changes in the TeO₂ network. The same inference could be made for PbO-TeO₂ glasses that the PbO environment remains similar throughout the composition range and the local order of the TeO₂ network exhibits a change. O number density shows 3 groups of values calculated from the Sciglass data, marked as (1), (2), and (3) and which originate from different reports (as indicated). The differences could suggest a real difference in O environments in these glasses, resulting from different preparation history, or could reflect different density measurement techniques or actual compositions. From the point of preparation history, all glasses were melted in Pt/Au crucibles, except for those studied by Stanworth [9] (zirconia, alumina, and silica crucibles). The information on the melting temperatures for specific lead tellurite glasses is however not available. The Archimedes method was used to measure the density values in most of the studies, however, there is no clear classification based on the measuring method.

As PbO is added to the TeO₂ network, all of the atom number densities decrease, except for Pb. This reflects the replacement of the 3 atoms of TeO₂ by just 2 atoms in PbO and is consistent with the decrease observed in molar volume, despite the larger size of the Pb²⁺ ion compared to Te⁴⁺. This glass structure shrinkage is comparable to the trend observed in the Li₂O-TeO₂ glasses, though in that case it is the small size of the Li⁺ ion which is the cause.

6.3.3 X-ray diffraction

From visual inspection, the glasses with $x = 10, 12.5, 15, 17.5, 20(a)$ and $20(b)$ mol% were judged to be amorphous, based on their clarity. However, HEXRD revealed that the glass samples with $x = 10, 20(a)$ and 25 mol% contain some crystal phase(s), whilst ND showed

that sample 20(a) had more crystal content than 20(b) so the latter sample was given greater neutron exposure (Table 6.1). As shown in Fig. 6.3, the X-ray diffraction patterns of these samples contain bright dots denoting the presence of crystals. The crystalline content at $x = 10$ mol% is negligible. However, at $x = 20$ and 25 mol%, the content is much higher and this affects the composition of the residual glass.

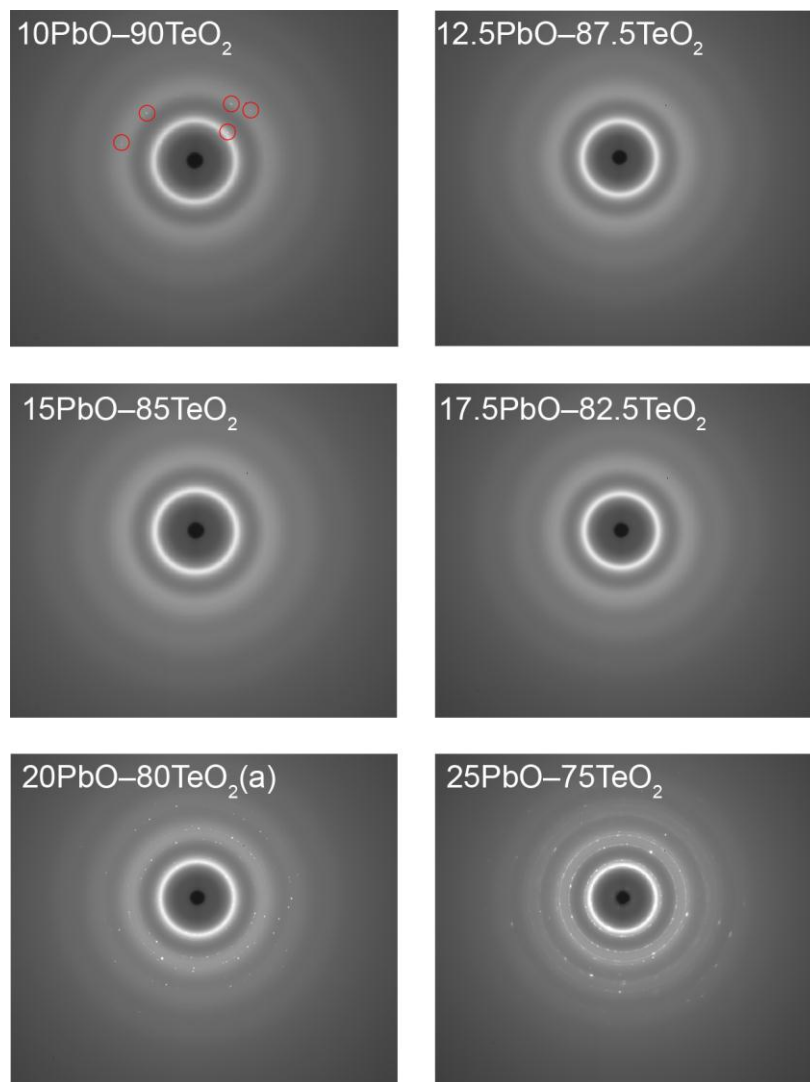


Figure 6.3: High energy X-ray diffraction patterns for $x\text{PbO}-(100-x)\text{TeO}_2$ glasses for $x = 10, 12.5, 15, 17.5, 20(a)$ and 25 mol%. Significant crystallisation is seen in 20(a) and 25 mol% PbO samples. Negligible crystallisation is seen in 10 mol% PbO sample (spots ringed in red).

The crystal phase present in the $x = 10$ mol% glass is probably $\alpha\text{-TeO}_2$ (based on the high TeO_2 content) but there is insufficient present to be able to determine the d -spacings. Fig. 6.4 shows 1D plots of the HEXRD spectra from the samples and Fig 6.4(a) gives the d -spacings of the 4 sharp crystal peaks. These are similar to those obtained by Kaur *et al.* [10] for glasses of $x = 19$ and 21 mol% prepared via splat quenching between two brass plates. In

the same glasses, prepared at a slower cooling rate, the crystal phases formed in the glasses are γ -TeO₂, Pb₂Te₃O₈, and PbTeO₃. The 4-sharp peaks observed in the splat-quenched glasses were therefore assigned by those authors to a mixture of γ -TeO₂, Pb₂Te₃O₈, and PbTeO₃ phases. The PanAnalytical X-Ray Suite database matches the crystalline peaks in the 20 mol% and 25 mol% samples to both PbTe₃O₇ and Pb₂Te₃O₇ phases. Culea *et al.* [11] assigned the crystal phase to Pb₂Te₃O₇ based on the better fit. However, the Pb₂Te₃O₇ stoichiometry seems unlikely for Pb²⁺ and Te⁴⁺ cations. PbTe₃O₇ is stoichiometrically more reasonable and was first reported by Tromel *et al.* who referred to it as an “anti glass” phase with fluorite-type structure and defined it as a metastable and non-stoichiometric crystal having irregularly displaced atoms such that the short-range order is undefined [12]. This metastable phase was also reported by Silva *et al.* [13] and Kabalci *et al.* [14] in their studies of lead halide tellurite glasses. PbTe₃O₇ is not reported in Fig. 6.1, the nearest phase being PbO.4TeO₂ (equivalent to PbTe₄O₉, not reported). PbTe₅O₁₁ (16.67 mol% PbO) however, has the composition which is closest to the PbO–TeO₂ glasses of this study and this crystal phase was obtained in a devitrified 20PbO–80TeO₂ glass sample [5].

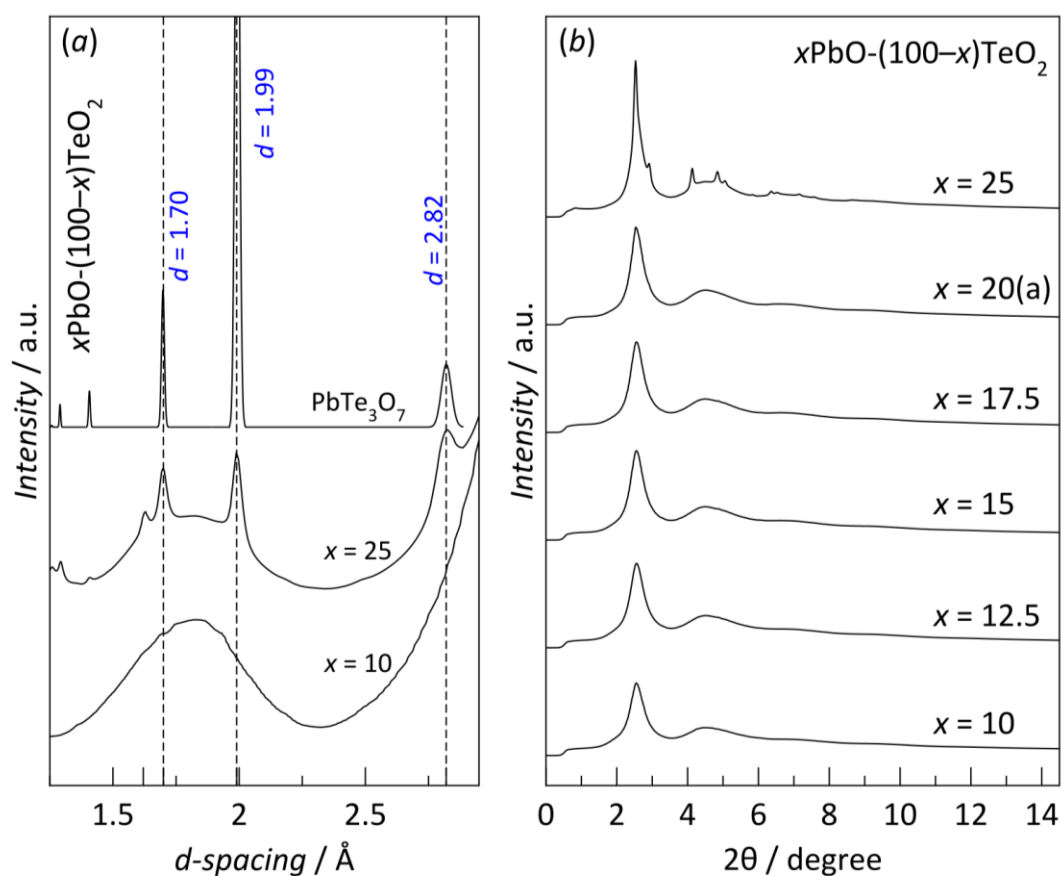


Figure 6.4: 1D plots of high energy X-ray diffraction spectra for $x\text{PbO}-(100-x)\text{TeO}_2$ glasses for (a) $x = 10$ and 25 mol% compared to published data for PbTe_3O_7 from PanAnalytical software database and (b) stack plot of $x = 10, 12.5, 15, 17.5, 20(a)$ and 25 mol%

Table 6.3 summarises the physical appearance of the glasses, which includes the amorphicity of the glasses, based on diffraction information.

*Table 6.3: Physical appearance and diffraction information. *Crystal diffraction spots were revealed in the synchrotron X-ray diffraction experiment.*

Nominal x (mol% PbO)	Observation			State
	Visual inspection	HEXRD	Neutron diffraction	
10	Clear	Glass + Crystal	Glass*	~90TeO ₂ glass + "α-TeO ₂ "
12.5	Clear	Glass	Glass	~87.5TeO ₂ glass
15	Clear	Glass	Glass	~85TeO ₂ glass
17.5	Clear	Glass	Glass	~82.5TeO ₂ glass
20(a)	Clear	Glass + Crystal	Glass + Crystal	>80TeO ₂ glass + crystals
20(b)	Clear	–	Glass + Crystal	>80TeO ₂ glass + crystals
25	Clear, with cloudy bits	Glass + Crystal	Glass + Crystal	>75TeO ₂ glass + crystals

6.4 Raman spectroscopy

Fig 6.5(a) shows the measured Raman spectra of $x\text{PbO} \cdot (100-x)\text{TeO}_2$ glasses ($x = 5, 7.5, 10, 15, 20(a)$ and 25 mol%) collected at room temperature from 100 cm^{-1} to 1000 cm^{-1} . Glass samples of $x = 5, 7.5, 20(a)$, and 25 mol% PbO are partially crystallised. The clear glass bits were selected to be analysed using Raman spectroscopy. The spectra show the typical broad Boson peak to up to 400 cm^{-1} , and the Te-O stretching and vibration modes for TeO₂-based glasses from 400 to 900 cm^{-1} [15-18]. Fig. 6.5(b) shows the reduced and area-normalised Raman spectra, which were obtained by multiplying the experimental intensity with the correction factors for the wavelength-dependent scattered intensity and temperature-dependent mean number for phonon occupation in the glasses as discussed in Section 3.5. The reduction was done so that the main features of the Te-O vibrations in the glass can be highlighted for study. The Raman spectra show a broad continuous peak manifold from approximately 500 to 900 cm^{-1} , characteristic of Te-O vibrations as typically observed in tellurite glasses encompassing the vibrations in various Te environments, e.g., 3, 3+1, and 4 coordinated Te. As PbO content is increased, a major change was observed in the shape of the manifold, i.e., the peak at 600 cm^{-1} decreased whilst the peak at about 800 cm^{-1} increased.

The assignment of peaks to various TeO₂ species is discussed in Chapter 5, where the region from 500 to 900 cm^{-1} is typically resolved into 4 peaks assigned to the vibrational modes of either a 4-coordinated pseudo-trigonal bipyramidal (tbp) unit or a 3-coordinated

trigonal pyramidal (tp). The Raman shifts covering the lower wavenumbers in the broad peak (Peak 3 and Peak 4, from 620 to 670 cm^{-1}) are assigned to the $[\text{TeO}_4]$ unit whereas the higher wavenumber region (Peak 1 and Peak 2, from 720 to 780 cm^{-1}) is attributed to the vibrations of the $[\text{TeO}_3]$ units.

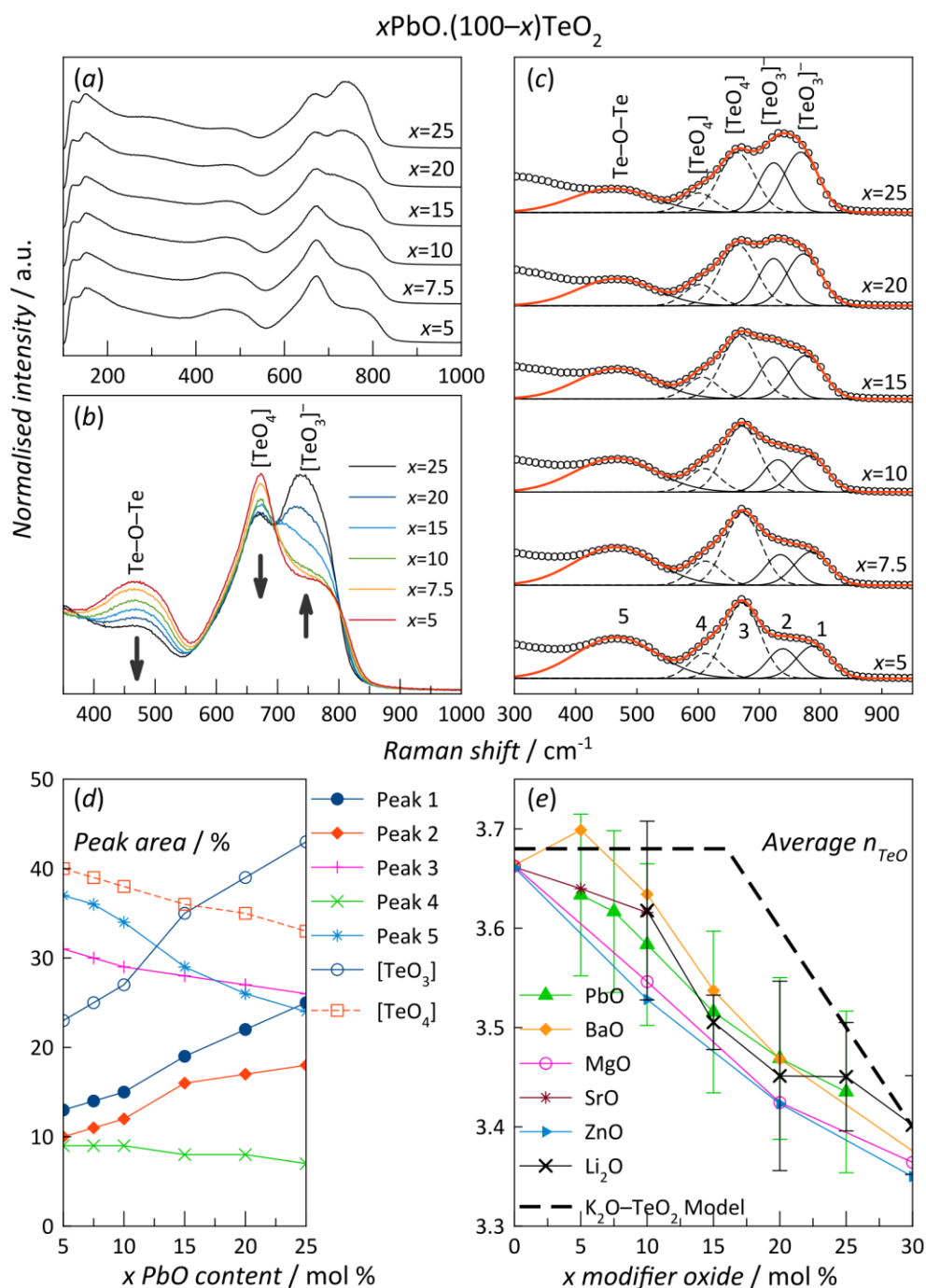


Figure 6.5: (a) experimentally obtained Raman spectra (normalised); (b) reduced and area-normalised Raman spectra showing the region of interest encompassing the Te-O vibrations; (c) Raman peak deconvolution of contributions from $[\text{TeO}_4]$ and $[\text{TeO}_3]$ units; (d) area of the peaks in (c) as a function of x ; and (e) average n_{TeO} obtained compared to the values from Sekiya et. al. [17] $x = 20$ represents 20(a) mol% of PbO.

The peak at about 490 cm^{-1} is attributed to the bending modes of --Te--O--Te-- bridges and is not included in determining the average Te-O coordination number, n_{TeO} , in the glass. From the fits shown in Fig. 6.5(c), the areas of the individual peaks were extracted and the n_{TeO} for each glass composition was calculated. Similar peak width was applied for the individual peaks in the figure. The sum of the fits gives good agreement with the experimental spectrum. The average Raman shifts of the peaks from the fit are consistent with the expected values from the literature.

In Fig. 6.5(d), the areas for Peak 1 and Peak 2, contributed from the vibrations of Te-O bonds in $[\text{TeO}_3]$ units [15] increases as a function of PbO content. This simply means that, as Pb^{2+} is added, there is formation of $[\text{TeO}_3]$ units in the glasses. Peak 3 and Peak 4 are the contributions from Te-O vibrations in $[\text{TeO}_4]$ units and the areas for these peaks both decrease slightly as PbO content is increased. As a function of PbO content, the area of Peak 5 decreases, reflecting the decrease of Te-O-Te bridges because of the formation of non-bridging oxygens, NBO. This implies that Pb^{2+} behaves as a charge compensator (i.e. modifier) in the glass.

The average n_{TeO} values for PbO- TeO_2 glasses are shown in Fig 6.5(e). The values and their trend with x are comparable to those in TeO_2 glasses modified by divalent cations such as Ba^{2+} , Mg^{2+} , Sr^{2+} , and Zn^{2+} [17]. This suggests that Pb^{2+} behaves as a divalent modifier. Surprisingly, the average n_{TeO} values are also similar to those of the $\text{Li}_2\text{O--TeO}_2$ glasses, suggesting that the Te environments in PbO- TeO_2 and $\text{Li}_2\text{O--TeO}_2$ are similar. However, because Raman spectroscopy is semi-quantitative, the average n_{TeO} obtained is less reliable and associated with greater error as shown in the figure.

6.5 Total diffraction

6.5.1 Neutron and X-ray diffraction

Fig. 6.6(a) shows the distinct scattering, $i(Q)$ for the PbO- TeO_2 glasses, to up to 40 \AA^{-1} . A Q_{max} value of 35 \AA^{-1} is used for Fourier transformation to the total correlation function, $T^N(r)$, due to the limitation caused by the Te resonance. Fig. 6.6(b) shows the $T^N(r)$, transformed with the Q_{max} value of 35 \AA^{-1} . The asymmetric peak at about $\sim 2\text{ \AA}$ represents the Te-O distances and the peak at $\sim 3\text{ \AA}$ represents the overlap of Te-O, O-O, and Pb-O distances in the glass. Fig. 6.7 (a) and (b) show the X-ray distinct scattering, $i^X(Q)$, and the total correlation function, $T^X(r)$, obtained from the Fourier transform of $i^X(Q)$ with a Q_{max} value of 20 \AA^{-1} . In Fig 6.7(b), the peak at about 2 \AA corresponds to the asymmetric Te-O distances. The peak at about 2.4 to 3 \AA contains a significant contribution from either PbO or longer TeO distances. The

strong peak at about 4 Å arises from the pairs of stronger X-ray scatterers (Pb–Pb, Te–Te, and Te–Pb)

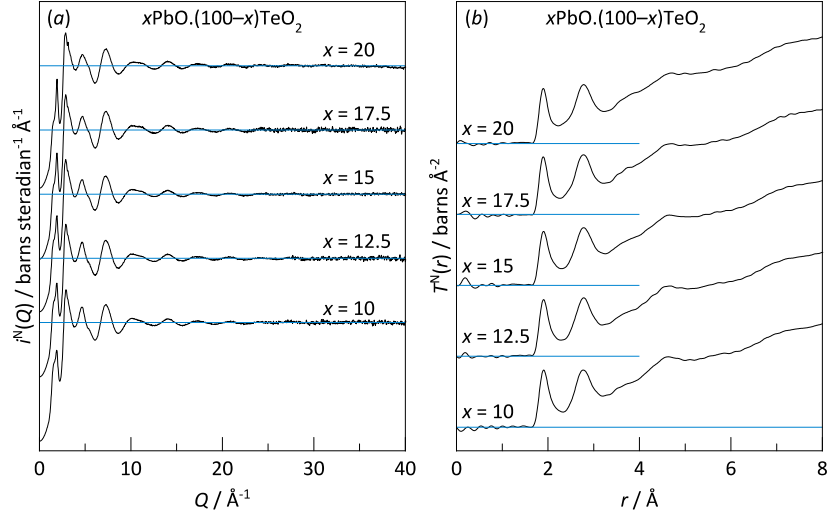


Figure 6.6: (a) shows the neutron distinct scattering function $i^N(Q)$ for PbO-TeO_2 glasses with 10, 12.5, 15, 17.5, and 20 mol% PbO and (b) shows the neutron total correlation function $T^N(r)$ obtained by taking the Fourier transforms of the functions in (a) with a Q_{max} value of 35 Å $^{-1}$

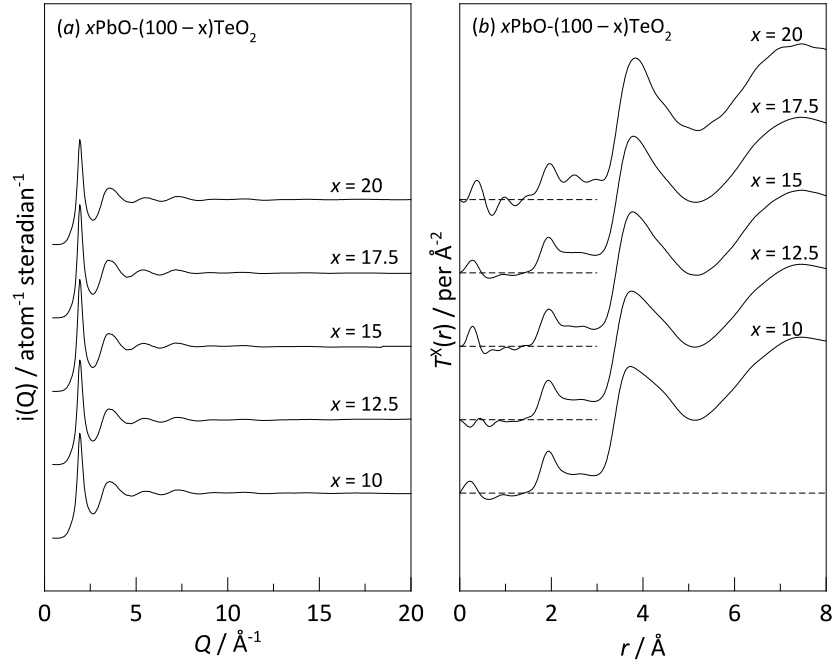


Figure 6.7 (a) shows the X-ray distinct scattering function $i^X(Q)$ for PbO-TeO_2 glasses with 10, 12.5, 15, 17.5, and 20 mol% PbO and (b) shows the X-ray total correlation function $T^X(r)$ obtained by taking the Fourier transforms of the functions in (a) with a Q_{max} value of 20 Å $^{-1}$

Fig. 6.8 shows the quality of the simultaneous neutron and X-ray data fitting in terms of the sum of fit and the residual of the fit. A balanced weighting factor of 0.5 was used for each pair of data sets. The detailed fitting steps using NXFit are discussed in Section 6.5.3.

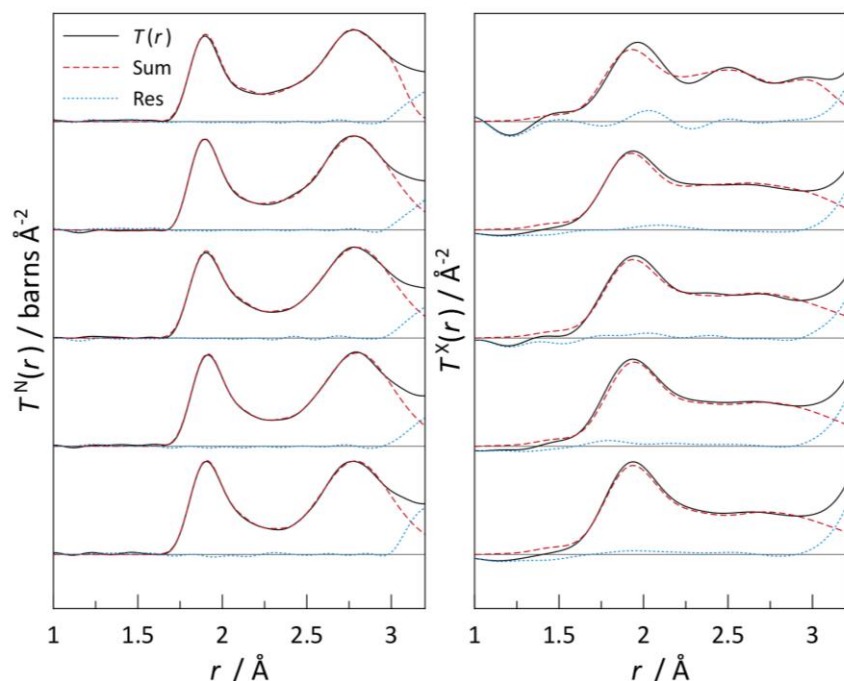


Figure 6.8: The sums of fit and the residuals from the simultaneous fitting of the X-ray and neutron diffraction data.

In Fig. 6.8, the first coordination shell in $T(r)$ (1.5 Å – 2.25 Å) consists of the asymmetric Te-O distances, arbitrarily fitted with 3 peaks using the leading edge of the residual of each preceding peak. By simultaneous fitting of X-ray and neutron diffraction total correlation functions, Barney *et al.* [to be published] have extracted the Te environment in the second coordination shell where there are two Te-O distances at 2.59 Å and 3.03 Å. The shorter distance is the distance from a Te atom to one of the equatorial O atoms in the neighbouring TeO_4 polyhedron, characteristic of a highly ordered structure as found in $\gamma\text{-TeO}_2$ and possibly retained in the pure TeO_2 glass. This distance is not included in the fitting due to its negligible contribution in glasses, however, the longer 3.03 Å is included to suggest the Te-O distances associated with 2 TeO_2 units connected by a corner. The absence of this peak would indicate that the TeO_2 units are all isolated $[\text{TeO}_4]$ units.

6.5.2 Comparison with a- TeO_2 and related tellurite glasses

Fig. 6.9 shows that the $T(r)_{\text{Te-O}}$ for $x = 10, 12.5$, and 15 mol% PbO are similar to that of the pure TeO_2 glass. This indicates that the proportions of $[\text{TeO}_4]$ and $[\text{TeO}_3]$ units present at these compositions are similar, in nature and quantity, as in pure TeO_2 glass. For $x = 17.5$ mol% PbO, a small increase in the contribution of the shorter r_{TeO} corresponding to the Te-O distance in $[\text{TeO}_3]$ is seen. This would indicate that the average n_{TeO} for $x = 10, 12.5$, and 15

mol% PbO is close to 3.68 (the value found in pure TeO_2 glass), and for $x = 17.5$, the average n_{TeO} is slightly less than 3.68 because more $[\text{TeO}_3]$ units are formed.

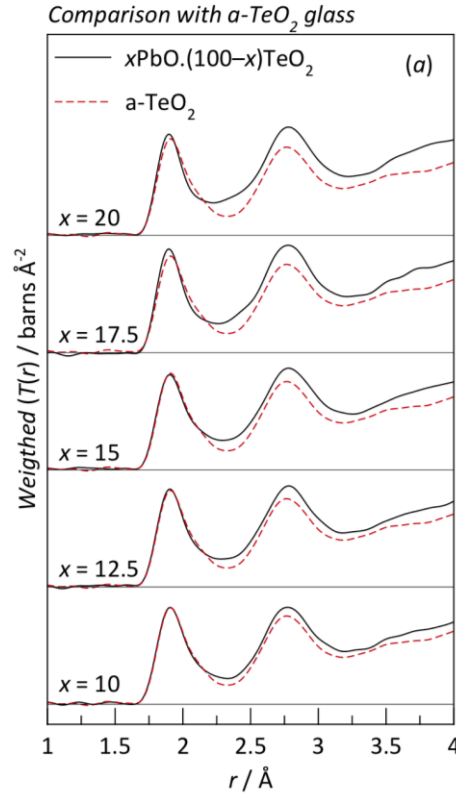


Figure 6.9: Comparison of the total $T(r)$ (weighted to the Te-O pair weighting factors) to highlight the Te-O pair environment in the glasses with respect to the pure TeO_2 glass.

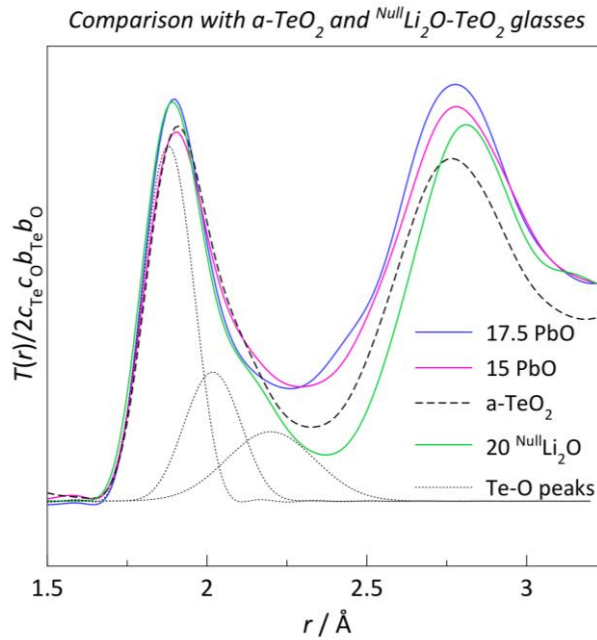


Figure 6.10: Comparison of the weighted $T(r)$ of $15\text{PbO-}85\text{TeO}_2$ to pure TeO_2 glass and of $17.5\text{PbO-}82.5\text{TeO}_2$ to $^{\text{Null}}20\text{Li}_2\text{O-}80\text{TeO}_2$ glasses to show the plateau and post-plateau similarities respectively. Individual Te-O peaks represent the 17.5PbO sample.

Fig. 6.10 shows the comparison of the $T(r)$ for 17.5 mol% PbO glass with pure TeO₂ glass and ^{Null}20Li₂O-80TeO₂ glass (there is no $x = 17.5\%$ sample for the Li₂O-TeO₂ system). The $T(r)_{\text{Te-O}}$ for the Li₂O-TeO₂ glass matches the $T(r)_{\text{Te-O}}$ for the $x = 17.5\%$ mol% PbO glass.

In Section 5.4.3, the calculated average n_{TeO} for the ^{Null}20Li₂O-80TeO₂ glass is 3.65(5). This would mean that for $x = 17.5\%$ mol% PbO glass, the average n_{TeO} value is also about 3.65 suggesting that the average n_{TeO} values in PbO-TeO₂ glasses behave as in the alkali tellurite glasses with the presence of plateau and post-plateau regions in the average n_{TeO} values as a function of x .

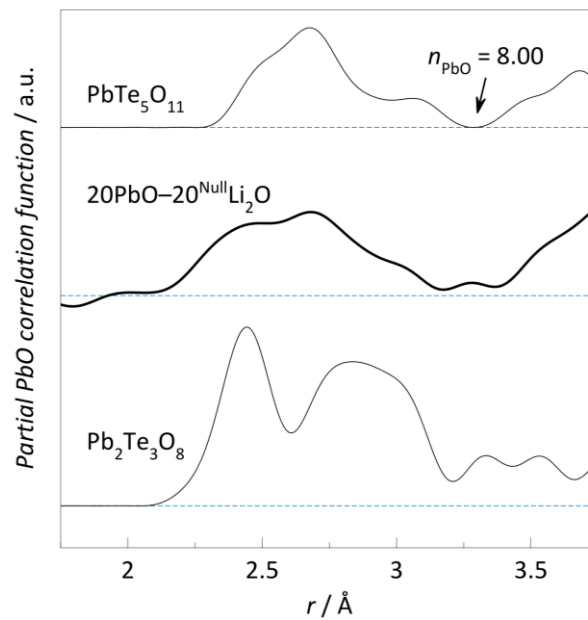


Figure 6.11: The residual of $T(r)$ 20PbO-TeO₂ – $T(r)$ 20^{Null}Li₂O-TeO₂ glasses, showing the “PbO” peak. The data for the 20PbO(b) sample are used.

Isostoichiometric technique can be used to partly investigate the Pb²⁺ environment using the null lithium tellurite data if the short range order of PbO-TeO₂ and ^{Null}Li₂O-TeO₂ glasses are close to being identical; for example, the 20 mol % Li₂O and 20 mol % PbO glasses. The residual (20PbO-TeO₂ – $T(r)$ ^{Null}20Li₂O-TeO₂ glasses) would yield the “ $T(r)_{\text{PbO}}$ partials” (which contain the PbO and also OO due to the difference of the oxygen environments in lithium and lead tellurite glasses). The n_{PbO} obtained by integrating the “PbO peak” from the residual will therefore be inaccurate (n_{PbO} obtained was about 6, and not 8). As seen in Fig 6.11 however, the “PbO peak” shape from the residual is very similar to the PbO peak in PbTe₅O₁₁ crystal phase of which was simulated using the much lower RMS bond variation value (0.05), as discussed in Section 4.4.4 (also included $T(r)_{\text{PbO}}$ for Pb₂Te₃O₈ for comparison).

6.5.3 Parameterising complex Te-O distances

6.5.3.1 Te-O peak fitting

The Te-O peaks were fitted using the leading edges of both neutron and X-ray data (weighted to 50% each) as shown in Fig. 6.12. The second Te-O(II) peak was fitted from the residual of the $T(r)$ after the Te-O(I) peak was fitted. The same process was done for the third Te-O(III) peak. The fit parameters obtained are shown in Table 6.4.

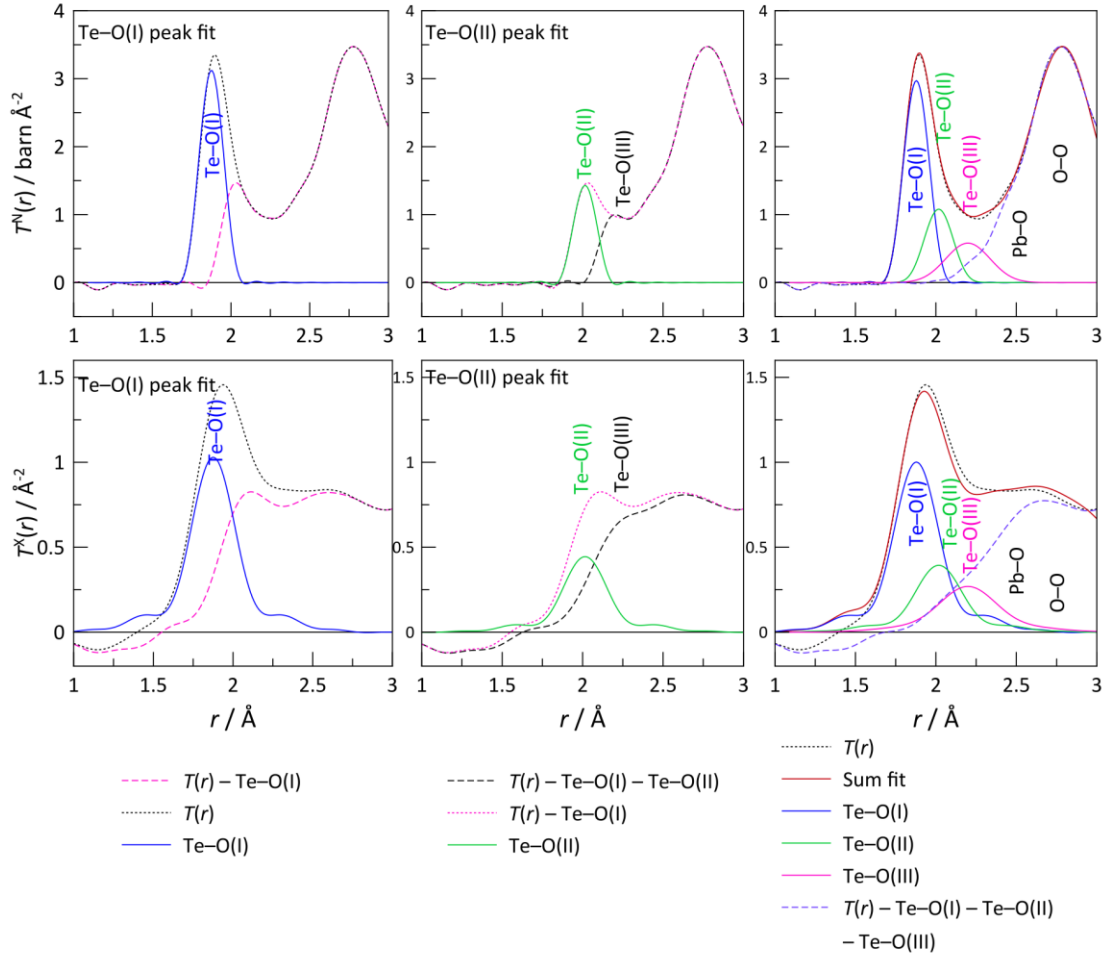


Figure 6.12: Fitted Te-O peaks for 17.5PbO-82.5TeO₂ glass from NXFit

In the plateau region, (for $x < 15$ mol%) the average n_{TeO} is approximately constant and has the value of 3.69(9). The error is represented by the difference between the value obtained by peak fitting and that obtained by integration of the Te-O peak manifold, arising from the first coordination sphere from which the other contributions (O-O, Pb-O, and Te-O(IV)) are removed. The large error is associated with the limitation in Q_{max} of the X-ray data which broadens the $T^X(r)$ and lowers the quality of the fit. It seems that the fraction of the [TeO₃] units present in pure TeO₂ glass is retained in PbO-TeO₂ glass for $x < 15$ mol% PbO and suggests that Pb²⁺ changes the TeO₂ network in a similar fashion to the alkali ions. In the

plateau region, the NBOs (O1b) created by adding PbO, combined with the pre-existing terminal oxygens (O1a) of the $[\text{TeO}_3]^-$ units, are sufficient to supply the required coordination for Pb^{2+} without the need for creating more NBOs (O1c) by the formation of the $[\text{TeO}_3]^-$ unit. This only breaks the TeO_2 bridges and does not transform units, hence the short range Te-O environments (distance distribution) are similar for $x < 15$ mol%, as shown in the comparison of $T(r)$ of these glasses with a- TeO_2 .

Table 6.4: Peak parameters for Te-O and Pb-O peaks obtained from NXFit

x / mol% PbO	Te environment	
	$\langle r \rangle / \text{\AA}$	n_{TeO}
10.0	1.98	3.69(12)
12.5	1.99	3.70(6)
15.0	1.98	3.68(10)
17.5	1.97	3.64(4)
20.0	1.98	3.58(8)
Average	1.98(1)	–
$\text{PbTe}_5\text{O}_{11}$		3.70

For $x = 17.5$ mol%, the average n_{TeO} obtained is 3.64(4). Within error, this value is not significantly different from those in the plateau region but this composition can be considered to fall within the post-plateau region by comparison of its $T^N(r)$ with that of a- TeO_2 (Fig. 6.9) where the contribution of short Te-O distances corresponding to r_{TeO} in the created $[\text{TeO}_3]^-$ units (O1c) is visible as indicated by the mismatch of the leading edge. This n_{TeO} value is similar to that of the 20 mol% Li_2O glass and, as shown in Fig. 6.10, the normalised $T(r)/w_{\text{TeO}}$ is identical to the $T(r)/w_{\text{TeO}}$ of the 20 mol% $^{\text{Null}}\text{Li}_2\text{O}$ glass, proving the similarity of the Te environment (distance distribution) in these compositions. In this post plateau region, the value of $b = 2.1$ is obtained by fitting the two data points. This value is significantly larger than the value in Li_2O - TeO_2 glasses ($b = 0.8$).

6.5.4 Extension of the TeO_2 model

6.5.4.1 Plateau region

Based on the similarity of the first peak in $T^N(r)$ of 10, 12.5, and 15 mol% PbO tellurite glasses to that of pure TeO_2 glass, it is reasonable to infer that the proportions of $[\text{TeO}_4]$ and $[\text{TeO}_3]^-$ units present in these glasses are similar, giving an average n_{TeO} value of 3.69(9). This assumption is consistent with the results obtained by simultaneously fitting the X-ray and neutron diffraction data. These compositions are therefore in the plateau region. In considering the TeO_2 model, the value of average n_{TeO} in the plateau region from here on will

be fixed at 3.70 to make the average n_{TeO} in $\text{PbO}-\text{TeO}_2$ similar to that in $\text{Li}_2\text{O}-\text{TeO}_2$ so that the b value obtained is comparable to the $\text{Li}_2\text{O}-\text{TeO}_2$ system. This n_{TeO} value corresponds to:

$$n_{\text{TeO}} = 3.70 = (0.3)[\text{Te3}] + (0.7)[\text{Te4}] \quad 6.1$$

Therefore, in $\text{RPbO}-1\text{TeO}_2$ glass with R and 1 units of PbO and TeO_2 respectively,

$$\begin{aligned} \text{RPbO}-1\text{TeO}_2 \Rightarrow & 0.3[\text{Te3}] + 0.7[\text{Te4}] + 0.3[\text{O1a}] + 2R[\text{O1b}] + \\ & (1.7-R)[\text{O2}] + R[\text{Pb}] \end{aligned} \quad 6.2$$

From this equation, the deviation composition x_D can be determined based on these assumptions:

- (1) Pb^{2+} is coordinated to an average of 8 oxygen atoms as will be discussed in Section 6.5.5 later (Bond valence for $\text{Pb}-\text{O}$ is therefore 0.25 v.u., average r_{PbO} is $\sim 2.62 \text{ \AA}$)
- (2) $\text{Te}-\text{O1a}$ has a bond valence value of 1.5 v.u., therefore O1a could coordinate 2 Pb^{2+}
- (3) $\text{Te}-\text{O1b}$ (determined from $\text{PbTe}_5\text{O}_{11}$) has a bond valence value of 1.4 v.u., therefore O1b could coordinate to the average number of 2.4 Pb^{2+} ions

Therefore, combining (1), (2), and (3)

$$8(\text{NPb}) \leftrightarrow 2(\text{NO1a}) + 2.4(\text{NO1b})$$

$$8(R) \leftrightarrow 2(0.3) + 2.4(2R)$$

$$R \leftrightarrow 0.1875$$

$$x_D = R/(1+R) \approx 15.8 \text{ mol\%}$$

This x_D value agrees well with the experimental $n_{\text{TeO}}(x)$ plot in Fig. 6.13 where x_D is a value between 15 and 17.5 mol% of PbO . Therefore when Pb^{2+} is coordinated to 8 oxygen atoms and each $\text{Pb}-\text{O}$ bond has the average bond valence value of 0.25 v.u, all O1a and O1b, are fully bonded to Pb^{2+} at 15.8 mol%, which means that $x = 10, 12.5$, and 15 mol% PbO tellurite glasses are within the plateau region of n_{TeO} .

6.5.4.2 Post plateau region

Since x_D for $\text{PbO}-\text{TeO}_2$ is similar to $\text{Li}_2\text{O}-\text{TeO}_2$, from Eqn 5.10, n_{TeO} for post plateau is

$$n_{\text{TeO}} = 3.70 - Qb \quad 6.3$$

Where Q is the further unit added, $[(0.1875 + Q)\text{PbO}-1\text{TeO}_2]$ (Similar as M in Eqn, 5.7 and 5.8, Q is chosen to represent $\text{PbO}-\text{TeO}_2$ glasses). As seen in Fig. 6.13, the value of $b = 2.1$ fits the experimental data well, but this is obtained by using only two points, giving rise to a large error value, where the b value could be between 0.8 to 4. Fig. 6.14 compares the

$n_{\text{TeO}}(x)$ for Li, K, and Pb and their b values. In this case, a fixed value of x_D is chosen to represent Li, K, and Pb, to highlight the difference in the b values.

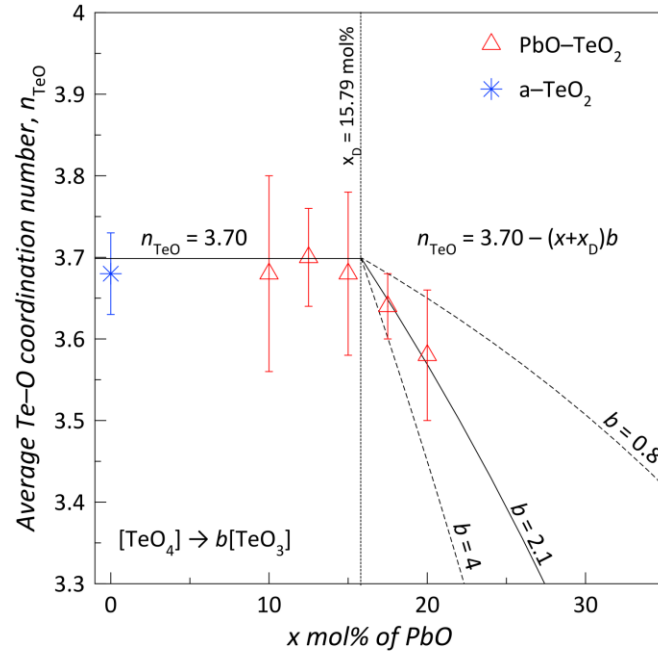


Figure 6.13: The determination of b value for PbO-TeO_2 glasses

In the plateau region, the condition: $8(\text{NPb}) \leftrightarrow 2(\text{NO1a}) + 2.4(\text{NO1b})$ is based on the assumption that r_{PbO} values in the $[\text{PbO}_8]$ unit are similar. Adding up the contribution of bonds from O1c;

$$8(\text{NPb}) \leftrightarrow 2(\text{NO1a}) + 2.4(\text{NO1b}) + 2.8(\text{NO1c}) \quad 6.4$$

and substituting the fraction of each unit, we have,

$$8(R) \leftrightarrow 2(0.3) + 2.4(2R) + 2.8(Rb - 0.1875b) \text{ where } b = 2.1 \quad 6.5$$

This condition however creates an excess number of bonds in the plateau region: available bonds > required bonds. If the system energy is minimised when the number of available bonds matches the number of required bonds, Eqn. 6.5 can be further broken down into various equalities. In this case, only 3; (a), (b), or (c) are considered, as follows;

$$(a) \quad 8(R) \leftrightarrow 2(0.3) + 2.4(2R) + 2.8(Rb - 0.1875b) \text{ where } b = 1.15 \quad 6.5.a$$

$$(b) \quad 8(R) \leftrightarrow 2(0.3) + 2.4(2R) + 1.3(Rb - 0.1875b) \text{ where } b = 2.1 \quad 6.5.b$$

$$(c) \quad 8(R) \leftrightarrow 2(0.3) + 2.4(2R) + 2.8(Rb - 0.1875b) \text{ where } b = 2.1 \quad 6.5.c$$

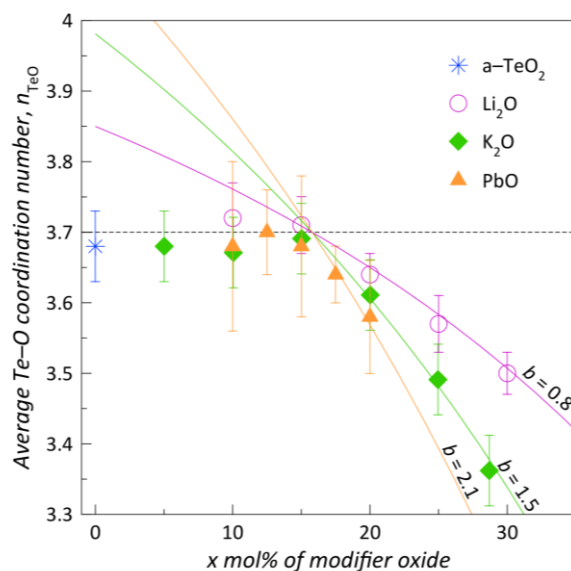


Figure 6.14: The average n_{TeO} for PbO-TeO₂ glasses, compared with Li₂O-TeO₂ and K₂O-TeO₂ glasses.

In the case of (a), this would mean that the number of Te–O bonds broken in the transformation process of [TeO₄][–] to [TeO₃][–] unit is less than the value obtained from fitting the n_{TeO} (post plateau region). This b value of 1.15 is however within the error of b as discussed. A smaller b value would mean that the number of Pb–O_{1c} bonds is less than the number of Pb–O_{1a}, or Pb–O_{1b} bonds, to be exact; for the [PbO₈] unit, there are 2.8 Pb–O_{1a} + 4.8 Pb–O_{1b} + 0.4 Pb–O_{1c} bonds where the distance of Pb–O_{1a} = Pb–O_{1b} = Pb–O_{1c} = ~ 2.6 Å. In the case of (b), this would, however, mean that $r_{\text{O1c-Pb}}$ is 2.31 Å (0.58 v.u.) which is not a typical r_{PbO} within this range of PbO composition ($x < 20$ mol%). Therefore, this would indicate that, in the post-plateau region, Pb²⁺ changes its environment as a preparation to entering the glass former state (to start forming shorter Pb–O bond). Pb²⁺ environments in lead tellurite crystals vary depending on the PbO content. As discussed in Section 4.4.4, in PbTe₅O₁₁ (16.7 mol% PbO), there is 1 [PbO₄₊₄] unit (subscript 4 + 4 means there are 4 short and 4 longer PbO distances), this PbO distance distribution, however, can be approximated by a single Gaussian. In the much higher PbO content Pb₂Te₃O₈ crystal (40 mol% PbO), there are two Pb sites: [Pb₄₊₄], and [Pb₃₊₅]. In the 50 mol% PbO content crystal (PbTeO₃), there are 2 [PbO₂₊₆] and a [PbO_{8-long}] units present. Based on this trend, it is apparent that, as the PbO content increases, shorter PbO distances are formed such that, at 50 mol% PbO, the distance resembles a typical Pb–O distance for Pb²⁺ behaving as a glass former, which is the case in (c). This simply means O_{1a}, O_{1b}, and O_{1c} are connected to Pb²⁺ at different r_{PbO} , however, $r_{\text{Pb-O1a}}$, $r_{\text{PbO-O1b}}$, and $r_{\text{PbO-O1c}}$ cannot be separately determined from the diffraction data. Fig. 6.15 shows the conditions as in the case of (a) as discussed.

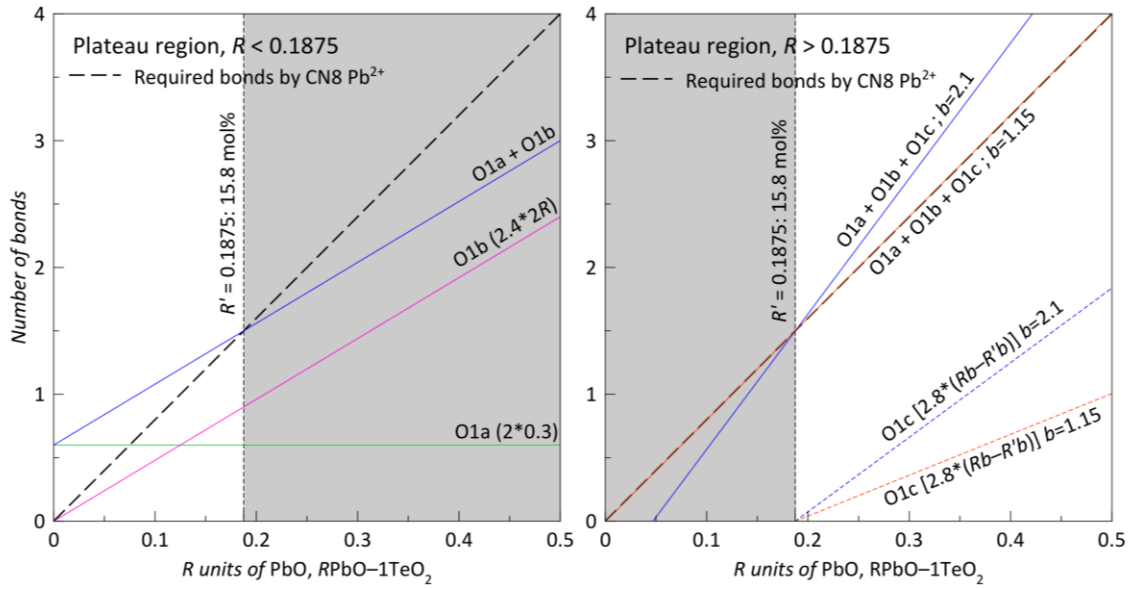


Figure 6.15: The number of bonds in the plateau and post-plateau regions for $b = 2.1$, and $b = 1.15$.

6.5.5 Lead (II) environment

6.5.5.1 PbO distances and coordination number

The Pb^{2+} ion generally adopts a high coordination (average PbO coordination number, $n_{\text{PbO}} = 6$ to 8) when present at low concentrations in glasses. This is evidenced from high energy X-ray diffraction [2, 19-21], neutron diffraction [2, 21-23], and extended X-ray absorption fine structure [24-25] studies on $\text{PbO-VO}_{2.5}$ [20], PbO-TeO_2 [25], PbO-SiO_2 [2, 20-21], $\text{PbO-BO}_{1.5}$ [19] for PbO content less than 30 mol%. When present in more than about 50 mol% PbO, the average n_{PbO} decreases to 2 – 4 in $\text{PbO-AlO}_{1.5}$ [22], $\text{PbO-GaO}_{1.5}$ [26], $\text{PbO-BO}_{1.5}$ [19], PbO-SiO_2 [2, 20-21], and PbO-TeO_2 [25]. Because of the overlapping Pb–O and O–O distances, determining the average n_{PbO} value requires removal of the n_{OO} partial associated with the glass cation polyhedra. This is feasible in tetrahedral unit glass formers where r_{OO} can be obtained by simple trigonometry, but not in complex glass formers where the geometry of the glass cation polyhedron is uncertain and several related polyhedra may be present. The average n_{PbO} in various glass formers is summarised in Fig. 6.16 where it is plotted as a function of PbO content in $x\text{PbO}-(100-x)\text{MO}_{z/2}$. The average n_{PbO} in PbO-GeO_2 glasses was not calculated since n_{OO} is unknown due to the presence of $[\text{GeO}_5]^-$ units. However, the Pb^{2+} ion behaves as an intermediate at compositions where $[\text{GeO}_5]$ and/or $[\text{GeO}_6]$ units are present [2].

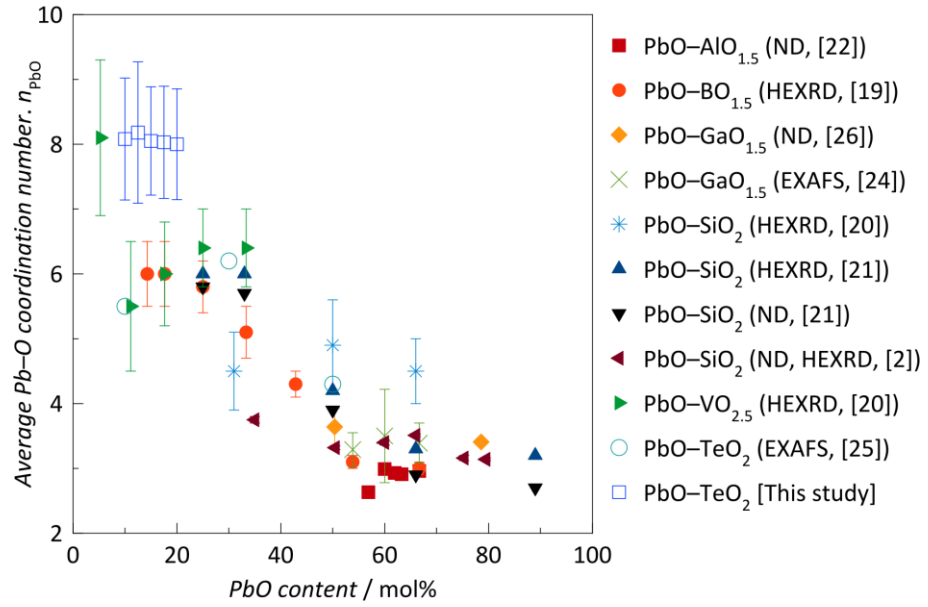


Figure 6.16: The average PbO coordination number, n_{PbO} , reported in various binary lead glasses.

Ref: d [22], b [19], e [26], f [24], a [20], c [21], h [2] and g [25].

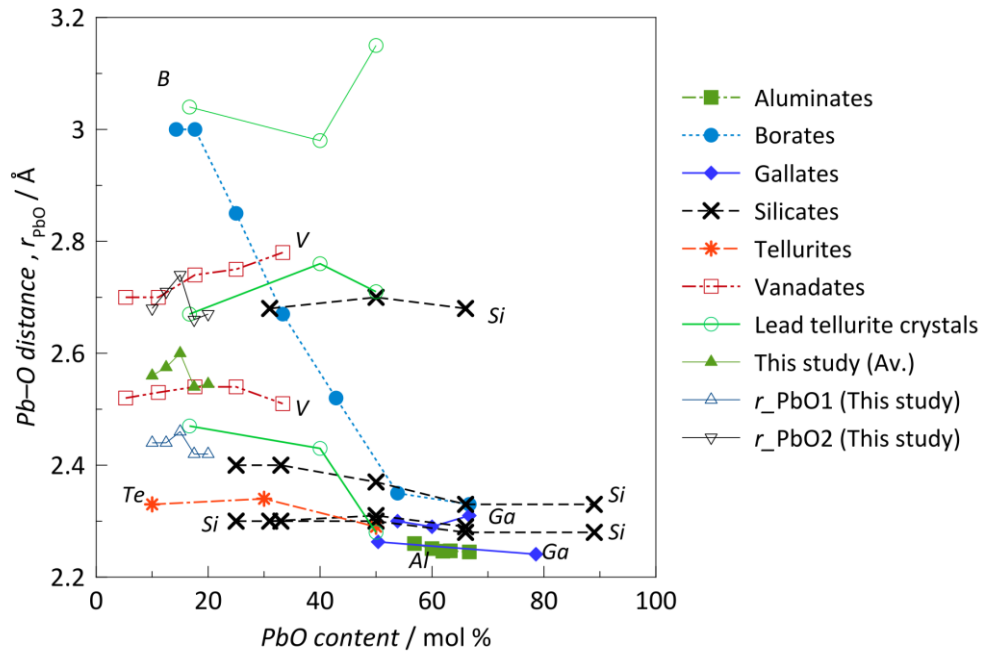


Figure 6.17: PbO distance, r_{PbO} , reported for various binary lead glasses as in Fig. 6.16 and references therein. The distances are as expected from Brese and O'Keefe [27]

Fig 6.17 shows the PbO distances, r_{PbO} , corresponding to the glasses in Fig. 6.16. A general trend is seen that, at compositions where Pb^{2+} behaves as a glass former with low coordination number, r_{PbO} is short (2.2 – 2.4 Å), and at compositions where Pb^{2+} behaves as a glass modifier, r_{PbO} is longer (>2.4 Å)

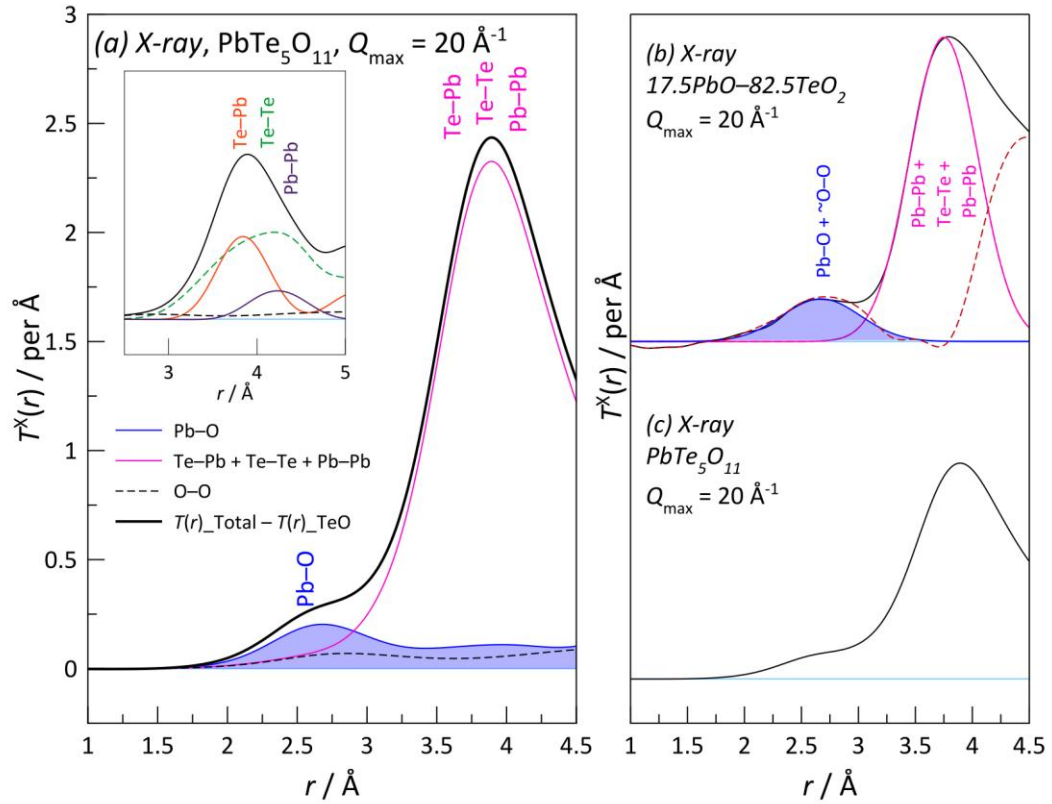


Figure 6.18: PbO and OO peaks from NXFit in 17.5PbO-82.5TeO₂ and PbTe₅O₁₁

Fig. 6.18(a) shows the simulated $T^X(r)$ for PbTe₅O₁₁ with the Te-O peaks removed. The inset in Fig. 6.18(a) shows the simulated broad peak containing the individual Te-Pb, Te-Te, and Pb-Pb peaks, whose total is shown in pink in Fig. 6.18(a) and 6.18(b). Fig 6.18(b) and Fig 6.18(c) compare the $T^N(r)$ for the 17.5 mol% PbO sample with that from crystalline PbTe₅O₁₁, in both cases after the Te-O peaks have been removed. From the comparison, the $T^N(r)$ are similar, suggesting the similarity of Pb-O and O-O environments in these two systems. As evident by the peak fitting in Fig. 6.28(b), the shoulder at about 2.5 Å in the 17.5 mol% PbO glass can be fitted with a single Gaussian to represent the sum of the Pb-O and O-O peaks, similarly to PbTe₅O₁₁ (Fig. 6.18(a)). Since n_{PbO} is ~8 for Pb²⁺ in PbTe₅O₁₁, the average n_{PbO} value in the 17.5 mol% PbO glass is assumed to be also 8, as a starting point. This can be supported by the absence of any short PbO distance in the shoulder which would correspond to the average n_{PbO} value of 2 – 3. The absence of any short Pb-O distance and the average n_{PbO} value of 8 are consistent with Pb²⁺ acting as a modifier. In Fig. 6.19, after the Pb-O peak was fitted, the residual was fitted with a broad O-O peak as well as another long Te-O(IV) peak. Once all peaks were obtained, they were “shaken” simultaneously using

the NXFit program (allowing all parameters to vary by a small fraction) so the peaks could be relaxed and a better fit could be obtained.

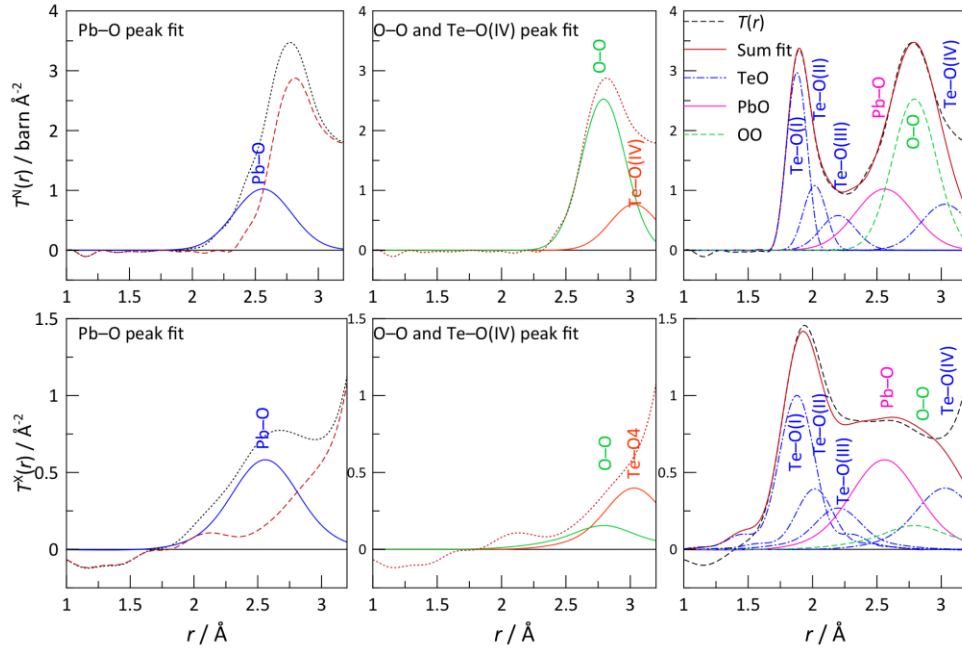


Figure 6.19: Fitted peaks for 17.5PbO-82.5TeO₂ glass from NXFit

For more accurate isolation of Pb–O, O–O and possibly Te–O peaks from 2 to 3 Å, the average n_{OO} must be calculated. However, there is not enough information to calculate the O–O distances associated with the various (and asymmetric) [TeO₄], [TeO₃₊₁], [TeO₃], and [PbO₈] units present. In PbTe₅O₁₁, where there are [TeO₄], [TeO₃₊₁], and [PbO₈] present, the r_{OO} associated with these units are shown in Fig. 6.20.

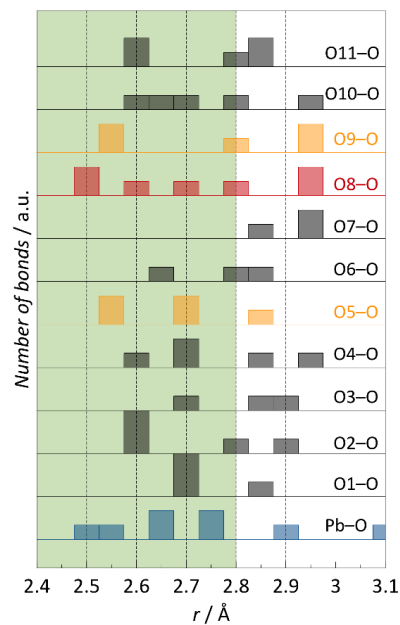


Figure 6.20: The distances of PbO and OO in PbTe₅O₁₁ from 2.4 to 3.1 Å

The short r_{Oo} ($< 2.6 \text{ \AA}$) from O5, O8, and O9 are associated with edge-sharing TeO_2 polyhedra, as shown in Fig. 6.21 and Fig. 6.22. According to Zachariasen's theory of glasses [28], this type of network connectivity is unlikely to be present, therefore, this short r_{Oo} is likely to be absent in the $\text{PbO}-\text{TeO}_2$ glasses. Typical corner-wise TeO_2 network connectivity in the glasses is shown in Fig. 6.23 when the r_{Oo} is about 2.6 \AA . Based on the absence of r_{Oo} for $r < 2.6 \text{ \AA}$, it is appropriate to fit this region with only the Pb–O peak.

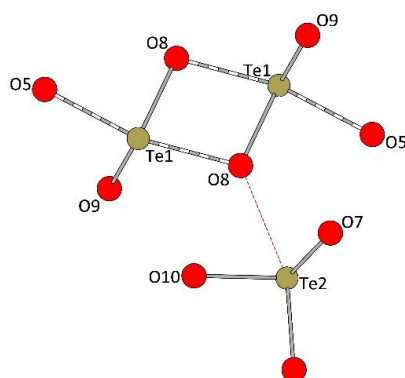


Figure 6.21: Contribution of short r_{Oo} (O8) in an edge-sharing connection in $\text{PbTe}_5\text{O}_{11}$.

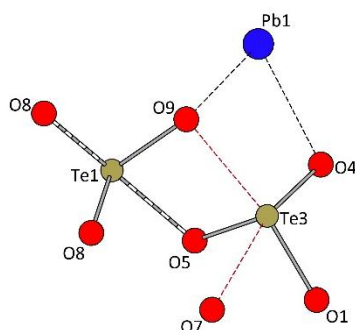


Figure 6.22: Contribution of short r_{Oo} (O9) in an edge-sharing connection in $\text{PbTe}_5\text{O}_{11}$.

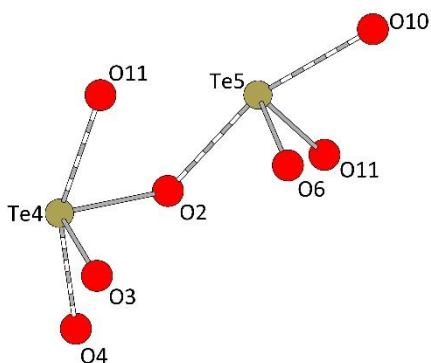


Figure 6.23: Typical corner-wise TeO_2 network connectivity in the glasses where the r_{Oo} is about 2.6 \AA .

The fit parameters obtained are shown in Table 6.5. Within the composition range covered, Pb^{2+} has a constant average Pb-O coordination number n_{PbO} of 8.08(6), which indicates that Pb^{2+} behaves as a modifier.

Table 6.5: Peak parameters for Pb-O and O-O peaks obtained from NXFit

x / mol% PbO	Pb environment			O environment
	$r / \text{\AA}$	n_{PbO}	$\langle u \rangle^{1/2}$	n_{OO}
10.0	2.57	8.08	0.26	5.62
12.5	2.58	8.18	0.23	5.46
15.0	2.59	8.05	0.24	5.40
17.5	2.56	8.03	0.22	5.02
Average	2.58(1)	8.09(7)	0.24(2)	
PbTe₅O₁₁	–	7.84	0.25	5.14

In Fig. 6.16, the average n_{PbO} values in 10 to 20 mol% PbO tellurite glasses are consistent (high average n_{PbO} , 6 – 8) with the average n_{PbO} values obtained from borates, silicates, and vanadates for the same PbO content. The trend in r_{PbO} , as a function of PbO content, is shown in Fig. 6.17 for the various PbO binary glasses, along with the r_{PbO} in crystalline $\text{PbTe}_5\text{O}_{11}$, $\text{Pb}_2\text{Te}_3\text{O}_8$, and PbTeO_3 . The shortening of r_{PbO} in high PbO content tellurite crystals is consistent with the r_{PbO} from other PbO glasses. The Pb^{2+} ion in $\text{PbTe}_5\text{O}_{11}$ (the closest crystal composition to the PbO-TeO₂ glasses) adopts a distorted $[\text{PbO}_8]$ unit as discussed in Section 4.4.4, and the Pb^{2+} environment in these glasses could be similar.

6.5.5.2 Parameterising Pb-O distances

Based on EXAFS [25] and Brillouin scattering [29] studies on PbO-TeO₂ glasses, for glasses with less than 30 mol% PbO, Pb^{2+} was found to behave as an intermediate with high average lead-oxygen coordination number ($n_{\text{PbO}} = 8$), therefore, this information is partially used in extracting the Pb^{2+} environment from the simultaneous fitting process of X-ray and neutron data using NXFit [30]. The distorted $[\text{PbO}_8]$ unit is represented by 1 average PbO distance at about 2.6 Å with a larger broadening. From Table 6.5, the width of the Pb–O peak obtained is broad to reflect the wide distribution of r_{PbO} in the glasses. The average r_{PbO} of 8-coordinated Pb^{2+} is consistent with the average r_{PbO} obtained from the fit. The asymmetric Pb–O distance (hence different Pb–O bond valences) in theory, would change the average number of Pb^{2+} ions that could be bonded to the oxygen sites. In the alkali tellurite glasses, it is assumed that there are 3 O1 sites; O1a, O1b, and O1c with different Te–O bond valences which would mean they would be coordinated to different average number of Pb^{2+} ions. However, since we do not have enough information to assign the short or long bonds to

either Pb–O1a, Pb–O1b, or Pb–O1c, we would have to assume that Pb–O1a, Pb–O1b, and Pb–O1c all have the same distance of ~ 2.62 Å (bond valence = 0.25 v.u). This distance is rather an approximation because the calculation of bond valence for Pb^{2+} is more complex due to the presence of the lone pair. However, the broad PbO peak could be further fitted with 2 peaks, consistent with the r_{PbO} found in $\text{PbTe}_5\text{O}_{11}$.

6.5.6 $\text{PbTe}_5\text{O}_{11}$ and TeO_2 glass similarity

Comparing the $T(r)$ for PbO- TeO_2 glasses with the pure TeO_2 glass and $\text{PbTe}_5\text{O}_{11}$ crystal (Fig. 6.24), a similar peak shape is observed, suggesting similarity of the Te-O distances in both systems. Similarities are also observed by comparing the $T(r)$ of $\text{PbTe}_5\text{O}_{11}$ with those from the lead tellurite glasses, especially for PbO contents higher than 16.67 mol%. $\text{PbTe}_5\text{O}_{11}$ could therefore be used in parameterising the TeO distances in TeO_2 glasses. To investigate further, Fig 6.25 shows the radial probability distribution for Te-O pairs (5 Te sites) in $\text{PbTe}_5\text{O}_{11}$. The Te1, Te3, and Te4 sites are the $[\text{TeO}_4]$ type with two longer axial and two shorter equatorial Te-O bonds as found in $\alpha\text{-TeO}_2$. The Te2 site is the $[\text{TeO}_{3+1}]$ type, with 3 shorter Te-O bonds and 1 longer Te-O bond. This is the intermediate unit from the transformation of $[\text{TeO}_4]$ to $[\text{TeO}_3]$. The Te3 site can be described as a $[\text{TeO}_3]$ unit where the average short Te-O distance is comparable to the Te-O distance as in PbTeO_3 . $\text{PbTe}_5\text{O}_{11}$ has an average n_{TeO} value of 3.70, close to the average n_{TeO} value for pure TeO_2 glass.

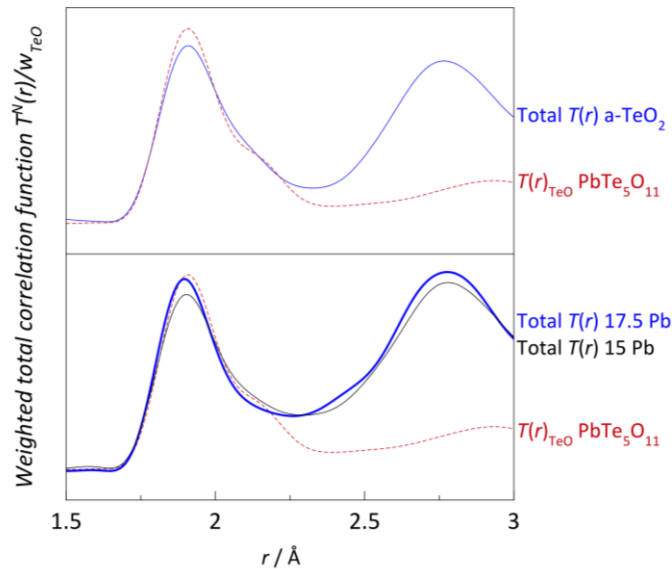


Figure 6.24: Similarity of $T(r)_{\text{TeO}}$ in pure TeO_2 glass, $\text{PbTe}_5\text{O}_{11}$, and PbO- TeO_2 glasses

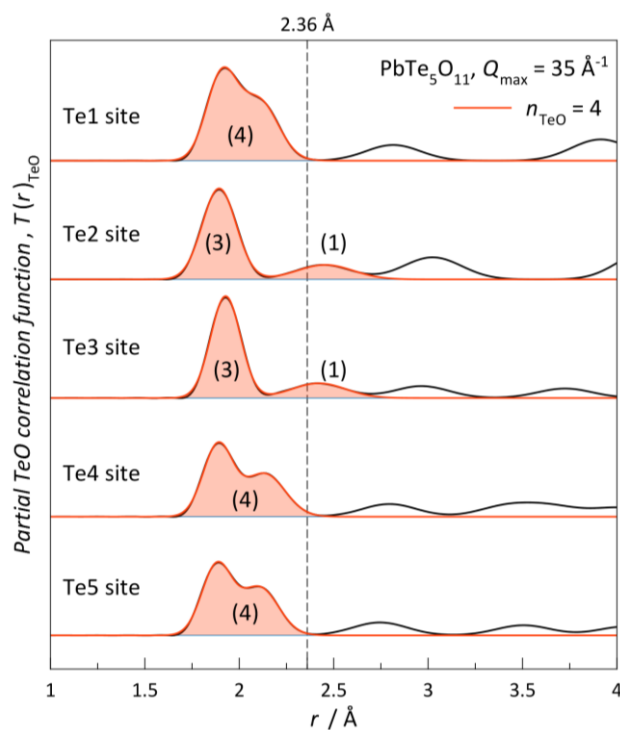


Figure 6.25: Individual TeO environment for 5 Te sites in $\text{PbTe}_5\text{O}_{11}$

6.6 Conclusions

Samples of $x\text{PbO}-(100-x)\text{TeO}_2$ glasses for $x = 10, 12.5, 15, 17.5$, and 20 mol% were successfully prepared and confirmed to be amorphous except for $x = 10$ (insignificant crystallisation) and $x = 20$ (significant PbTe_3O_7 phase present) mol%. The glass compositions were verified using EDX, where consistent loss of ~ 1 mol% of PbO was measured in all compositions. However, the compositions were treated as approximately nominal since their density values were within the scatter of values from the SciGlass database. Number density analysis revealed the tellurite anomaly in the Te and O number densities, but not Pb number density, which suggests that it is the TeO_2 network which undergoes the changes as a function of PbO content in this composition range. Raman scattering, which is sensitive to species, revealed that PbO causes the change in the TeO_2 network by transforming $[\text{TeO}_4]$ units to $[\text{TeO}_3]$ units, consistent with the alkali tellurite glasses. The semi quantitative average n_{TeO} values of PbO- TeO_2 glasses were determined to decrease similarly as in the TeO_2 glasses modified by divalent modifier cations. The average n_{PbO} obtained in the glasses, using total neutron and X-ray diffraction, is about 8 which suggests that Pb^{2+} behaves as a modifier. The average n_{TeO} extracted exhibited the plateau and post plateau regions as described by the TeO_2 Model. Due to the limitation of $Q_{\text{max}} = 20 \text{ Å}^{-1}$ for the X-ray data, the peaks are significantly broadened which makes deconvolution of the PbO peaks difficult.

Using the null lithium neutron data, combined with the neutron and X-ray data, the Pb^{2+} environment was closely examined, and found to be comparable to $\text{PbTe}_5\text{O}_{11}$. The Te environment in the plateau region is similar to that in pure TeO_2 glass. In the post plateau region, the b value was obtained, and was greater than the b value found for the $\text{Li}_2\text{O}-\text{TeO}_2$ system, though with large error bounds.

In (low) PbO content glasses in this study, the average PbO coordination number n_{PbO} is constant at 8.09(7) and the average n_{TeO} shows a plateau and post-plateau region (similar to $\text{Li}_2\text{O}-\text{TeO}_2$ glasses). Pb^{2+} ions are coordinated to 8 oxygens atoms at similar r_{PbO} distances of 2.58(1) Å. The Te environment is close to that of pure TeO_2 glass or low Li_2O content TeO_2 glass where r_{TeO} is averaged out from combinations of the asymmetric units of $[\text{TeO}_4]$, $[\text{TeO}_3]$, and $[\text{TeO}_{3+1}]$ at approximately similar fractions and distance distributions. At this composition, based on the density analysis, the glass network can be described as more open (than it is at higher PbO content). The Te environments in Pb^{2+} and Li^+ tellurite glasses for PbO and Li_2O content less than ~15 mol% are found to be similar. For PbO or Li_2O content greater than ~15 mol%, Pb^{2+} ions convert more $[\text{TeO}_4]$ to $[\text{TeO}_3]$ units than Li^+ ions as reflected by the higher b value (2.1 for Pb^{2+} than 0.8 for Li^+). This would suggest that any optical activity arising from $[\text{TeO}_n]$ polyhedra should be similar for $\text{Li}_2\text{O}-\text{TeO}_2$ and $\text{PbO}-\text{TeO}_2$ for Li_2O or PbO content of less than 15 mol% and for greater than 15 mol%, the optical activity for $\text{PbO}-\text{TeO}_2$ should be lower than $\text{Li}_2\text{O}-\text{TeO}_2$, since Pb^{2+} induces more $[\text{TeO}_3]$ units. Nonlinearity of tellurite glasses generally decreases as $[\text{TeO}_4]$ is replaced by $[\text{TeO}_3]$ units, i.e. as n_{TeO} decreases. n_{TeO} for $\text{Li}_2\text{O}-\text{TeO}_2$ glasses can be used to describe the optical activity [31] but not for $\text{PbO}-\text{TeO}_2$ glasses because the optical activity of $\text{PbO}-\text{TeO}_2$ glasses is dominated by the higher activity of PbO [31].

6.7 References

1. Stavrakieva, D., Ivanova, Y., Pyrov, J. *Journal of Materials Science* 1988, 23, 1871-1876.
2. Alderman, O. L. G. The Structure of Vitreous Binary Oxides: Silicate, Germanate and Plumbite Networks. PhD Thesis, Warwick, Warwick, 2013.
3. In *SciGlass Professional 7.3*, ITC Inc.: 2008.
4. Barney, E. R., Hannon, A. C., Holland, D., Umesaki, N., Tatsumisago, M., Orman, R. G., Feller, S. *Journal of Physical Chemistry Letters* 2013, 4, 2312-2316.
5. Oufkir, A., Dutreilh, M., Thomas, P., Champarnaud-Mesjard, J., Marchet, P., Frit, B. *Materials Research Bulletin* 2001, 36, 693-703.
6. Dewan, J. C., Edwards, A. J., Jones, G. R., Young, I. M. *Journal of the Chemical Society, Dalton Transactions* 1978, 1528-1532.
7. Champarnaud-Mesjard, J.-C., Thomas, P., Colas-Dutreilh, M., Oufkir, A. *Zeitschrift für Kristallographie. New Crystal Structures* 2001, 216, 185-186.

8. Zavodnik, V. E., Ivanov, S. A., Stash, A. I. *Acta Crystallographica Section E: Structure Reports Online* 2008, *64*, i16-i16.
9. Baynton, P., Rawson, H., Stanworth, J. *Nature* 1956, *178*, 910 - 911.
10. Kaur, A., Khanna, A., Pesquera, C., González, F., Sathe, V. *Journal of Non-Crystalline Solids* 2010, *356*, 864-872.
11. Culea, E., Vida-Simiti, I., Borodi, G., Culea, E. N., Stefan, R., Pascuta, P. *Journal of Materials Science* 2014, *49*, 4620-4628.
12. Tromel, M., Burckhardt, H., Heydarian, H., Hutzler, F., Munch, E. In *New Metastable Tellurium Oxide Phases with Highly Disordered CaF₂ Structures*, *Acta Crystallographica Section A*, 1984; pp C216-C216.
13. Silva, M., Briois, V., Poulain, M., Messaddeq, Y., Riberio, S. *J. Phys. Chem. Solids* 2002, *4*, 799-808.
14. Öveçoğlu, M., Kabalcı, İ., Özen, G., Öz, B. *Journal of the European Ceramic Society* 2007, *27*, 1801-1804.
15. Sekiya, T., Mochida, N., Ohtsuka, A., Tonokawa, M. *Journal of Non-Crystalline Solids* 1992, *144*, 128-144.
16. Kalampounias, A. G., Boghosian, S. *Vibrational Spectroscopy* 2012, *59*, 18-22.
17. Sekiya, T., Mochida, N., Ohtsuka, A. *Journal of Non-Crystalline Solids* 1994, *168*, 106-114.
18. Duverger, C., Bouazaoui, M., Turell, S. *Journal of Non-Crystalline Solids* 1997, *220*, 169-177.
19. Takaishi, T., Jin, J., Uchino, T., Yoko, T. *Journal of the American Ceramic Society* 2000, *83*, 2543-2548.
20. Hoppe, U., Kranold, R., Ghosh, A., Landron, C., Neuefeind, J., Jónvári, P. *Journal of Non-Crystalline Solids* 2003, *328*, 146-156.
21. Takaishi, T., Takahashi, M., Jin, J., Uchino, T., Yoko, T. *Journal of the American Ceramic Society* 2005, *88*, 1591-1596.
22. Barney, E., Hannon, A., Holland, D., Winslow, D., Rijal, B., Affatigato, M., Feller, S. *Journal of Non-Crystalline Solids* 2007, *353*, 1741-1747.
23. Hannon, A. C., Parker, J. M., Vessal, B. *Journal of Non-Crystalline Solids* 1998, *232*, 51-58.
24. Choi, Y. G., Kim, K. H., Chernov, V. A., Heo, J. *Journal of Non-Crystalline Solids* 1999, *246*, 128-135.
25. Silva, M. A. P., Messaddeq, Y., Ribeiro, S. J. L., Poulain, M., Villain, F., Briois, V. *Journal of Physics and Chemistry of Solids* 2001, *62*, 1055-1060.
26. Hannon, A. C., Parker, J. M., Vessal, B. *Journal of Non-Crystalline Solids* 1996, *196*, 187-192.
27. Brese, N., O'Keefe, M. *Acta Crystallographica Section B: Structural Science* 1991, *47*, 192-197.
28. Zachariasen, W. H. *Journal of the American Chemical Society* 1932, *54*, 3841-3851.
29. Chakraborty, S., Arora, A. K., Sivasubramanian, V., Krishna, P. S. R., Krishnan, R. V. *Journal of Physics: Condensed Matter* 2012, *24*, 505401.
30. Pickup, D., Moss, R., Newport, R. *Journal of Applied Crystallography* 2014, *47*, 1790-1796.
31. El-Mallawany, R. A., *Tellurite Glasses Handbook: Physical Properties and Data*; CRC Press, 2011.

Chapter 7 – Alkali borogermanate glasses

7.1 Introduction

This chapter presents preliminary results and discussion on the structures of two ternary systems, namely potassium and lithium borogermanate glasses, particularly in comparison with the structures of lithium [1] and sodium [2] borosilicate glasses, respectively. Where possible, each of the ternary alkali borogermanate glasses is compared to the relevant binary alkali borate and alkali germanate glasses. Similarities and differences between lithium and potassium borogermanate glasses are also described. This chapter describes the preparation method of the glass samples and general characterisation methods that include density measurement and energy dispersive X-ray analysis. These initial procedures are used to confirm the glass nominal composition. Subsequently, Raman scattering is used in an attempt to probe the presence of various units or species of interest in these ternary glasses. In the ^{11}B MAS NMR section, the environment of ^{11}B isotope in both lithium and potassium borogermanate glasses are studied. The average n_{BO} value obtained for each system is compared to the alkali borosilicate models of lithium [1] and sodium [2] to extract the possible mechanism of change of the B environment in borogermanate glasses. In the neutron diffraction (ND) section, total correlation functions $T(r)$ for the glasses are presented. From these $T(r)$, the average $n_{\text{BO}}(\text{ND})$ is obtained and compared to the $n_{\text{BO}}(\text{NMR})$ for both ternary systems. In a case where $n_{\text{BO}}(\text{ND})$ differs significantly from the $n_{\text{BO}}(\text{NMR})$ due to deviation from nominal stoichiometry, the actual composition of the glasses is probed using $n_{\text{BO}}(\text{NMR})$ and the EDX data (for potassium only) to enable a more accurate measurement of the average Ge-O coordination number, n_{GeO} value from the diffraction data. The average n_{GeO} for potassium and lithium borogermanate glasses are then compared and discussed in conjunction with the n_{BO} value for each system to highlight similarities and differences of the Ge environment in the two systems. For lithium borogermanate glasses, the lithium environment is derived for a few selected samples using the difference (nat – null) diffraction technique. The lithium environment is later considered in conjunction with the boron and germanium environments to obtain a consistent description of the glass structure. The chapter is concluded by summarising the general findings, followed by presentation of the short and intermediate range structural information deduced from the study (species/unit presents, average coordination number and distances).

7.2 Introduction to borate, germanate, and borogermanate glasses.

7.2.1 Borogermanate glasses

Borogermanate glasses possess useful technological properties (such as density and refractive index) suitable for uses in wave-guide systems [3]. These properties depend on the structure of the glass, partly related to the constituent borate and germanate glasses. In pure B_2O_3 glass, the glass structure is made up of $[BO_3]$ units in the form of boroxol rings linked by $[BO_3]$ [4-7]. The addition of alkali oxide will transform $[BO_3]$ to $[BO_4]^-$ until a saturation point at ~ 30 mol% [8-10]. Beyond this point, the $[BO_4]^-$ units are destroyed with the creation of $[BO_3]^-$ with non-bridging oxygen NBO [11]. The average boron-oxygen coordination number n_{BO} , will, therefore increase from 3 to a maximum value ($4 > n_{BO} > 3$) at ~ 30 mol% and later decrease to ~ 3 . Anomalies in the physical properties of the glasses [12-14] are observed, in conjunction with the behaviour of n_{BO} . The borate model, which involves the presence of various borate superstructural units has successfully described this *borate anomaly* [11, 15]. In alkali germanate glasses, as a function of alkali content, a similar *germanate anomaly* in the physical properties is also observed [16-20]. This anomaly is caused by the conversion of $[GeO_4]$ units to higher coordinated $[GeO_5]^-/[GeO_6]^-$ units [21-23]. Further addition of alkali destroys the higher coordinated units with the formation of $[GeO_4]^-$ with NBO and the glass structure will experience a decrease in n_{GeO} . The structure of ternary alkali borogermanate glasses is complicated because both boron and germanium can adopt more than one stable coordination. In addition, it is not known what preferential association of alkali with either B or Ge might occur. Therefore, this could cause unexpected changes in the structural/superstructural species formed in the glass. This thesis examines the borate and/or germanate anomaly in ternary lithium and potassium borogermanate glasses.

7.2.2 Binary alkali borate glasses [4, 7-10, 24-26]

7.2.2.1 Boron environment

In pure B_2O_3 glass, the B–O coordination number n_{BO} is 3, where the glass network is made up of all $[BO_3]$ units (Fig. 7.1) arranged in boroxol ring superstructural units connected by non-ring $[BO_3]$. As alkali oxide M_2O is added, to give a binary glass of composition $xM_2O-(100-x)B_2O_3$, $[BO_3]$ units in the boroxol ring are transformed into $[BO_4]^-$ units (one per M^+) such as in the superstructural units of tetraborate (pentaborate and triborate connected by oxygen) and diborate. For $M_2O < \sim 30$ mol%, the average n_{BO} increases due to the transformation of $[BO_3]$ to $[BO_4]^-$ according to:

$$n_{BO} = 3 + x/(100-x) \quad 7.1$$

At $M_2O > \sim 30$ mol%, the superstructural units are destroyed with the formation of $[BO_3]^-$ units, each with a non-bridging oxygen NBO. This is reflected in the decrease of n_{BO} at $M_2O > 30$ mol% as shown in Fig. 7.2. The behaviour of n_{BO} explains the anomalous change in the physical properties of the glasses.

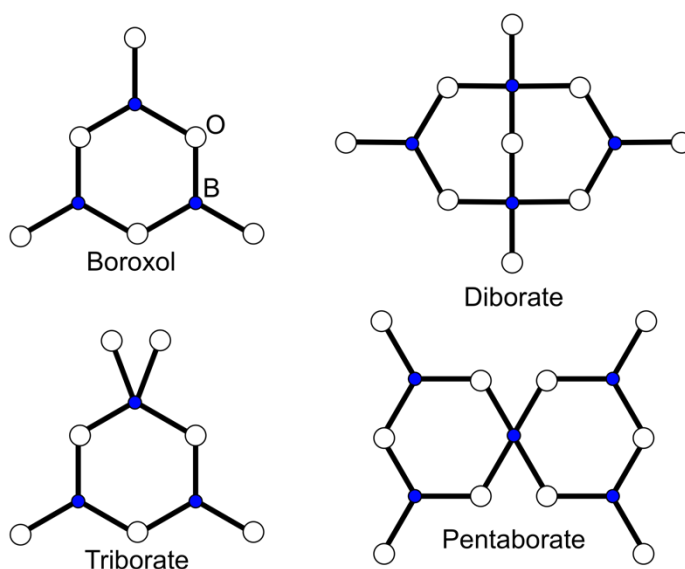


Figure 7.1: Superstructural borate units [27]

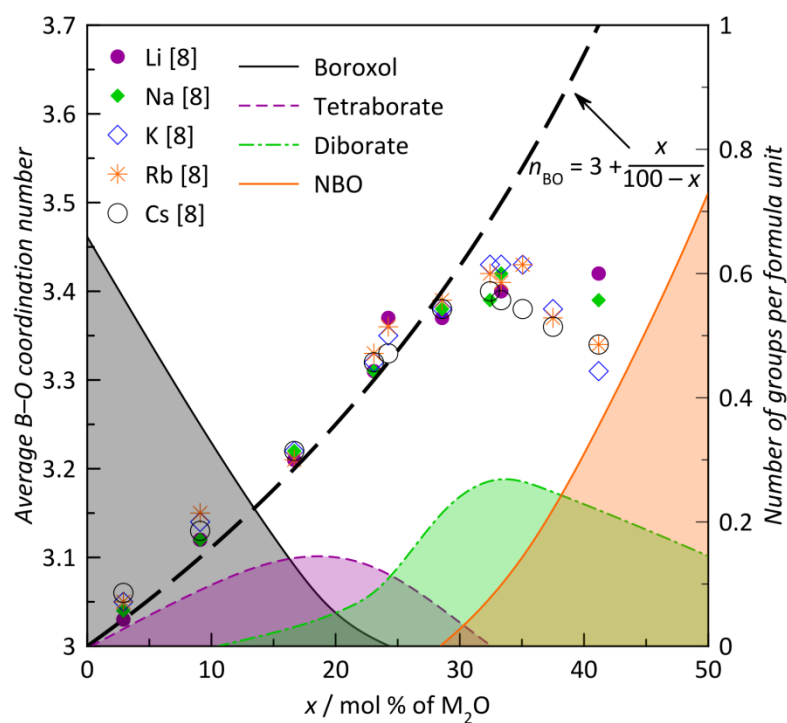


Figure 7.2: n_{BO} in alkali borates and the borate model, $n_{BO} = 3 + x/(100-x)$, n_{BO} values for Li, Na, K, Rb, and Cs were taken from [8]. The thick dashed line represents initial $[BO_4]^-$ formation (Eqn. 7.1)

In borate systems, the Raman spectra are particularly important because the technique is sensitive to the species present, rather than the averaged information of n_{BO} . Figs. 7.3 show the Raman spectra for lithium and alkali borate glasses, taken from Dwivedi and Khanna [25].

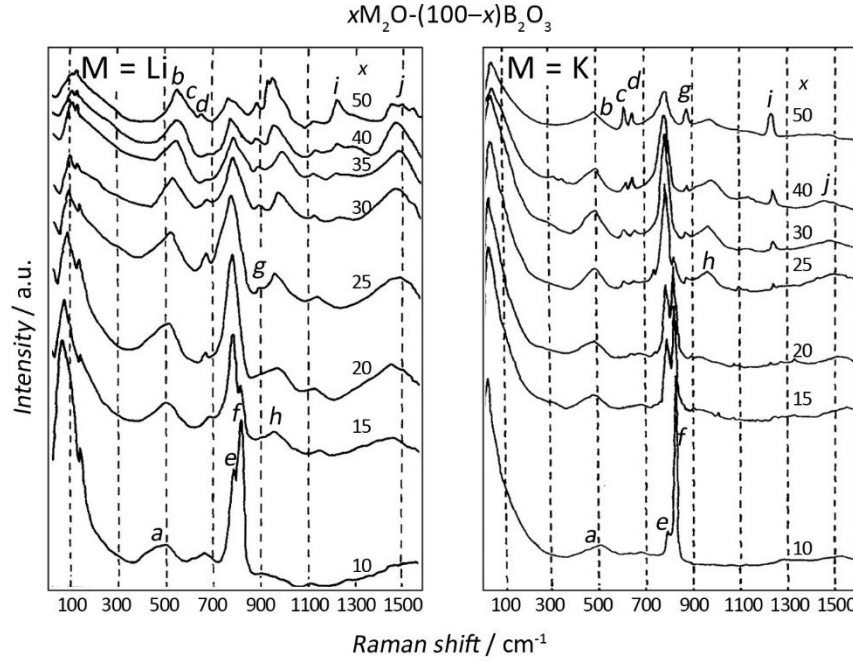


Figure 7.3: Raman spectra for lithium and potassium borate glasses, taken from Dwivedi and Khanna [25]

Table 7.1: Raman shift values for borate units [24-26, 28-29], b=broad, s=sharp.

Peak	Structural unit	Raman shift / cm^{-1}
<i>f</i>	Boroxol ring	~ 805 (s)
<i>a, e</i>	Triborate	~ 450 (b) and ~ 770 (s)
<i>a, e</i>	Pentaborate	~ 450 (b) and ~ 770 (s)
	Metaborate (Chain)	~ 720
<i>c</i>	Metaborate (Ring)	~ 630
<i>a</i>	Diborate	~ 1100 (b)
<i>i, j</i>	NBO	~ 1400 to ~ 1550 (b)

In general, the Raman spectra for alkali borate glasses are similar in terms of the vibrations present, however, the ratio of the areas is different, as discussed elsewhere [25, 30]. This is because, in alkali borate glasses, the modification of the borate network is strongly dependent on the alkali cation, especially at high alkali content [25, 29] giving the same species (superstructural units) but in different quantities. Smaller cations such as Li^+ and Na^+ , with high charge density, tend to completely disrupt the borate network into isolated units, compared to larger alkali cations. This would explain the discrepancy in the quantity of the species (qualitatively judged from the area). The region of interest of B–O vibrations in this

study is the vibration of boron to non-bridging oxygen (B–O[−]) since the detection of such units is difficult or even impossible by ¹¹B NMR or neutron diffraction. In general, in the Raman shift region of <1100 cm^{−1}, the spectrum is dominated by the vibrations of the superstructural units (containing 3 and 4-coordinated B). The vibration of B–O[−] however, is assigned to the high shift region at 1400 cm^{−1}. The complete Raman shifts associated with the structural units are shown in Table 7.1. The structural analyses of the binary alkali borate glasses are discussed elsewhere [25, 29-30].

7.2.3 Binary alkali germanate glasses [16-19, 21-22]

7.2.3.1 Germanium environment

In pure GeO₂ glass, the structure consists of 4-coordinated Ge in [GeO₄] units. When alkali oxide is added to the network, the [GeO₄] units are converted to higher coordinated Ge ([GeO₅] and/or [GeO₆]) at the rate $x/(100-x)$ without the creation of NBO. This increases the average Ge–O coordination number n_{GeO} of the system, up to a maximum value, after which, further addition of alkali oxide will create NBO as [GeO₄][−] units and n_{GeO} will decrease. The changes of n_{GeO} as a function of alkali oxide content and species formed are shown in Fig. 7.4 [31-34]. Hannon *et al.* [33] confirmed the presence of [GeO₅] rather than [GeO₆] in Cs₂O–GeO₂ glasses. Limited literature data on $n_{\text{GeO}}(x)$ in alkali germanate glasses are shown in Fig. 7.4 for K₂O–GeO₂ (neutron and x-ray diffraction) [32, 34], Na₂O–GeO₂ (neutron diffraction) [35], and Li₂O–GeO₂ (EXAFS) [31]. (Note: Two data points for $n_{\text{GeO}}(\text{K}_2\text{O})$ from this study is also included in Fig. 7.4. n_{GeO} was obtained by peak integration using the cutoff distance of 2.27 Å, where at this distance, $T(r)$ has the minimum value).

Quantification of the GeO_{*n*} (*n* = 4, 5, or 6) species by Raman is rather difficult due to the overlap of the Ge(*n*)–O vibrations (*n* is the number of O oxygen coordinated to the Ge). This may indicate the similarity of the bond parameters / environment of Ge in GeO₄ and GeO₅ and/or GeO₆. Table 7.2 summarises the Raman peak shift assignment for different Ge–O units. The low shift region 300 – 550 cm^{−1} is dominated by the vibrations of [GeO₄] species, whilst the intermediate region 600 – 750 cm^{−1} is dominated by the higher coordinated Ge species (mostly assigned to the [GeO₆] based on the alkali germanate crystals. The highest region 800 – 900 cm^{−1} includes the vibrations of O–Ge–O bridges and Ge–O[−], which makes the quantification of Ge species difficult since the bridges persist throughout the composition whilst the NBO in binary alkali germanate only starts forming at alkali oxide content >20 mol%.

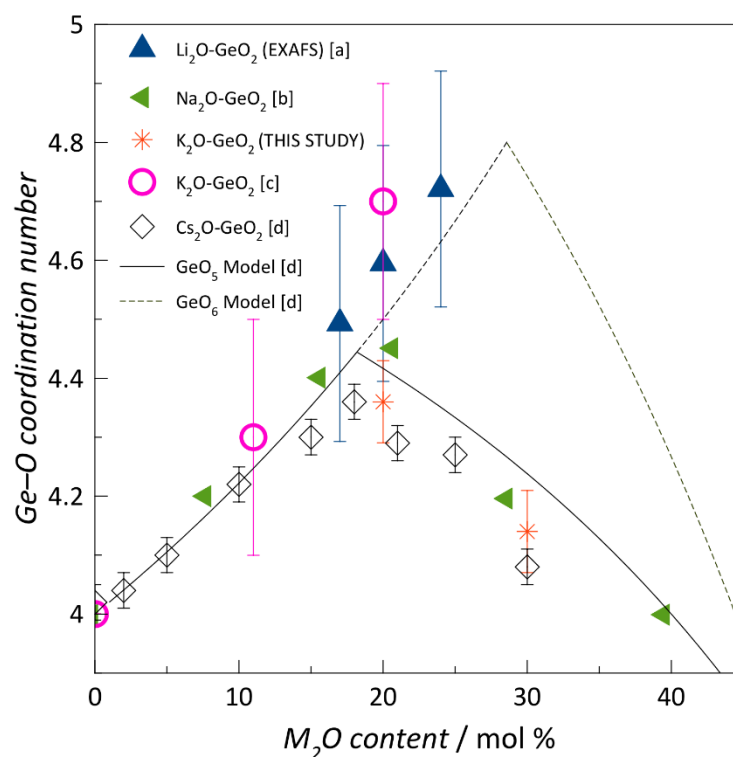


Figure 7.4: n_{BO} in alkali germanates, a[31], b[35], c[32, 34], d[33] and the germanate model [21]

As seen in Fig. 7.5, the Raman spectra are similar for low alkali content, $x < 15$ mol% in terms of both species present and their relative quantity. Beyond this composition, the spectra for lithium and potassium germanate glasses of the same composition differ in terms of relative area. This may arise from the different structural role of Li and K in these glasses, as Li are reported to behave differently from the rest of the alkali members [36]. The structural analyses of the binary alkali germanate glasses are discussed elsewhere [18-22, 31-32, 34, 36-38].

Table 7.2: Raman shift values for germanate units [19, 37-40]

Unit	Raman shift / cm^{-1}
$[\text{GeO}_4]$	~ 340 (e), ~ 440 (d), and ~ 529 (d)
Higher coordinated Ge units ($[\text{GeO}_5]$ / $[\text{GeO}_6]$)	~ 600 (d), ~ 650 (d), and ~ 745 (c)
Ge-O^- and O-Ge-O bridges	~ 800 (b) and ~ 900 (a)

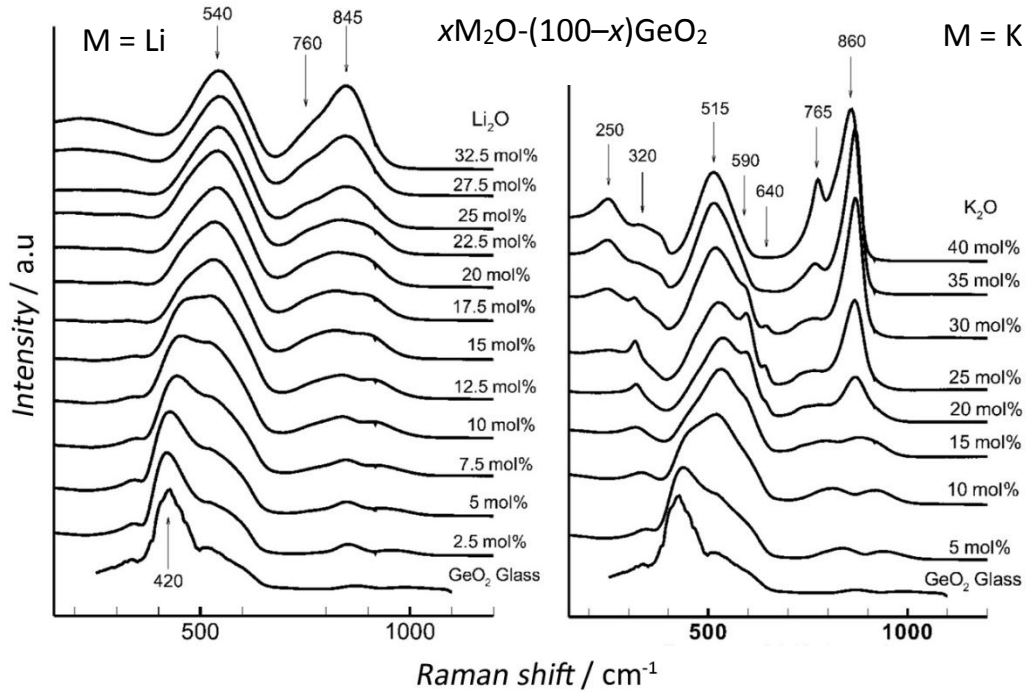


Figure 7.5: Raman spectra for lithium and potassium germanate [17].

7.2.4 Binary borogermanate glasses [41]

7.2.4.1 Borate and germanate species

In mixed glass former, binary borogermanate glasses, all boron and germanium atoms are coordinated to 3 and 4 oxygen atoms, $[\text{BO}_3]$ and $[\text{GeO}_4]$ respectively [41]. In pure B_2O_3 glass, about 75% of the $[\text{BO}_3]$ units are arranged in the boroxol ring type structure and the remaining 25% form links between the rings [42]. As GeO_2 is added to the B_2O_3 network, the boroxol ring structure is replaced by non-ring $[\text{BO}_3]$ until about 80% GeO_2 , where boron is present only as non-ring $[\text{BO}_3]$ [41]. In this study, there are three binary borogermanate base glasses with GeO_2 content >80 mol%.

Fig. 7.6 shows the distances for germanium-oxygen r_{GeO} in Ge–O–Ge and Ge–O–B environments and boron-oxygen distances r_{BO} in B–O–B and B–O–Ge environments, as optimised by Lee *et al.* using quantum chemical calculation [41]. In pure GeO_2 and B_2O_3 glasses, the r_{GeO} and r_{BO} distances are 1.75 Å (1.748 Å, as predicted by the bond valence calculation [43]) and 1.371 Å, respectively. The r_{GeO} in Ge–O–Ge connections is slightly longer in the binary borogermanate glasses, whereas r_{BO} is slightly shorter. The binary borogermanate glasses show greater intermixing (B–O–Ge) than binary borosilicate (B–O–Si), hence, the glasses are not phase separated. In the same study [41], the oxygen

clusters are not well resolved in the ^{17}O NMR, and the Ge–O–Ge fraction was seen to increase as a function of GeO_2 content.

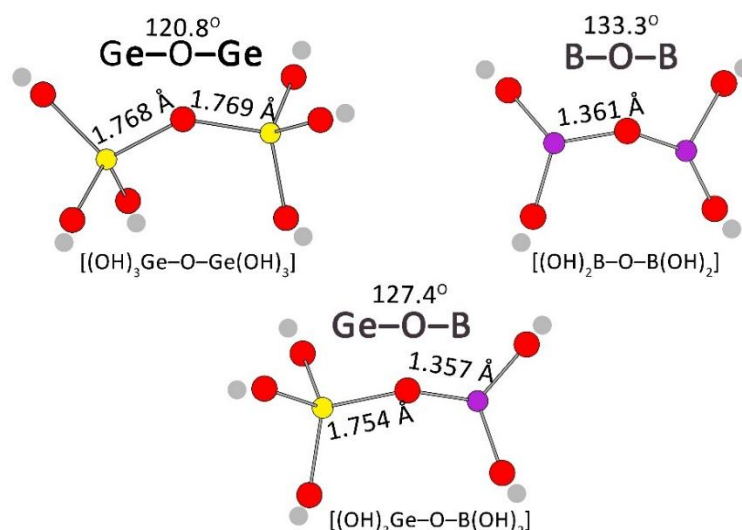


Figure 7.6: Optimised bridging oxygen environments in binary borogermanate glasses [41].

7.2.5 Alkali borogermanate glasses

Currently, there are no reports of quantitative total scattering diffraction measurements on these systems. However, complementary probes such as density [44], glass transition temperature [45-46], and Raman analysis [47-50] have been used to study the glass structure. Ma *et al.* [45] concluded a great similarity between sodium borosilicate and sodium borogermanate by comparing their density and T_g values based on the widely accepted sodium borosilicate model of Dell and Bray [2]. The Raman studies by Yoshimura *et al.* [51] and Mansour [47] agree on the distribution of alkali (Li^+) ions to both borate and germanate networks using the evidence of the observation of vibrations associated with the higher coordinated borate and germanate networks.

7.3 Sample preparation and general methodology

Glass samples were prepared from reagent grade GeO_2 (99.99 % purity), ^{11}B -enriched boric acid H_3BO_3 (99.9 % purity), and K_2CO_3 (99.9 % purity, for potassium borogermanate glasses), or Li_2CO_3 (99.9 % purity, for lithium borogermanate glasses). For preparing null lithium borogermanate glasses, the (natural) Li_2CO_3 was mixed in a specific ratio with ^6Li -enriched Li_2CO_3 (99.9 % purity). The compositions of the glasses prepared are shown in Table 7.3 and Fig.7.7. $\text{K}_2\text{O}-\text{BO}_{1.5}-\text{GeO}_2$ (KBG) glasses were prepared earlier by Dr. Diane Holland. They are labelled as $x\text{M}-y\text{B}$, corresponding to $x\text{M}_2\text{O}-y\text{BO}_{1.5}-(100-x-y)\text{GeO}_2$. $\text{g-M}_a\text{B}_b\text{Ge}_c\text{O}_d$ is a glass where the composition is similar to the crystal phase of $\text{M}_a\text{B}_b\text{Ge}_c\text{O}_d$, respectively.

Table 7.3: Alkali borogermanate glasses in this study (with EDX K/Ge value, density, and neutron exposure). Typical K/Ge error is shown in parentheses

Sample	Nominal composition			K/Ge ratio	Exposure (μA)		Density (g cm^{-3}) (± 0.0001)		
	M ₂ O	BO _{1.5}	GeO ₂	Nom, EDX	Li null (nat)	K	M = Li (nat)	M = Li (null)	M = K
GeO ₂	0	0	100	–	–	–	–	3.4724	–
10M-0B	10	0	90	–	–	–	–	–	3.8664
20M-0B	20	0	80	–	–	1000	–	–	3.6937
30M-0B	30	0	70	–	–	1000	–	–	3.3580
0M-10B	0	10	90	–	–	–	–	3.4248	–
10M-10B	10	10	80	0.249, 0.248(5)	1200	1000	3.8407	3.8378	3.7377
20M-10B	20	10	70	0.573, 0.561(5)	1200 (600)	1000	3.9147	3.9075	3.5944
30M-10B	30	10	60	1.000, 1.139(5)	1200	1000	3.6970	3.6819	3.2580
0M-20B	0	20	80	–	–	–	–	3.2713	–
10M-20B	10	20	70	0.285, 0.277(5)	1200	1000	3.6884	3.6833	3.5829
20M-20B	20	20	60	0.666, 0.722(5)	1200 (600)	1000	3.7433	3.7324	3.4290
30M-20B	30	20	50	1.198, 1.263(5)	1200	1000	3.5101	3.4966	3.1391
0M-30B	0	30	70	–	1000	–	–	3.2268	–
10M-30B	10	30	60	0.334, 0.367(5)	1200	1000	3.5199	3.5172	3.4238
20M-30B	20	30	50	0.799, 0.867(5)	1200 (600)	1000	3.5531	3.5452	3.3009
30M-30B	30	30	40	1.499, 1.337(5)	1200	1000	3.3060	3.2920	3.0271
g-KBGe ₂ O ₆	14.3	28.6	57.1	–	–	500	–	–	3.4377
g-K ₂ B ₂ Ge ₃ O ₁₁	16.7	33.5	50.0	0.667, 0.680(5)	–	500	–	–	3.3389
g-LiBGeO ₄	20	40	40	–	–	–	3.3492	3.3388	–

The oxides and carbonate were mixed thoroughly in an agate and pestle mortar for 30 minutes. The mixture was melted in a Pt/Rh crucible and heated at 5°C/min from room temperature to 1100 °C (for both potassium and lithium borogermanate glasses) and held at that melting temperature for 15 minutes before being quenched by dipping the crucible base in room temperature water. The amorphicity of the glasses was judged visually and later confirmed by the diffraction experiments. A Zeiss Supra55-VP Scanning Electron Microscope (SEM) operated at an accelerating voltage of 10 kV (Section 3.7) was used to determine the K and Ge atomic ratios of the potassium borogermanate glass samples.

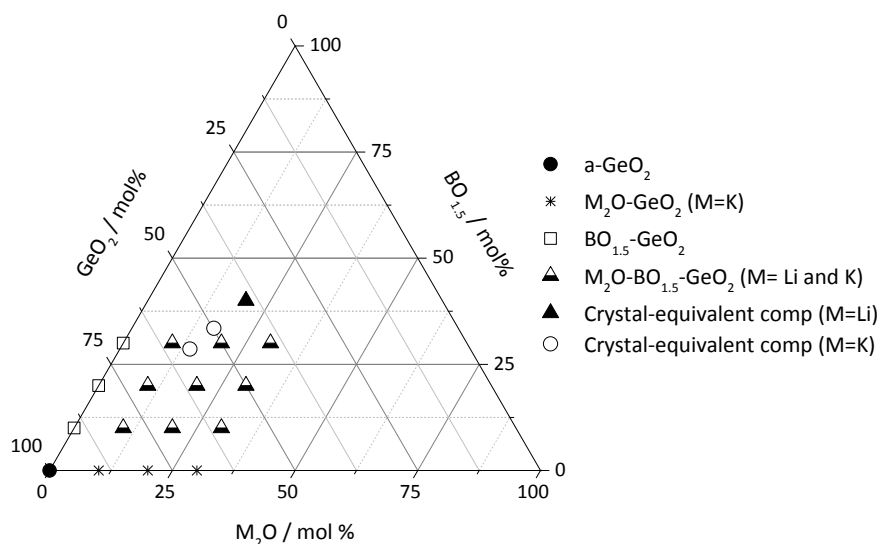


Figure 7.7: Ternary plot for nominal glass compositions in this study

A Renishaw inVia Raman Microscope, equipped with either a 514.5 nm Ar⁺ laser source or a 532 nm diode-pumped solid state laser was used to collect the Raman spectra of the potassium borogermanate and lithium borogermanate glass samples, respectively. The details of the general Raman data acquisition and processing are given in Section 3.5. However, in this chapter, semi-quantitative analysis of the spectra was not possible due to the complexity of the spectra, but a qualitative analysis was performed. High-resolution neutron diffraction data were obtained at ISIS (RAL, UK) using the GEM diffractometer (Section 2.2) on the glass samples. 4 – 7 g of the glass samples were packed into V-cans with 40 – 50 % packing. Total beam-time exposure for the samples was from 500 – 1200 μ A as shown in Table 7.3. The exposure is higher in the null lithium borogermanate glasses in order to compensate for the lower S/N ratio in the high neutron absorbing null lithium glasses. ¹¹B NMR spectra were collected using a 14.1 T Bruker Avance II+ 600 MHz spectrometer tuned to 192.3 MHz using a Bruker 4 mm probe (lithium borogermanate system) or a 14.15 T Varian spectrometer using a 4 mm Varian T3 probe tuned to 193.1 MHz with magic angle spinning (MAS) frequency 12 kHz in both cases. BPO₄ was used as a secondary reference material with chemical shift -3.3 ppm with respect to the primary reference boron trifluoride ether (BTE). More details on NMR are given in Section 3.10. From the EDX analysis (only for the M = K glasses), the glass composition can be estimated only from the ratio of K to Ge, due to the inaccuracy of the detection of B and O using X-rays. The ratio of K/Ge is calculated from each nominal composition (ignoring B and O), and compared with the K/Ge ratio obtained from the EDX analysis.

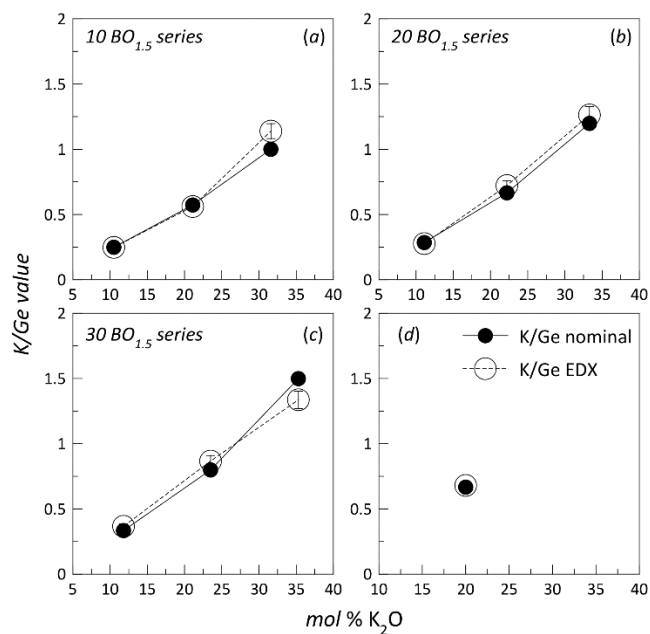


Figure 7.8: K/Ge ratio from EDX and nominal composition

Fig. 7.8 shows the comparison of the EDX K/Ge and the nominal K/Ge ratio. For an EDX K/Ge ratio lower than the nominal K/Ge ratio, the glass composition can be assumed to have lost some K₂O, and vice versa if GeO₂ is lost due to the volatilisation. These calculated losses are used in neutron diffraction analysis to estimate the error in the average coordination number.

7.4 Density

7.4.1 Results

Table 7.3 shows the density values of the glasses for the nominal compositions. 10M-Ge, 20M-Ge and 30M-Ge are the binary alkali germanate glasses; 0M-10B, 0M-20B, and 0M-30B are the binary borogermanate glasses, whilst the rest are the ternary potassium and lithium borogermanate glasses, as labelled. In general, the densities of the potassium borogermanate glasses are lower than the corresponding lithium borogermanate glasses for the same composition, despite containing the more massive potassium atom. This may arise from the structural origin in the glasses. The differences between the density values for the natural and null lithium borogermanate glasses are small, as expected to arise from the small difference in the molecular masses due to the different ratios of ⁶Li and ⁷Li isotopes.

7.4.2 Binary borogermanate glasses

Fig. 7.9 shows the density (a), molar volume (b), and number densities (c – e) for the binary borogermanate glasses. The values measured (half-coloured triangles) are compared to those from the SciGlass database [52] (open circles). The glasses used in this study are GeO_2 -rich, hence, the density value and its molar volume are dominated by the GeO_2 network. The density decreases as heavier GeO_2 is replaced by lighter $\text{BO}_{1.5}$. The rate of decrease however is not linear. The straight line in each figure connects $\alpha\text{-GeO}_2$ (all $[\text{GeO}_4]$ units) and crystalline, $c\text{-B}_2\text{O}_3$ (all non-ring $[\text{BO}_3]$ units). In the density plot, if the borogermanate glasses had units as found in these end oxides, the density would decrease as described by the line. The cubic fit of the SciGlass data overlaps with this line from 0 to 33.3 mol% $\text{BO}_{1.5}$ content.

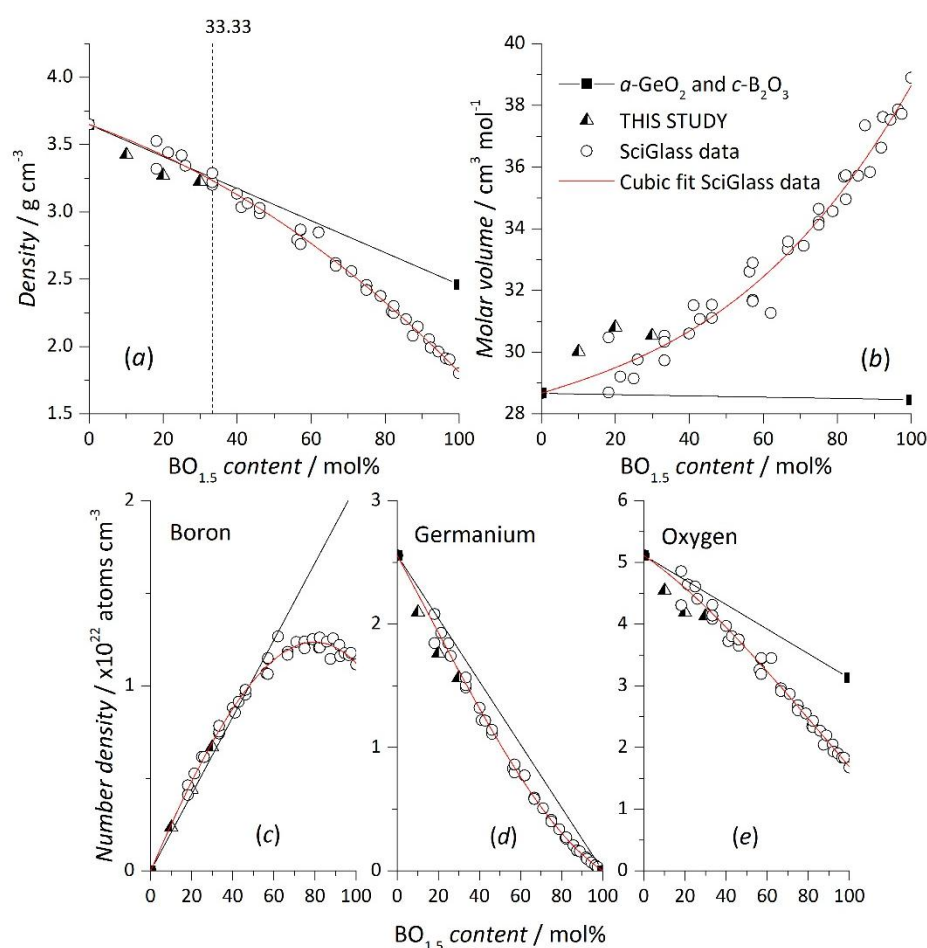


Figure 7.9: The density value and its derivatives for the binary borogermanate glasses

This suggests that, within this composition range, the $[\text{GeO}_4]$ and $[\text{BO}_3]$ units present are similar to those in $\alpha\text{-GeO}_2$ and $c\text{-B}_2\text{O}_3$ phases. From the NMR studies of binary borogermanate glasses, boroxol ring $[\text{BO}_3]$ units were not observed below about 30 mol% $\text{BO}_{1.5}$ [41]. Beyond ~ 33.33 mol% $\text{BO}_{1.5}$, the density values deviate from the straight line and

continue to decrease to the density value corresponding to pure B_2O_3 glass. The pure B_2O_3 network is characterised by its ring and non-ring $[BO_3]$ units. Therefore, it could be inferred that the deviation of the density values is due to the formation of the boroxol ring units in the glasses. The binary glasses in this study however contain some air bubbles, which decrease the density values measured. Deviation from nominal composition could also contribute to the discrepancy, however, this is very unlikely, since for the glasses to have lower values, the losses must be attributed to GeO_2 (which is less probable since GeO_2 is less volatile than B_2O_3), and furthermore, those density values (for $10BO_{1.5}$ - $90GeO_2$ and $20BO_{1.5}$ - $80GeO_2$) would indicate the loss of about ~ 10 mol% GeO_2 .

Fig. 7.9 (b) shows that, as $BO_{1.5}$ replaces GeO_2 , the molar volume increases, nonlinearly, similar to the trend observed in the density plot. Initially, the glass structure expands approximately linearly as one non-ring $[BO_3]$ replaces one $[GeO_4]$. Beyond about 30 mol%, planar boroxol $[BO_3]$ rings, with higher molar volume, also form, increasing the average molar volume of the glass more rapidly. The values for the samples in this study are seen to be higher than the cubic fit line, as a consequence of having the lower density values. From the number density plots, the number densities for Ge and O decrease almost linearly as GeO_2 content decreases, whilst B deviates strongly indicating that the borate network is responsible for most of the changes in the binary borogermanate glasses. It will be shown later in this chapter that the borogermanate binaries are significantly different from the ternary alkali borogermanates.

7.4.3 Ternary alkali borogermanate glasses

In cases of binary glasses, glass compositions can be estimated by comparison with SciGlass data. For the ternary glasses, however, because of the limited data from the SciGlass database for similar compositions, measured density values can only be compared with those interpolated from the contours in the 3D plots which will not be accurate. Data are therefore presented in Fig 7.10 in the form of pseudobinaries of fixed $BO_{1.5}$ content.

Fig. 7.10 shows the density plots for the lithium and potassium borogermanate glasses. The data for Li are open symbols, with closed symbols for K. Binary alkali borate and germanate glasses are represented by blue and red, respectively. 10B series (10 mol% $BO_{1.5}$), 20B series (20 mol% $BO_{1.5}$), and 30B series (30 mol% $BO_{1.5}$) are represented by green, orange, and purple, respectively.

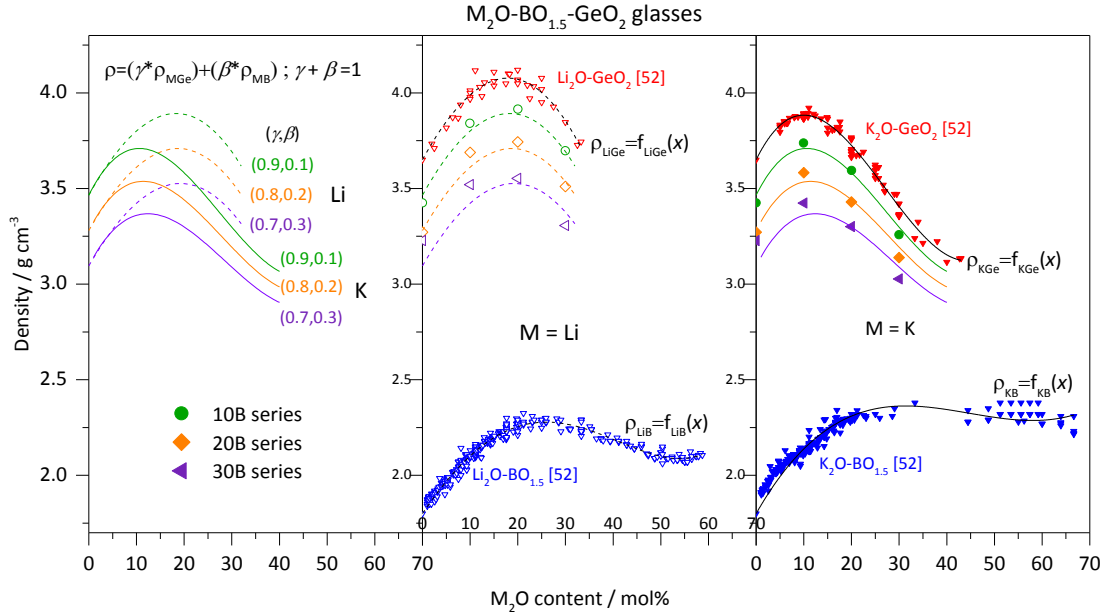


Figure 7.10: Density plot for lithium and potassium borogermanate glasses

The density values for the ternary lithium and potassium borogermanate glasses are closer to their respective binary germanate glasses than the binary borate glasses. This is expected since, as seen in Table 7.3, the alkali borogermanate glasses used in this study contain more GeO_2 than B_2O_3 (minimum 2.5: 1, and maximum 16:1 ratio of $\text{GeO}_2\text{:B}_2\text{O}_3$). As $\text{BO}_{1.5}$ content increases (for fixed M_2O content), density decreases, because the heavier GeO_2 is replaced by lighter $\text{BO}_{1.5}$. For fixed $\text{BO}_{1.5}$ content, as M_2O is increased, the change in density is similar to the binary alkali germanate, reflecting the increasing interconnectivity due to the formation of higher coordinated germanate species [53]. For increasing $\text{BO}_{1.5}$ content (fixed M_2O) the decrease in the density suggests that the dominance of the germanate network is diluted by the borate networks suggesting a possible intermixing of borate-germanate networks.

In Fig. 7.11, for the binary potassium borate and germanate glasses, the molar volumes decrease to a minimum value and then increase, whereas for lithium it only decreases. This is due to the difference in the sizes of Li^+ (1.67 Å) and K^+ (2.43 Å), resulting in the non-is structural induced changes [44]. The smaller Li^+ enables it to enter existing voids in the glass network, causing the molar volume to be smaller than for the larger K^+ , which has to push the glass network apart. The molar volumes of the alkali borogermanate glasses in the figure are closer to the alkali germanate glasses, mainly because the glass composition is predominantly germanate. However, as the $\text{BO}_{1.5}$ content is increased, the molar volume of the alkali borogermanate glasses increases, due to the introduction of the borate network

with much higher molar volume value. Assuming ideal behavior, the solid lines fitting the data points for the ternary glasses in Fig 7.11 are calculated from a weighted summation of the contributions from the binaries:

$$\rho = (\gamma)\rho_{\text{MGe}} + (\beta)\rho_{\text{MB}}; \gamma + \beta = 1 \quad (7.2)$$

where γ and β are the fractions of the binary germanate and borate contributions, respectively. These show quite good agreement with the experimental data points but there are discrepancies which suggest a greater complexity than a simple combination of two networks – i.e. these are not two-phase mixtures on whatever scale.

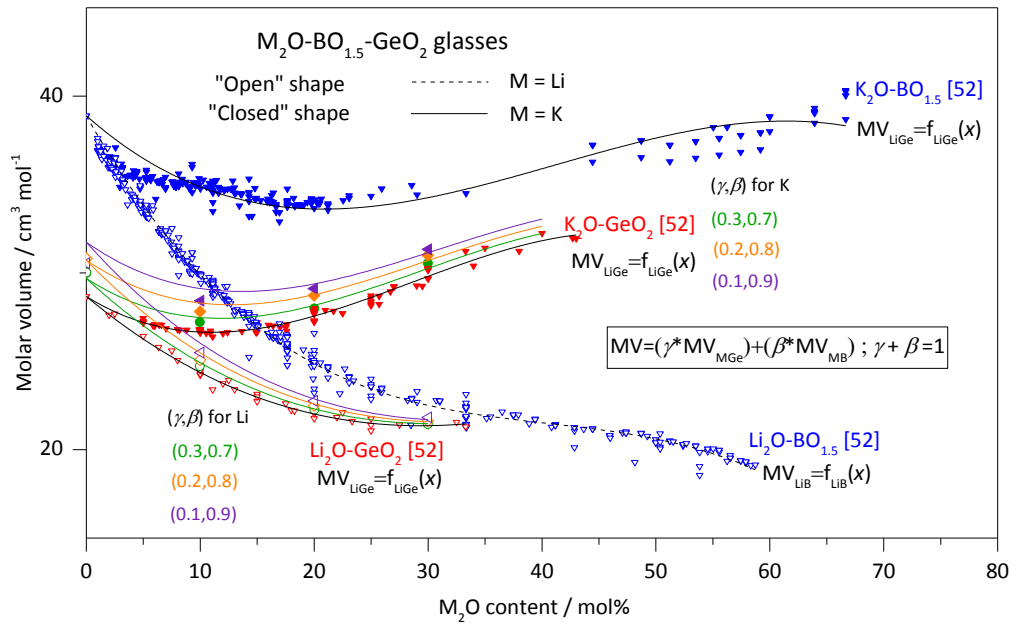


Figure 7.11: Molar volume plot for lithium and potassium borogermanate glasses

Figs. 7.12 (a) and (b) show the number density plots for B and Ge atoms for the lithium and potassium borogermanate glasses. Again, they illustrate the ease of packing of Li compared to K in both the binaries and ternaries. The solid (for K) and dashed (for Li) lines fitting the ternary data points are weighted sums of the binaries and their effectiveness suggests that the added alkali ions associate with both network formers. It is notable that there is very good agreement for the B number density but less good for Ge. The number density for B atom in 10, 20, and 30 mol% $\text{BO}_{1.5}$ series can be simulated by using β values of 0.2, 0.4, and 0.6, respectively, which corresponds to the values of 20, 40, and 60 mol% $\text{BO}_{1.5}$, twice as high as expected for simple mixing of non-interacting networks (phase separation).

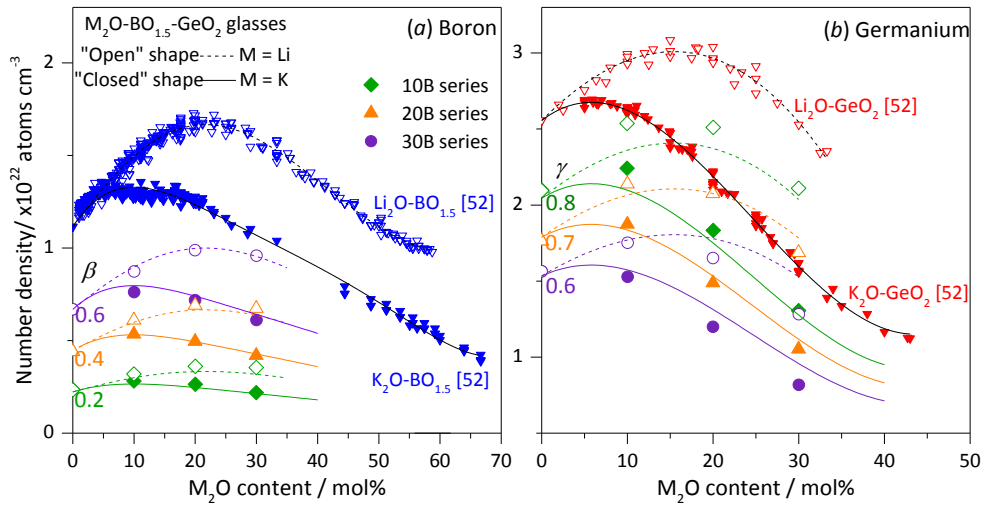


Figure 7.12: Number density plot for B and Ge in lithium and potassium borogermanate glasses

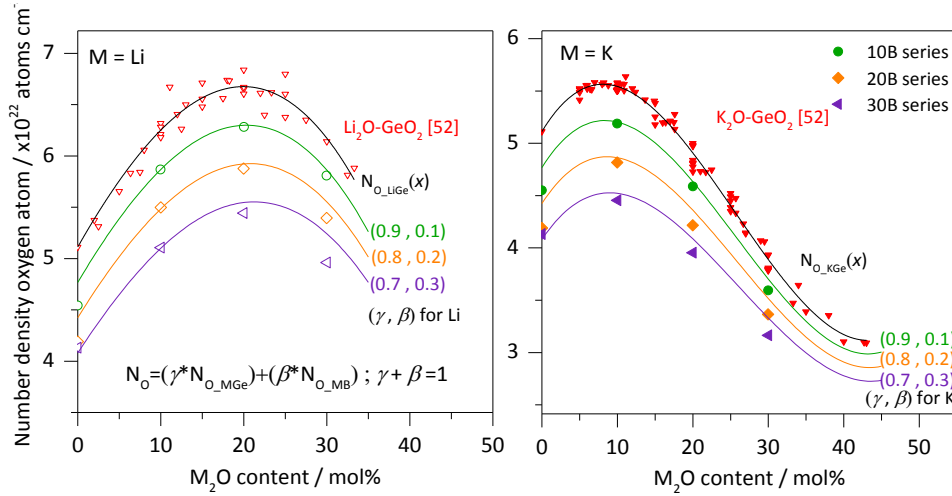


Figure 7.13: Number density plot for O in lithium and potassium borogermanate glasses

Fig. 7.13 and 7.14 show the number density of O and M (Li and K) respectively. For O, the number density changes in a similar manner to the binary germanate, but at lower number density, due to being diluted by the introduction of borate structures into the germanate network. For M (Li and K), the same trend (dilution) is also observed. The solid lines in these figures (connecting the data point for the ternary glasses) are the weighted sum of both borate and germanate binaries. For Li, the factor β used is consistent with the percentage of $\text{BO}_{1.5}$ present. The same applies for K except for the highest K_2O content in each $\text{BO}_{1.5}$ series, where the percentage of borate contribution is higher. This could simply mean that Li^+ and K^+ are associated equally to both borate and germanate networks, except for 30% K_2O where association of K^+ to the borate network is higher than it is to the germanate network.

With better accuracy and consistency of density data, using this simple relationship, the changes in the density can be quantitatively attributed to originate from the constituent network. Thus, both B and Ge changes are affected by the M^+ ion.

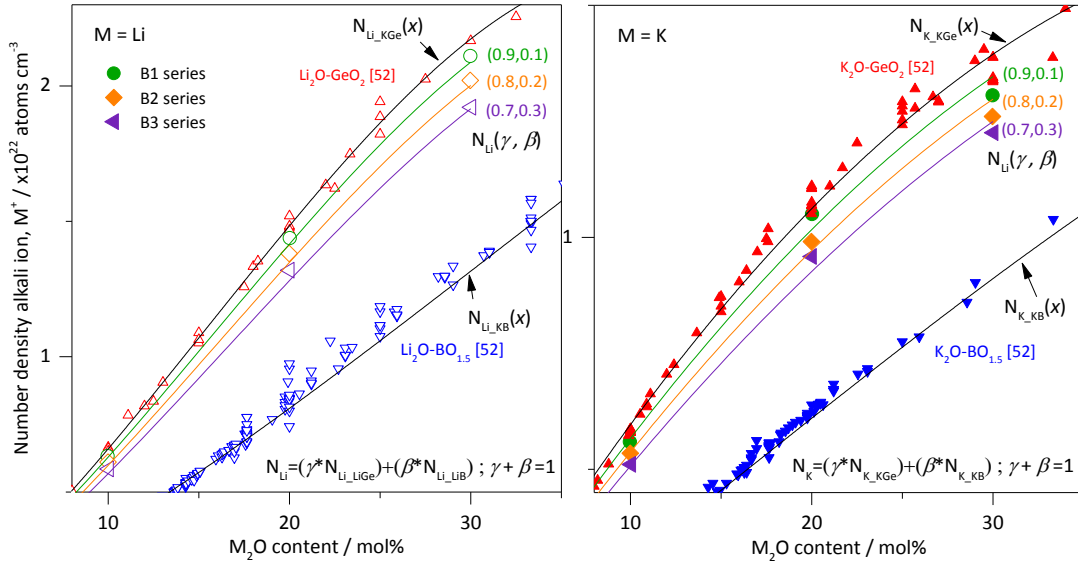


Figure 7.14: Number density plot for Li and K in lithium and potassium borogermanate glasses

7.5 Raman scattering

7.5.1 Introduction

In the literature, the number of Raman studies of these borogermanate glasses is limited to lithium [47] and potassium [48-49]. Mansour [47] conducted a study on a series of glasses with fixed Li_2O content (42.5 mol%) while increasing the GeO_2 content at the expense of B_2O_3 . No anomaly was observed in the density value (linear decrease), revealing that average density is a simple contribution from each oxide by a specific factor and Li^+ is distributed into both borate and germanate networks [47]. For the potassium borogermanate glasses, the study was conducted on high B_2O_3 content (65 and 85 mol %). From the Raman analysis, it was concluded that K^+ goes to mainly borate sites and NBO units (for $\text{K}_2\text{O} > 20$ mol%) are associated with germanate sites rather than the borate sites [48]. In both systems, the Raman spectra are described as being a superposition of the vibrations of the borate and germanate species. In this section, the Raman spectra will only be analysed qualitatively, due to overlapping, which makes species quantification difficult and inaccurate. The ternary potassium borogermanate glasses will be compared with binary potassium germanate glasses to deduce similarities and differences between these two systems. Later on, the potassium borogermanate glasses will be compared with the lithium

borogermanate glasses, though the comparison will be difficult since even in binary borates or germanates, Li^+ behaves differently than K^+ ion. The main purpose of the Raman spectra analysis is to probe the presence of vibrations associated with the NBO units (which, for borate, do not overlap with any other vibration)

7.5.2 Binary borogermanate glasses

Fig. 7.15 compares the experimentally obtained Raman spectra with the simulated spectra (based on pure B_2O_3 and GeO_2 glasses). In other words, the simulated spectra would resemble phase separated binary borogermanate glasses. As seen in Fig. 7.15 (a), the spectra are dominated by the germanate network, due to the compositional factor. The Raman shifts for the Ge–O vibrations are in the lower range, $< 600 \text{ cm}^{-1}$ (Figs. 7.15 (b) and (c)), whereas the B–O vibrations are in the higher range, specifically at $\sim 800 \text{ cm}^{-1}$ (for the boroxol ring) (Fig. 7.15 (d)).

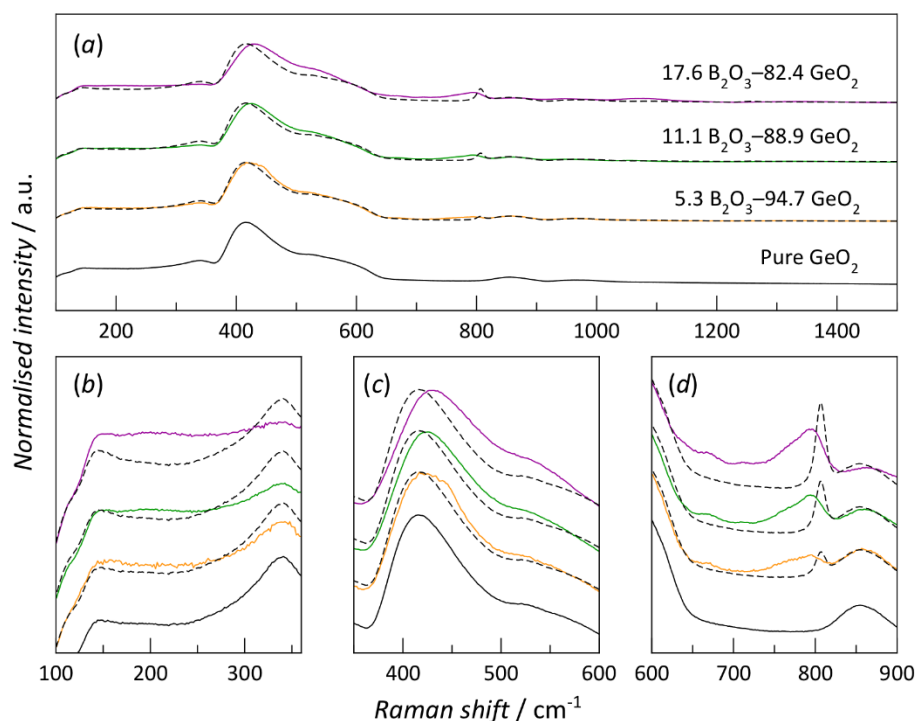


Figure 7.15: (a) Raman spectra of pure GeO_2 glass (solid black line) and binary borogermanate glasses (solid colour lines) with their simulated spectra from pure GeO_2 and pure B_2O_3 glasses (dashed lines); (b), (c), and (d) are the same spectra divided into 3 regions: 100–360, 300–600, and 600–900 cm^{-1} to highlight the region of interest for Ge–O and B–O vibrations.

The vibrations of $[\text{GeO}_4]$ units in a ring structure give the principal peaks at about $\sim 350 \text{ cm}^{-1}$, $\sim 450 \text{ cm}^{-1}$, and 550 cm^{-1} , as discussed previously in the introductory section of this chapter. As B_2O_3 is increased, the vibrations associated with the $[\text{GeO}_4]$ unit in a 6-membered ring

structure, particularly at $\sim 450\text{ cm}^{-1}$ decrease, suggesting the disruption of the rings. A consequent, increase in the vibration associated with smaller (3-membered) ring structure at about 500 cm^{-1} occurs. The vibration of $[\text{BO}_3]$ species, Fig. 7.12 (d) ($\sim 800\text{ cm}^{-1}$), is seen to move to lower Raman shift, indicating that the B–O bond strength is getting weaker. This simply means that the rigid B–O in the boroxol ring is transformed into less rigid B–O in the non-ring units.

7.5.3 Lithium borogermanate glasses

Due to the experimental setup limitation, these spectra were collected at lower laser power (compared to potassium borogermanate spectra, though comparable to the Raman spectra of Mansour [47]). To reduce the effect of noise in these spectra, they were smoothed. The region $250 - 1000\text{ cm}^{-1}$ in Fig. 7.16, is heavily overlapped with various Ge–O and B–O vibrations, causing peak parameterisation to be inaccurate. For simplification, the spectra are divided into regions (I, II, and III) as shown in Fig. 7.17. Region I covers the vibrations from $[\text{GeO}_4]$, $[\text{GeO}_5]/[\text{GeO}_6]$, pentaborate and metaborate units, Region II covers the vibrations from $[\text{GeO}_5]/[\text{GeO}_6]$, Ge–NBO, Ge–O–Ge, pentaborate, metaborate, boroxol ring, and diborate units, and Region III covers the vibration of B–NBO.

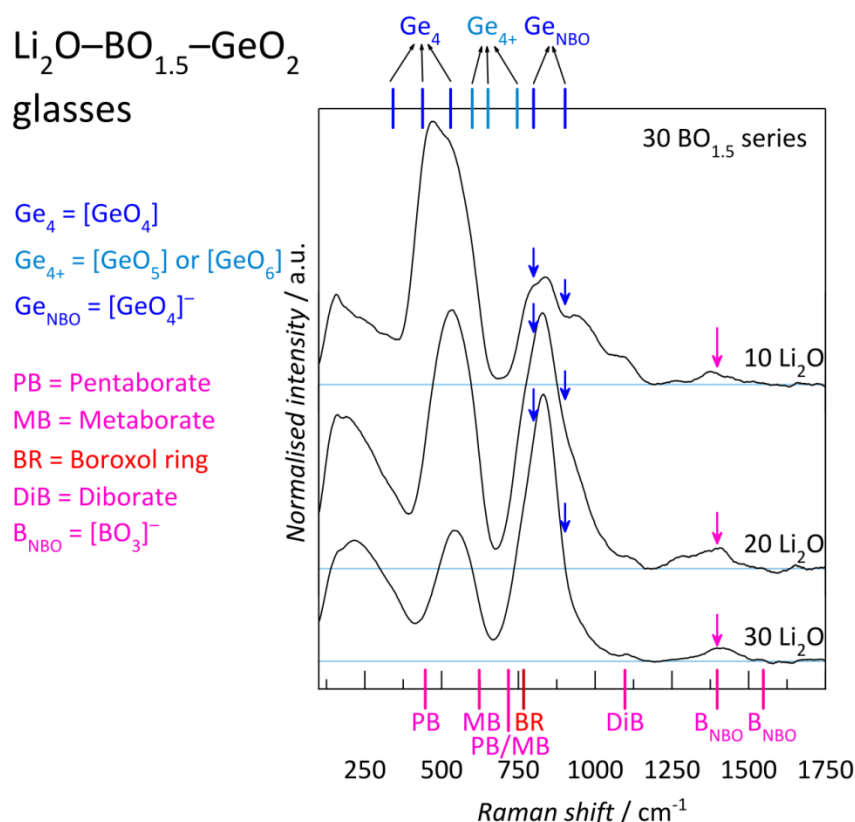


Figure 7.16: Assignment of borate and germanate vibrations in lithium borogermanate glasses

In this particular section, the region of interest is the third region where the vibration from B–NBO is clearly visible. As seen in Fig. 7.17, for low $\text{BO}_{1.5}$ content, vibrations in Region III are almost negligible. The peak starts to appear in the 20 $\text{BO}_{1.5}$ series and becomes more significant in the 30 $\text{BO}_{1.5}$ series. This may suggest that within these compositions, there is formation of non-bridging oxygens associated with the borate network. This however is subjective to the baseline selection. The reliability of determining the presence of NBO units in these glasses will be discussed later in the neutron diffraction section.

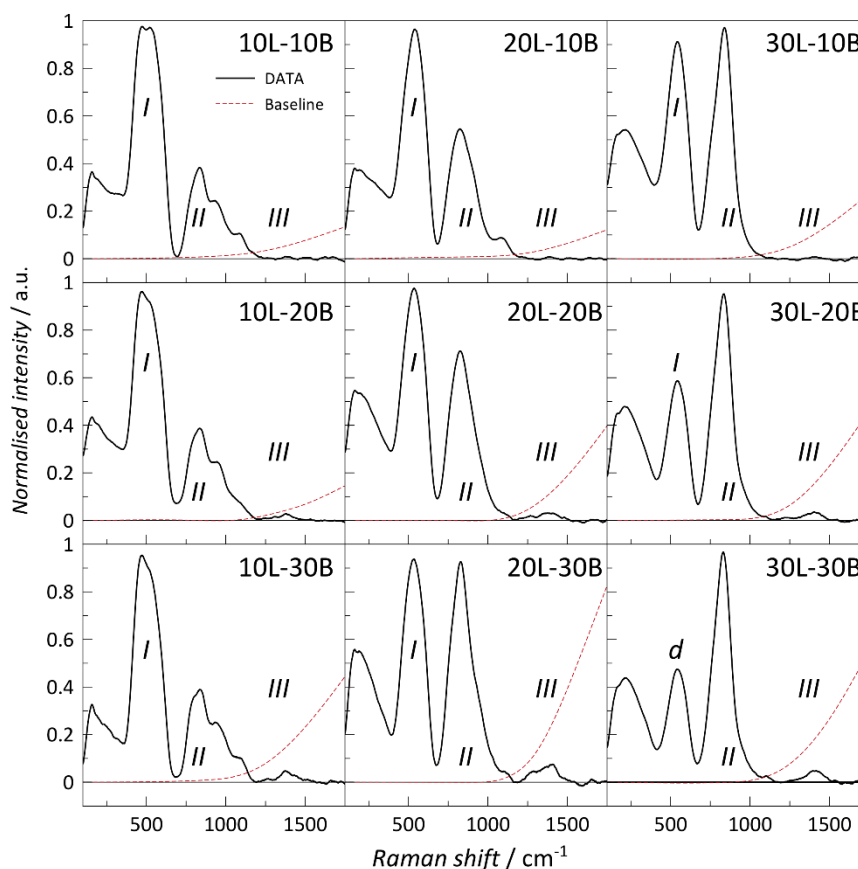


Figure 7.17: The Raman spectra of the lithium borogermanate glasses.

Figure 7.17 shows the Raman spectra for the lithium borogermanate glasses, grouped by Li_2O content. The general shape of the spectra for 10, 20, and 30 Li_2O series resemble the binary lithium germanate glasses of the same composition, due to the compositional factor since these glasses are mostly germanate. Within the 10 Li_2O group, there is no significant systematic change to the spectra as GeO_2 is replaced by $\text{BO}_{1.5}$. In 20 and 30 Li_2O group however, a decrease in the Ge–O vibrational region is observed whilst an increase is observed in the B–O vibrational region. It should be noted that within this vibrational region of B–O, there are some contributions from Ge–O vibrations as well. However, it is only logical

to assign the changes in the peak shape due to B-O vibrations since any change associated with Ge-O vibration should be decreasing. From these spectra, since changes can be attributed to both borate and germanate network, it can be inferred that Li^+ is affecting both borate and germanate networks.

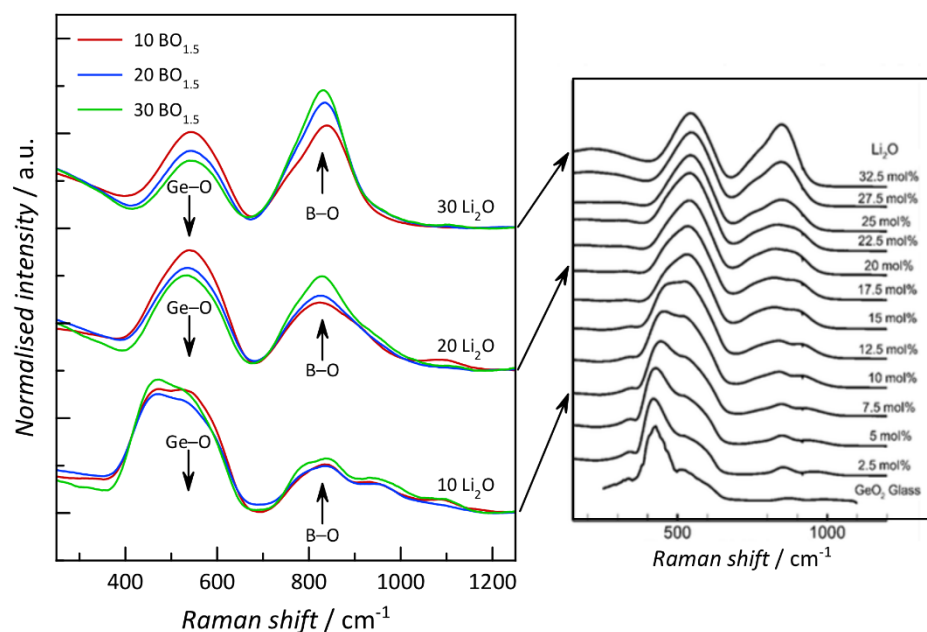


Figure 7.18: LBG Raman spectra compared to LG, taken from Henderson [17].

7.5.4 Potassium borogermanate

Unlike for lithium borogermanate glass, the Raman spectra for the potassium borogermanate and potassium germanate glasses were collected using a setup at an optimum laser power, hence quantification will be slightly more accurate. The spectra were reduced (Section 3.5) and normalised to the total area. Figs. 7.19 compare the Raman spectrum for each ternary potassium borogermanate (KBG, red line) to the binary potassium germanate (KG, dashed black line) for the same K_2O content. The purpose of the comparison is to see how similar the Raman spectra are for the Ge-rich glasses to the germanate glasses of the same K_2O content. The comparison is however, not straight forward since the proportion of K_2O units associated with the germanate group may not be similar to the binary KG glasses for the same K_2O content.

The vibrations of each borate and germanate species are discussed in detail in Section 7.2.2.1 and 7.2.3.1. For simplicity, Fig. 7.19 marks only the vibrations of the units of interest, with the vertical lines. From the left, a solid black line ($_{6R}\text{Ge}$) arises from the Ge-O vibration in 6 membered $[\text{GeO}_4]$ rings (420 cm^{-1}). Moving to the right, the thick blue strip

marks the vibration of Ge-O units in 3-membered $[\text{GeO}_4]$ rings. These lines, fall within the horizontal arrow (marked as GeO_2), showing the vibrations mostly due to the $[\text{GeO}_4]$ units. Next, at about 770 cm^{-1} , the orange thick line indicates the vibration of $[\text{BO}_4]$ units (could be in triborate, tetraborate, or pentaborate groups). Overlapping this is a vibration from Q^2 species (marked with the black line). This species is a $[\text{GeO}_4]$ species with 2 non-bridging oxygens. The dash-dotted blue line at 800 cm^{-1} is the contribution from non-ring $[\text{BO}_3]$, whereas the Q^3 line at 865 cm^{-1} is associated with the $[\text{GeO}_4]$ unit with 1 nonbridging oxygen.

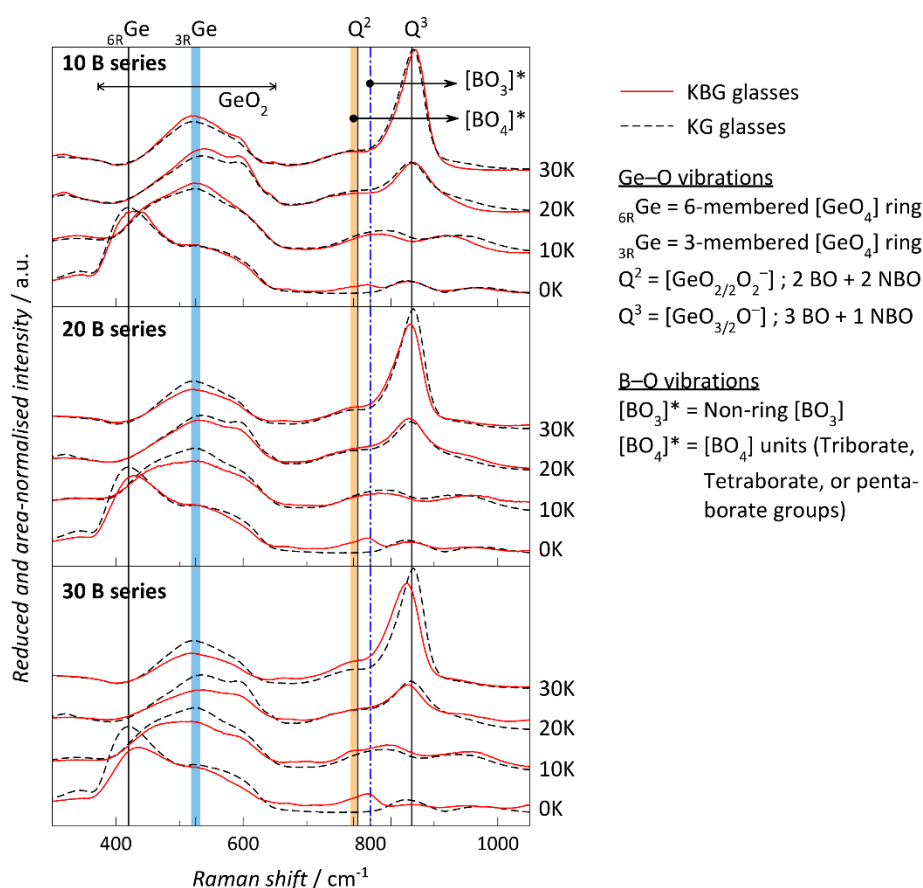


Figure 7.19: Raman spectra for potassium borogermanate glasses, compared to potassium germanate glasses

In general, the Raman spectra of the ternary Ge-rich KBG glasses are very similar to the binary potassium germanate glasses, especially for low $\text{BO}_{1.5}$ content (10 mol% $\text{BO}_{1.5}$). Detection of B-O vibrations in the Raman spectra seems to be impossible. This is because, for 10 and 20 mol% K_2O series, in the region of interest for the B-O vibration, the spectrum for the KBG is very similar to KG. In fact, it is only the $30\text{K}_2\text{O}-30\text{BO}_{1.5}-40\text{GeO}_2$ sample which shows significant difference from the binary $30\text{K}_2\text{O}-70\text{GeO}_2$.

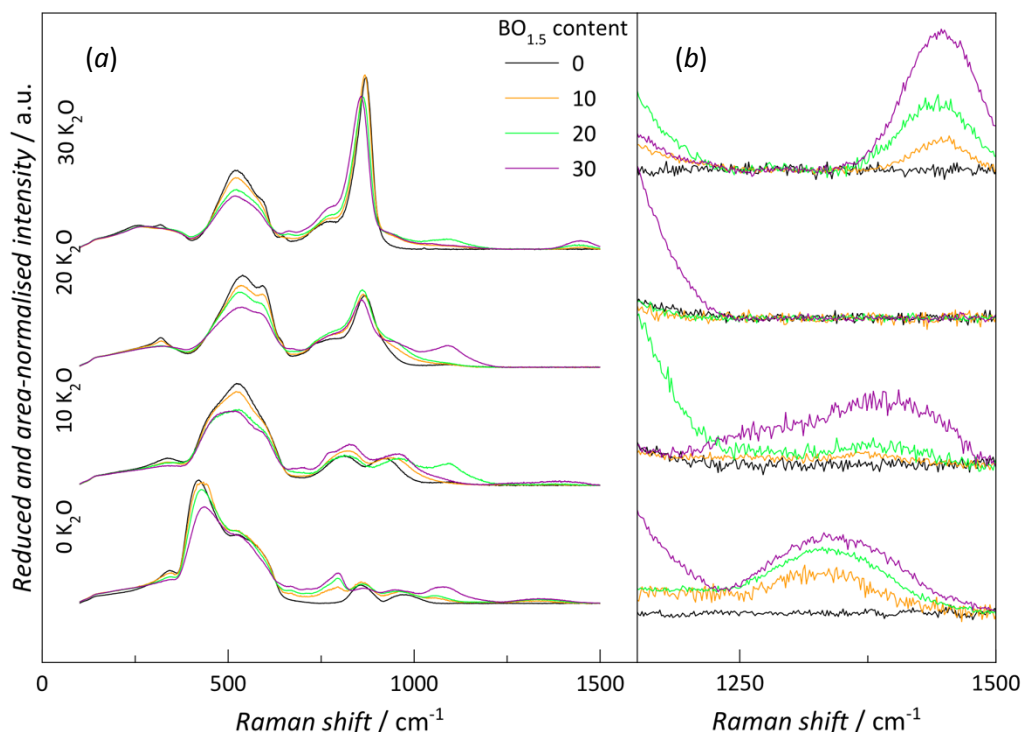


Figure 7.20: Vibrations of B-O associated with NBO in KBG glasses

Fig. 7.20 (a) groups the Raman spectra for the potassium borogermanate according to K_2O content. Unlike LBG, the Ge-O vibrational region for KBG shows systematic decrease with decreasing GeO_2 content. The higher frequency region ($700 - 1000\text{ cm}^{-1}$) however shows no systematic change. In LBG, the changes in this region were attributed to the changes in the borate network. This could suggest that Li and K change the B network differently. In Fig. 7.20 (b), for high K_2O content, there is a contribution from possibly a $B-O^-$ at about 1400 cm^{-1} , a typical range for $B-O^-$ in binary alkali borate glasses. However, for 10 K_2O group, there is a peak at the high frequency range as well, this peak may be the residual peak from the binary borogermanate glasses, as seen in the figure.

7.6 ^{11}B MAS NMR

7.6.1 Introduction

A thorough understanding of the behaviour of boron in binary alkali borate glasses is essential when studying the behaviour of B in the more complex ternary alkali borogermanate glasses (MBGe). In addition, it is also helpful to consider its environment in the more widely studied alkali borosilicate glasses (MBSi) which are structurally simpler than MBGe in the sense that only B changes its coordination number and $n_{SiO} = 4$, whereas in

MBGe, both B and Ge could change their environments, as observed in the binary borate and germanate glasses.

In alkali borate glasses, n_{BO} (from ^{11}B NMR [8]) is alkali dependent at high alkali content, with the lighter ions (Li and Na) producing a higher fraction of 4-coordinated $[BO_4]$ units compared to the heavier ions (K, Rb, and Cs). The lighter alkali borates also produce just one $[BO_4]$ peak whilst that from the heavier alkali borates is split. While the peak width is seen to vary as a function of the alkali content for the lighter atoms, it seems to be independent of the alkali content for the heavier atoms. This suggests a size dependent change in the borate network where Li and Na, being smaller in size, are incorporated differently than the larger K, Rb, and Cs ions.

In MBSi glasses, the environment adopted by B is affected by the alkali oxide to boron oxide ratio ($R = M_2O/B_2O_3$), and the silicon oxide to boron oxide ratio ($K = SiO_2/B_2O_3$). Fig 7.21 shows the structural models (n_{BO} v R) proposed, from ^{11}B NMR data, for lithium [1] and sodium [2] borosilicate glasses. Initially, in terms of the N_4 value, Li and Na affect the borosilicate structure in a similar fashion to the binary alkali borate glasses (as characterised by the $n_{BO} = 3 + R$ line). However, beyond a certain R -value which is dependent on K , N_4 v R is different for Li and Na, indicating some difference in the mechanism of incorporation of Li and Na in the mixed glass former network.

In sodium borosilicate glasses (NBS), all the Na^+ ions go initially to the borate network, ($N_4 = R$ until $R = 0.5$). For convenience, Dell and Bray *et. al* [2] assumed these 4-coordinated $[BO_4]$ units to be in the diborate superstructural unit, supported by the presence of the Raman peaks associated with this unit [2]. This process however extends to a higher R value than in the binary alkali borate glasses giving a new maximum value for N_4 at $R = \frac{1}{2} + K/16$. This is caused by the combination of the alkali ion with some of the diborate groups to form a reedmergnerite-like boron-silicon group (Fig 7.22) until all the SiO_2 is used up at $R = \frac{1}{2} + K/16$. From this point until $R = \frac{1}{2} + K/4$, N_4 stays constant at $\frac{1}{2} + K/16$ because the Na^+ added are taken up by the reedmergnerite group by the creation of NBO on Si (Q^3). The process of NBO creation is completed when the reedmergnerite group takes an additional of 1.5 Na_2O molecules which translates to the end value of $R = \frac{1}{2} + K/4$. Beyond this point, Na^+ ions combine with the remaining diborate and reedmergnerite groups to create NBO on pyroborate units (via the formation of metaborate units) and in the case of reedmergnerite, pyroborate and Q^2 unit (of SiO_2) are formed, at the fractions of $(2 - K/4) / (2 + K)$ and $(K + K/4) / (2 + K)$, respectively. As a consequence, N_4 decreases linearly as a

function of R and K . In general the N_4 (expressed as n_{BO} , where $n_{BO} = 3 + N_4$) can be summarised as:

$$n_{BO} \begin{cases} R < 0.5 & = 3 + R & \text{"Diborate"} & (1) \\ 0.5 < R < (\frac{1}{2} + \frac{K}{16}) & = 3 + R & \text{"Reedmergnerite + Diborate"} & (2) \\ (\frac{1}{2} + \frac{K}{16}) < R < (\frac{1}{2} + \frac{K}{4}) & = 3 + \frac{1}{2} + \frac{K}{16} & \text{"Reedmergnerite + NBO}_{Si} + \text{Diborate"} & (3) \\ (\frac{1}{2} + \frac{K}{4}) < R < (2 + K) & = 3 + ((K - 8) / 16)(R + K - 2) & \text{"Pyroborate + Q}^2\text{"} & (4) \end{cases}$$

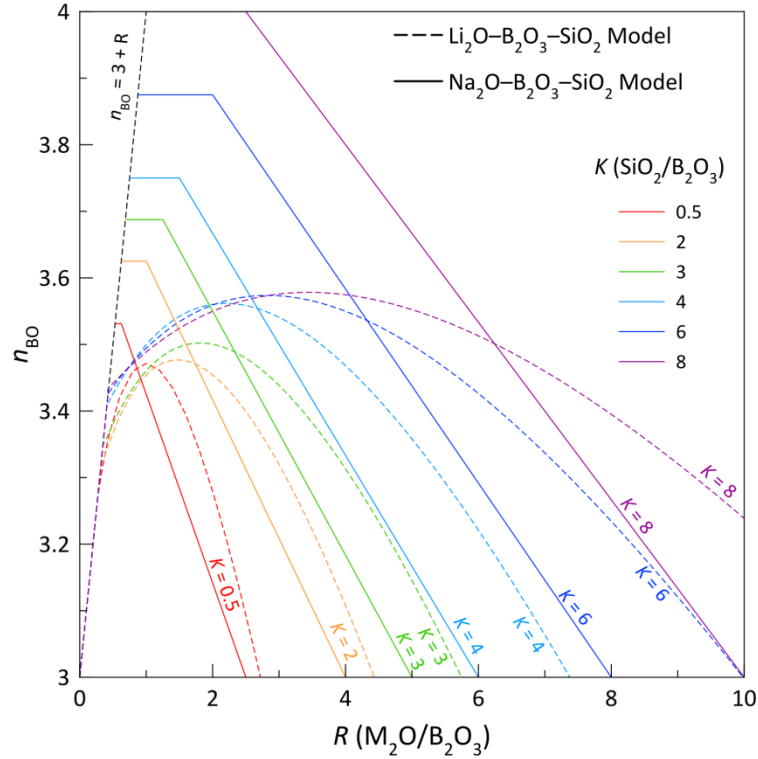


Figure 7.21: The lithium [1] and sodium [2] borosilicate models for n_{BO}

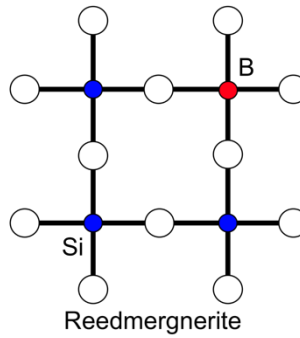


Figure 7.22: The reedmergnerite group, taken from [27]

In lithium borosilicate glasses (LBS), for low Li content, N_4 changes similarly to the sodium borosilicate glasses ($N_4 = R$) until a certain value R_c . Initially, NBO units form in the glass, which are associated with $[BO_3]$ units, but not $[SiO_4]$ units; in NBS, this is not the case since the formation of NBO is delayed by the formation of the reedmergnerite groups. In LBS

however, the model does not suggest the formation of the reedmergnerite unit, as evidenced by the low N_4 value (compared to NBS). Beyond R_c (which is obtained by computer simulation), Li^+ is distributed to both B and Si sites, similarly to the NBS glasses. The Li^+ in the B sites is shared by the $[\text{BO}_4]$ and $[\text{BO}_3]$ (with NBO) units, with β being the fraction of Li^+ associated with the $[\text{BO}_3]$ units with NBO. The value of n_{BO} in the LBS glasses can be summarised as follows:

$$n_{\text{BO}} \begin{cases} R < R_c & = 3 + R & (1') \\ R > R_c & = 3 + \left(R_c + \left[\frac{R - R_c}{1 + K} \right] \right) \left(1 - \frac{\beta [(R - R_c) / (1 + K)]}{1 + R + K} \right) & \text{where } \beta = 1.8 + 2.42K & (2') \end{cases}$$

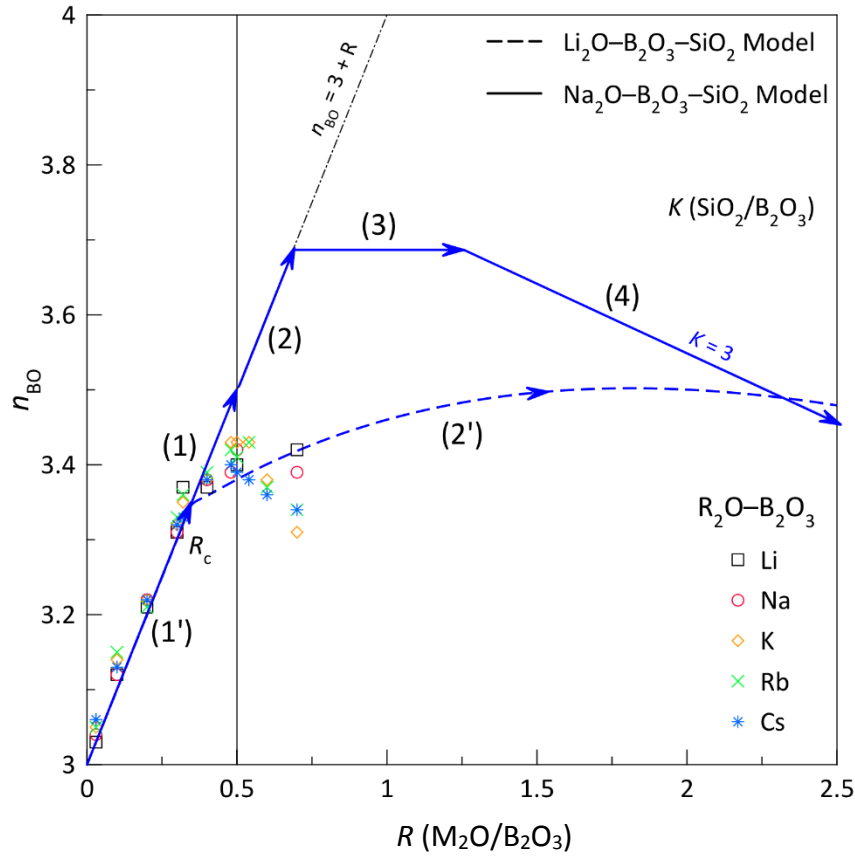


Figure 7.23: The mechanism of alkali distribution in borosilicate network

As a summary from these Dell and Bray *et. al.* [2] and Zhong *et al.* [1] models for alkali borosilicate glasses, for low Li and Na content, all the alkali ions are distributed into the borate network as in the binary glasses. In NBS, the N_4 is extended to a higher value due to the formation of the reedmergnerite groups whereas in LBS, the group is not reported to form. Another important point is, Si does not change its coordination number in the borosilicate glasses. In this study of borogermanate glasses, both B and Ge could adopt a higher coordination state without the creation of NBO. Because no models of the ternary

borogermanate glasses have been reported, it seems fairly reasonable to compare the ternary borogermanate glasses with the ternary borosilicate glasses. The process of alkali distribution in the borosilicate network is summarised as in Fig. 7.23.

7.6.2 ^{11}B NMR Results

7.6.2.1 Binary borogermanate glasses

Fig. 7.24 shows the ^{11}B MAS NMR spectra for vitreous B_2O_3 and binary borogermanate glasses, confirming the presence of only $[\text{BO}_3]$ units. The line shapes and chemical shifts of the $[\text{BO}_3]$ units in the binary borogermanate glasses are similar to each other, but noticeably different from vitreous B_2O_3 , where about 75% of $[\text{BO}_3]$ are in the 3-membered boroxol ring units and 25% connect the rings [42]. In the binary borogermanate glasses, it has been shown that boroxol ring units are absent below about 33.33 mol% $\text{BO}_{1.5}$ [41]. These glasses could be regarded as base glasses for the ternary alkali borogermanate glasses used in this study but the very high melt temperatures required to make them indicate that structural equilibria may be quite different in the absence of alkali oxide.

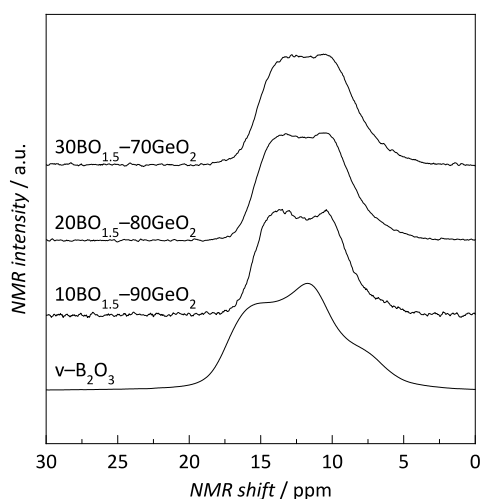


Figure 7.24: ^{11}B MAS NMR spectra for vitreous B_2O_3 and binary borogermanate glasses

7.6.2.2 Lithium and potassium borogermanate glasses

Figs. 7.24 show the NMR spectra for the lithium and potassium borogermanate glasses. As seen in the figure, there are two peaks present in the regions 20 – 5 ppm and 5 – 0 ppm, which can be attributed to the $[\text{BO}_3]$ and $[\text{BO}_4]$ units, respectively. The n_{BO} values were calculated from the ratio of the intensities of the peaks ($n_{\text{BO}} = 3 + N_4 = 3 + [\text{BO}_4]/([\text{BO}_4] + [\text{BO}_3])$) and are presented as in Table 7.4

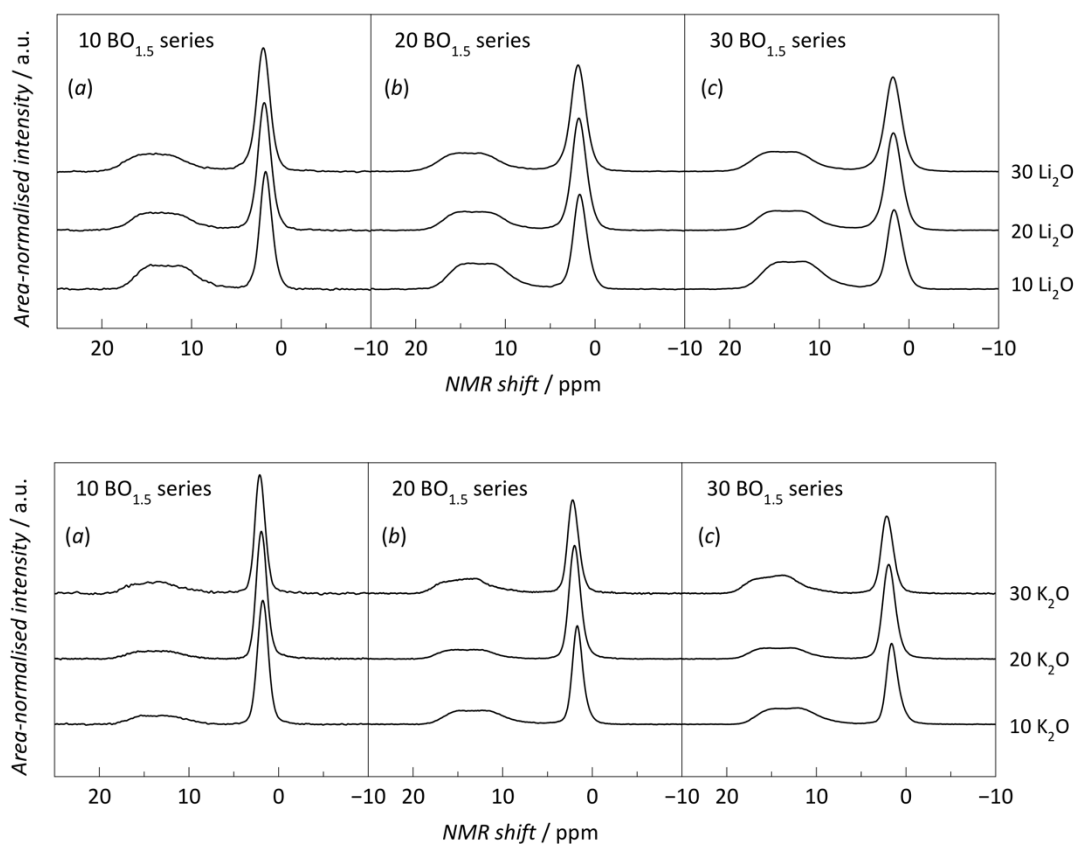


Figure 7.25: ^{11}B NMR spectra for the lithium and potassium borogermanate glasses

Table. 7.4: n_{BO} for for the lithium and potassium borogermanate glasses

	Sample	Nominal composition			R	K	$n_{\text{BO}} (\pm 0.10)$	
		M_2O	$\text{BO}_{1.5}$	GeO_2			M = Li	M = K
20B series	0M-10B	0	10	90	–	–	3.00	
	10M-10B	10	10	80	2	16	3.53	3.78
	20M-10B	20	10	70	4	14	3.64	3.78
	30M-10B	30	10	60	6	12	3.65	3.67
30B series	0M-20B	0	20	80	–	–	3.00	
	10M-20B	10	20	70	1	7	3.48	3.59
	20M-20B	20	20	60	2	6	3.63	3.74
	30M-20B	30	20	50	3	5	3.63	3.61
	0M-30B	0	30	70	–	–	3.00	
	10M-30B	10	30	60	0.7	4	3.44	3.53
	20M-30B	20	30	50	1.3	3.4	3.60	3.69
	30M-30B	30	30	40	2	2.6	3.60	3.53

7.6.3 Discussion

7.6.3.1 Lithium borogermanate glasses and lithium borosilicate model

Fig. 7.26 (a) compares the n_{BO} for the lithium borogermanate glasses (open) to the lithium borosilicate model [1] (dashed lines). Figs. 7.26 (b) to (g) compare n_{BO} for each K value.

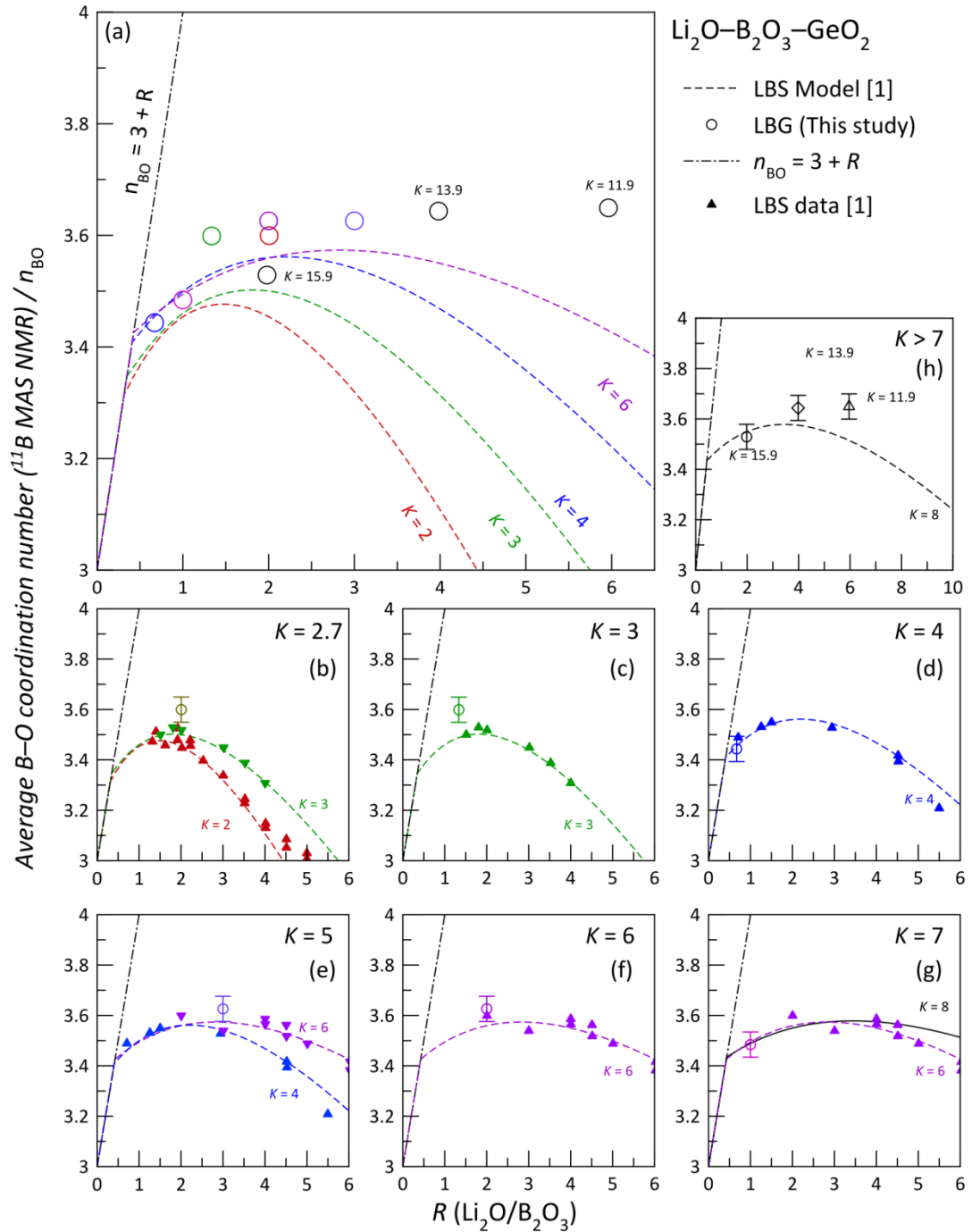


Figure 7.26: Comparison of the n_{BO} for the LBG glasses to the lithium borosilicate model [1]

For data points with $K > 8$, n_{BO} is compared with the highest K value available from the LBS model (Fig. 7.26 (h)). To illustrate the error on the model, the data points of Zhong and Bray

[1] are included. For K values of 2.7, 3, 5, and 6, n_{BO} obtained is slightly higher than, but within error of, the model, whilst for other K values ($K = 4$, and 7), the n_{BO} is as predicted by the model. An alternative view is that, for samples with $R < 1$, corresponding to $K = 4$ and 7, n_{BO} values fit the model well and for $R > 1$ n_{BO} is slightly higher (but within error) from the model. The difference is subtle yet it is tempting to suggest that for $R < 1$, Li^+ enters the LBG structure as described by the LBS model whilst for the higher R values, more tetrahedral $[\text{BO}_4]$ units are being created and stabilised in the tetrahedral germanate network. However, with limited data points, such an inference is tentative and the main conclusion is that B in LBG may undergo similar change in environment as a function of Li_2O content as in LBS glasses and that, initially, all Li^+ goes into the borate network until a certain R value (R_c).

Beyond this R_c value Li^+ may be distributed to both B and Ge sites, and NBO units may be formed which are associated with $[\text{BO}_3]$ units, but not $[\text{GeO}_{4+}]$ units. On the B sites, Li^+ is shared by the $[\text{BO}_4]$ and $[\text{BO}_3]$ (with NBO) units, with linearly increasing fraction of Li^+ associated with the latter as a function of K . However, taking the analogy with LBS further would suggest that the Ge environment should be similar to that of Si, with no change in the n_{GeO} values. The actual changes in the n_{GeO} values (and the anomalous behaviour of Ge in LBG glasses) will be discussed later in the neutron diffraction section.

7.6.3.2 Potassium borogermanate glasses and sodium borosilicate model

There is no potassium borosilicate model but potassium borogermanate (KBG) glasses, can be successfully compared with the sodium borosilicate (NBS) model [2]. Figs. 7.27 (b) to (g) show this comparison for each K value and, for the data points with $K > 8$, n_{BO} is compared with the highest K value available from both the NBS and LBS models (Fig. 7.26 (h)). The data points (open triangles) from the Zhong *et al.* [1] and Dell *et al.* [2] study are included. The n_{BO} for the potassium borogermanate glasses are shown as closed circles, the sodium borosilicate model [2] as solid lines. The n_{BO} for KBG follow the NBS model more closely for all K values, except $K = 7$ where n_{BO} is slightly lower than the model. With the limited data points, it is not possible to discuss the trend of $n_{\text{BO}}(R)$ for each K value in the KBG glasses, however, the local environment change of B in KBG and NBS are closely similar. The first conclusion from the comparison is that, in KBG, for $R < 0.5$, all K^+ go to the borate network and change n_{BO} as in the binary alkali borate. At $R > 0.5$, addition of K^+ creates more $[\text{BO}_4]$ units, which are stabilised in the germanate network until the R value of $0.5 + K/16$. In the

NaBS system, this is based on the stabilisation of 1 $[\text{BO}_4]$ unit in 3 $[\text{SiO}_2]$ units in a reedmergnerite-like unit.

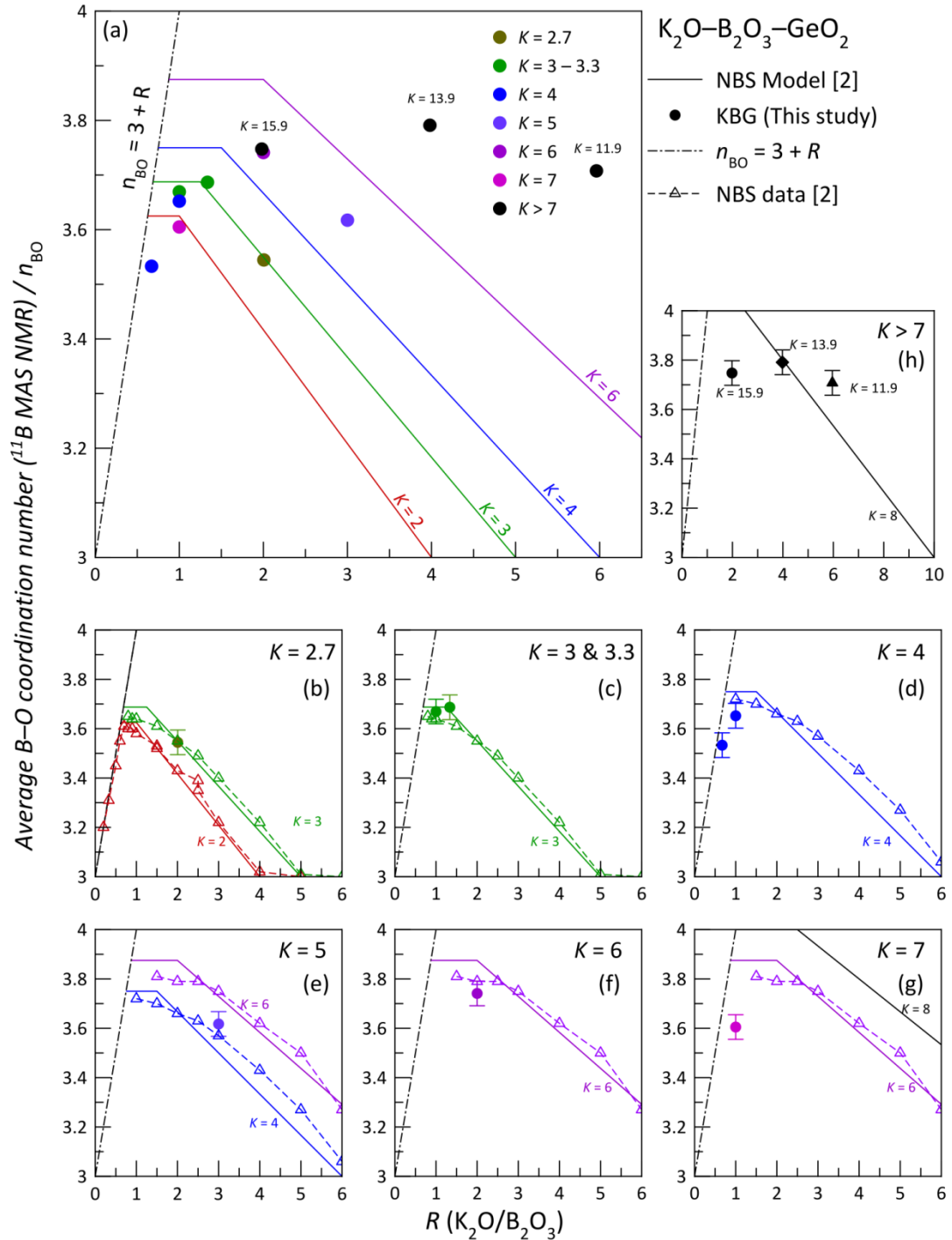


Figure 7.27: Comparison of the n_{BO} for the KBG glasses to the sodium borosilicate model [2]

In KBG however, to our knowledge, no crystal phase containing an equivalent group has been reported. Ge on the other hand could change its coordination number with the formation of charged $[\text{GeO}_5]$ or $[\text{GeO}_6]$ units and may decrease the number of $[\text{GeO}_4]$ sites

available for stabilising the $[\text{BO}_4]$ units, due to the charge avoidance principle. The NBS model is also characterised by the constant n_{BO} region where alkali ions become associated with the silicate/borosilicate network. If the same trend is followed by K^+ in KBG glasses and there is a region where K^+ are associated with the germanate network, the n_{BO} would stay constant as well. This may not be a problem for high K value where statistically, B and Ge can be separated further apart, but for low K value, the formation of charged $[\text{GeO}_{4+}]$ units may have an effect on the borate network. The only conclusion from the comparison is that B in KBG behave similarly to the NBS model, with the assumption that Ge behaves like Si. The environment of Ge can only be probed by neutron diffraction, as discussed later in this chapter.

7.6.3.3 Boron in lithium and potassium borogermanate glasses

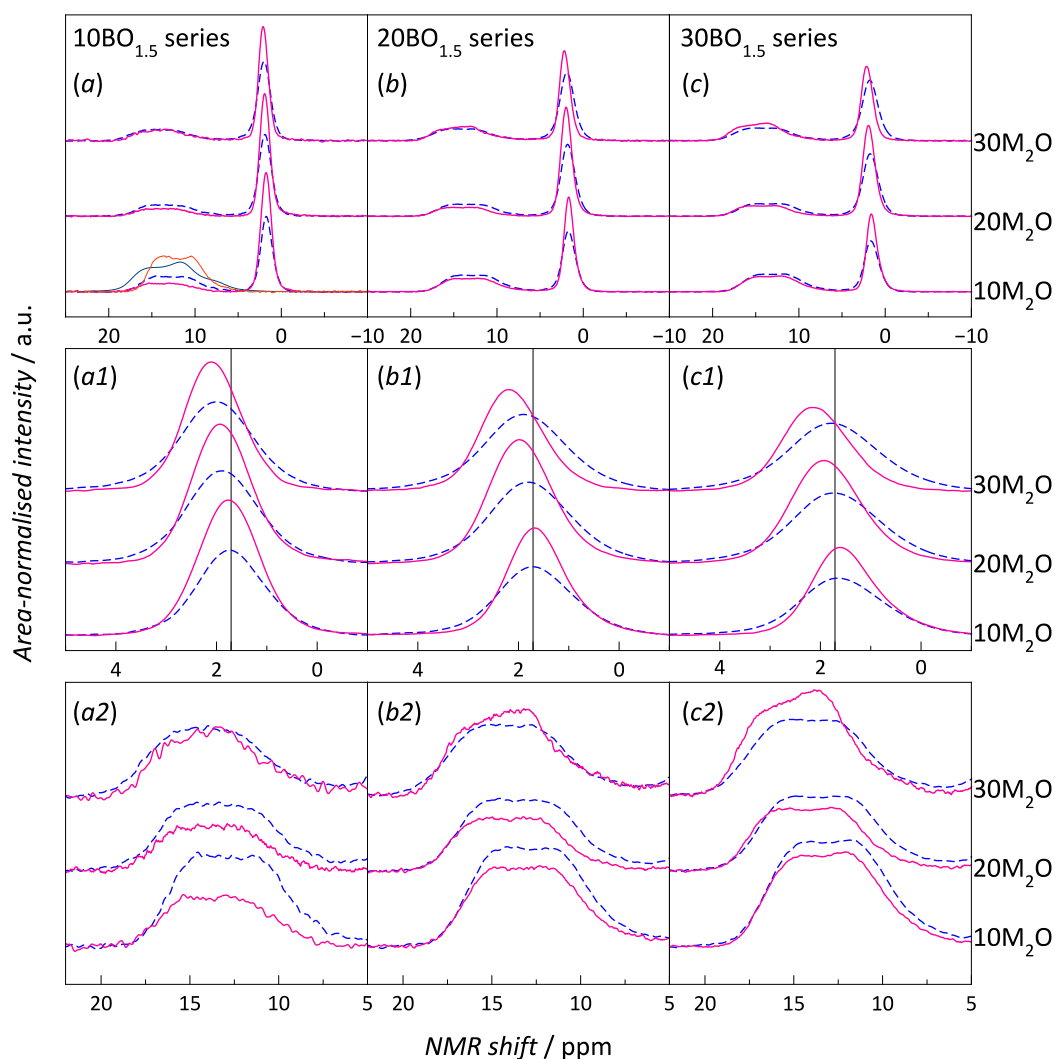


Figure 7.28: ^{11}B NMR spectra for $\text{M}_2\text{O}-\text{BO}_{1.5}-\text{GeO}_2$ ($\text{M}=\text{Li}$ (dashed blue, 14.15 T) and K (solid pink, 14.1 T))

Figure 7.28 shows the high field (14 T) ^{11}B MAS NMR spectra for lithium and potassium borogermanate glasses. The spectra were normalised to the integrated area. Figures in the top row (Figs (a), (b), and (c)) compare the spectra for both R = Li and K whilst figures in the second (a1 to c1) and third row (a2 to c2) compare the spectra in detail for the region of 4 and 3-coordinated B, B_3 , and B_4 respectively. For the 4-coordinated boron environment, in each $\text{BO}_{1.5}$ series, as M_2O is added to the GeO_2 network, it is seen that there is a systematic change in the shift downfield (to a more positive value), denoting change in the next-nearest neighbours of $[\text{BO}_4]$ i.e. B or Ge. In borosilicate glasses, $[\text{BO}_4]$ connected to 4 Si atoms, $[\text{B}(4\text{Si})]$ has the lowest NMR shift value, and this increases on going to $[\text{B}(\text{B},3\text{Si})]$ and $[\text{B}(2\text{B},2\text{Si})]$ [54]. A similar trend may occur for borogermanate glasses.

For low M_2O content (hence high GeO_2 content, for fixed $\text{BO}_{1.5}$ content), the $[\text{BO}_4]$ units produced are likely to be associated with the GeO_2 network. The magnitude of change in shift however is different, with KBG being higher than LBG, especially in high $\text{BO}_{1.5}$ content glasses. This simply means that in KBG glasses, as K_2O is added (and GeO_2 content decreases), the number of the neighbouring $[\text{GeO}_4]$ units around the created $[\text{BO}_4]$ will decrease and therefore the downfield shift. Relative to the KBG, the network intermixing is however less in LBG glasses evidenced from the smaller change in shift, suggesting little change in the number of neighbouring $[\text{GeO}_4]$ to $[\text{BO}_4]$ and possible presence of phase separation. For the $[\text{BO}_3]$ peak, in general the shift is seen to be unchanged. Comparison of the peak is however difficult due to the overlapping and complexity of the peaks due to the quadrupole interaction.

7.7 Neutron diffraction

7.7.1 Results

Figures 7.29 and 7.30 shows the distinct scattering $i(Q)$ and total correlation function $T(r)$ for the natural and null lithium (LBG) and potassium borogermanate (KBG) glasses. The $T(r)$ were obtained using a Q_{max} value of 40 \AA^{-1} in both cases. The comparison analysis of the glasses (g-KBGe₂O₆ and g-K₂B₂Ge₃O₁₁) with the crystalline phases (c-KBGe₂O₆ and c-K₂B₂Ge₃O₁₁) is not included in this preliminary discussion.

In these $T(r)$ for the alkali borogermanate glasses, the first peak at about 1.5 Å corresponds to the boron-oxygen distance(s) in the glasses and the second peak at about 1.8 Å corresponds to the germanium-oxygen distance(s). Using the M-O bond-valence values [43], the boron-oxygen peak can be parameterised with 2 peaks at 1.371 Å and 1.477 Å, representing $[\text{BO}_3]$ and $[\text{BO}_4]$ respectively. Similarly, the germanium-oxygen peak can be

assigned to $[\text{GeO}_n]$ units with the dominant $[\text{GeO}_4]$ giving an r_{GeO} of 1.748 Å. There is also contribution from at least one other peak on the trailing edge, corresponding to the higher coordinated $[\text{GeO}_5]$ and/or $[\text{GeO}_6]$ units. In binary alkali germanate glasses (K_2O – see below; Na [35]; and Cs [33]) the $[\text{GeO}_5]$ unit is favoured over the $[\text{GeO}_6]$. The parameterisation of this higher coordinated unit is however difficult due to the complex geometry of the $[\text{GeO}_5]$ polyhedron [55]. In this study, only the B-O peak is parameterised and the Ge-O peak is simply integrated to determine n_{GeO} .

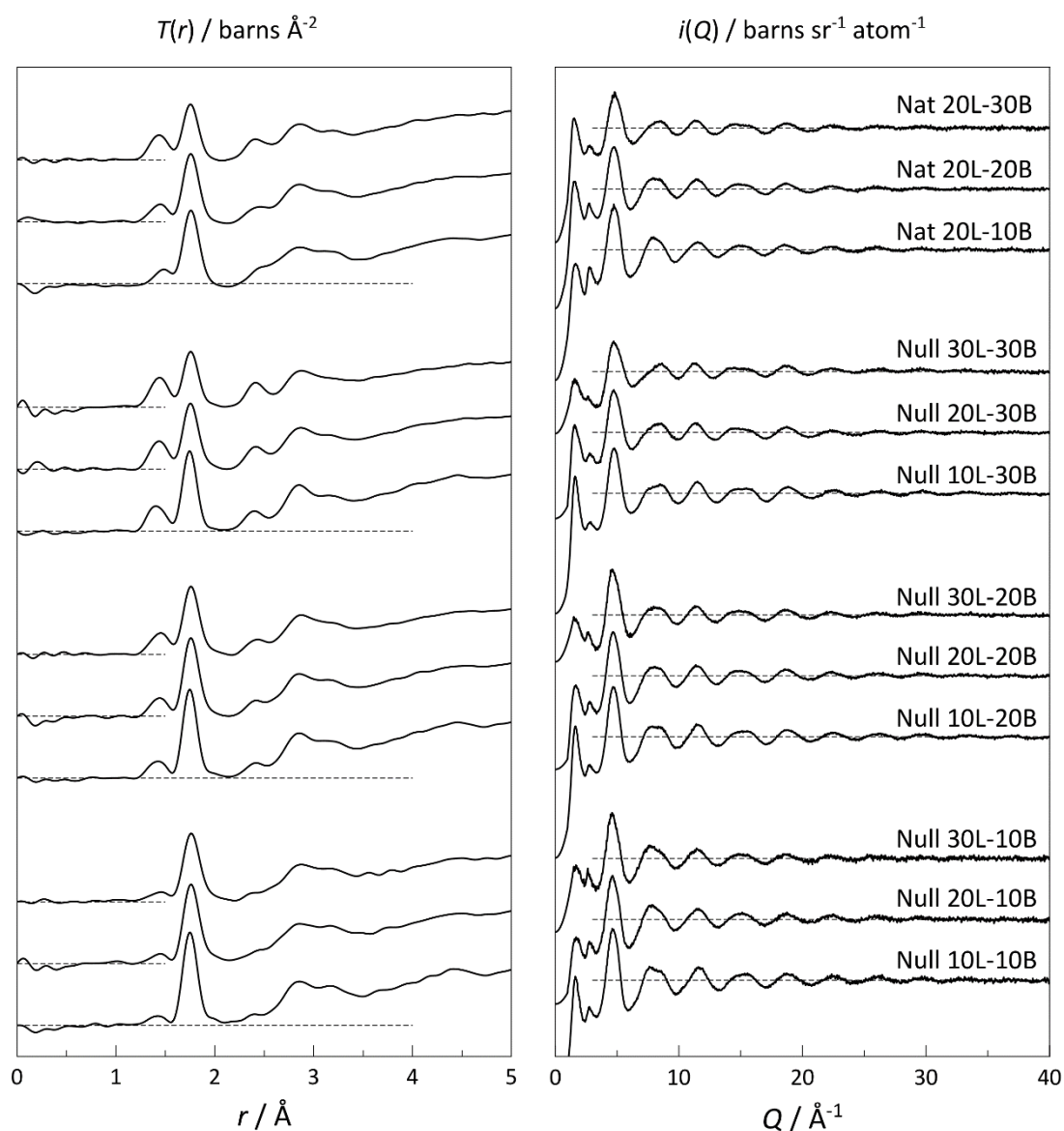


Figure 7.29: Total correlation function $T(r)$ and distinct scattering $i(Q)$ for lithium borogermanate glasses

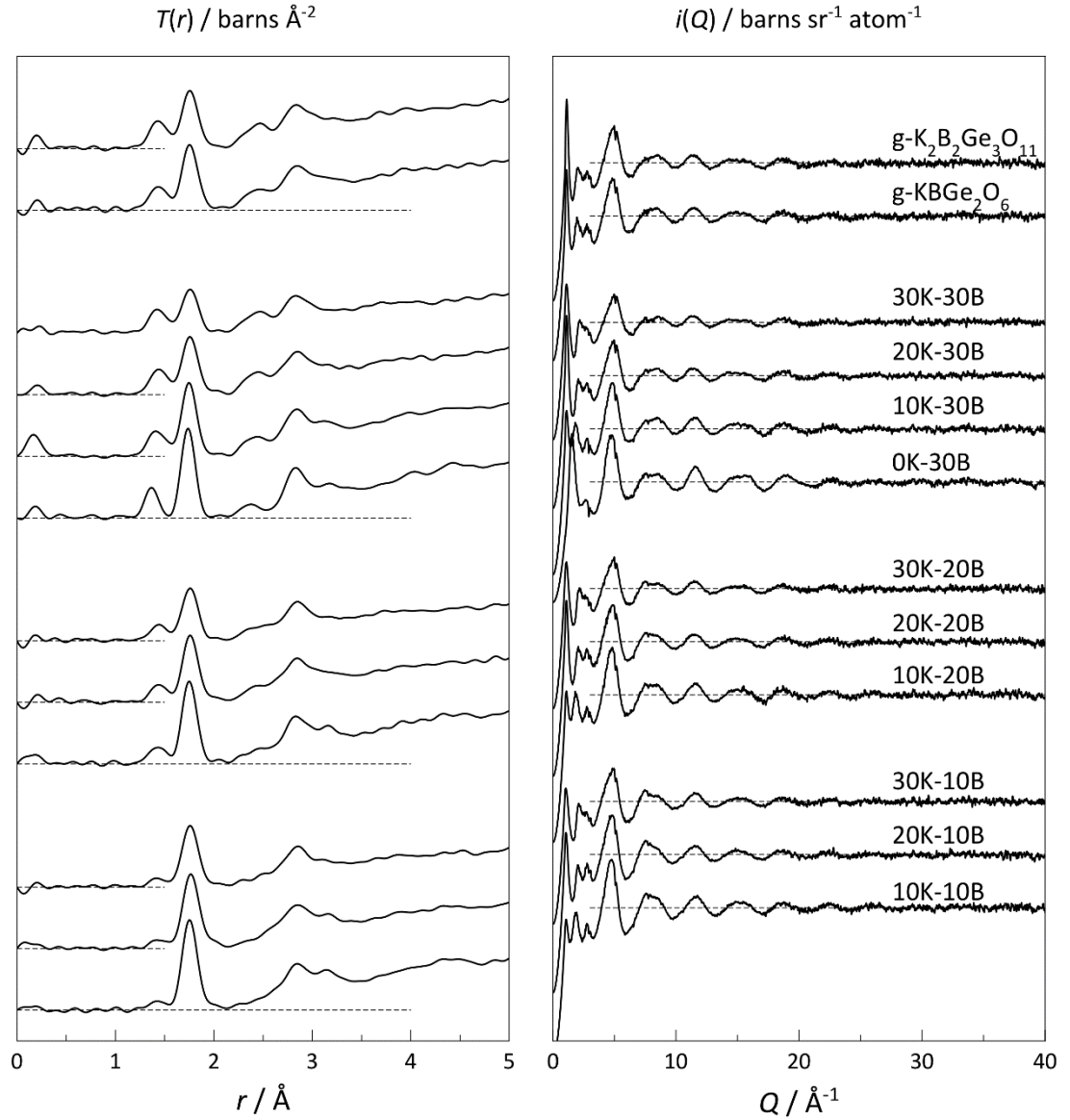


Figure 7.30: Total correlation function $T(r)$ and distinct scattering $i(Q)$ for potassium borogermanate glasses

7.7.2 n_{BO} (^{11}B NMR and ND) and n_{GeO}

Fig. 7.31 shows the $T(r)$ v r plot for a potassium borogermanate glass, to illustrate the process of obtaining average n_{BO} from ND. For n_{BO} (NMR), the n_{BO} is obtained from the area of the $[\text{BO}_4]$ and corrected $[\text{BO}_3]$ peak, for n_{BO} (Integration), the n_{BO} is obtained by dividing the integrated $r \cdot T(r)$ of the B-O region (where the overlapping Ge-O peak is removed) by a factor of $t_{\text{BO}} = 2c_{\text{B}}b_{\text{B}}b_{\text{O}}$ and for n_{BO} (ND – Peak ratio), the average n_{BO} is obtained by fitting the $T(r)$ with B-O peaks associated to $[\text{BO}_3]$ and $[\text{BO}_4]$ units using calculated B-O distances [43] and the ratio of the peaks is calculated, as shown in Eqn 7.3. Accurate n_{BO} is obtained from this method provided that the peak positions assigned to the r_{BO} in $[\text{BO}_3]$ and $[\text{BO}_4]$ units are

correct. n_{BO} values obtained by NMR and peak ratio are consistent if the glass composition is close to nominal. The calculation of n_{BO} from integration (ND), however, has compositional factor of c_B associated. Therefore, the accuracy of n_{BO} depends on c_B .

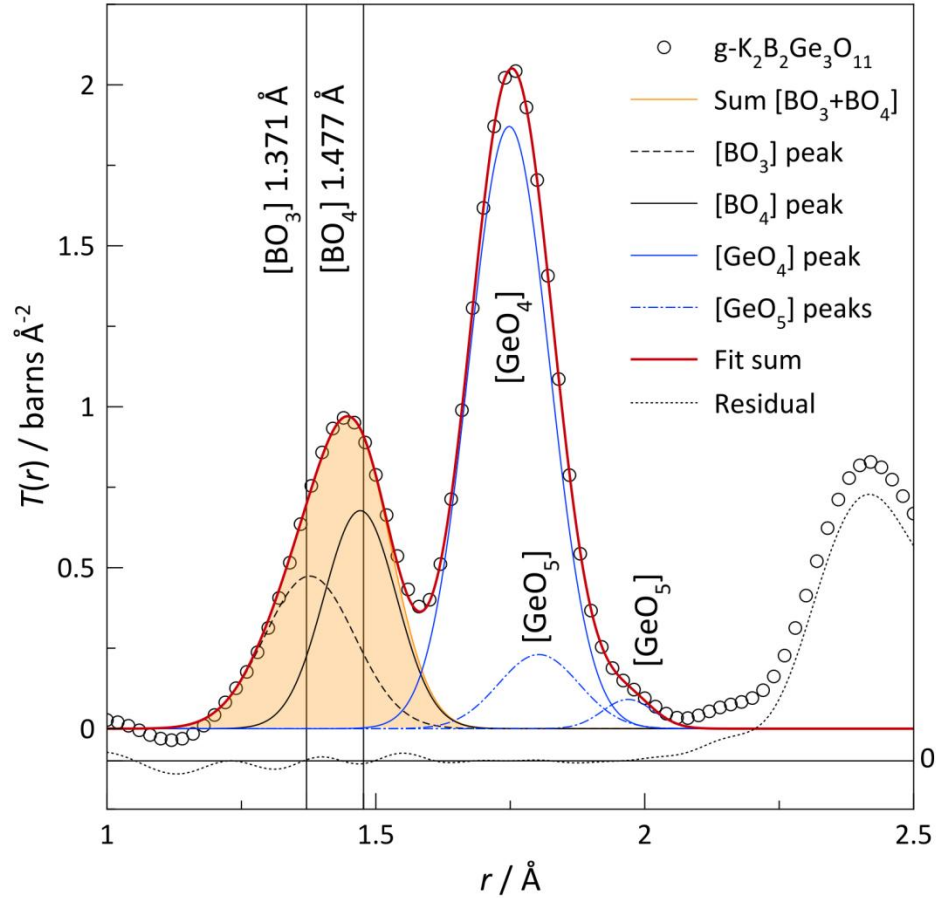


Figure 7.31: Parameterisation of the B-O peak corresponding to $[BO_3]$ and $[BO_4]$ units

In these ternary glass systems, determination of c_B , c_M , c_{Ge} , and c_O (via EDX, only K/Ge ratio is obtained) is difficult due to the limited information available, such as the unknown B/K to B/Ge ratio. This is more problematic in LBG glasses where only Ge peaks can be quantitatively measured from EDX. c_B in both cases however can be optimised to give a value of n_{BO} equal to the n_{BO} obtained by ^{11}B (NMR) or ND(Peak ratio). This however has a knock on effect on the $T_o(r)$ line ($4\pi\rho_o r(\sum c_i b_i)^2$) since new c values would change the $T_o(r)$ value and hence affect the normalisation of $i(Q)$ (Note that, $i(Q)$ is normalised using the nominal compositions). To illustrate the magnitude of error, for the null10L10B sample, a 0.001 error in c_B gives rise to a n_{BO} error value of about 0.20, which is 3 times the “typical” error for ND derived coordination numbers in similar glasses (for example in Chapter 5, and 6, and elsewhere [56-57]. Figs. 7.32 and 7.33 (top row) shows the n_{BO} values obtained from these different methods. It is seen that for LBG glasses, n_{BO} obtained by integration differs

greatly from values obtained by other methods at high Li₂O. This could arise from the error in normalisation due to the compositional factor and would have the greatest effect where the $T_o(r)$ values are the lowest, i.e. for the highest Li₂O content in each series. For this preliminary study, the determination of n_{BO} by peak ratio will now be used since it excludes the compositional factor and is therefore more accurate. However, this can only be used where information on average coordination is available from another source – e.g. ¹¹B NMR

$$\begin{aligned}
 n_{BO} \text{ (NMR)} &= 3 + N_4 \\
 n_{BO} \text{ (ND-Integration)} &= \frac{\int_a^b r * T(r)_{BO} dr}{2c_B b_B b_O} \\
 n_{BO} \text{ (ND-Peak ratio)} &= \left(3 * \frac{A_{B3}}{A_{B3} + A_{B4}} \right) + \left(4 * \frac{A_{B4}}{A_{B3} + A_{B4}} \right) \\
 \text{where;} & \\
 N_4 &= \frac{\text{Area}[BO_4]}{1.04 * \text{Area}[BO_3] + \text{Area}[BO_4]} \\
 T(r)_{BO} &= T(r) - T(r)_{GeO_4} \\
 A_{B3} &= \text{Area}[BO_3], A_{B4} = \text{Area}[BO_4]
 \end{aligned} \tag{7.3}$$

However, the average n_{GeO} value can only be obtained by integration and not peak ratio since the geometry of the higher-coordinated [GeO_n] unit is unknown ($n = 5$ and/or 6).

$$\begin{aligned}
 (1) n_{GeO} (c_{Ge} \text{ nominal}) &= \frac{\int_a^b r * T(r)_{GeO} dr}{2[c_{Ge}^{Nom}] b_{Ge} b_O} \\
 (2) n_{GeO} \text{ (Optimised } [^1]c_{Ge} \text{ from } n_{BO} \text{ NMR and M/Ge ratio [1])} &= \frac{\int_a^b r * T(r)_{GeO} dr}{2[^1]c_{Ge} b_{Ge} b_O} \\
 (3) n_{GeO} \text{ (Optimised } [^2]c_{Ge} \text{ from } n_{BO} \text{ NMR and M/Ge ratio [2])} &= \frac{\int_a^b r * T(r)_{GeO} dr}{2[^2]c_{Ge} b_{Ge} b_O}
 \end{aligned} \tag{7.4}$$

where;

$$\begin{aligned}
 [^1]c_{Ge} \text{ is where for } M &= \text{Li, } \Delta \text{Li/Ge ratio} = \Delta K / 3 * Ge \\
 M &= \text{K, } K/Ge \text{ ratio} = K/Ge \text{ EDX} \\
 [^2]c_{Ge} \text{ is where } M &= \text{Li, } Li/Ge \text{ ratio} = \text{Nominal } Li/Ge \text{ ratio} \\
 M &= \text{K, } K/Ge \text{ ratio} = \text{Nominal } K/Ge \text{ ratio}
 \end{aligned}$$

For case (1) n_{GeO} is obtained directly from the area of the Ge-O peaks, divided by the $t(r)_{Ge-O}$ as calculated [58]. For case (2) and (3), the fraction of c_B is the optimised c_B calculated from the ¹¹B NMR value. Since for LBG glasses, the Li/Ge ratio cannot be determined experimentally, two extremes are considered. Case (1), [Li/Ge]_{Nominal} – [Li/Ge]₍₁₎ is 1/3 of

$[K/Ge]_{\text{Nominal}} - [K/Ge]_{\text{EDX}}$. The factor of 1/3 based on the volatilisation loss study on KBS and LBS by Shimbo [59], and (2), $[Li/Ge]_{\text{Nominal}} = [Li/Ge]_{(2)}$.

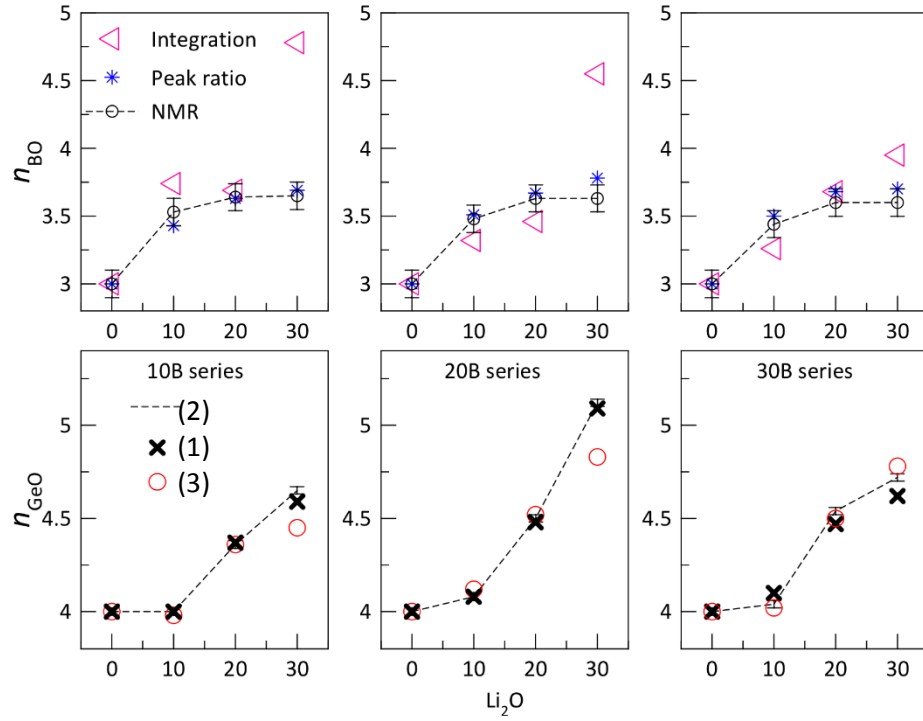


Figure 7.32: n_{BO} and n_{GeO} for LBG glasses from various methods. (1), (2), and (3) refers to Eqn. 7.4.

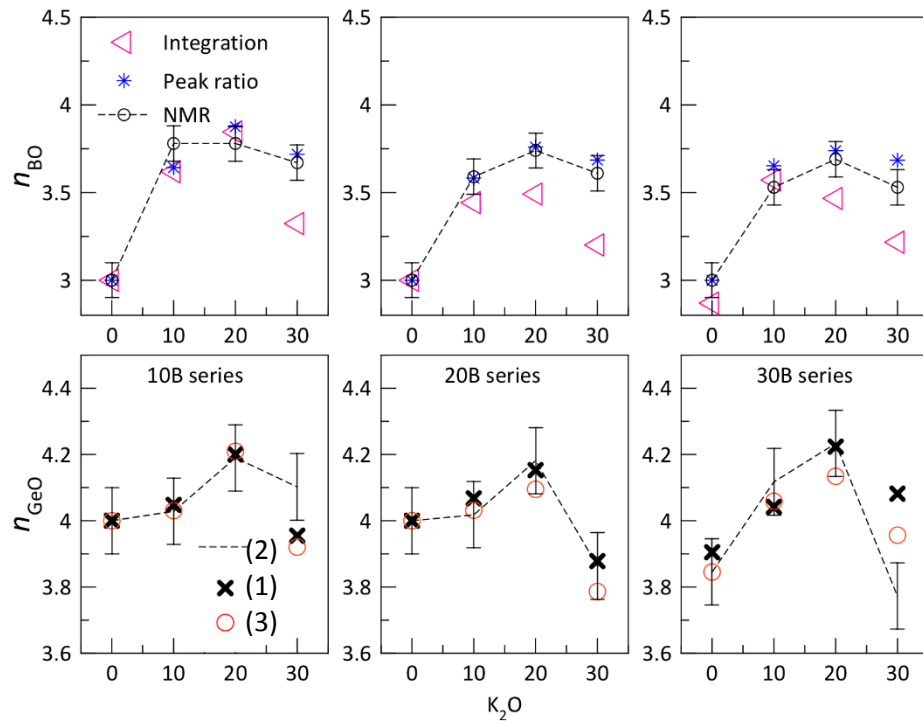


Figure 7.33: n_{BO} and n_{GeO} for KBG glasses from various methods. (1), (2), and (3) refers to Eqn 7.4.

For LBG samples, n_{GeO} values were obtained from the null Li isotope samples where Li partials are removed. The B-O and Ge-O overlapping distributions are treated using complementary n_{BO} values from ^{11}B MAS NMR. As seen in the n_{GeO} plots in Figs. 7.32 and 7.33, these corrections produce little effect on the n_{GeO} values. A c_{Ge} loss of about 0.001 translates to an error of ± 0.02 in n_{GeO} which is 10 times smaller than the error of n_{BO} . For KBG glasses (Fig 7.33) the n_{GeO} values at high K_2O content are less than 4, and also for the binary $30\text{BO}_{1.5}\text{--}70\text{GeO}_2$ the value obtained was about 3.80, which is unlikely; the value should be 4.00 since it was obtained from the optimised c_{B} . This is due to the knock on effect of the normalisation. In theory, the optimised c_{B} , c_{Ge} , c_{M} , and c_{O} should correspond to the $T_{\text{o}}(r) = 4\pi\rho_{\text{o}}r(\sum c_i b_i)^2$ constant, which is the value used to fit the baseline for the $D_{\text{o}}(r)$ (Eqn 2.10). This would also mean that, the appropriate fractions should be used to process the data, however, for convenience and simplicity, the nominal composition is used and the error is relative to the nominally derived parameters. In this study the optimised parameters are used in obtaining the final coordination number.

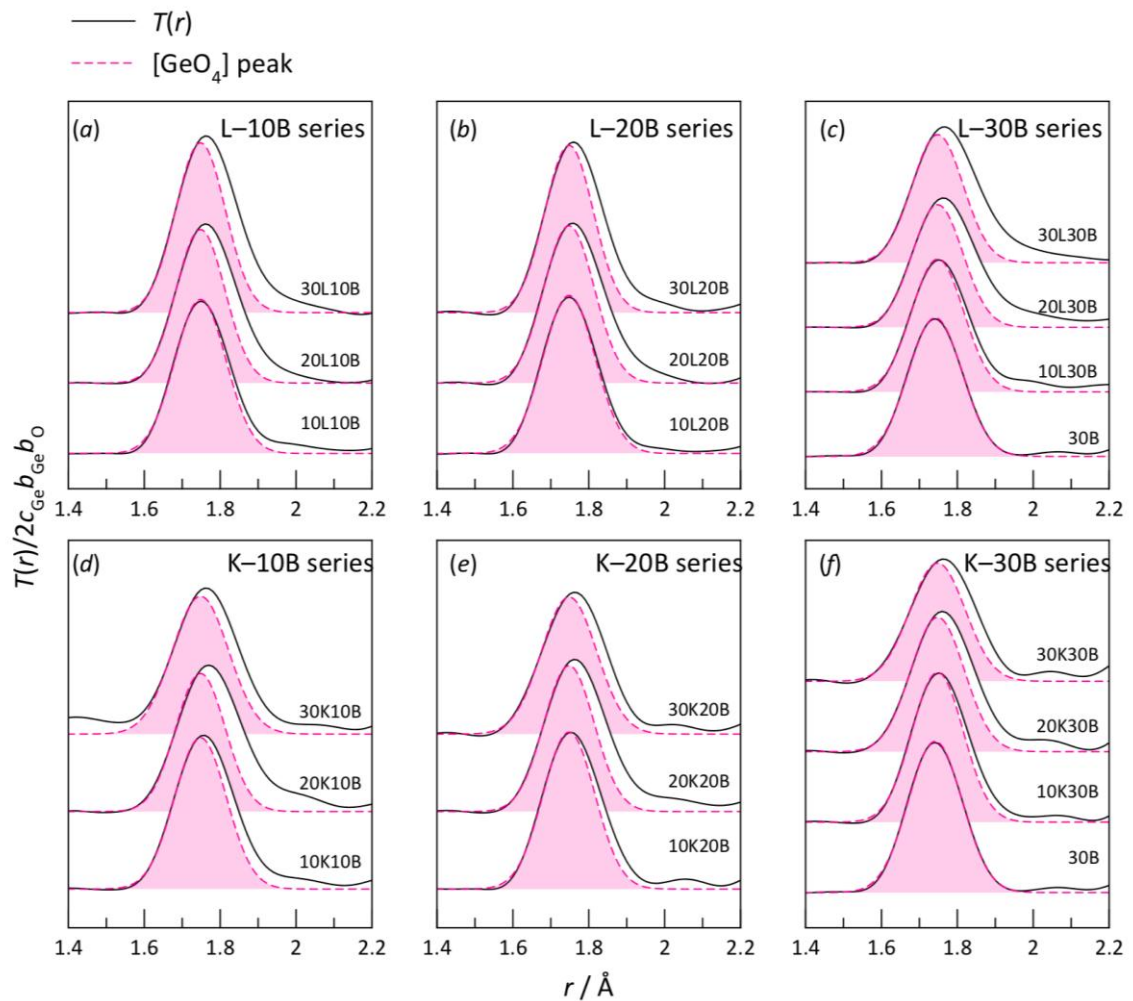


Figure 7.34: $T(r)$ of LBG and KBG glasses fitted with a peak corresponding to a $[\text{GeO}_4]$ to highlight the necessity of more peak(s) corresponding to a higher coordinated $[\text{GeO}_{4+}]$ unit.

To support the claim that n_{GeO} should not be lower than 4.00, Fig. 7.34 shows the weighted $T(r)$ to compare the contribution from higher coordinated $[\text{GeO}_{4+}]$ units. As seen in the figure, the $T(r)$ is fitted with a peak at 1.748 Å to correspond to the Ge-O distance in tetrahedral $[\text{GeO}_4]$, obtained from bond valence calculation [43]. For 30K-10B, 30K-20B, and 30K-30B, to achieve a good fit, at least one other peak should be included. This peak should correspond to a higher coordinated $[\text{GeO}_{4+}]$ unit, which means that the average n_{GeO} in these samples should be greater than 4. This suggests that the errors are slightly larger than expected. The minimum error on n_{BO} is about ± 0.1 with ± 0.2 (at least, for $M = \text{K}$) on the n_{GeO} values. To obtain accurate n_{BO} and n_{GeO} values, the errors associated must be evaluated in more detail.

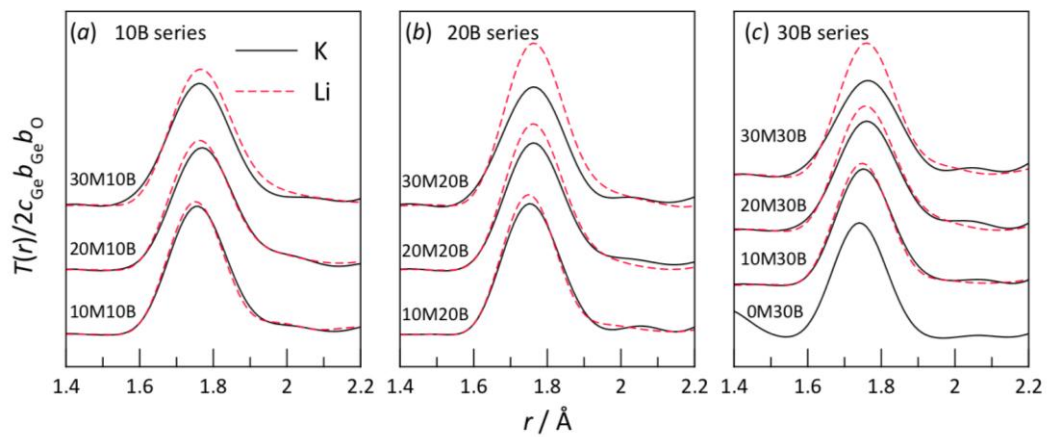


Figure 7.35: Comparison of the $T(r)_{\text{GeO}}$ for LBG and KBG glasses highlighting the area, hence n_{GeO} difference.

Fig. 7.35 compares the $T(r)_{\text{GeO}}$ for the LBG and KBG glasses to directly illustrate the difference in Ge environment (and by extension, the n_{GeO} value). In general, the area for GeO in LBG is always greater than in KBG. For the 10 $\text{BO}_{1.5}$ series, the difference is less pronounced, compared to the higher $\text{BO}_{1.5}$ contents. From NMR, n_{BO} values for KBG are higher than for LBG, which means KBG has less K^+ available for association with Ge, compared to LBG glasses. The preference of Li^+ to modify the germanate structure rather than borate may be due to several factors; (1) the limiting behaviour of B in the glass network, where, as observed in LBS [1], non-bridging oxygen atoms are created at fairly low R, compared to NBS and this limits the amount of $[\text{BO}_4]$ units that can be stabilised into the germanate network; (2) the formation of more stable “superstructural groups” of boron-germanium in the presence of Li^+ , which in turn, limits the number of available Li^+ for borate group.

In Figs 7.36 and 7.37, the dashed-blue line (n_{GeO}^*) is the estimated n_{GeO} based on the residual Li^+ or K^+ remaining after accounting for the alkali associated with borate units (calculated from n_{BO} (NMR) with the assumption that there is no nonbridging oxygen in the glasses;

For $a\text{M}_2\text{O} - b\text{B}_2\text{O}_3 - c\text{GeO}_2$

$$(1) \quad M^+ \text{ associated with B is} = (n_{\text{BO}} - 3).2b$$

$$(2) \quad \text{Total } M^+ \text{ is} = 2a$$

$$(2) - (1) \quad M^+ \text{ associated with Ge is} = (2a) - [(n_{\text{BO}} - 3).2b] = (n_{\text{GeO}}^* - 4).c \quad (7.5)$$

Rearrange (2) - (1);

$$n_{\text{GeO}}^* = \frac{(2a) - [(n_{\text{BO}} - 3).2b]}{c} + 4$$

*If no M^+ is associated with NBO units

The error band is marked by the green shaded area. Any values lower than the line would indicate some association of Li^+/K^+ with NBO in the form of $[\text{BO}_3]^-$ or $[\text{GeO}_4]^-$. Theoretically, n_{GeO} should never exceed this line. In LBG glasses, n_{GeO} increases as a function of M_2O content, to an extent that no NBO is created in the glass network, whereas in KBG glasses, it is obvious that there is formation of NBO at higher K_2O content (possibly at 20 mol% K_2O and definitely at 30 mol% K_2O). In KBG, n_{BO} and n_{GeO} both have a maximum, which means that the decrease in the average coordination number is due to the formation of NBO in both borate and germanate networks. In LBG, both n_{BO} and n_{GeO} continue to rise and there is no maximum present. This reflects that Li^+ modifies the borogermanate structure differently from K^+ .

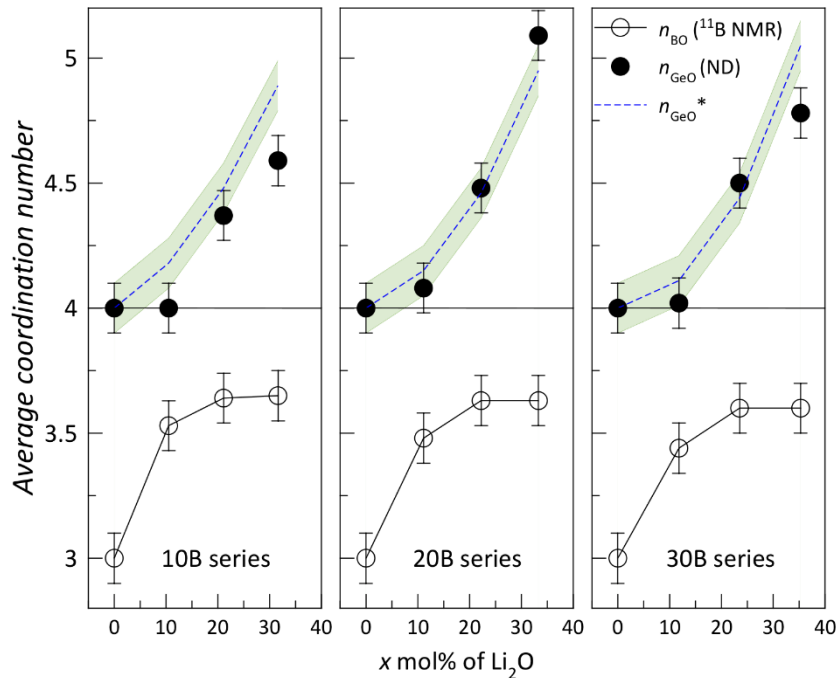


Figure 7.36: n_{GeO} and n_{BO} agreement in LBG glasses

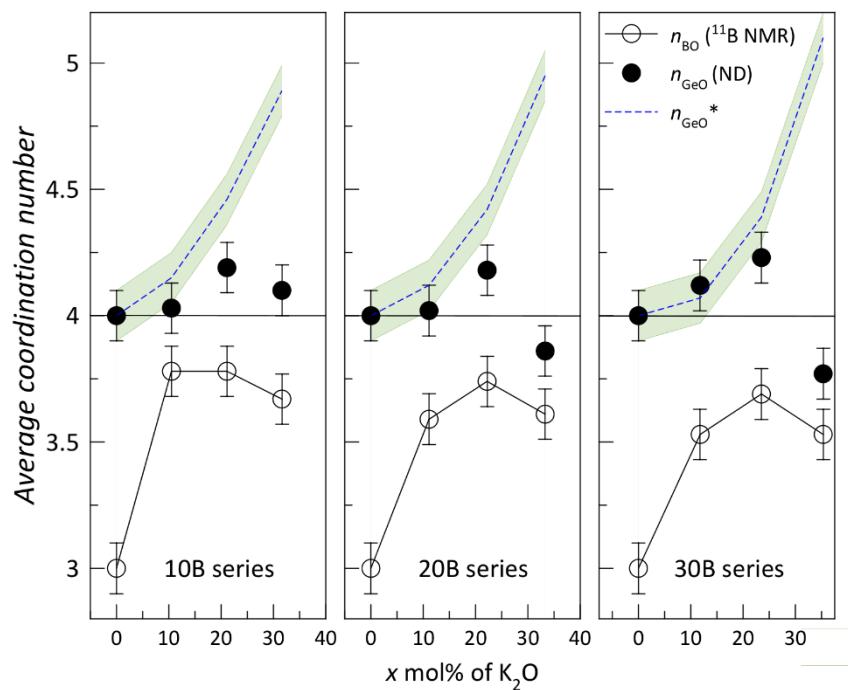


Figure 7.37: n_{GeO} and n_{BO} agreement in KBG glasses

7.7.3 Lithium environment

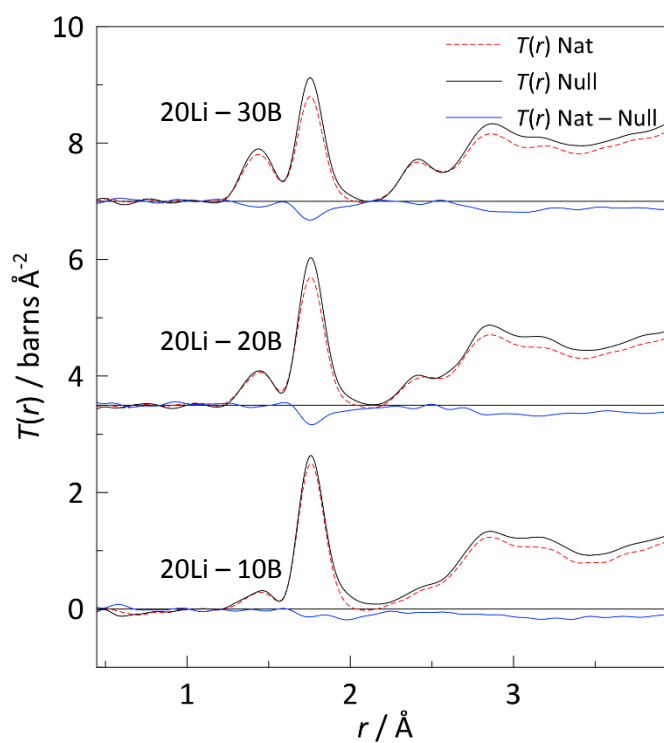


Figure 7.38: $T(r)$ -Nat, $T(r)$ -Null, and $T(r)$ -Difference for the selected samples of 20 mol% Li_2O for each B series

Due to beamtime/absorption limitations, data on sample pairs of $T(r)$ -Nat and $T(r)$ -Null were restricted to the 20 mol% Li_2O samples for each B series (it is hoped that data can be collected for the remaining Nat samples in future). With the Nat-Null pairs, the Li environment can be probed using the difference technique. As shown in Fig. 7.38, the difference between $T(r)$ -Nat and $T(r)$ -Null yield negative Li,O partial correlation functions due to the negative scattering length of Li in the natural samples.

Fig. 7.39 shows the partial $T(r)_{\text{Li,O}}$ for each sample (as labelled). There is a peak at $r < 1.5 \text{ \AA}$, for 20L-30B which could indicate a difference in $\text{BO}_{1.5}$ content between Null and Nat, or could reflect the rather poor statistics in these neutron absorbing samples (Note that the truncation effect is reduced since Lorch modification function is used). The Li-O distances reported in crystalline LiBGeO_4 [60] are 1.76 \AA (in Li-O_B) and 1.86 \AA (in Li-O_Ge) (Fig. 7.40) and 1.979 \AA is typical of 4-coordinated $[\text{LiO}_4]$ [43]. Therefore, the distances observed in the borogermanate glasses of 1.75 \AA (Peak 1) and 1.98 \AA (peak 2) could well indicate Li in borate or germanate networks. The Li-O peaks in Fig. 7.39 are fitted with fixed FWHM values of 0.0776 and 0.1333 \AA for Peak 1 and Peak 2. The quality of the fit is judged by the consistency of the residual with the background noise. The area of Peak 1 increases with increasing $\text{BO}_{1.5}$ content and the area of Peak 2 decreases with decreasing GeO_2 content, further supporting the assignment of the peaks to Li in predominantly borate or germanate networks. The parameters obtained from the fit are shown in Table 7.5.

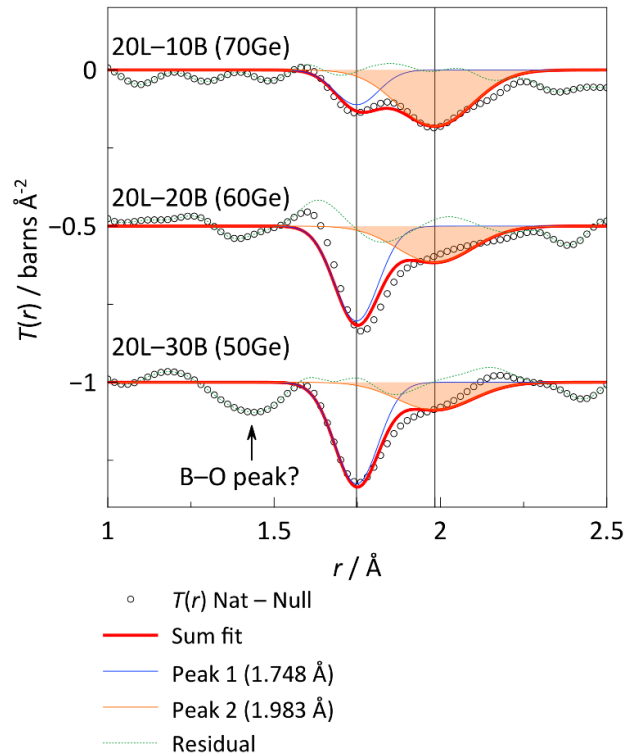


Figure 7.39: $T(r)$ -Difference for the selected samples of 20 mol% Li_2O for each B series with Li-O peaks

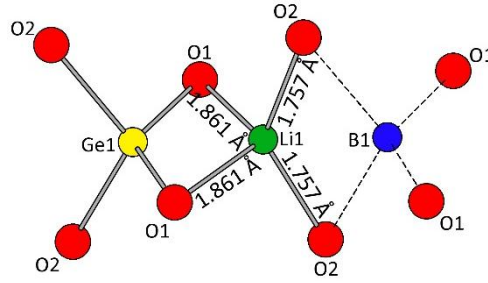


Figure 7.40: Li site (1/1) found in approximated LiBGeO₄ crystal phase [60].

Table 7.5: Li-O peak parameters from peak fitting and integration. t_{LiO} is the coefficient for Li-O partial correlation function.

Sample	t_{LiO}	n_{LiO}		Av n_{LiO}	n_{LiO}	σ	Centre of gravity ($r_{\text{LiO}} / \text{\AA}$)
		Peak 1 (1.7477 \AA)	Peak 2 (1.9833 \AA)		Integration (1.6 - 2.24 \AA)		
20L-10B	-2.99E-02	1.08	3.40	4.48	4.60	0.12	1.9191
20L-20B	-3.04E-02	2.88	2.16	5.04	4.85	0.20	1.8413
20L-30B	-3.09E-02	3.03	1.62	4.65	4.24	0.41	1.8231

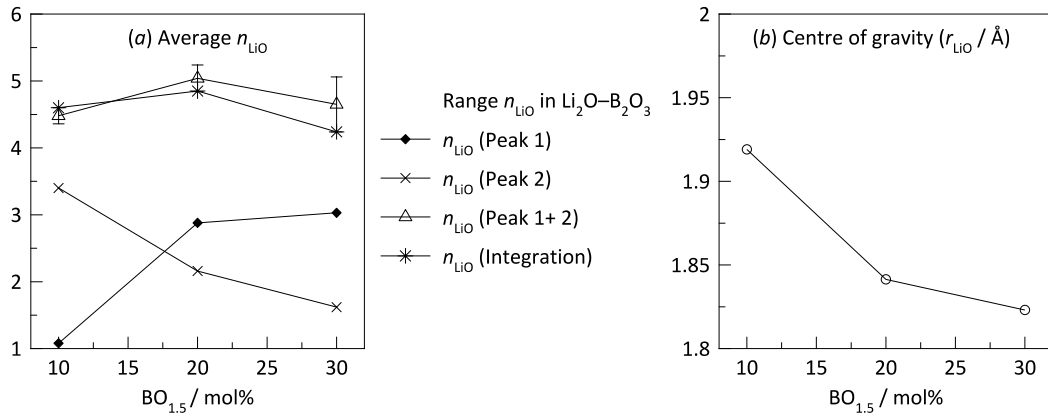


Figure 7.41: Average n_{LiO} in $20\text{Li}_2\text{O}-x\text{BO}_{1.5}-(80-x)\text{GeO}_2$ for $x = 10, 20, \text{ and } 30 \text{ mol\%}$

Fig. 7.41 (a) shows the average n_{LiO} obtained from the peak fitting and integration. The average n_{LiO} obtained in this study is consistent with the range of average n_{LiO} values found in $\text{Li}_2\text{O}-\text{B}_2\text{O}_3$ glasses [61-62] (shown as the orange bar in the Fig. 7.41). n_{LiO} values in $\text{Li}_2\text{O}-\text{GeO}_2$ have not been published [63]. This value of 4 – 5 is also consistent with Li^+ behaving as a modifier. At low B content, assuming homogeneous distribution of Li, an average of 3 out of 4 oxygen atoms bonded to Li^+ are in the germanate network. This could possibly suggest that 1 $[\text{BO}_4]$ unit is being stabilised by 3 $[\text{GeO}_4]$ units, because, at this composition, no NBO is associated with either borate or germanate units and also due to the charge avoidance. Fig. 7.41 (b) shows the mean r_{LiO} in the series. It is seen that, as $\text{BO}_{1.5}$ content is increased at the expense of GeO_2 , the mean Li-O distance decreases.

7.8 Conclusion

Ternary glass samples of natural and null $x\text{Li}_2\text{O}-y\text{BO}_{1.5}-(100-x-y)\text{GeO}_2$ (LBG) for $x = 10, 20$, and 30 mol% and $y = 10, 20$, and 30 mol% were successfully prepared. EDX, showed some K loss, greater for high K_2O and $\text{BO}_{1.5}$ contents. Density and its derivatives (molar volume and number density) analyses revealed anomalous change in both B and Ge environment as a function of M_2O content ($\text{M} = \text{Li}$ and K). Raman scattering, which is sensitive to species, revealed that the spectra are dominated by Ge-O vibrations (since the glasses in this study are Ge-rich glasses). Trends in the spectrum shape (intensity) were observed, which confirms the density analysis, that both borate and germanate networks are changed.

^{11}B MAS NMR was performed on both LBG and KBG glasses. From the N_4 value, average n_{BO} was obtained. The n_{BO} for LBG and KBG are seen to change in a similar manner to the lithium borosilicate (LBS) [1] and sodium borosilicate (NBS) [2] models respectively. From preliminary results on neutron diffraction, $n_{\text{BO}}(\text{NMR})$ is used to obtain average n_{GeO} values. The n_{GeO} values are remarkably different in LBG and KBG glasses: in LBG, n_{GeO} increases as predicted for the absence of non-bridging oxygen NBO in the glass. For KBG, n_{GeO} shows a maximum suggesting the presence of NBO atoms at high K_2O content. The lithium environment is extracted from one series (fixed 20 mol% Li_2O content and $10, 20$, and, 30 mol% $\text{BO}_{1.5}$) using the difference technique. 2 Li-O peaks are seen in the difference plot, showing discrimination between Li-O distances in the borate and germanate networks. Average n_{LiO} ranges from $4 - 5$, confirming the typical behaviour of Li^+ as a modifier. This preliminary work will be completed with the extraction of n_{LiO} for each sample so the trend of Li^+ association to either borate and germanate network can be studied for fixed $\text{BO}_{1.5}$ content and increasing Li_2O content. Future work involving the extraction of n_{KO} value (possibly by means of simulation, or using isostoichiometric method using other alkali oxide which is known to induce isostructural changes in glass network) will also be useful for studying the preferential association of K^+ to either borate or germanate network.

7.9 References

1. Zhong, J., Wu, X., Liu, M., Bray, P. *Journal of Non-Crystalline Solids* 1988, **107**, 81-87.
2. Dell, W. J., Bray, P. J., Xiao, S. Z. *Journal of Non-Crystalline Solids* 1983, **58**, 1-16.
3. Sigaev, V. N., Lotarev, S. V., Orlova, E. V., Stefanovich, S. Y., Pernice, P., Aronne, A., Fanelli, E., Gregora, I. *Journal of Non-Crystalline Solids* 2007, **353**, 1956-1960.
4. Pye, L. D., Fréchette, V. D., Kreidl, N. J., *Borate Glasses: Structure, Properties, Applications*; Springer Science & Business Media, 2012; Vol. 12.
5. Bray, P. J. *Inorganica Chimica Acta* 1999, **289**, 158-173.

6. Holland, D., Feller, S., Kemp, T. F., Smith, M. E., Howes, A., Winslow, D., Kodama, M. *Physics and Chemistry of Glasses-European Journal of Glass Science and Technology Part B* 2007, **48**, 1-8.
7. Bray, P. J., Feller, S. A., Jellison, G. E., Yun, Y. H. *Journal of Non-Crystalline Solids* 1980, **38**, 93-98.
8. Kroeker, S., Aguiar, P. M., Cerquiera, A., Okoro, J., Clarida, W., Doerr, J., Olesiuk, M., Ongie, G., Affatigato, M., Feller, S. A. *Physics and Chemistry of Glasses-European Journal of Glass Science and Technology Part B* 2006, **47**, 393-396.
9. Clarida, W., Berryman, J., Affatigato, M., Feller, S., Kroeker, S., Ash, J., Zwanziger, J., Meyer, B., Borsa, F., Martin, S. *Physics and Chemistry of Glasses* 2003, **44**, 215-217.
10. Bray, P., O'Keefe, J. *Phys. Chem. Glasses* 1963, **4**, 37-46.
11. Shelby, J. E., *Introduction to Glass Science and Technology*; Royal Society of Chemistry, 2005.
12. Doweidar, H. *Journal of Materials Science* 1990, **25**, 253-258.
13. Kapoor, S., Bola George, H., Betzen, A., Affatigato, M., Feller, S. *Journal of Non-Crystalline Solids* 2000, **270**, 215-222.
14. Affatigato, M., Feller, S., Khaw, E. J., Feil, D., Teoh, B., Mathews, O. *Physics and Chemistry of Glasses* 1990, **31**, 19-24.
15. Wright, A. C. *International Journal of Applied Glass Science* 2015, **6**, 45-63.
16. Henderson, G. *Journal of Non-Crystalline Solids* 2007, **353**, 1695-1704.
17. Henderson, G. S. *European Journal of Mineralogy* 2002, **14**, 733-744.
18. Gee, I., Hussin, R., Holland, D., McConville, C., Mekki, A. *Physics and Chemistry of Glasses* 2000, **41**, 175-181.
19. Di Martino, D., Santos, L., Marques, A., Almeida, R. *Journal of Non-Crystalline Solids* 2001, **293**, 394-401.
20. Yiannopoulos, Y. D., Varsamis, C. P. E., Kamitsos, E. I. *Journal of Non-Crystalline Solids* 2001, **293-295**, 244-249.
21. Hannon, A. C., Di Martino, D., Santos, L. F., Almeida, R. M. *Journal of Non-Crystalline Solids* 2007, **353**, 1688-1694.
22. Wang, H., Henderson, G. *Physics and Chemistry of Glasses* 2005, **46**, 377-380.
23. Nanba, T., Kieffer, J., Miura, Y. *Journal of Non-Crystalline Solids* 2000, **277**, 188-206.
24. Kamitsos, E., Chrysikos, G. D., *Vibrational Structural Studies of Alkali Borate Glasses*. 1991.
25. Dwivedi, B., Khanna, B. *Journal of Physics and Chemistry of Solids* 1995, **56**, 39-49.
26. Sinclair, R. N., et al. *Physics and Chemistry of Glasses: European Journal of Glass Science and Technology Part B* 2006, **47**, 405-411.
27. Howes, A., Vedishcheva, N., Samoson, A., Hanna, J. V., Smith, M. E., Holland, D., Dupree, R. *Physical Chemistry Chemical Physics* 2011, **13**, 11919-11928.
28. Barrio, R. A., Castillo-Alvarado, F., Galeener, F. L. *Physical Review B* 1991, **44**, 7313.
29. Kamitsos, E., Chrysikos, G. D. *Journal of Molecular Structure* 1991, **247**, 1-16.
30. Konijnendijk, W. L., Stevels, J. M. *Journal of Non-Crystalline Solids* 1975, **18**, 307-331.
31. Arima, H., Kawamata, T., Sugiyama, K. *Journal of Mineralogical and Petrological Sciences* 2015, **110**, 60-64.
32. Hoppe, U., Kranold, R., Weber, H.-J., Hannon, A. *Journal of Non-Crystalline Solids* 1999, **248**, 1-10.
33. Hannon, A. C., Di Martino, D., Santos, L. F., Almeida, R. M. *Journal of Physical Chemistry B* 2007, **111**, 3342-3354.
34. Hoppe, U., Kranold, R., Weber, H.-J., Neufelind, J., Hannon, A. *Journal of Non-Crystalline Solids* 2000, **278**, 99-114.
35. Ueno, M., Misawa, M., Suzuki, K. *Physica B+ C* 1983, **120**, 347-351.
36. Soltay, L. G., Henderson, G. S. *The Canadian Mineralogist* 2005, **43**, 1643-1651.

37. Henderson, G. S., Fleet, M. E. *Transactions of the American Crystallographic Association* 1991, 27, 269-278.
38. Mochida, N., Sakai, K., Kikuchi, K. *Yogyo-Kyokai-Shi* 1984, 92, 164-172.
39. Verweij, H., Buster, J. *Journal of Non-Crystalline Solids* 1979, 34, 81-99.
40. Furukawa, T., White, W. B. *Journal of Materials Science* 1980, 15, 1648-1662.
41. Lee, S. K., Kim, H. N., Lee, B. H., Kim, H.-I., Kim, E. J. *Journal of Physical Chemistry B* 2009, 114, 412-420.
42. Soper, A. K. *Journal of Physics: Condensed Matter* 2011, 23, 365402.
43. Brese, N., O'Keefe, M. *Acta Crystallographica Section B: Structural Science* 1991, 47, 192-197.
44. Feller, S., Lower, N., Affatigato, M. *Physics and Chemistry of Glasses* 2001, 42, 240-246.
45. Ma, C., Kiczinski, T., McRae, J., Affatigato, M., Feller, S. *Physics and Chemistry of Glasses* 2000, 41, 365-368.
46. Youchak, A. L., Shelby, J. E. *Physics and Chemistry of Glasses-European Journal of Glass Science and Technology Part B* 2007, 48, 307-312.
47. Mansour, E. *Physica B: Condensed Matter* 2010, 405, 281-286.
48. Chakraborty, I. N., Condrate, R. A. *Journal of the American Ceramic Society* 1983, 66.
49. Chakraborty, I., Condrate Sr, R., The Raman Spectra of Potassium Borogermanate Glasses. In *Advances in Materials Characterization*, Springer: 1983; pp 223-237.
50. Chakraborty, I. N., Condrate, R. A. *Journal of Non-Crystalline Solids* 1986, 81, 271-284.
51. Takuji Yoshimura, J. F., Masayoshi Ihara. *Yogyo-Kyokai-Shi* 1971, 79, 428-434.
52. In *SciGlass Professional 7.3*, ITC Inc.: 2008.
53. Kiczinski, T., Ma, C., Hammarsten, E., Wilkerson, D., Affatigato, M., Feller, S. *Journal of Non-Crystalline Solids* 2000, 272, 57-66.
54. Du, L.-S., Stebbins, J. F. *Journal of Non-Crystalline Solids* 2003, 315, 239-255.
55. Alderman, O. L. G. The Structure of Vitreous Binary Oxides: Silicate, Germanate and Plumbite Networks. PhD Thesis, Warwick, Warwick 2013.
56. Barney, E. R., Hannon, A. C., Holland, D., Umesaki, N., Tatsumisago, M., Orman, R. G., Feller, S. *Journal of Physical Chemistry Letters* 2013, 4, 2312-2316.
57. Barney, E., Hannon, A., Holland, D., Umesaki, N., Tatsumisago, M. *Journal of Non-Crystalline Solids* 2015, 414, 33-41.
58. Soper, A. *Rutherford Appleton Laboratory Technical Report* 2011.
59. Shimbo, M. *Journal of the Ceramic Association, Japan* 1968, 76, 431-432.
60. Ihara, M. *Yogyo-Kyokai-Shi* 1971, 79, 152-155.
61. Cormier, L., Calas, G., Beuneu, B. *Journal of Non-Crystalline Solids* 2007, 353, 1779-1784.
62. Majérus, O., Cormier, L., Calas, G., Soper, A. *Physica B: Condensed Matter* 2004, 350, 258-261.
63. Hannon, A., Holland, D., 2016.

Chapter 8 – Conclusions and future work

8.1 Introduction

This chapter concludes the study by summarising Chapter 5 (Lithium tellurite) and Chapter 6 (Lead tellurite) into a section on tellurite glass structure, and Chapter 7 (Alkali borogermanate glasses) into a section on borogermanate glass structure. Future work to be considered is also included in this chapter.

8.2 Tellurite glasses

In this thesis, the structure of tellurite glasses was studied by controlling the type of the second (modifier) oxide used. For the first study, a monovalent typical modifier Li^+ cation was used in the form of Li_2O , whilst for the second study, the more complex divalent Pb^{2+} cation (with $6s^2$ lone-pair of electrons) in the form of PbO was used. Unlike Li^+ , Pb^{2+} is reported to behave as a modifier at low PbO content, and more like an intermediate (conditional network former) at much higher PbO content. Moreover, Pb^{2+} has the active lone pair of electrons which may interact with the $5s^2$ lone pair of Te hence affecting the TeO_2 network differently than the Li^+ ion.

Two tellurite glass series of 10, 15, 20, 25, and 30 mol% Li_2O and 10, 12.5, 15, 17.5, and 20 mol% PbO were made. The nominal compositions of the glasses were confirmed to be close to nominal by comparing density values with those from the SciGlass database (in addition, for PbO-TeO_2 the composition was confirmed by EDX). In $\text{Li}_2\text{O-TeO}_2$, the density decreases as TeO_2 increases due to the larger atomic mass of Te ($\text{Te} = 52 \text{ a.m.u.}$). For PbO-TeO_2 however, since Pb is heavier than Te ($\text{Pb} = 82 \text{ a.m.u.}$), the density decreases as TeO_2 content increases. Excluding the mass contribution, molar volume values revealed that, as TeO_2 decreases, the molar volume value decreases in both Li and Pb modified tellurite glasses, where smaller molar volume is observed for $\text{Li}_2\text{O-TeO}_2$, compared to PbO-TeO_2 glasses, mainly due to the size of Li^+ which is smaller than Pb^{2+} . Consequently, number density for Li^+ is higher than for Pb^{2+} . From the number density analysis, similar trends are observed in both Te and O environments which suggest that changes to the TeO_2 network occur in both of these glass systems. The molar volume and number density plots for Li and K are compared in Fig. 8.1. In each plot in Fig. 8.1, polynomial fit lines are drawn as guides to the eye to suggest possible behaviour of each parameter from pure TeO_2 glass to the binary tellurite glasses. It should be noted, however, that pure TeO_2 glass and the binary tellurite

($\text{Li}_2\text{O}-\text{TeO}_2$ and $\text{PbO}-\text{TeO}_2$) glasses were prepared using two different preparation methods, where the pure TeO_2 glass was roller-quenched, whilst the latter were splat-quenched with slower cooling rate.

In tellurite glasses, these 5 basic units are often associated when describing the glass structure; $[\text{TeO}_{4/2}]$, $[\text{TeO}_{2/2}\text{O}]$, $[\text{TeO}_{3/2}\text{O}^-]$, $[\text{TeO}_{1/2}\text{O}_2^-]$, and $[\text{TeO}_3^{2-}]$. From Raman spectroscopy however, these units are simplified into only two; $[\text{TeO}_4]$ and $[\text{TeO}_3]$ units. The Raman spectra for both $\text{Li}_2\text{O}-\text{TeO}_2$ and $\text{PbO}-\text{TeO}_2$ glasses are similar, showing the various vibrations of Te-O bonds in $[\text{TeO}_4]$ and $[\text{TeO}_3]$ units, and it is concluded that, as Li_2O / PbO is added to the glass network, $[\text{TeO}_4]$ units are being converted to $[\text{TeO}_3]$.

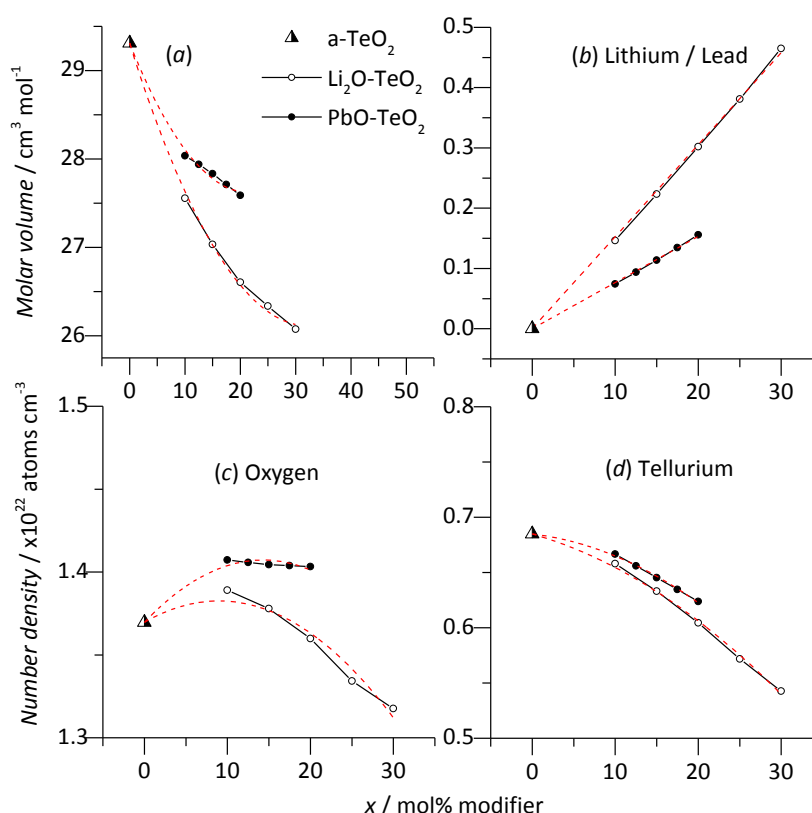


Figure 8.1: Molar volume and number density for constituent atoms in $\text{Li}_2\text{O}-\text{TeO}_2$ and $\text{PbO}-\text{TeO}_2$ glasses. Red dashed line is a guide-to-the-eye fit, connecting the glasses and the pure- TeO_2 glass (a-TeO_2).

The Te environment in $\text{Li}_2\text{O}-\text{TeO}_2$ glasses is obtained from neutron diffraction of null lithium isotope glasses to remove Li-O partials which overlap with the Te-O distances, whereas in $\text{PbO}-\text{TeO}_2$, the Te (as well as Pb) environment is obtained from combined neutron and X-ray diffraction where the O-O peak (which overlaps with the Pb-O distance) is contrasted. The average coordination number of Te-O, n_{TeO} shows two regions; plateau (independent of cation type), and post-plateau (dependent of cation type). $n_{\text{TeO}}(\text{Li})$ and $n_{\text{TeO}}(\text{Pb})$ are

compared with $n_{\text{TeO}}(\text{K})$ from [1] as in Fig 8.2. In the plateau region, the cation induces silica-like changes to the tellurite structure by creating non-bridging oxygen NBO atoms, which maintains n_{TeO} as found in pure TeO_2 glass [1] until a certain “deviation” composition x_D where the NBO produced are insufficient and more NBO atoms are created by breaking the Te-O bond. This transforms a $[\text{TeO}_4]$ to a $[\text{TeO}_3]$ unit and the average n_{TeO} decreases. The transformation process is described as $[\text{TeO}_4] \rightarrow b[\text{TeO}_3]$, where b is the number of Te-O bonds broken, which is also equal to the number of $[\text{TeO}_3]$ units produced. b is seen to be dependent on the cation type where, smaller Li^+ (0.59 Å) has the lowest b value of 0.8, whilst for slightly larger K^+ (1.38 Å), the b value increases to 1.5. Pb^{2+} (1.29 Å) is slightly smaller than K^+ , the b value is however larger. This means that b is not just a function of cation size. The origin of the large b value for Pb^{2+} maybe speculated to arise from its lone pair activity. For future work, Tl^+ is a suitable candidate to be studied since it also has a lone pair and it behaves like an alkali metal in glasses. To improve the existing datasets and have better confidence in the b values, $\text{Li}_2\text{O}-\text{TeO}_2$, and $\text{PbO}-\text{TeO}_2$ glasses with lower and higher compositions (as well as more detailed increments) could be prepared by roller-quenching. The average n_{TeO} values in the post plateau region can be represented by;

$$n_{\text{TeO}}(x)_{\text{post-plateau}} = n_{\text{TeO}}(x)_{\text{plateau}} - b \left[\frac{x}{100} - x_D \right] \quad 8.1$$

where $n_{\text{TeO}}(x)_{\text{plateau}}$ (i.e. the dashed line in Fig. 8.2), b , and x_D are variables. To be able to accurately determine the value of each variable, more data points are required. From this relationship, it is seen that the value of b depends on the value of x_D (which depends on the value of $n_{\text{TeO}}(x)_{\text{plateau}}$).

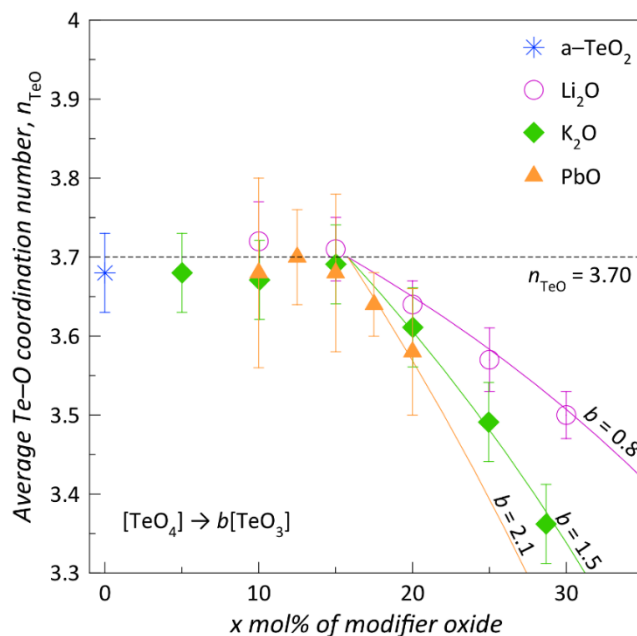


Figure 8.2: n_{TeO} for $\text{Li}_2\text{O}-\text{TeO}_2$, $\text{K}_2\text{O}-\text{TeO}_2$, and $\text{PbO}-\text{TeO}_2$ glasses

The Li^+ environment in $\text{Li}_2\text{O}-\text{TeO}_2$ glasses was studied for 10, 15, 20, 25, and 30 mol% Li_2O glasses by using isotope substitution neutron diffraction, whilst the Pb^{2+} environment in $\text{PbO}-\text{TeO}_2$ glass for 10, 12.5, 15, 17.5, and 20 mol% PbO was extracted from X-ray and neutron diffraction data. For Li^+ , in all compositions, Li^+ behaves as a modifier. The average n_{LiO} was found to be 5 at 10 and 15 mol%, decreasing to 4.5 at 20 mol% and 4 at 25 and 30 mol%. For $n_{\text{LiO}} > 4$, the LiO unit can be regarded as $[\text{LiO}_{4+1}]$ with 4 almost equal distances at about 1.967 Å and another longer distance at 2.233 Å (Whilst the classification of these $[\text{LiO}_{4+1}]$ units is unclear, they can be regarded as a mixture of $[\text{LiO}_4]$ and $[\text{LiO}_{4+1}]$, but not $[\text{LiO}_5]$). These distances are also found in one of the Li sites in the high temperature phase of $\beta\text{-Li}_2\text{Te}_2\text{O}_5$. In $\text{PbO}-\text{TeO}_2$ glasses, at these low PbO contents (10 – 20 mol% PbO), Pb^{2+} behaves as a modifier with average $n_{\text{PbO}} = 8$ and 1 broad distribution centred at $r_{\text{PbO}} = 2.58$ Å. (From bond valence calculation [2], symmetric $[\text{PbO}_7]$ and $[\text{PbO}_8]$ have r_{PbO} distances of 2.58 Å and 2.62 Å, respectively). The PbO peak shape and distance in all the compositions resemble the (short-range order) PbO peak as found in $\text{PbTe}_5\text{O}_{11}$, the crystal with the composition closest to the glasses studied. For future work, the study of $\text{PbO}-\text{TeO}_2$ glasses at high PbO contents (> 50 mol% PbO), where Pb^{2+} is likely to behave as a glass former will be useful to elucidate the interaction of the $5s^2$ lone-pair of Te^{4+} with the $6s^2$ lone-pair of Pb^{2+} . For further understanding of the environments of Te^{4+} and $\text{Li}^+/\text{Pb}^{2+}$ in lithium and lead tellurite glasses, the structure factors which were obtained experimentally could be simulated, for instance using Reverse Monte Carlo, molecular dynamics, or Empirical Potential Structure Refinement [3] method.

8.3 Borogermanate glasses

Nine compositions of Ge-rich lithium and potassium borogermanate glasses were made for 10, 20, and 30 mol% M_2O for each 10, 20, and 30 $\text{BO}_{1.5}$ series, as shown in Fig. 8.3. The density and molar volume of the ternary glasses change similarly as the alkali germanate glasses, due to the compositional factor of Ge atom. From number density analysis, both B and Ge in both systems change in a similar fashion to alkali borate and germanate glasses, respectively, suggesting that B and Ge change their environments in each B series as a function of alkali content. This is also supported by the Raman analysis. These glasses were made in those compositions so that the germanate environments (anomaly) can be studied. To analyse the boron environment in terms of previous studies on borosilicate glasses, the compositions are converted into R ($\text{M}_2\text{O}/\text{B}_2\text{O}_3$) and K ($\text{GeO}_2/\text{B}_2\text{O}_3$) values which produces

limited $N_4=f(K,R)$ lines. It was found out that $N_4=f(K,R)$ in KBG and LBG glasses changes in a similar fashion to the sodium borosilicate (NBS) model by Dell and Bray *et al.* [4] and the lithium borosilicate model (LBS) model by Zhong *et al.* [5] respectively.

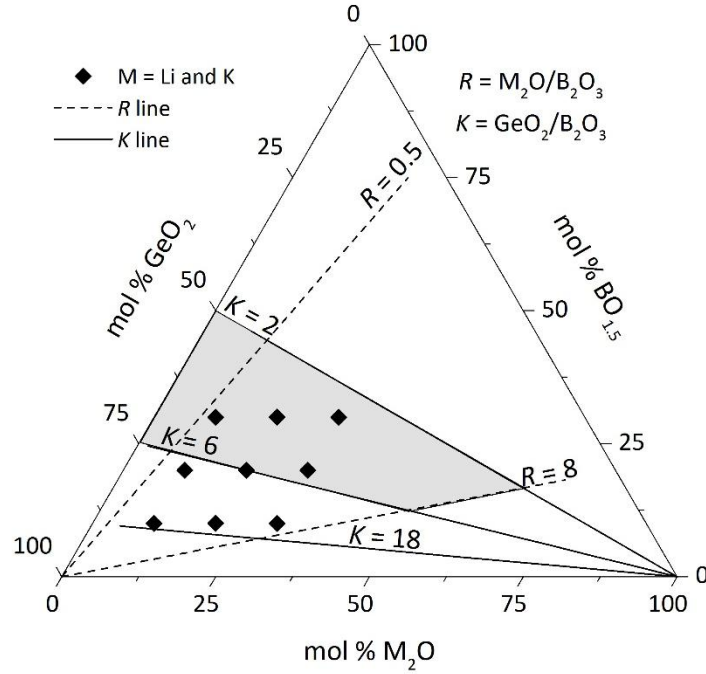


Figure 8.3: Glass compositions of $M_2O-BO_{1.5}-GeO_2$ for $M = Li$ and K in this study

For Ge, $n_{GeO}(K)$ shows a maximum at 20 mol% K_2O content in each B series, however for $n_{GeO}(Li)$, n_{GeO} increases as a function of Li_2O content with the absence of the maxima. In LBG, experimental n_{GeO} follows the values predicted for the absence of NBO for all Li_2O contents. For KBG however, at high (30 mol% K_2O in all B series), the discrepancy of the number of K^+ ions (where $K^+_{Total} < K^+_B + K^+_{Ge}$) indeed suggests that at this composition, NBO are present in the glass. Based on the different trends of n_{BO} and n_{GeO} obtained for lithium and potassium borogermanate glasses, it is inferred that Li^+ and K^+ induce non-isostructural changes to the borogermanate network, making the investigation of Li^+ and K^+ environments using isostoichiometric neutron diffraction method invalid. For Li^+ however, the environment is extracted for 20 Li_2O mol% samples in each B series using the difference nat – null (isotope substitution) neutron diffraction technique. Two $Li-O$ peak distances are obtained, and assigned to the distance of $Li-O_B$ (shorter, 1.75 Å) and $Li-O_{Ge}$ (1.98 Å) based on the trend of peak areas as a function of $BO_{1.5}$ or GeO_2 composition, and also by comparison to the approximate crystal structure of $LiBGeO_4$. In all samples, n_{LiO} was found to range from 4 to 5, where Li^+ behaves as a simple modifier. For future work, n_{LiO} for the rest of the samples would be obtained to study the effects of Li^+ environment on Ge (if the Ge anomaly is really

absent) in LBG glasses. To study the K^+ environment closely, it would be useful to have the diffraction data for sodium borogermanate glasses since Na^+ is likely to behave similarly as K^+ , hence the environments of Na^+ and K^+ can be obtained by the isostoichiometric neutron diffraction method. For recommendations, LBG and KBG samples with compositions similar to the LBS and NBS studied by Bray and co-workers should also be prepared so more detailed study of the B environment in borogermanate glasses can be done.

8.4 References

1. Barney, E. R., Hannon, A. C., Holland, D., Umesaki, N., Tatsumisago, M., Orman, R. G., Feller, S. *Journal of Physical Chemistry Letters* 2013, 4, 2312-2316.
2. Brese, N., O'Keefe, M. *Acta Crystallographica Section B: Structural Science* 1991, 47, 192-197.
3. Alderman, O. L. G. The Structure of Vitreous Binary Oxides: Silicate, Germanate and Plumbite Networks. PhD Thesis, Warwick, Warwick, 2013.
4. Dell, W. J., Bray, P. J., Xiao, S. Z. *Journal of Non-Crystalline Solids* 1983, 58, 1-16.
5. Zhong, J., Wu, X., Liu, M., Bray, P. *Journal of Non-Crystalline Solids* 1988, 107, 81-87.

Appendix A

A.1 Unit nomenclature

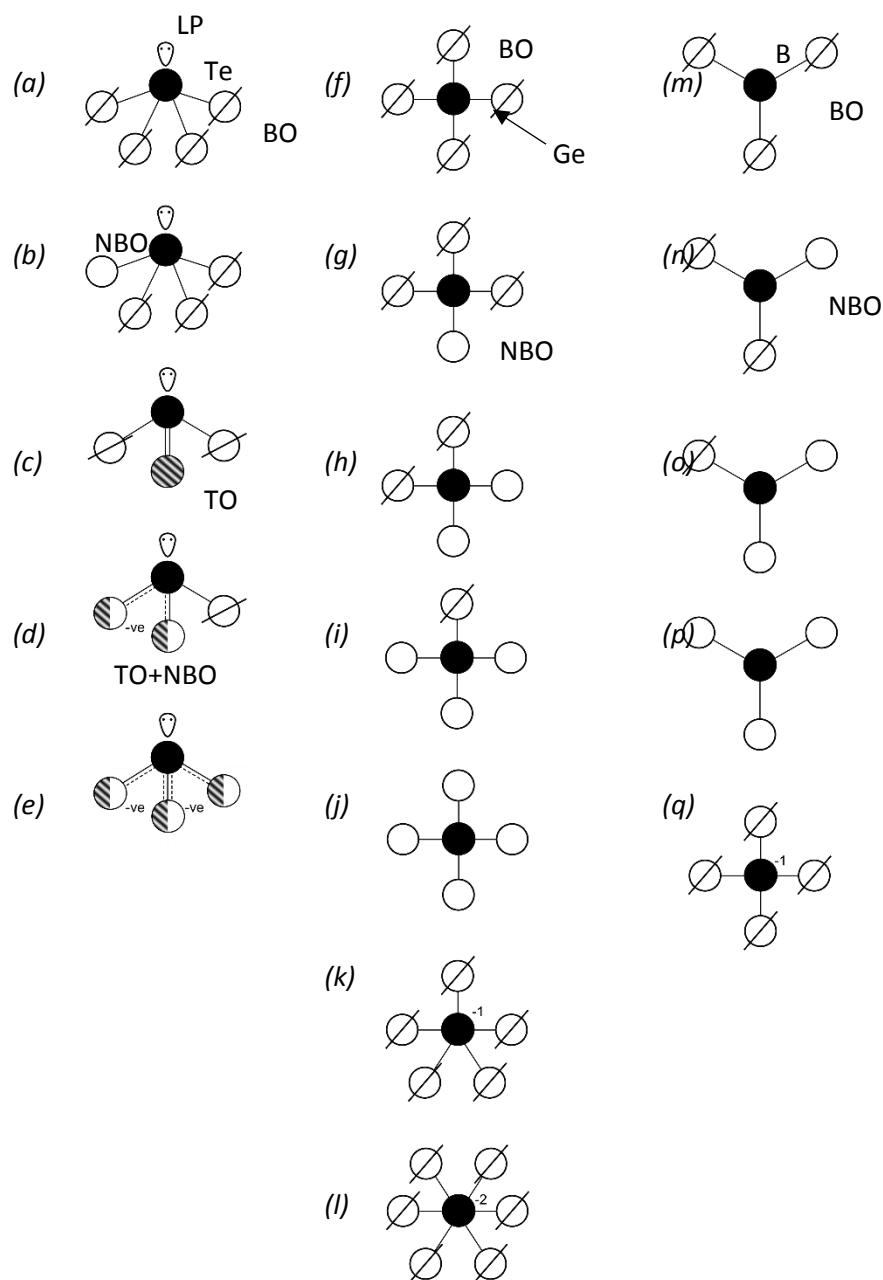


Figure A.1: Units of tellurite, germanate, and borates in glasses

Figure A.1 shows the species/units often used when describing the structure of tellurite (a – e), germanate (f – l), and borate (m – q) glasses. In the figure, the network former cations (Te^{4+} , Ge^{4+} , and B^{3+}) are represented by the black solid circle. The bridging oxygen BO (crossed

circle), non-bridging oxygen NBO (empty circle), terminal oxygen TO (striped circle), and terminal–non-bridging resonance oxygen TO+NBO (half striped, half empty) are labelled accordingly. The nomenclature of these units are shown as in Table A.1. For example for $\text{TeO}_{4/2}$ unit, or $[\text{TeO}_{4/2}]$, the Te is connected to bridging oxygen BO ($\text{O}_{1/2}$) atoms; 1 Te to 4 BO = $[\text{TeO}_{4/2}]$. For $\text{TeO}_{3/2}\text{O}^-$, 1 Te is connected to 3 BO ($\text{O}_{1/2}$) and 1 NBO (O^-), and for $\text{TeO}_{1/2}\text{O}_2^-$, 1 Te is connected to 1 BO ($\text{O}_{1/2}$) and 1 NBO (O^-) + 1 TO (O), where 1 NBO and 1 TO resonate as (O_2^-).

In terms of Q-speciation, for Te, Q is represented as Q^m_n where m and n are the numbers of bridging oxygen and total oxygen bonded to Te, respectively. Whereas for Ge, Q^n is used, where n is the number of bridging oxygens.

Table A.1: Nomenclature of tellurite, germanate and borate units

System	Unit		Q-speciation /
Tellurite	<i>a</i>	$\text{TeO}_{4/2}$	Q^4_4
	<i>b</i>	$\text{TeO}_{3/2}\text{O}^-$	Q^3_4
	<i>c</i>	$\text{TeO}_{2/2}\text{O}$	Q^2_3
	<i>d</i>	$\text{TeO}_{1/2}\text{O}_2^-$	Q^1_3
	<i>e</i>	TeO_3^{2-}	Q^0_3
Germanate	<i>f</i>	$\text{GeO}_{4/2}$	Q^4
	<i>g</i>	$\text{GeO}_{3/2}\text{O}^-$	Q^3
	<i>h</i>	$\text{GeO}_{2/2}\text{O}_2^{2-}$	Q^2
	<i>i</i>	$\text{GeO}_{1/2}\text{O}_3^{3-}$	Q^1
	<i>j</i>	GeO_4^{4-}	Q^0
	<i>k</i>	GeO_5^-	–
	<i>l</i>	GeO_6^{2-}	–
Borate	<i>m</i>	$\text{BO}_{3/2}$	–
	<i>n</i>	$\text{BO}_{2/2}\text{O}^-$	–
	<i>o</i>	$\text{BO}_{1/2}\text{O}_2^{2-}$	–
	<i>p</i>	BO_3^{3-}	–
	<i>q</i>	BO_4^-	–